Novel Analysis and Calibration Techniques for the Simultaneous Measurement of Plasma Ion Temperatures and Velocities using Multi-Delay Coherence Imaging

Mr. Rhys Seán Doyle B.Sc.

A dissertation submitted in fulfilment of the
requirements for the award of
Doctor of Philosophy (Ph.D.)

presented to the
School of Physical Sciences
Dublin City University

Supervisors:
Prof. Miles Turner
Dr. Huw Leggate

June 2025

Declaration

I hereby certify that this material, which I now submit for assessment on the programme of study leading to the award of Doctor of Philosophy is entirely my own work, that I have exercised reasonable care to ensure that the work is original, and does not to the best of my knowledge breach any law of copyright, and has not been taken from the work of others save and to the extent that such work has been cited and acknowledged within the text of my work.

Signed: Rhys Seán Doyle

Student ID: 15364306

Date: 13th June, 2025

Publications

Peer Reviewed Publication

During the course of this research the following peer reviewed paper was published:

- Based on chapter 3: R. S. Doyle, N. Lonigro, J. S. Allcock, S. A. Silburn, M. M. Turner, X. Feng, H. Leggate; Development and calibration of a multi-delay coherence imaging diagnostic on the MAST-U tokamak. Rev. Sci. Instrum. 1 May 2024; 95 (5): 053505. https://doi.org/10.1063/5.0205584

Poster Contributions

Additionally, the following posters have been presented at conferences:

- Development and Initial Results of the MAST-U Coherence Imaging Spectroscopy Diagnostic - 49th European Conference Conference on Plasma Physics, Bordeaux, France.
- Simultaneous inversion of synthetic C III temperatures and velocities in MAST-U Super-X using Coherence Imaging Spectroscopy - 48th European Conference Conference on Plasma Physics - Online

Contents

List of Figures vi

List of Tables ix

Abbreviations xi

Abstract xii

Acknowledgements xiii

1 Introduction 1
- 1.1 Fusion Energy . . . 2
- 1.2 Magnetic Confinement Fusion . . . 4
  - 1.2.1 The Mega Ampere Spherical Tokamak Upgrade . . . 5
- 1.3 Fusion Power Exhaust Problem . . . 7
  - 1.3.1 MAST-U Super-X Divertor . . . 8
- 1.4 Diagnosing Fusion Devices . . . 10
  - 1.4.1 Mach Probes . . . 11
  - 1.4.2 Line-Integrated Spectroscopy . . . 12
  - 1.4.3 Retarding Field Energy Analysers . . . 13
- 1.5 Motivation . . . 14
- 1.6 Thesis Outline . . . 15

2 Coherence Imaging Spectroscopy 17
- 2.1 Impurity Line Emission . . . 17
  - 2.1.1 Spectral Lineshape Models . . . 18
- 2.2 Introduction to Interferometry . . . 21
- 2.3 Fourier Transform Spectroscopy . . . 25
  - 2.3.1 Quasi-monochromatic Light . . . 26
  - 2.3.2 Delay Dispersion . . . 32
  - 2.3.3 Inhomogeneous Sources . . . 33
- 2.4 Polarisation Interferometry . . . 35
  - 2.4.1 Uniaxial Crystals . . . 36
  - 2.4.2 Stokes Vectors . . . 39
  - 2.4.3 Mueller Calculus . . . 40
  - 2.4.4 General Imaging System . . . 42
- 2.5 Single-Delay CIS . . . 44

2.5.1 Linear Phase Mask . . . 45
2.5.2 Pixelated Phase Mask . . . 48
2.6 Multi-Delay CIS . . . 50
2.7 Previous CIS Investigations . . . 52
2.8 Summary . . . 55

3 MAST-U Coherence Imaging Diagnostic 56
3.1 Triple-Delay Coherence Imaging . . . 57
3.1.1 CIS Design . . . 58
3.2 MWI Related Issues . . . 63
3.2.1 CIS Focus Planes . . . 63
3.2.2 CIS Ghosting . . . 65
3.3 Interferogram Demodulation . . . 67
3.4 Diagnostic Calibration . . . 70
3.4.1 Wavelength Dependant Behaviour . . . 72
3.4.2 Temperature Dependant Behaviour . . . 84
3.4.3 Determining Calibration Parameters . . . 91
3.4.4 Camera Photon Transfer Curve . . . 94
3.5 Summary . . . 95

4 Simultaneous Measurement of C III Temperatures and Velocities 97
4.1 Modelling the Lineshape of Carbon III . . . 98
4.2 Simultaneous Fitting Technique . . . 100
4.2.1 Flow and Temperature Inversion Method . . . 101
4.2.2 Synthetic Testing . . . 108
4.3 Spectral Contamination . . . 118
4.3.1 Continuum Emission . . . 118
4.3.2 Oxygen Contamination . . . 120
4.3.3 Zeeman Splitting . . . 122
4.3.4 Performance Comparison - Single-Delay . . . 125
4.4 MAST-U Experiments . . . 127
4.4.1 Line-of-sight Integrated Data . . . 131
4.4.2 2D Poloidal Profiles . . . 139
4.4.3 Comparison with Simulations . . . 147
4.5 Summary . . . 157

5 Summary and Future Work 159
5.1 Triple-Delay Coherence Imaging . . . 159
5.2 Calibration Procedures . . . 160
5.3 MAST-U CIS Measurements of Temperature and Velocity . . . 162
5.4 Future Work . . . 164
5.4.1 Diagnostic Knowledge and Upgrades . . . 164
5.4.2 Physics Studies . . . 166

A Component Specifications 168

B Triple-Delay CIS Mueller Matrices **170**

C General CIS Phase Equations **172**
C.1 Single-Delay 173
C.2 Quad-Delay 173

Bibliography **175**

List of Figures

1.1 Schematic of a Tokamak 5
1.2 Cross-section of the MAST-U tokamak 6
1.3 MAST-U Divertor Geometries 9

2.1 Measured interferogram intensity as a function of delay, for different spectra 28
2.2 Schematic showing the coordinates used to define ray paths through a uniaxial crystal 37
2.3 Diagrams of how a uniaxial crystal creates an optical path difference between orthogonal polarisation states. 38
2.4 General CIS interferometer setup 43
2.5 Variation of incidence angle and azimuthal angle across CIS sensor 44
2.6 Interferograms produced by a simple polariser-crystal-polariser interferometer with $\theta = 0°$, $3°$ and $0°$ 45
2.7 Plot showing how instrumental contrast decreases with fringe width. 46
2.8 Plot of how contrast and phase vary with delay for singlet spectra 47
2.9 Schematic of single-delay CIS instrument 49
2.10 Schematic of quad-delay CIS instrument 51

3.1 Orientation of the CIS components for a triple-delay CIS system 59
3.2 Simulated triple-delay CIS image of a Super-X MAST-U plasma 59
3.3 Modelled interferometer delays for triple-delay pixelated system 60
3.4 Schematic and image of the MAST-U MWI 61
3.5 Detailed schematic of triple-delay pixelated CIS interferometer . 61
3.6 Diagram showing our angular misalignment in a polychromator can cause ghosting 65
3.7 Calibration image taken before and after ghosting was eliminated on MAST-U CIS 66
3.8 Figure showing the raw Cd calibration image captured by our instrument along with the raw and synchronous product PSDs . 68
3.9 Optical bench setup for measuring the phase images used to characterise the dispersion of our instrument 72
3.10 Phase difference between 467.82 and 468.01 nm, showing a clear hyperbolic pattern 73
3.11 Comparison of fit residuals for single wavelength of a misaligned system 74

3.12 Images of CIS mounting cogs and temperature controlled cell . . 75
3.13 Optical bench angular testing setup - quad-delay system 76
3.14 Phase differences measured at various degrees of misalignment for a triple-delay system 78
3.15 Comparison of measured and calculated phase differences for a misaligned system 80
3.16 Phase difference on which our fitting of instrument parameters was conducted 81
3.17 Comparison of how to the fit residuals vary when fitting with and without misalignment effects accounted for 83
3.18 Schematics of the voltage dividing circuit and temperature measurement circuit used for temperature characterisation 86
3.19 Image of the Arduino Uno device used for temperature measurement 87
3.20 Comparison of measured and calculated phase difference for each interferometer crystal assuming ideal temperature effects . 88
3.21 Fit parameters calculated during temperature characterisation . 89
3.22 Comparison between the change in the measured ϕ_{2+1} and ϕ_{2-1} terms with those calculated using eq. (3.20) 90
3.23 Comparison of temperature characterisation performance 91
3.24 Graph showing the have the retardance of the QWP used in this study varies with wavelength 93
3.25 Photon transfer and signal-to-noise curves for the FLIR camera used in this study 94

4.1 Emission spectrum of C II and C III showing their multiplet structure 98
4.2 MAST-U sightline span for typical ED and SXD magnetic geometries 102
4.3 Profiles showing the ability of the SART algorithm used in this study to recover emissivity profiles from noisy intensity images . 109
4.4 Expected standard deviation in phase and contrast across the range of possible DC and contrast values 111
4.5 Comparison of velocity inversion performance using noisy input data generated from a SOLPS-ITER simulation of shot #46860 113
4.6 Comparison of temperature inversion performance using noisy input data generated from a SOLPS-ITER simulation of shot #46860 114
4.7 Comparison of velocity inversion performance using noisy input data generated from a SOLPS-ITER simulation of shot #47079 115
4.8 Comparison of temperature inversion performance using noisy input data generated from a SOLPS-ITER simulation of shot #47079 116
4.9 MAST-U CIS sightline coverage for a typical ED and SXD magnetic geometry 117
4.10 Filter bandpass for the C III spectral filter used in this study . . 119

4.11 Contrast response vs interferometer delay of the filter bandpass used in this study . . . 120
4.12 Estimated effect of Zeeman splitting on each CIS delay for MAST-U . . . 124
4.13 Comparison of inversion performance using a triple and single-delay CIS and spectrally contaminated data . . . 126
4.14 Summary plots of MAST-U shots #48333 and #48334 . . . 128
4.15 Comparison between simulated and measured upstream plasma profiles for the SXD and ED shots used in this study . . . 130
4.16 Experimental interferograms and DC measured by the MAST-U CIS during MU03 . . . 132
4.16 Figure showing raw interferogram and extracted DC images for the MAST-U shots used in this research . . . 133
4.17 Demodulated Phase and Contrast Images for Shot #48333 . . . 134
4.18 Demodulated Phase and Contrast Images for Shot #48334 . . . 135
4.19 PSD for shot #48333 showing cause of striping artefacts in our MAST-U data . . . 138
4.20 Line-integrated velocity and temperature measurements following Fourier filtering for shot #48333 . . . 140
4.21 Line-integrated velocity and temperature measurements following Fourier filtering for shot #48334 . . . 141
4.22 Inverted 2D profiles of C III emissivity, velocity and temperature for shot #48333 . . . 142
4.23 Inverted 2D profiles of C III emissivity, velocity and temperature for shot #48334 . . . 143
4.24 Comparison of the calculated and measured C III spectra obtained from shot #48333 . . . 145
4.25 Comparison of the calculated and measured C III spectra obtained from shot #48334 . . . 146
4.26 C III emission profiles for the SOLPS-ITER profiles and CIS measurements used in this study . . . 149
4.27 Comparison between simulation and inverted C III velocity profiles used in this study . . . 151
4.28 Comparison between the simulated and inverted SXD 1D velocity profiles as a function of distance from the C III front . . . 152
4.29 Comparison between the simulated and inverted ED 1D velocity profiles as a function of distance from the C III front . . . 153
4.30 Comparison between simulation and inverted C III temperature profiles for the shots used in this study . . . 155
4.31 Comparison between the simulated and inverted 1D temperature profiles as a function of distance from the C III front . . . 156

List of Tables

3.1 Nominal and optimised instrument parameters for the MAST-U CIS system, where f_3 is the focal length of system imaging lens and ρ is the orientation of a given component in the interferometer cell. 82

3.2 Nominal and optimised crystal specific parameters for the MAST-U CIS system. ψ_x and ψ_y are the tilts of each crystal about the x and y axis of the instrument, respectively. θ is the cut angle of the crystal and A_e, B_e, C_e, D_e are the Sellmeier coefficients of the crystal. 82

4.1 Given are the accepted relative intensities, I_i of each C III emission line along with the relative frequency difference, $\Delta\nu_i = (\nu_i - \nu_c)/\nu_c$ between the line's emission frequency and the centre-of-mass frequency of the spectra. These values can be used to reliably calculate the asymmetry phase and contrast images for a given CIS instrument. 100

A.1 Summary of component specifications for the MAST-U triple-delay CIS diagnostic. [1]Component previously used on Magnum-PSI in a quad-delay CIS system [61]. [2]Component previously used on MAST in a single-delay CIS system [30]. Each crystal and polariser was placed in custom mount designed at Australian National University. All quoted tolerances are those reported by the manufacturer of the component. 169

Abbreviations

α-BBO alpha Barium Borate

ASDEX-Upgrade Axially Symmetric Divertor Experiment Upgrade

CCD charge-coupled device

CD conventional divertor

CIS Coherence Imaging Spectroscopy

COA crystal optic axis

D-T Deuterium-Tritium

DEMO DEMOnstration power plant

DOP degree of polarisation

E-ray extraordinary ray

ED elongated conventional divertor

ELMs edge-localised modes

FTS Fourier transform spectroscopy

FWHM full width half maximum

ITER International Thermonuclear Experimental Reactor

KSTAR Korea Superconducting Tokamak Advanced Research

LPM linear phase mask

MAST Mega Ampere Spherical Tokamak

MAST-U Mega Ampere Spherical Tokamak Upgrade

MCF Magnetic Confinement Fusion

MLE maximum likelihood estimation

MP Mach Probe

MWI Multi-Wavelength Imaging

NBI neutral beam injection

O-ray ordinary ray

OPD optical path difference

PDF probability density function

PFCs plasma-facing components

PPM pixelated phase mask

QWP quarter waveplate

RFEA Retarding Field Energy Analyser

SART simultaneous algebraic reconstruction technique

SNR signal-to-noise ratio

SOL scrape-off layer

SXD Super-X divertor

W7-X Wendelstein 7-X

Novel Analysis and Calibration Techniques for the Simultaneous Measurement of Plasma Ion Temperatures and Velocities using Multi-Delay Coherence Imaging

Rhys Doyle

Abstract: The role and importance of impurities in the power exhaust of tokamak fusion reactors is long-established, and so too are the negative effects such impurities have on the effectiveness of these devices and the lifetime of their components. It is therefore essential for the development of future fusion devices, such as ITER and DEMO, that a comprehensive understanding of impurity behaviour be obtained. Currently, impurity understanding is primarily based on computational models validated using diagnostics with limited coverage and/or spatial resolution. For this reason, it is desirable for fusion devices to use imaging systems where possible.

This thesis presents a new analysis technique for multi-delay coherence imaging spectroscopy (CIS), a narrowband interferometric spectral imaging diagnostic. This technique, based on the Doppler shift and broadening of impurity spectra, enables simultaneous measurement of impurity velocities and temperatures in 2D with a high spatial resolution. We focus on C III emission, an abundant impurity in carbon-walled fusion devices, and present how the negative effects of spectral contamination and the complex spectral structure of C III are mitigated by this analysis technique using multiple fixed interferometer delays. We present the first use of a triple-delay CIS system on a fusion device and discuss the effect its installation within the Multi-Wavelength Imaging (MWI) diagnostic has on measurements.

Additionally, we present further development of accepted CIS calibration procedures and suggest modifications to the diagnostic, enabling greater usability and cementing coherence imaging spectroscopy as a cost-effective and powerful diagnostic in the development of fusion devices.

Acknowledgements

First, I would like to thank my supervisors, Miles Turner and Huw Leggate at DCU, for their support through many ups and downs, including a pandemic. I am particularly grateful for Huw's good humour during times when progress was slower than we had expected.

Next, I am deeply appreciative of the support I received at CCFE, particularly from Sam Blackmore, Clive Michael, James Harrison, Rory Scannell, and Kevin Verhaegh. Each of them helped me immensely throughout the course of my research, whether through hours at an optical bench or guidance in navigating the complexities of the MAST-U diagnostic environment.

Scott Silburn has been a constant presence since the start of my journey. His PhD work formed the initial foundation for my research, and his guidance thereafter has been a lynchpin in shaping this thesis. As one of the kindest and warmest people at CCFE, I always enjoyed our meetings and am extremely grateful for the time he generously gave to assist me.

To Joe Allcock and Nicola Lonigro, I extend my profound gratitude. Both of them were by my side at every turn. I have the warmest (and most stressful) memories of late nights in the lab, trying to figure out how to get everything to work, as well as frantic times in the blockhouse with Nicola, working to fix problems we did not yet understand—but in the end, we did. I could not have completed this thesis without the dedication and camaraderie of these two gentlemen.

More broadly, I want to thank my friends who have supported me throughout this journey. Special thanks go to the Memory Core: Luke, Daniel, Adam, Simon, and Darragh. These friends have been my rock during the most challenging times of my research. I would not be here without their unwavering honesty, kindness, and support.

To my Nan and Jose, I owe my deepest gratitude for their unconditional love and guidance. Finally, to my Mum, to whom I owe everything: she could not have known what she was signing up for when I decided to embark on this journey, but her steadfast support has meant everything to me. Níl aon tinteán mar do thinteán féin.

There can be no doubt that our descendants will learn to exploit the energy of fusion for peaceful purposes even before its use becomes necessary for the preservation of human civilisation.

LEV ARTSIMOVICH

Chapter 1

Introduction

As global energy demands surge alongside growing populations and industrial expansion, the search for a sustainable and secure energy source has become a critical issue. Traditional methods of energy production, heavily reliant on fossil fuels, are not only unsustainable but are also major contributors to climate change and other forms of environmental degradation. As of 2023 approximately 80% of the world's electricity generation currently depends on fossil fuels [1]. Renewable energy sources, such as solar, wind, and hydro-electric power, present promising alternatives. However, these resources have inherent limitations due to their intermittent nature, geographic dependencies, and often low energy density. Future energy infrastructure must balance the global demand for power with these challenges, pushing us to explore more dependable options for large-scale, low-emission, economically viable energy generation [2]. One promising avenue is nuclear fusion, a process that powers stars and offers the potential for a safe, clean, and nearly limitless energy source [3].

1.1 Fusion Energy

Fusion, unlike fission, does not produce high-level radioactive waste, and the risk of uncontrolled chain reactions is minimised due to the nature of the reaction mechanics [4]. When hydrogen isotopes, such as deuterium and tritium, collide at extremely high temperatures, they fuse to form a heavier nucleus, releasing substantial amounts of energy. This Deuterium-Tritium (D-T) fusion reaction is particularly advantageous for future power generation because it has a high reaction cross-section, compared to other fusion reactions, meaning it is more likely to occur at reactor achievable energy levels (10-30 eV) in a controlled setting [5]. Additionally, the D-T reaction releases a large amount of energy per fusion event, as shown in the following equation:

$$ {}^{2}_{1}\mathrm{D} + {}^{3}_{1}\mathrm{T} \rightarrow {}^{4}_{2}\mathrm{He}\,(3.5\,\mathrm{MeV}) + {}^{1}_{0}\mathrm{n}\,(14.1\,\mathrm{MeV}) \tag{1.1} $$

In this reaction, a deuterium nucleus (${}^{2}_{1}$D) and a tritium nucleus (${}^{3}_{1}$T) fuse to create a helium nucleus (${}^{4}_{2}$He) and a neutron (${}^{1}_{0}$n), releasing a total of 17.6 MeV of energy [6]. The high energy yield and favourable reaction rates make D-T fusion the best candidate for initial fusion power plants [7].

While the D-T fusion reaction offers significant advantages, there remain considerable scientific and engineering challenges to its practical realisation. Achieving and sustaining the high temperatures and pressures required for fusion is a formidable task. Unlike chemical reactions, which can occur at relatively low temperatures, fusion reactions require temperatures of several million degrees to overcome the electrostatic forces between nuclei. The confinement of the resulting plasma requires innovative containment methods, such as magnetic confinement or inertial confinement using high-power lasers [8, 9]. These containment methods are still under development, as they must not only contain but also stabilise the plasma to achieve a net-positive energy

gain.

For fusion to become a viable energy source, it must meet the Lawson criterion, which establishes conditions for density, temperature, and confinement time to sustain a self-heating plasma, achieving what is known as "ignition" [5]. At this point, the fusion reactions produce enough energy to maintain the necessary conditions without external heating. This metric is crucial in assessing the efficiency and economic viability of fusion reactors. The latest advancements in tokamak technology, such as the International Thermonuclear Experimental Reactor (ITER) project and other high-performance reactors, are aimed at reaching these benchmarks [10, 11]. ITER, in particular, targets a fusion power output that surpasses its input power by a factor of ten, setting a precedent for future fusion energy plants.

To push fusion research toward a commercially viable outcome, scientists have developed an array of plasma diagnostics and experimental techniques to measure, analyse, and control plasma behaviour. This thesis furthers this development, aiming to provide tools that deepen our understanding of the conditions in fusion reactors.

The successful implementation of nuclear fusion as an energy source could fundamentally reshape our energy landscape, offering a clean and virtually limitless alternative to fossil fuels and overcoming many of the environmental and safety concerns associated with traditional nuclear fission. Though considerable work remains, the rapid developments in fusion research bring us closer to harnessing this powerful process, moving toward a sustainable energy future.

1.2 Magnetic Confinement Fusion

Magnetic Confinement Fusion (MCF) utilises powerful magnetic fields to contain and control the hot plasma required for nuclear fusion. In the MCF approach, charged particles within the plasma are constrained by the Lorentz force, eq. (1.2), where $\vec{F}$ represents the Lorentz force on a particle of charge q and velocity $\vec{v}$ in the presence of electric field $\vec{E}$ and magnetic field $\vec{B}$. This force drives the particles to spiral around the magnetic field lines, effectively confining them in the direction perpendicular to $\vec{B}$. This confinement minimises direct plasma contact with reactor walls, preventing rapid cooling and maintaining the high temperatures necessary for sustained fusion. MCF configurations are particularly effective in a toroidal (doughnut-shaped) geometry, as it allows for closed magnetic field lines that prevent plasma escape [8].

$$\vec{F} = q\left(\vec{E} + \vec{v} \times \vec{B}\right) \tag{1.2}$$

The magnetic confinement process combines two magnetic field components: a strong toroidal field (B_ϕ) generated by external magnetic coils surrounding the plasma and a weaker poloidal field (B_θ) created by a current within the plasma itself. By shaping these surfaces MCF devices can stabilise the plasma and reduce particle losses. However, confinement losses can still occur due to field line curvature and radial gradients in B_ϕ, which can lead to particle drift [12].

The tokamak, one of the leading magnetic confinement fusion configurations, confines the plasma within a toroidal chamber. In a tokamak, the poloidal magnetic field component is generated by passing a substantial electric current, typically around 1 MA, through the plasma in the toroidal direction via the transformer effect from a central solenoid. According to Ampère's law,

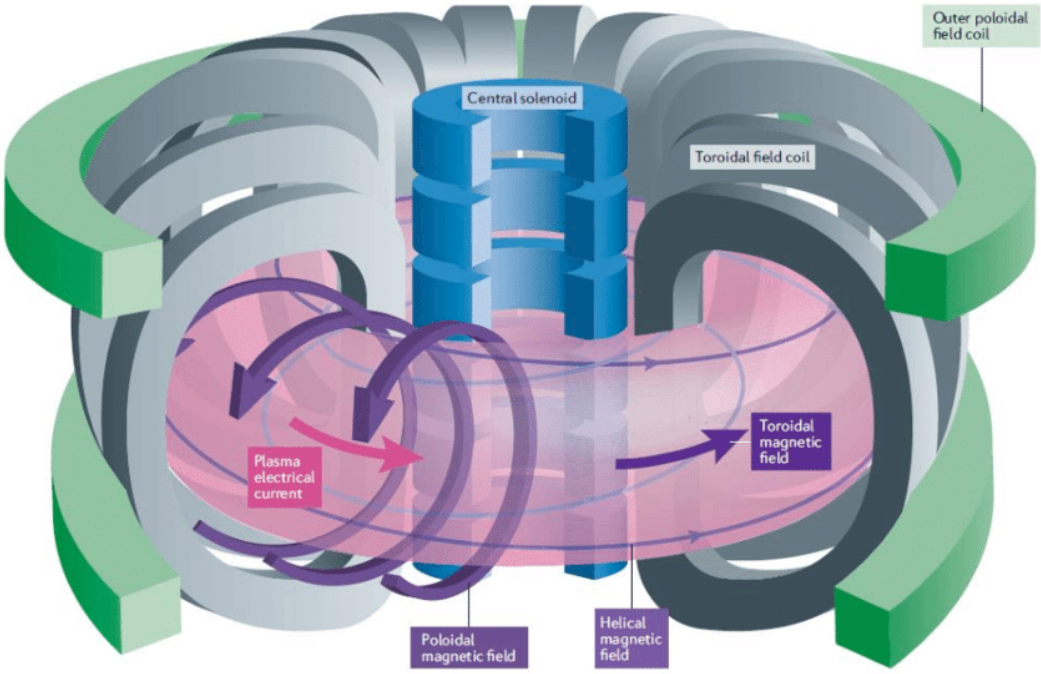

Figure 1.1: Schematic of a tokamak including the toroidal and poloidal field coils and the central solenoid. Shown are the magnetic field lines in the toroidal direction which wrap around the centre column and the poloidal field lines which encircle the plasma itself. Together these result in a magnetic field which wraps around the centre column but moves up/down in vessel. The outer poloidal field coils are also shown which are used for plasma shaping. Image courtesy of EUROfusion.

this current creates the necessary poloidal field. Due to the plasma's finite resistance, this process also leads to Ohmic heating as a beneficial by-product. However, sustaining this induced plasma current requires continuous ramping of the central solenoid's current which cannot be maintained indefinitely, therefore tokamaks can only operate in a *pulsed* way.

1.2.1 The Mega Ampere Spherical Tokamak Upgrade

The Mega Ampere Spherical Tokamak Upgrade (MAST-U), fig. 1.2 is a cutting-edge spherical tokamak developed to address critical issues in plasma confinement and stability unique to low aspect ratio[1] tokamaks [13]. Unlike tradi-

[1] *Aspect ratio* refers to the ratio of major radius R_{maj} to minor radius R_{min} of a tokamak

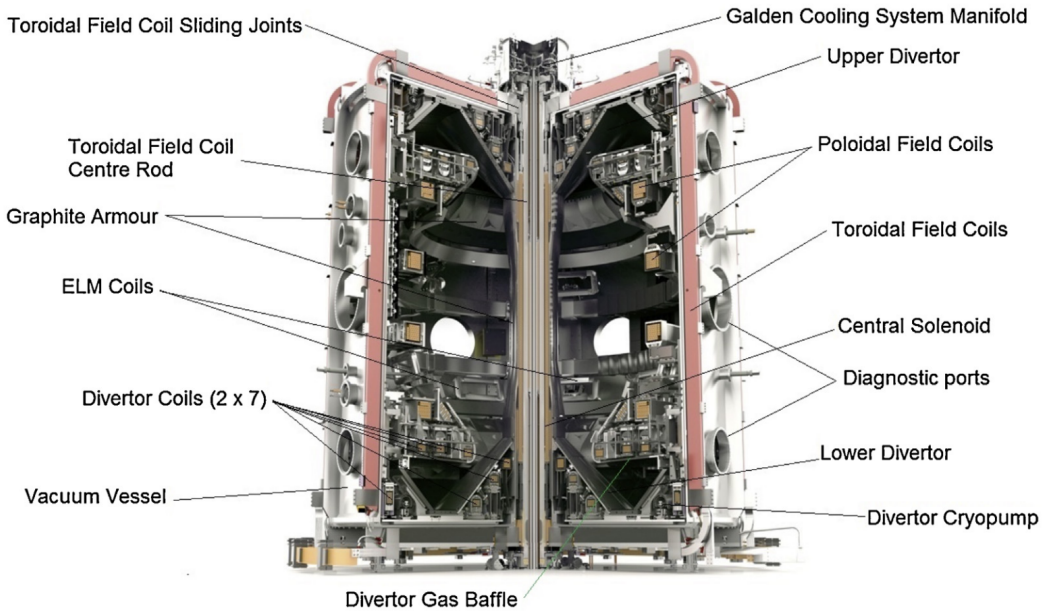

Figure 1.2: Cross-section of the MAST-U tokamak with the main device features labelled [13]. The lower divertor region is of particular interest to this study.

tional tokamaks, which have a high aspect ratio, MAST-U adopts a spherical tokamak design, giving it a "cored apple" shape. This design reduces the aspect ratio, increasing plasma pressure and enhancing confinement efficiency. The spherical geometry also allows for a smaller distance between the plasma and toroidal field coils, which reduces the power requirements for generating the necessary magnetic field strengths within the plasma [14, 8].

MAST-U's shape and divertor design also provides several other advantages, particularly for achieving higher plasma stability and exploring new methods of exhaust handling. One of the primary challenges in magnetic confinement fusion devices is managing heat fluxes to the plasma-facing components (PFCs). High-energy particles escaping the plasma carry substantial heat which can damage reactor walls over time. MAST-U tackles this issue with an advanced divertor system that channels excess heat and particles away from critical components, section 1.3.

The spherical tokamak configuration also offers an ideal test bed for ex-

ploring alternative exhaust solutions [15]. In addition, the high number of diagnostic ports on MAST-U enables the study of turbulence and transport phenomena within the plasma, helping researchers understand confinement improvements that can be applied to larger reactors like ITER and other future fusion power plants.

1.3 Fusion Power Exhaust Problem

One of the significant engineering challenges in magnetic confinement fusion reactors is the power exhaust problem. In these devices, high-energy particles created during fusion reactions, particularly neutrons and helium nuclei (α particles), carry a substantial portion of the fusion energy. While α particles are confined by magnetic fields and can contribute to heating the plasma, neutrons are not and escape the plasma, depositing their energy into the reactor walls. Additionally, impurity particles[2] and heat fluxes must be managed as they inevitably reach plasma-facing components, particularly in the divertor region, where heat and particle loads are highest. Without effective heat management strategies, the integrity of the reactor components can be compromised, resulting in thermal damage, erosion, and reduced component lifetimes [8, 16].

In tokamak devices, the divertor is a specially designed region at the bottom and/or top of the device that plays a critical role in managing plasma exhaust. In the divertor excess particles travel through the scrape-off layer (SOL), an area of open field lines, away from the core plasma and toward specially designed plates, called divertor targets. These plates absorb the high heat fluxes and particle loads, reducing the thermal load on the reactor walls

[2] *Impurity* refers to any plasma species which is not involved in the core fusion. Commonly includes, but is not limited to, carbon, oxygen and helium.

and protecting critical components from excessive wear. Traditional divertor designs, however, face challenges as they encounter very high heat fluxes, especially in devices expected to operate at higher power levels [16, 17].

A key metric in exhaust management is the heat flux limit, or the maximum power per unit area that the divertor targets can withstand. For standard tokamak divertors, this limit can be up to $10\,\mathrm{MW/m^2}$[16]. In high-power reactors, heat flux densities can significantly exceed this limit, resulting in rapid wear on divertor plates, increased maintenance needs, and potentially, unscheduled reactor shutdowns [18]. To address this, advanced divertor configurations, such as the Super-X divertor (SXD) in MAST-U, have been developed to spread out and reduce these heat loads [19, 20].

1.3.1 MAST-U Super-X Divertor

The upgrade of the Mega Ampere Spherical Tokamak (MAST) to MAST-U involved the addition of new baffling to create a unique divertor design with a *closed* divertor chamber, fig. 1.3. This design allowed for a new magnetic geometry called the Super-X divertor (SXD) aimed at addressing the fusion power exhaust problem in spherical tokamaks. The SXD utilises increased magnetic flux expansion and divertor leg extension to spread heat loads on the divertor tiles over a larger surface area. Conversely, in traditional conventional divertor (CD) configurations, heat and particle fluxes are concentrated over a small area, which exacerbates thermal loading issues. A third magnetic geometry is also possible on MAST-U, the elongated conventional divertor (ED), which is a hybrid between an CD and SXD geometry [21].

The addition of the upper divertor baffling also has a significant effect on the plasma dynamics within the divertor due to neutrals. As the plasma cools along the divertor leg various recombination processes occur creating neutrals [22]. In traditional tokamaks with open divertors these neutrals would

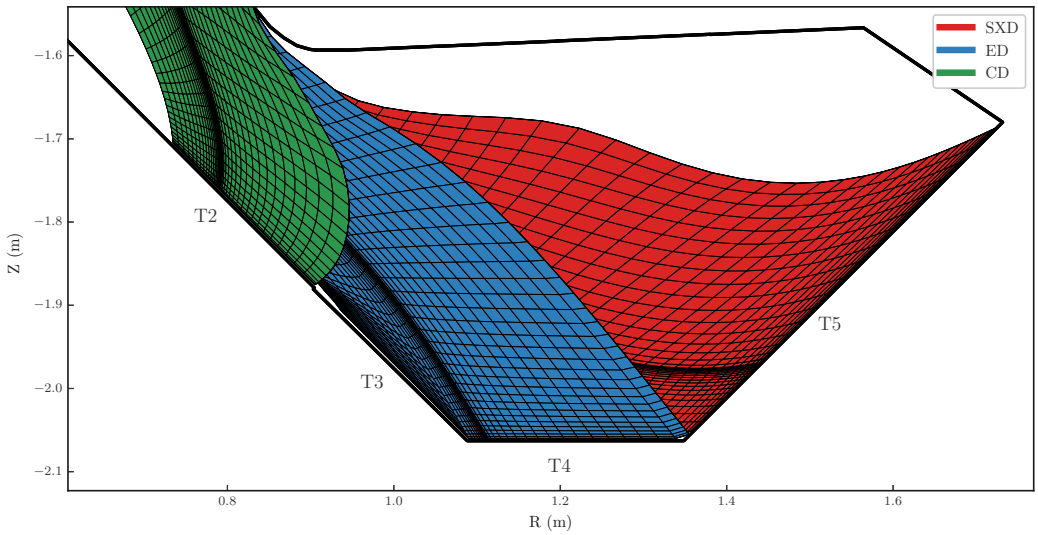

Figure 1.3: Three types of magnetic geometry are possible on MAST-U: Super-X (SXD) shown in red, which utilises full divertor chamber, Elongated Conventional (ED) which extends the divertor leg to the lower divertor tiles (T3 and T4) and Conventional (CD) which finishes on T2

escape, however in the MAST-U SXD they remain in place unperturbed by the magnetic field subsequently inducing a state called *detachment*. In this state the divertor tile heat loads are significantly reduced as this area of the reactor is 'protected' by a low temperature blanket of neutral particles [23, 19]. Detachment is likely to play a significant role in future reactors, however control of this state is imperative, not least for scientific studies. We will see in chapter 4 that the strength and relative ease to which the MAST-U SXD detaches has negative effects on impurity studies as the ionisation region of the plasma is pushed high in the divertor.

Notwithstanding the diagnostic challenges of the MAST-U Super-X, its ability to reduce peak heat loads and enhance particle management represents a significant advancement in exhaust control for magnetic confinement fusion reactors. Going forward solutions like the SXD will be essential for scaling up fusion power systems to commercial viability, where effective exhaust management will be crucial to reactor longevity and economic feasibility.

1.4 Diagnosing Fusion Devices

Fusion devices, like any experimental apparatus dedicated to physical research, are useless without a comprehensive array of tools and diagnostics with which to extract large amounts of high quality data. In the case of fusion science this suite of diagnostics can be separated into two types: passive and perturbative. This research will focus on one specific type of diagnostic, imaging spectroscopy, but any diagnostic that does not act on the plasma itself would be considered passive. Perturbative diagnostics would include probes, whether they oscillate or not, that enter the plasma or diagnostics that inject gas into a specific area [24, 25]. Here we will focus on diagnostics that are relevant to this research, that is those which measure ion temperature and flow velocities.

Plasma ion flows are an important part of the physics in the scrape-off layer and divertor regions, and therefore have been the focus of many studies [26, 27, 28]. These flows have a significant impact on the transport of heat and particles within the SOL and may influence core plasma conditions [29]. The interactions between main ion flows and impurities are especially critical, as they facilitate the removal of helium and other impurities from the plasma core, preventing their reintroduction after they reach the divertor plates. Understanding these flows is also useful for managing the erosion through sputtering of the divertor plates. Observations highlight the complex nature of SOL and divertor flows, characterised by various particle sources and sinks across plasma regions and flow elements that both align with and deviate from magnetic field configurations [30, 29]. Comprehensive and detailed measurements are therefore necessary to enhance the understanding of these intricate processes.

Similarly, measuring ion temperature T_i is crucial for accurately characterising the plasma exhaust in the divertor, as critical parameters such as ion

sound speed, ion pressure, and sputtering rates—depend directly on ion temperatures. Observations have shown that T_i can exceed electron temperatures, T_e in the scrape-off layer, due to different transport behaviours of ions and electrons along open magnetic field lines [31]. However, it is common to assume that $T_i = T_e$, primarily because ion temperature measurements are less commonly available. On large devices, such as ITER or commercial devices, accurate measurements of T_i will be essential for predicting the heat load from burning plasma.

We will now discuss the most common diagnostics used to obtain ion flow and temperature measurements.

1.4.1 Mach Probes

The simplest, and often most robust, way of taking any experimental measurement is to do it directly with a probe. A Mach Probe (MP) in its most fundamental form is the simplest and most widely used diagnostic for the measurement of ion flow velocities. It operates by measuring the ion saturation currents upstream J_{up} and downstream J_{dn} of the probe. Ion saturation currents are the currents collected by a probe when it is biased sufficiently negative with respect to the plasma potential, such that all electrons are repelled and only ions contribute to the current. These currents provide a measure of the ion flux in the plasma. From the difference between the upstream and downstream ion saturation currents, the Mach number (M_∞) of the plasma flow can be derived using eq. (1.3), which quantifies the flow speed relative to the local sound speed. A detailed engineering explanation can be found in the review paper by Chung et al. [32].

$$M_\infty = ln\left(\frac{J_{up}}{J_{dn}}\right)/K \tag{1.3}$$

Provided Mach probes are calibrated properly ion saturation currents measured should be accurate, however eq. (1.3) contains another value, K the calibration factor. The calibration factor is a theoretically determined value, often obtained from simulation, relating to the experimental conditions present. The possible number of simulation methods, codes and models used to determine K are as numerous as the phenomena they simulate, thus leading to an uncomfortable dependence of the Mach probes on the simulations they should be validating.

To this point, it has been found that MPs tend to overestimate ion flows in the SOL when compared to simulation, with suggestions that plasma-surface interactions with the probe can create impurities which in turn cause this overestimation [33, 34]. Another disadvantage of the MPs, is their position in the vessel. By design, a Mach probe must be in contact with the SOL plasma which, naturally, means that the probe will have an effect on the plasma conditions.

Additionally, Mach probes are by their nature localised, only providing data at a fixed location and cannot differentiate between ion species. Although useful in order to obtain an overview of the plasma conditions, these disadvantages make it difficult to do complex physical studies based on Mach probes alone.

1.4.2 Line-Integrated Spectroscopy

In cooler areas of the plasma, line-integrated spectroscopy can be effective as the impurities remain partially ionised. Typically these diagnostics consist of one or more collection lenses, positioned outside the vacuum vessel to view the plasma through diagnostic ports, with optical fibres capturing the impurity emission and passing the light to spectrometers positioned elsewhere. Within the spectrometers, the light is dispersed, using a diffraction grating, onto a charge-coupled device (CCD) to measure the spectrum. Emission lines can

then be analysed by fitting the appropriate lineshape functions to find the central wavelengths. Comparing this to the rest wavelengths of the emission line yields the line-of-sight integrated ion flows, as the Doppler effect will shift the centre-of-mass of the spectral line according to the ion's velocity.

If the spectral resolution of the spectrometer is high enough ion temperature can also be obtained from these line-integrated spectra [35]. However, these lineshape models often include multiple broadening mechanisms acting on the spectrum simultaneously and are therefore more complex than Doppler shift measurements.

Unlike Mach probes, spectrometers are not perturbative, a distinct advantage. As the spectrometers are positioned outside the reactor hall calibrations are often possible inter-shot if needed, along with modifications as necessary. However, standard spectroscopic techniques generally have a low spatial resolution due to limited number of sightlines. This can vary widely from the 40 available on MAST-U, which spread over 3 regions, to 150 on Axially Symmetric Divertor Experiment Upgrade (ASDEX-Upgrade) [36, 37]. Nevertheless, spectrometers are an important part of any fusion device's diagnostic array and have even been used to calibrate other diagnostics.

1.4.3 Retarding Field Energy Analysers

A Retarding Field Energy Analyser (RFEA) is a less common but potentially more accurate method for measuring ion flow velocities than Mach probes. RFEAs consist of four components: an entrance slit, two grids and a collector. The entrance slit and second grid are typically biased negative to prevent incoming electrons and secondary electrons which may be created within the device from reaching the collector. The first grid is scanned from a high to a low positive potential in order to determine the ion distribution function.

Methods similar to that used for Mach probes, whereby the ion saturation

current is used to determine the Mach number have been presented by Fredriksen et al. [38] and Kreuger et al. [39], however each author took a different approach. Fredriksen et al. included the orientation of the probe entry with respect to the plasma flow, θ eq. (1.4), whereas Kreuger et al. included the ion and electron temperatures eq. (1.5):

$$M = \frac{ln(R)}{K} \frac{1}{cos\theta} \frac{\Delta\theta}{sin\Delta\theta} \tag{1.4}$$

$$M = \frac{ln(R)}{K} \sqrt{\frac{T_e}{T_e + \gamma_i T_i}} \tag{1.5}$$

where R is the ratio of the current detected by opposite detectors and K again is a calibration parameter. To supplement this Kreuger et al. also detailed how ion temperature can be determined using an RFEA [39]. Although the method requires that temperature be averaged over time, this addition may provide more accurate velocity measurements than traditional Mach probes. More recently, an RFEA has been used on MAST-U to determine ion temperature by fitting to a graph of collector current and the voltage of the first grid [40]. This study also confirmed that the assumption of $T_i = T_e$ does not hold in the MAST-U SXD, with the T_i/T_e found to be ≈ 0.5.

Nevertheless, RFEAs share the same issues of plasma disturbance, localisation and ion differentiation as with Mach probes.

1.5 Motivation

In the previous sections we have outlined the importance of understanding ion dynamics within a tokamak, which centres around heat load management. To do this a suite of accurate diagnostics capable of measuring ion velocities and temperatures are required. However, the significant drawbacks of plasma disturbance, measurement localisation, low spatial resolution and an inability

to differentiate between ion species, plague these diagnostics.

These disadvantages are brought to bear most notably when dealing with detached plasma. In this state, the divertor plasma undergoes a large number of physical process in different regions along magnetic field lines [41]. The interplay between these regions is the focus of much research as understanding their effect on plasma stability and heat exhaust will be imperative for future devices such as ITER and DEMOnstration power plant (DEMO). However, this is not fulfilled effectively by the current suite of diagnostics.

To solve this problem many devices employ Coherence Imaging Spectroscopy (CIS) systems [42, 43, 35]. At its core, CIS is a camera and therefore can collect data from outside the vessel in 2D. As CIS is a type of spectroscopy, the system can differentiate between different ion species allowing for a wide range of physical studies. For these reasons, a CIS system capable of measuring ion velocities and temperatures fills a gap in the diagnostic setup on MAST-U. When combined with MAST-U's unique ability to study detachment such a system has the potential to significantly impact on physics research going forward.

1.6 Thesis Outline

The goal of this thesis is to design and construct a coherence imaging spectroscopy system capable of measuring C^{2+} ion velocities and temperature simultaneously with a single system. It was also important to this research that such a system not require the assistance of other MAST-U diagnostics, such as spectrometers, to achieve its goals. To this end this thesis is organised as follows:

In chapter 2, we introduce the concepts that underpin all CIS instruments, namely Fourier transform spectroscopy and polarisation interferometry. We

will then use Mueller calculus to describe the interferograms produced by CIS systems and differentiate between the two most common types: linear phase mask and pixelated phase mask. Lastly, we will briefly discuss previous CIS studies on which this research is built.

Chapter 3 centres around our diagnostic, the MAST-U CIS. We will describe its construction, presenting details of the first triple-delay CIS system with a pixelated sensor, and its integration on MAST-U. To do this we will also describe the MAST-U Multi-Wavelength Imaging (MWI) diagnostic within which our system is located. Installation of a CIS interferometer within an optical polychromator posed significant challenges which we will also detail in this chapter along with our solutions. Lastly, we present new calibration methods for CIS systems, the goal of which was to ensure that our diagnostic could operate independently of other diagnostic. These calibration methods also maintain the cost-effective nature of CIS, as they reduce the need for the complex and expensive calibration systems used on other fusion devices.

In chapter 4, we present a 2D inversion process capable of determining ion flow velocities and temperatures from a single CIS interferogram. This procedure is tested using simulations of MAST-U plasmas with different magnetic geometries. We also address the effect of spectral contamination on the measurement of velocities and temperatures and include this in our fitting procedures. Finally we will present the first measurements of C^{2+} emission, velocity and temperature profiles in the MAST-U divertor along with a comparison to spectroscopy measurements and the simulations used earlier in the chapter.

Finally, in chapter 5 we will summarise our work and make recommendations on how our diagnostic and inversion process could be improved in future studies.

Chapter 2

Coherence Imaging Spectroscopy

In this chapter we review the theory which forms the basis for coherence imaging spectroscopy (CIS) instruments. By combining two beams of light which are out of phase with each other an interference pattern is produced. This interferogram encodes how correlated the beams of light are, otherwise known as their coherence. The structure of this pattern is strongly related to the spectrum of the measured light which in turn is connected to various physical processes. By leveraging this, one can measure a narrow spectral range of a plasma in which these processes are well understood and infer the underlying physical phenomena. This chapter introduces the most common line emission models used in tokamak physics and provides the necessary theory for understanding CIS, including Fourier transform spectroscopy and polarisation interferometry, along with a description of previous CIS instruments.

2.1 Impurity Line Emission

The spectra emitted from the SOL and divertor regions of a tokamak is primarily dominated with ion emission due to the typical energies of < 100 eV [44, 45].

These conditions are generally not sufficient to fully ionise the most common tokamak impurity species, carbon, therefore carbon ions will undergo radiative de-excitation [46]. Within the MAST-U divertor C^{1+} and C^{2+} (C II and C III in spectroscopic notation) are the most abundant ion states, the latter of which is the focus of this research. The most relevant physical processes to these spectra are now discussed.

2.1.1 Spectral Lineshape Models

We begin by noting three significant physical mechanisms that influence the observed structure of a line spectrum: the Doppler effect, Stark broadening, and Zeeman splitting. A line spectrum can be represented as

$$I(\nu) = I_0\, g(\nu) \tag{2.1}$$

where $I(\nu)$ denotes the intensity as a function of frequency ν, $I_0 = I(\nu)\, d\nu$ is the total (integrated) intensity, and $g(\nu)$ is a normalised function describing the line's shape.

Doppler Effect

When an ion moves relative to the observer, the measured frequency ν is given by the Doppler shift formula: $\nu = \left(1 - v/c\right)\nu'$, where ν' is the frequency in the ion's rest frame, v is the ion's velocity as perceived by the observer, and c is the speed of light. We can also describe this shift using a dimensionless frequency change:

$$\xi = -\mathbf{v} \cdot \hat{\mathbf{l}} \,/\, c,$$

where $\mathbf{v}$ is the velocity vector of the emitter and $\hat{\mathbf{l}}$ is a unit vector along the observer's line of sight.

Because ions in a plasma have a range of velocities distributed according

to some function $f(\mathbf{v})$, the observed line is broadened. To find the overall line shape $g(\xi)$, one integrates over all ion velocities that yield the same Doppler shift ξ:

$$g(\xi) = \int f(\mathbf{v})\, \delta\Big(\xi + \mathbf{v} \cdot \hat{\mathbf{l}}/c\Big)\, d\mathbf{v}. \tag{2.2}$$

Now, suppose the plasma is in thermodynamic equilibrium and also has a bulk flow $\mathbf{v_D}$. By transforming to a frame moving with $\mathbf{v_D}$ (thus eliminating the bulk flow in that frame), we label quantities in this new frame with primes. There, the ion velocity distribution is taken to be isotropic and Maxwellian:

$$f'(v') = \left(\pi\, v_{th}^2\right)^{-\frac{1}{2}} \exp\left(-\left[v'/v_{th}\right]^2\right), \tag{2.3}$$

where $v_{th} = \sqrt{\frac{2\,k_B\,T_i}{m_i}}$, T_i is the ion temperature, m_i is the ion mass, and k_B is the Boltzmann constant. From this Maxwellian distribution, one obtains the Doppler-broadened Gaussian line shape in the primed frame:

$$g'(\xi') = \left(\pi\, \frac{v_{th}^2}{c^2}\right)^{-\frac{1}{2}} \exp\left(-\left[\xi'\, \frac{c}{v_{th}}\right]^2\right). \tag{2.4}$$

Lastly, to express this in the laboratory frame, we use the relation

$$\xi' = \xi + \frac{\mathbf{v_D} \cdot \hat{\mathbf{l}}}{c}.$$

Thus, the observed line shape in the lab frame is

$$g(\xi) = \left(\pi\, \frac{v_{th}^2}{c^2}\right)^{-\frac{1}{2}} \exp\left(-\left[\left(\xi + \mathbf{v_D} \cdot \hat{\mathbf{l}}/c\right)\, \frac{c}{v_{th}}\right]^2\right). \tag{2.5}$$

This illustrates how both thermal motion and a bulk flow contribute to Doppler broadening of the observed spectral line.

Stark Broadening

Stark broadening is a phenomenon observed in the spectral lines emitted by plasmas in the presence of strong electric fields [47, 24]. In plasma spectroscopy, understanding Stark broadening is crucial for analysing and interpreting the spectral lines emitted by the plasma, providing insights into its density. In a homogeneous plasma, the electric fields experienced by the charged particles are randomly distributed and fluctuate over time. These electric fields perturb the energy levels of atoms and ions, causing the spectral lines to broaden. The Stark effect, which describes the splitting and shifting of atomic energy levels in the presence of electric fields, is responsible for this broadening phenomenon, which causes the spectral lineshape to resemble a Lorentzian.

The full width half maximum (FWHM) of the lineshape component due to Stark broadening varies according to $n_e^{2/3}$, where n_e is the plasma electron density. Thus, observing this phenomenon can serve as a method for determining plasma density through spectroscopy, provided an appropriate spectral line is selected. Leveraging the relationship between density and FWHM, and using available data the Stark broadening expected for impurities present in fusion devices is estimated to be much smaller than Doppler broadening [48]. Therefore, Stark broadening will not be discussed further in this thesis.

Zeeman Splitting

The Zeeman effect, discovered by Pieter Zeeman in 1896, is a phenomenon that occurs when an atomic or molecular spectrum splits into several components in the presence of an external magnetic field. This splitting provided critical insights into the atomic structure and has profound implications in fields ranging from astrophysics to quantum mechanics.

Zeeman splitting specifically refers to the division of a single spectral line into multiple components when subjected to an external magnetic field. This

occurs because the imposed magnetic field interacts with the magnetic dipole moments of electrons, changing the degeneracy of their energy levels. The extent of the splitting is directly proportional to the strength of the magnetic field, eq. (2.6).

$$\Delta E = \mu_{\mathrm{B}}\, g\, m_j\, B \tag{2.6}$$

Where ΔE is the energy shift due to the Zeeman effect, μ_{B} is the Bohr magnetron, g is the Landé g-factor, m_j is the magnetic quantum number associated with the total angular momentum J and B is the external magnetic field strength. Understanding Zeeman splitting can be crucial for interpreting spectroscopic data, especially on high magnetic field fusion devices [35], but was found to be a small effect on MAST [43]. We address this for our use case in the MAST-U divertor in section 4.3.3.

2.2 Introduction to Interferometry

At the heart of coherence imaging spectroscopy lies the concept of interference, wherein two or more coherent waves combine to produce a resultant wave with a distinctive pattern of constructive and destructive interference. We note a potential confusion between the use of the terms coherent and coherence, which will be used frequently in this thesis. To clarify our intended meanings: we will use *coherent* to describe the property of a single light source, indicating that its electromagnetic waves maintain a stable, predictable phase relationship over time and space. Whereas, we will use *coherence* to specifically refer to the degree of correlation between the fields of two distinct light sources.

To explore this, we begin with Maxwell's description of light as the oscillation of an electromagnetic field travelling through space. We will only consider an electric field at position $\mathbf{r}$ and time, t, as in general the electric field exerts a

far greater force on matter than the magnetic field. With this the electric field is given by eq. (2.7), where $\mathbf{k}$ is the wave vector and the angular frequency, $\omega = 2\pi\nu$.

$$E(\mathbf{r}, t) = |\mathbf{E}| \exp(i[\mathbf{k} \cdot \mathbf{r} - \omega t]) \tag{2.7}$$

From quantum theory we know that light emitted from a single location on a thermal source exhibits random fluctuations. It follows that light emitted from two different points on a source will be uncorrelated. In turn the electric fields of a source measured at the same point in space generally only exhibit partial correlation. This is also observed with light emitted from the same point in space but at different times. To explore this we first examine Young's double slit experiment [49]. The electric field measured at point P, E_P, is equal to the sum of fields, E_1 and E_2, passing through apertures A_1 and A_2, given by:

$$E_p(t) = K_1 E_1(t - t_1) + K_2 E_2(t - t_2) \tag{2.8}$$

where $K_{1,2}$ are parameters, determined by the geometric properties of each aperture, which effect the magnitude of the transmitted field. As this interference field is stationary, i.e. does not vary in time, eq. (2.8) can be rewritten with $\tau = t_2 - t_1$:

$$E_p(\tau) = K_1 E_1(t + \tau) + K_2 E_2(t) \tag{2.9}$$

The intensity at P is then be given by eq. (2.10), the time-averaged product of $E_p(\tau)$ and its complex conjugate.

$$
\begin{aligned}
I_p &= \langle E_p(\tau) E_p^*(\tau) \rangle \\
&= |K_1|^2 I_1 + |K_2|^2 I_2 + 2|K_1 K_2| \operatorname{Re}\{\Gamma_{12}(\tau)\} \\
\Gamma_{12}(\tau) &= \langle E_1(t+\tau) E_2^*(t) \rangle
\end{aligned}
\tag{2.10}
$$

where I_1 and I_2 are the field intensities at each aperture and * denotes the complex conjugate. We also introduce Γ_{12}, the mutual coherence function of the electric fields at each aperture which normalised becomes the dimensionless quantity, complex degree of coherence:

$$
\gamma_{12}(\tau) = \frac{\Gamma_{12}(\tau)}{\sqrt{I_1 I_2}} \tag{2.11}
$$

So far we have described the division of a wavefront by two apertures, however in the case of a Michelson interferometer the amplitude of the field instead is divided between two paths of different path length using a beam-splitter. In this configuration eq. (2.10) reduces to eq. (2.12) and encodes the auto-correlation function of the field for time delay τ, $\Gamma_{11}(\tau)$ given by eq. (2.13). We will, however, refer to Γ_{11} as the temporal coherence, which is the mutual coherence function for a single point in space.

$$
I_p = \frac{1}{2}|k|^2 \left(I_1 + \operatorname{Re}\{\Gamma_{11}(\tau)\}\right) \tag{2.12}
$$

$$
\Gamma_{11}(\tau) = \langle E_1(t+\tau) E_1^*(t) \rangle \tag{2.13}
$$

By applying the same normalisation principles used in eq. (2.11) we can now obtain an equation for the degree of temporal coherence, eq. (2.14). We subsequently modify eq. (2.12) to describe the irradiance, $I(\mathbf{r}, \tau)$, measured at position $\mathbf{r}$ on a sensor, in terms of $\gamma_{11}(\tau)$ and the irradiance at $\mathbf{r}$ observed

when $\tau = 0$ where $I_0(\mathbf{r}) = |k|^2 I_1$.

$$\gamma_{11}(\tau) = \frac{\langle E_1(t+\tau)E_1^*(t)\rangle}{\langle E_1(t)E_1^*(t)\rangle} = \frac{\Gamma_{11}(\tau)}{\Gamma_{11}(0)} = \frac{\Gamma_{11}(\tau)}{I_0} \tag{2.14}$$

$$I(\mathbf{r},\tau) = \frac{I_0(\mathbf{r})}{2}\left(1 + \mathrm{Re}\{\gamma_{11}(\tau)\}\right) \tag{2.15}$$

Through the Wiener-Khinchin theorem, we know that the Fourier transform of the auto-correlation function of a signal yields the power spectrum of that signal[3] [50]. Using this we define $J(\nu)$, the frequency spectrum of measured field, which is given by:

$$J(\nu) = \int \Gamma_{11}(\tau)\, \exp(-2\pi i\nu\tau)\, d\tau \tag{2.16}$$

In turn it is now useful for us to define the area-normalised spectral irradiance $g(\nu)$, a Fourier transform pair of the complex degree of temporal coherence, $\gamma_{11}(\tau)$:

$$\begin{aligned} g(\nu) &\equiv \frac{J(\nu)}{\int J(\nu)\, d\nu} \\ &= \int \gamma_{11}(\tau) \exp(-2\pi i\nu\tau)\, d\tau \end{aligned} \tag{2.17}$$

Through the Hermitian symmetry of the Fourier transform of a real function, we know that $\gamma_{11}(\tau) = \gamma_{11}^*(-\tau)$. As $\mathrm{Re}\{\gamma_{11}(\tau)\}$ is an even function $g(\nu)$ can be found from though eq. (2.18).

$$g(\nu) = 2\int \mathrm{Re}\{\gamma_{11}(\tau)\} \cos(2\pi\nu\tau)\, d\tau \tag{2.18}$$

Thus, the spectrum can be determined from the interferogram of a two-beam

[3]This holds as long as the signal in question is a wide-sense stationary (WSS) random process.

interferometer, eq. (2.15). This method is commonly known as Fourier transform spectroscopy (FTS). For the remainder of this thesis we will use the term *degree of coherence* to mean complex degree of temporal coherence (eq. (2.14)) and denote it simply with $\gamma(\tau)$

2.3 Fourier Transform Spectroscopy

As discussed in section 2.2, a spectrum can be extracted from an interferogram $I(\mathbf{r})$ recorded as a function of interferometer delay τ, by isolating the coherence term and applying a cosine transform. In the context of Michelson's design τ is typically varied by displacing one of the mirrors parallel to the beam path.

In practical implementations, there exists a finite maximum delay τ_{max} at which the interferogram $I(\mathbf{r}, \tau)$ can be observed. Sampling $\gamma(\tau)$ at uniform intervals $\delta\tau$ from 0 to τ_{max} yields a frequency resolution of $\delta\nu \approx \tau_{max}^{-1}$ [51]. If the spectrum spans a frequency range of $\Delta\nu$, then the number of spectral samples required is given by $m = \Delta\nu/\delta\nu$. For a spectrum starting from $\nu \approx 0$, the minimum delay sampling interval, to avoid aliasing, is given by $\delta\tau = 1/(2\Delta\nu)$, as stated by the Nyquist-Shannon sampling theorem [52].

FTS instrument designs can be broadly classified into temporal multiplexing or spatial multiplexing categories based on whether the interferogram is sampled temporally or spatially. When the spectrum is encoded in the time domain, the full spatial resolution of the detector is retained, albeit with reduced time resolution. Whereas instruments that scan τ in space are termed "snapshot" devices, capable of capturing all spectral information in a single image but inevitably compromising some spatial resolution in the process [53].

Due to the computational complexity of calculating the cosine transform, in the past most interferometers used a diffraction grating or prism. Later advances in computing allowed for FTS instruments to be used more commonly.

This class of instrument, to which the Fabry-Perot interferometer belongs, benefited from a greater étendue, a measure of the spread of light in an optical system, when compared to grating or prism spectrometers [54, 55]. FTS instruments, such as the Michelson interferometer, also benefit from a signal-to-noise improvement proportional to $m^{1/2}$, where m is the number of frequency channels (or spectral elements) recorded simultaneously. This is known as the multiplex (or Fellgett) advantage. With these advantages FTS has now become a standard technique for measuring large spectral ranges to high accuracy at low-cost, particularly when dealing with quasi-monochromatic light sources.

2.3.1 Quasi-monochromatic Light

We now apply the principles of FTS to the spectral emission of an isolated plasma, which is said to be quasi-monochromatic, i.e. characterised by a narrow spectral width around a dominant frequency ($\Delta\nu/\nu_0 \ll 1$). One such physical phenomenon, which is the subject of this work, is the Doppler effect, briefly discussed in general terms earlier. To explore this we define the centre-of-mass frequency of the spectrum:

$$\nu_c = \int \nu g(\nu) d\nu = \nu_0 + \Delta\nu_D \tag{2.19}$$

$$\frac{\Delta\nu_D}{\nu_0} = \frac{\boldsymbol{v} \cdot \hat{\boldsymbol{l}}}{c} \tag{2.20}$$

where $g(\nu)$ is again the area-normalised spectrum, ν_0 is the rest-frame centre-of-mass frequency, $\Delta\nu_D$ is a small Doppler shift due to velocity, $\boldsymbol{v}$ of the emitting species along the observer's sightline vector $\hat{\boldsymbol{l}}$. It is known that the convolution of a signal with a shifted Dirac delta function results in the original signal being shifted by the same amount. With this we can write $g(\nu)$ as the convolution of the delta function $\delta(\nu - \nu_c)$ with a shifted spectrum

$g_c(\nu) \equiv g(\nu + \nu_c)$:

$$g(\nu) = \delta(\nu - \nu_c) * g_c(\nu) \tag{2.21}$$

Analogously to eq. (2.17), we can then write the degree of coherence of this spectrum as the inverse Fourier transform of eq. (2.21):

$$\gamma(\tau) = \exp(2\pi\tau i\,[\nu_0 + \Delta\nu_D]) \int g_c(\nu) \exp(2\pi i \nu\tau) d\nu \tag{2.22}$$

It is known that the inverse Fourier transform of a shifted Dirac delta function in the frequency domain is a phasor in time domain with a frequency equal to the delta function's shift. We can see this in the first part of eq. (2.22). The second part of this equation provides us with information about the structure of the spectrum and thus is fundamental to the study of the broadening mechanisms such as Doppler broadening. Together eq. (2.22) represents a co-sinusoidal signal within a slowly varying contrast envelope. By applying eq. (2.15), we can visualise this in fig. 2.1. Here, we first show a singlet spectrum in its rest frame along with the same spectrum with additional broadening and a Doppler shift. On the right we see that for both spectra the interferogram decays to $I_0/2$ as delay increases, with the additionally broadened spectrum decaying much faster. Also shown is a snapshot of the oscillations within the envelope where we can see the effect of the Doppler shift of the interferogram.

The second row in fig. 2.1 shows the same information but this time for a multiplet spectrum. Here again we see that the interferogram is a rapidly oscillating co-sinusoid within a contrast envelope, however in this case the contrast envelope is now complicated by the structure of the spectrum which is captured by the second part of eq. (2.22), which we will call the *asymmetry* of the spectrum. For convenience we now rewrite eq. (2.22) as eq. (2.23), where the *fringe contrast* is given by eq. (2.25). We introduce eq. (2.26) as shorthand

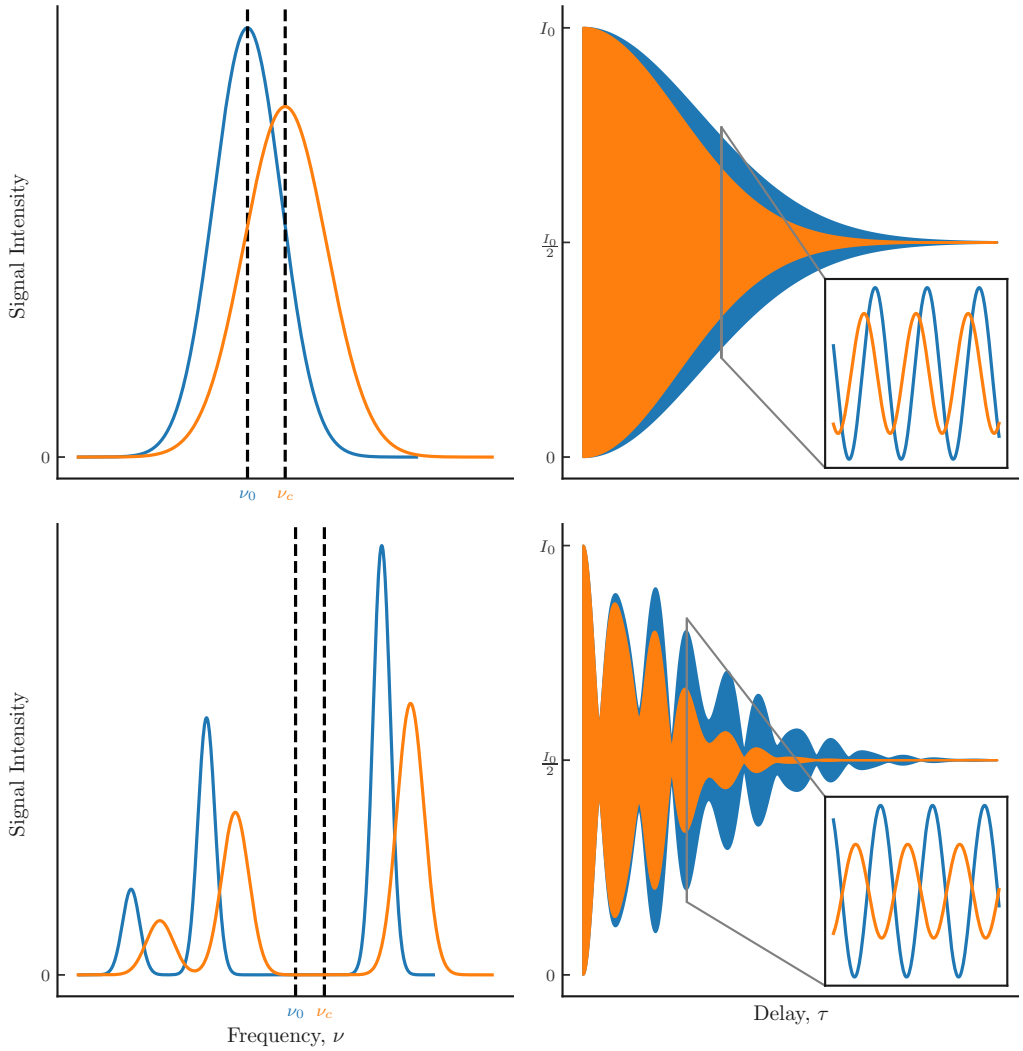

Figure 2.1: In this figure we see how interferometer delay affects measured intensity for different Doppler broadened and shifted spectra. The top row shows how the contrast envelope decays to $I_0/2$, for a singlet spectrum, with increasing delay at a rate dependent on how broadened a spectrum is. Within this envelope we see high frequency oscillations that experience a shift according to the Doppler shift of the spectrum. Similarly the bottom row shows that for multiplet spectra an additional low frequency oscillation in the contrast envelope exists. The blue lines represent rest frame spectra and the orange a Doppler shifted and broadened version of each spectrum.

for the constituent parts of the coherence phase.

$$\gamma(\tau) = |G_c(\tau)| \exp\left(i \left[2\pi\nu_0\tau + 2\pi\Delta\nu_D\tau + \arg\left[G_c(\tau)\right] \right] \right) \tag{2.23}$$

$$G_c(\tau) = \int g_c(\nu) \exp(2\pi i \nu\tau) d\nu \tag{2.24}$$

$$\zeta(\tau) \equiv |\gamma(\tau)| = |G_c(\tau)| \tag{2.25}$$

$$\begin{aligned} \Phi(\tau) &\equiv \arg(\gamma(\tau)) \\ &= 2\pi\nu_0\tau + 2\pi\Delta\nu_D\tau + \arg\left[G_c(\tau)\right] \\ &= \phi_0(\tau) + \phi_D(\tau) + \phi_A(\tau) \end{aligned} \tag{2.26}$$

Here, $\phi_0(\tau)$ represents the *rest-frame phase*, a phase term associated with the emission at the rest-frame frequency ν_0. The Doppler shift contributes $\phi_D(\tau)$, another phase term which varies more slowly than ϕ_0. We will refer to this as the *Doppler phase*. It is important to note that sensitivity to Doppler shifts increases with delay, a point we will return to later. Lastly, ϕ_A is the *asymmetry phase* which as mentioned is related to the structure of the spectrum, but more specifically encodes the structure of the inverse Fourier transformed centred lineshape $G_c(\tau)$. We call this the asymmetry phase as the Fourier transform of a spectrum symmetric about its centre-of-mass frequency (i.e. an even function) is purely real, thus $\phi_A(\tau) = 0$. In this case, shown in the top plots in fig. 2.1, the centred lineshape $g_c(\tau)$ is completely described by its contrast $\zeta(\tau)$.

From atomic studies and quantum theory, ν_0 for a given plasma emission is generally known to good accuracy, therefore ϕ_0 is taken as a calibration parameter for interferometer systems. This can be measured using a laser or a gas-discharge lamp (if available) both of which produce a coherent light source at ν_0. As interferometers tend to be highly sensitive to environmental changes ϕ_0 must be measured regularly to account for this and reduce systematic errors, this is explored in detail in chapter 3. Successfully measuring ϕ_0 is also required

if inferring ϕ_D and/or ϕ_A is the goal of such an interferometer, as is the case in this work.

So far we have examined how the rest-frame frequency of a spectrum and the Doppler shift of a spectrum affects the phase and contrast of its degree of coherence. We have also mentioned that $G_c(\tau)$ encodes information about the broadening of a given spectrum. In fig. 2.1 both spectra shown have experienced Doppler broadening due to the thermal velocity of the emitting species. Broadening of this type is well described by a Gaussian distribution, eq. (2.27), if the emitting species follows a Maxwellian velocity distribution, where v_{th} is the thermal velocity of the species, T_i is its temperature and m_i its mass.

$$g_D(\tau) = \left(\frac{c}{\sqrt{\pi}\nu_0 v_{th}}\right) \exp\left(-\left[\frac{c\,\nu}{\nu_0 v_{th}}\right]^2\right) \tag{2.27}$$

$$v_{th} = \sqrt{\frac{2k_B T_i}{m_i}} \tag{2.28}$$

As eq. (2.27) is symmetric about ν_0 we know that Doppler broadening does not contribute to the asymmetry phase. However, as mentioned, this will have a contrast contribution. This is given by eq. (2.29), where T_C is known as the 'characteristic temperature', and is the source of the Gaussian decay of the contrast envelope seen in the plots in fig. 2.1.

$$\zeta_D(\tau) = \exp\left(-\frac{T_i}{T_C(\tau)}\right) \tag{2.29}$$

$$T_C(\tau) = \frac{m_i\, c^2}{2k_B(\pi\,\tau)^2} \tag{2.30}$$

It follows that as Doppler broadening affects the measured contrast of an interferogram and Doppler shifts affect its phase, with adequate calibration one can resolve the temperature and velocity of an emitting species from a single spectrum. In reality, spectra can be more complicated than so far described

and hence require more advanced techniques, as presented in chapter 4.

We now consider the second spectrum shown in bottom of fig. 2.1, where multiple Dopper broadened emission lines are present at different frequencies. This type of spectrum can occur when a species emits at different frequencies over a very small frequency range, commonly known as a multiplet spectrum, an example of which is C III on which the spectrum in fig. 2.1 was modelled. A spectrum can also contain multiple emission lines when two or more species emit at nearby frequencies. Whether these species share the same temperature depends on whether they are in thermal equilibrium. This is discussed in chapter 4 in the case of oxygen impurities present in the C III spectrum of MAST-U.

Taking, for now, the first case of a single species in thermal equilibrium. The spectrum, $g_M(\nu)$ is described by the convolution of a Doppler broadened spectrum $g_D(\nu)$ with the sum of intensity weighted delta functions, imposing the condition that $\sum_i^N I_i = 1$, where N is the number of lines and I_i is the relative intensity of line i.

$$g_M(\nu) = g_D(\nu) * \sum_i^N I_i \delta(\nu - \Delta\nu_i) \tag{2.31}$$

Here $\Delta\nu_i = (\nu_i - \nu_c)/\nu_c$ where ν_i is the emission frequency of line i. We can then take the inverse Fourier transform of eq. (2.31) and, from eq. (2.27), $\mathscr{F}^{-1}\{g_D(\nu)\} = \zeta_D(\tau)$ to give an equation for $G_c(\tau)$ accounting for a spectrum with N distinct emission lines experiencing Doppler broadening.

$$G_c(\tau) = \zeta_D(\tau) \sum_i^N I_i \exp(2\pi i \Delta\nu_i \tau) \tag{2.32}$$

$$\zeta(\tau) \equiv |G_c(\tau)| = \zeta_D(\tau)\zeta_A(\tau) \tag{2.33}$$

It follows from eq. (2.25) that the fringe contrast is now given by eq. (2.33),

the product of the Doppler contrast $\zeta_D(\tau)$ and contrast due to the asymmetry of the spectrum $\zeta_A(\tau)$. We then also know that $\phi_A(\tau) \neq 0$ as the spectrum is not symmetric about ν_c, therefore $\phi_A = \arg(G_c(\tau))$. Lastly for simplicity we rewrite eq. (2.23) as eq. (2.34) and from eq. (2.15) the interferogram signal as eq. (2.35).

$$\gamma(\tau) = \zeta_D(\tau)\zeta_A(\tau) \exp\left(i\left[\phi_0(\tau) + \phi_D(\tau) + \phi_A(\tau)\right]\right) \tag{2.34}$$

$$S = \frac{I_0}{2}\left[1 + \zeta_D(\tau)\zeta_A(\tau)\cos(\phi_0 + \phi_D + \phi_A)\right] \tag{2.35}$$

2.3.2 Delay Dispersion

Until now we have considered an instrument with no optical dispersion i.e. the optical path difference produced by the interferometer is not frequency dependent. However, this is not the case in reality. To approximate this effect we linearly expand $\tau(\nu)$ about the rest-frame frequency ν_0:

$$2\pi\nu\tau(\nu) \approx 2\pi\nu_0\tau(\nu_0) + 2\pi(\nu - \nu_0)\left.\frac{d(\nu\tau(\nu))}{d\nu}\right|_{\nu=\nu_0} \tag{2.36}$$

$$\hat{\tau}_0 \equiv \left.\frac{d(\nu\tau)}{d\nu}\right|_{\nu=\nu_0} = \tau_0 + \nu_0\left.\frac{d\tau}{d\nu}\right|_{\nu=\nu_0} \tag{2.37}$$

This allows us to define the group delay, $\hat{\tau}_0$, which quantifies how much a wave packet (or group of closely spaced frequencies) is delayed as it travels through the interferometer. Going forward we replace time delay $\tau(\nu)$ with phase delay $\phi(\nu)$, where $\phi(\nu) \equiv 2\pi\nu\tau$ as used eq. (2.26). We therefore re-write eq. (2.36) as eq. (2.38), where analogously $\hat{\phi}_0$ is the group delay of the instrument in units of radians.

$$\phi(\nu) \approx \phi_0 + \hat{\phi}_0\left[\frac{\nu - \nu_0}{\nu_0}\right] \tag{2.38}$$

With this and applying the same derivations described in section 2.3.1 we can rewrite eq. (2.34) as

$$\gamma(\tau_0) = \zeta_D(\hat{\tau}_0)\zeta_A(\hat{\tau}_0)\exp\left(i\left[\phi_0(\tau_0) + \phi_D(\hat{\tau}_0) + \phi_A(\hat{\tau}_0)\right]\right) \tag{2.39}$$

where we can see that the rest-frame phase delay ϕ_0 is unchanged compared to a non-dispersive instrument but the Doppler and asymmetry terms depend on the group delay of the instrument.

2.3.3 Inhomogeneous Sources

In addition to what we have discussed in the previous sections, we must account for the fact that a plasma is three-dimensional and its spectrum, measured along a given sightline L, likely cannot be characterised by a single velocity and temperature, i.e. the plasma is inhomogeneous. This section follows an equivalent section from Clive Michael's thesis, section 2.5.1 [56]. We begin by defining the measured spectrum $\breve{g}(\nu)$ as the emissivity weighted average of the local spectrum $g(\nu, \mathbf{R})$, where $e(\mathbf{R})$ is the local emissivity at position $\mathbf{R}$ and $\breve{e}$ is the line-integrated emissivity.

$$\breve{g}(\nu) = \frac{1}{\breve{e}}\int_L e(\mathbf{R})g(\nu, \mathbf{R})dl \tag{2.40}$$

$$\breve{e} = \int_L e(\mathbf{R})dl \tag{2.41}$$

We can subsequently define the line-integrated degree of coherence $\breve{\gamma}(\tau)$ in terms of the local degree of coherence $\gamma(\tau, \mathbf{R})$:

$$\breve{\gamma}(\tau) = \frac{1}{\breve{e}}\int_L e(\mathbf{R})\gamma(\tau, \mathbf{R})dl \tag{2.42}$$

Writing both coherences explicitly in terms of their phase and contrasts as $\breve{\gamma}(\tau) = \breve{\zeta}(\tau)\exp\big(i\breve{\phi}(\tau)\big)$ and $\gamma(\tau, \mathbf{R}) = \zeta(\tau, \mathbf{R})\exp(i\phi(\tau, \mathbf{R}))$, allows us to see

that the measured phase $\check{\phi}(\tau)$ and contrast $\check{\zeta}(\tau)$ of an interferogram produced by an inhomogeneous plasma are both functions of the local phase $\phi(\tau, \mathbf{R})$ and contrast $\zeta(\tau, \mathbf{R})$:

$$\check{\zeta}(\tau) \exp\Big(i\check{\phi}(\tau)\Big) = \frac{1}{\check{e}} \int_L e(\mathbf{R})\zeta(\tau, \mathbf{R}) \exp(i\phi(\tau, \mathbf{R}))dl \tag{2.43}$$

We can further define the local phase as the sum of a local perturbation $\tilde{\phi}(\tau, \mathbf{R})$ and the measured phase: $\phi(\tau, \mathbf{R}) = \check{\phi}(\tau) + \tilde{\phi}(\tau, \mathbf{R})$, giving us

$$\check{\zeta}(\tau) = \frac{1}{\check{e}} \int_L e(\mathbf{R})\zeta(\tau, \mathbf{R}) \exp\Big(i\,\tilde{\phi}(\tau, \mathbf{R})\Big)dl \tag{2.44}$$

As we are assuming that the local phase perturbations are small (i.e. $\tilde{\phi}(\tau, \mathbf{R}) \ll 1$), we can apply a Maclaurin expansion to the complex exponential in eq. (2.44) $\exp\Big(i\tilde{\phi}(\tau, \mathbf{R})\Big) \approx 1 + i\tilde{\phi}(\tau, \mathbf{R})$. As we know measured contrast must be purely real we can then derive the following:

$$\check{\zeta}(\tau) \approx \frac{1}{\check{e}} \int_L e(\mathbf{R})\zeta(\tau, \mathbf{R})dl \tag{2.45}$$

Finally using the same series and applying eq. (2.45) we can also derive the formula for the measured phase:

$$\check{\phi}(\tau) \approx \frac{1}{\check{e}\check{\zeta}(\tau)} \int_L e(\mathbf{R})\zeta(\tau, \mathbf{R})\phi(\tau, \mathbf{R})dl \tag{2.46}$$

To summarise, we now have equations for the measured emissivity $\check{e}$ (eq. (2.41)), contrast $\check{\zeta}(\tau)$ (eq. (2.45)) and phase $\check{\phi}(\tau)$ (eq. (2.46)) in terms of the local emissivity, contrast and phase of the plasma. This allows us to link the physical phenomena already discussed in this chapter to measurable interferometer

quantities for example the Doppler contrast and phase now are now given by:

$$\breve{\zeta}_D \approx \frac{1}{\breve{e}} \int_L e(\mathbf{R}) \exp\left(-\frac{T_i(\mathbf{R})}{T_C}\right) dl \tag{2.47}$$

$$\breve{\phi}_D \approx \frac{\hat{\phi}_0}{\breve{e}\, c\, \breve{\zeta}} \int_L e(\mathbf{R}) \exp\left(-\frac{T_i(\mathbf{R})}{T_C}\right) \boldsymbol{v}(\boldsymbol{r}) \cdot \boldsymbol{l}\, dl \tag{2.48}$$

From eqs. (2.47) and (2.48) it is clear that in order to reconstruct local temperature values one must first reconstruct the local emissivity. Similarly, to determine velocities one must reconstruct both local emissivity and temperature values.

2.4 Polarisation Interferometry

So far we have discussed amplitude division interferometry in terms of a Michelson type design, whereby the light takes 2 different paths, however coherence imaging spectroscopy systems instead split the amplitude of incoming light into orthogonal polarisation states. In its simplest form this is achieved by placing a birefringent crystal between two linear polarisers oriented at 45° to the 'fast' axis of the crystal. Here the 'fast' and 'slow' axes of a birefringent crystal refer to the polarisation planes, perpendicular to the crystal's face, along which light travels with different speeds through the crystal due to its anisotropic optical properties. The refractive index of the crystal along each axis is denoted by n_E and n_O, respectively. The subscripts here are derived for the terms *extraordinary* and *ordinary*, which are assigned to rays of light whose polarisations are parallel to the crystal's fast and slow axes, respectively.

In this section, we introduce a framework for modelling how a polarisation interferometer produces an interferogram, the basis of which is the Stokes description of light and Mueller calculus. Other work of this type has used Jones calculus as an alternative to Mueller calculus, as Jones calculus acts on

the electric field directly thus preserving the absolute phase of the light [57, 30]. Conversely, a Mueller description uses the irradiance of the light, discarding the absolute phase information but allowing for mixed polarisation states.

2.4.1 Uniaxial Crystals

It is often assumed, for simplicity, that linear retarders consistently introduce a frequency-specific delay between orthogonal polarisation states. However, this delay actually varies with the trajectory of the incoming light. Utilising this variation across a sensor to sample different delays is a recognised technique in imaging Fourier transform spectroscopy, known as spatial multiplexing [58]. Here we briefly discuss the underlying physics that causes this variation as it is fundamental to the operation of the system used in this work.

Anisotropic materials exhibit differential distortion of their electron clouds under an electric field, leading to a refractive index n that is dependent on the electric field's orientation, dictated by the light's route and polarisation. This work is confined to uniaxial crystals, which are characterised by a singular axis of symmetry. From Maxwell's equations we know that this symmetry axis, known as the crystal optic axis (COA), allows for two distinct plane wave solutions exhibiting different phase velocities and orthogonal linear polarisations, [57, 59]. The ordinary ray (O-ray), aligned orthogonally to the COA, maintains a constant refractive index regardless of its path and adheres to Snell's law. Conversely, the extraordinary ray (E-ray), with its field component parallel to the COA, displays a path-dependent refractive index and does not generally follow Snell's law. When the ray's path coincides with the COA, both rays share a single refractive index, eliminating the birefringent effect. The extraordinary ray's path can be deduced via Huygens' principle [60].

In order to describe, in general, the delay imparted by a uniaxial crystal we must first define its geometry, fig. 2.2. The *principal section*, is defined as

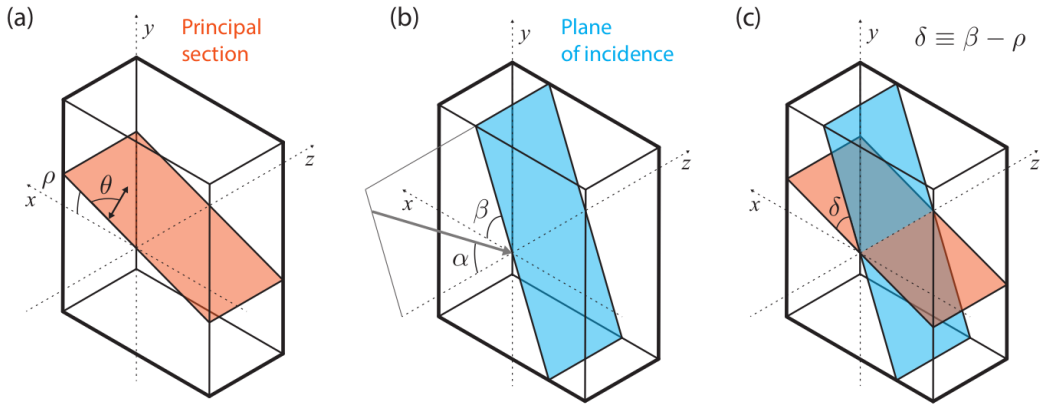

Figure 2.2: Shown are the angles used to define incident ray paths and crystal orientations. (a) shows the orientation of the principal section ρ, and the crystal cut-angle θ. (b) shows the incidence, α and azimuthal, β ray path angles. (c) defines δ the angle between principal section and the plane of incidence of incoming rays.[4]

any plane which contains both the surface normal and the crystal optic axis. On this plane we define the cut-angle θ of the crystal as the angle between the front face of the crystal and the COA. The orientation of the crystal is defined with ρ, the angle between the x-axis and the principle section. The incidence angle α, is the angle between the incident ray and the surface normal, and β is the angle the plane of incidence makes with the x-axis. Lastly, δ is the angle between the principal section and the ray's plane of incidence.

Returning to our example of an interferometer with a uniaxial crystal between two polarisers oriented at 45° to the principal section of the crystal (i.e. $\delta = 45°$) we examine the delay imparted. For an ideal waveplate ($\theta = 0°$) and light normally incident on the crystal surface ($\alpha = 0°$), the delay is given by eq. (2.49), where $B = n_E - n_O$ is the birefringence of the crystal, $n_{E,O}$ are the refractive indices of the extraordinary and ordinary rays and L is its thickness. This can be seen clearly in fig. 2.3 where the O and E-ray share the same path through the crystal therefore the optical path difference (OPD) is purely described by B. Figure 2.3 also clearly shows how light exiting a

[4]Figure kindly provided by Joseph Allcock [61]

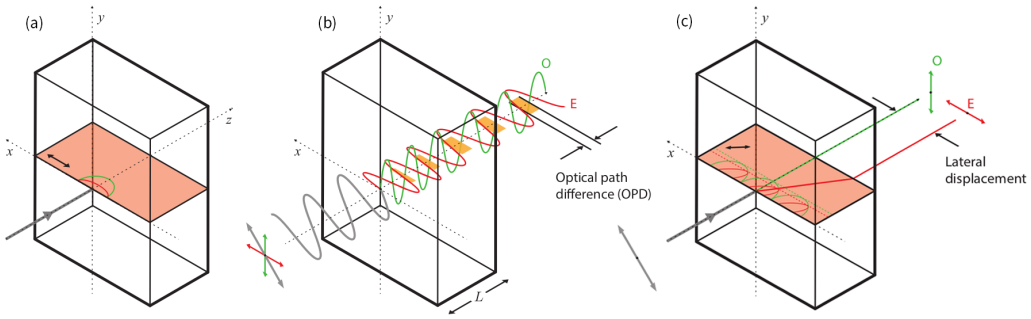

Figure 2.3: Images (a) and (b) show a waveplate with a cut angle of 0°. In (a) we see the Huygens wavelets corresponding to the ordinary and extraordinary rays. (b) shows the optical path difference between each ray, created by the crystal. Image (c) shows how by rotating the cut-angle (black arrow) of a waveplate the extraordinary axis also rotates creating a lateral displacement between the exiting rays.[5]

uniaxial crystal is split into two orthogonal polarisation states.

$$\phi = \frac{2\pi LB}{\lambda} \tag{2.49}$$

$$\phi = \frac{2\pi L}{\lambda}\left(\sqrt{n_O^2 - n^2\sin^2\alpha} + \frac{n\,(n_O^2 - n_E^2)\sin\theta\cos\theta\cos\delta\sin\alpha}{n_E^2\sin^2\theta + n_O^2\cos^2\theta} - \frac{n_O\sqrt{n_E^2(n_E^2\sin^2\theta + n_O^2\cos^2\theta) - n^2\sin^2\alpha\,(n_E^2 - (n_E^2 - n_O^2)\cos^2\theta\sin^2\delta)}}{n_E^2\sin^2\theta + n_O^2\cos^2\theta}\right) \tag{2.50}$$

This is not the case for non-zero values of θ where we use Huygens' principle of secondary wavelets to describe the E-ray's path through the crystal, resulting in a lateral displacement fig. 2.3. In this case, as well as for non-normally incident rays, the delay can be described by eq. (2.50), where n is the refractive index of the medium surrounding the crystal [62]. The ordinary and extraordinary refractive indices can be calculated using the Sellmeier coefficients[6] of a given crystal, eq. (2.51), which describe the dispersion of a

[5]Figure kindly provided by Joseph Allcock [61]

[6]Sellmeier coefficients are constants used in the Sellmeier equation, which describes the wavelength-dependent refractive index of a transparent material.

crystal.

$$n_{E,O}(\lambda) = \left(A_{e,o} + \frac{B_{e,o}}{\lambda^2 + C_{e,o}} + D_{e,o}\lambda^2 \right)^{1/2} \tag{2.51}$$

2.4.2 Stokes Vectors

Stokes vectors provide a framework for describing the polarisation state of light, including linear, circular, and elliptical polarisations. Defined as $S = (S_0, S_1, S_2, S_3)$, each component conveys specific polarisation information.

- S_0 describes the total irradiance of the light
- S_1 describes the difference in magnitude between orthogonal linear polarisations
- S_2 similarly describes the lights tendency to be polarised at +45 and -45 degrees with respect to the horizontal
- S_3 describes the tendency for the light to be right or left circular polarised

A critical parameter in polarisation studies, the degree of polarisation (DOP), is derived from the Stokes parameters and offers a quantitative evaluation of the light's polarisation purity. It is defined as:

$$DOP = \frac{\sqrt{S_1^2 + S_2^2 + S_3^2}}{S_0} \tag{2.52}$$

This expression produces a value ranging from 0 to 1, where 0 indicates unpolarised light and 1 represents fully polarised light.

Furthermore, the notion of a 'Stokes spectrum' expands the applicability of Stokes vectors across different wavelengths, enabling spectral analysis of polarisation. By examining the Stokes parameters over a spectrum, one can

acquire comprehensive insights into the wavelength-dependent dynamics of polarisation. The Stokes spectrum is denoted by eq. (2.53), where the frequency dependence has been made explicit.

$$\boldsymbol{S}(\nu) = \begin{pmatrix} S_0(\nu) \\ S_1(\nu) \\ S_2(\nu) \\ S_3(\nu) \end{pmatrix} \tag{2.53}$$

2.4.3 Mueller Calculus

Mueller calculus is an extension of the Stokes formalism, providing a comprehensive framework for modelling and analysing the propagation and transformation of polarised light through optical systems. It employs Mueller matrices, which are 4x4 matrices that describe the effect of an optical component or medium on the polarisation state of light. When a Stokes vector, representing the incoming light's polarisation state, is multiplied by a Mueller matrix, the result is a new Stokes vector that embodies the polarisation state of the light after interaction with the component or medium:

$$\boldsymbol{S}_{out}(\nu) = \mathbf{M}(\nu)\boldsymbol{S}_{in}(\nu) = \begin{pmatrix} M_{00} & M_{01} & M_{02} & M_{03} \\ M_{10} & M_{11} & M_{12} & M_{13} \\ M_{20} & M_{21} & M_{22} & M_{23} \\ M_{30} & M_{31} & M_{32} & M_{33} \end{pmatrix} \boldsymbol{S}_{in}(\nu) \tag{2.54}$$

For multi-component setups, $\mathbf{M}(\nu)$ is given by the product of the each component's Mueller matrix i.e. $\mathbf{M}(\nu) = \prod_i \mathbf{M}_i(\nu)$. To orient each component we can use the Mueller matrix for rotation of a component by ρ, eq. (2.55), where $\mathbf{M}(\nu)$ is then given by $\mathbf{M}(\nu) = \mathbf{R}(-\rho)\mathbf{M}(\nu)\mathbf{R}(\rho)$ and ρ is the angle each component is rotated by with respect to the horizontal.

$$\mathbf{R}(\rho) = \begin{pmatrix} 1 & 0 & 0 & 0 \\ 0 & \cos(2\rho) & \sin(2\rho) & 0 \\ 0 & -\sin(2\rho) & \cos(2\rho) & 0 \\ 0 & 0 & 0 & 1 \end{pmatrix} \tag{2.55}$$

In this work we deal with three types of optical components: linear polarisers, linear retarders and quarter waveplates (a special case of a linear retarder), the Mueller matrices of which are used to derive the general interferogram equation of the instrument used in this work. The matrix for a linear polariser with its transmission axis oriented at ρ to the x-axis is given by eq. (2.56). Similarly the Mueller matrix for a linear retarder imparting a phase delay $\phi(\nu)$ with its fast axis also oriented at ρ is given by eq. (2.57). The Mueller matrix for a quarter waveplate can then be obtained from eq. (2.57), $\mathbf{M}_{qwp}(\rho) = \mathbf{M}_{ret}(\rho, \frac{\pi}{2})$.

$$\begin{aligned} \mathbf{M}_{pol}(\rho) &= \mathbf{R}(-\rho)\frac{1}{2}\begin{pmatrix} 1 & 1 & 0 & 0 \\ 1 & 1 & 0 & 0 \\ 0 & 0 & 0 & 0 \\ 0 & 0 & 0 & 0 \end{pmatrix}\mathbf{R}(\rho) \\ &= \frac{1}{2}\begin{pmatrix} 1 & \cos(2\rho) & \sin(2\rho) & 0 \\ \cos(2\rho) & \cos^2(2\rho) & \cos(2\rho)\sin(2\rho) & 0 \\ 0 & \cos(2\rho)\sin(2\rho) & \sin^2(2\rho) & 0 \\ 0 & 0 & 0 & 0 \end{pmatrix} \end{aligned} \tag{2.56}$$

$$\mathbf{M}_{ret}(\rho,\phi) = \mathbf{R}(-\rho)\begin{pmatrix} 1 & 0 & 0 & 0 \\ 0 & 1 & 0 & 0 \\ 0 & 0 & \cos(\phi) & \sin(\phi) \\ 0 & 0 & -\sin(\phi) & \cos(\phi) \end{pmatrix}\mathbf{R}(\rho)$$

$$= \begin{pmatrix} 1 & 0 & 0 & 0 \\ 0 & \cos^2(2\rho)+\sin^2(2\rho)\cos(\phi) & \cos(2\rho)\sin(2\rho)(1-\cos\phi) & \sin(2\rho)\sin(\phi) \\ 0 & \cos(2\rho)\sin(2\rho)(1-\cos\phi) & \cos^2(2\rho)\cos(\phi)+\sin^2(2\rho) & -\cos(2\rho)\sin(\phi) \\ 0 & -\sin(2\rho)\sin(\phi) & \cos(2\rho)\sin(\phi) & \cos(\phi) \end{pmatrix} \tag{2.57}$$

2.4.4 General Imaging System

As discussed, the delay imparted by a uniaxial crystal is dependent on the incidence and azimuthal angles at which a ray contacts the crystal's surface. This fact can be used to the advantage of interferometry by using an imaging sensor to sample different delays. In order to do this, light incident on any linear retarder in the interferometer must be collimated. Figure 2.4 shows the full interferometer setup for the simple system discussed earlier in this section. The combination of the objective lens (l_1) and intermediate lens (l_2) results in collimated light by focusing l_1 to the back focal plane of l_2. Light then passes through the core of the interferometer and through a spectral bandpass filter before being focused onto the sensor plane by the imaging lens (l_3).

Using eq. (2.50), we can calculate the interferometer delay across the sensor, but first we must define α and β as function of sensor coordinates (x, y). To do this we assume l_3 is a thin lens, therefore α and β are described by eqs. (2.58) and (2.59), respectively, where f_3 is the focal length of the imaging lens.

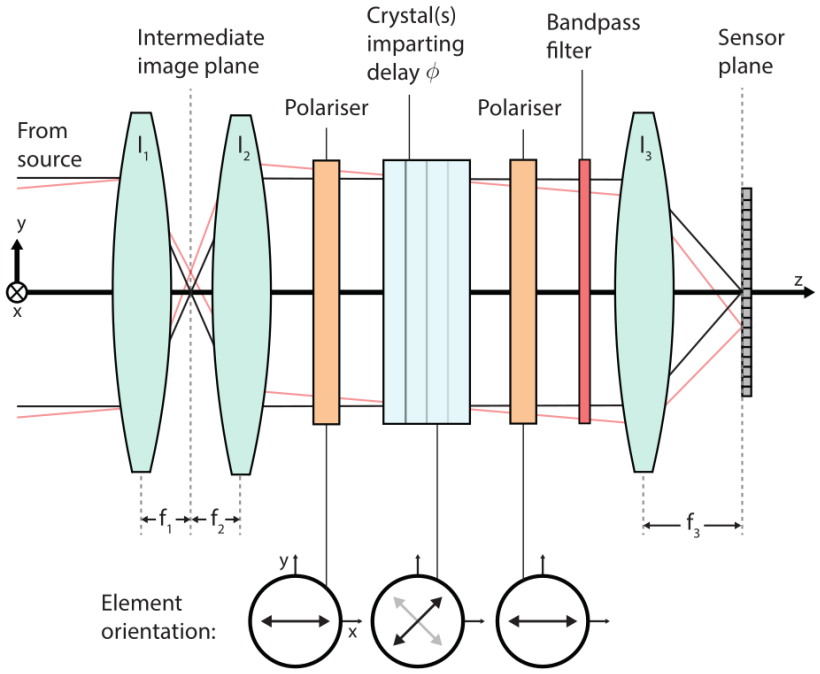

Figure 2.4: Shown is the general setup of a CIS interferometer. First the incoming light is collimated by l_1 and l_2 before being linearly polarised. The light then enters the crystal where a delay of ϕ is applied to it. Finally the light passes through another linear polariser and a spectral bandpass filter before being focused on to the sensor plane by imaging lens, l_3.[7]

$$\alpha(x, y) = \arctan\left(\frac{\sqrt{x^2 + y^2}}{f_3}\right) \tag{2.58}$$

$$\beta(x, y) = \arctan\left(\frac{y}{x}\right) + \pi \tag{2.59}$$

Figure 2.5 shows how α and β vary across a sensor when viewed with a 50 mm focal length imaging lens. With this we now define an equivalent equation to eq. (2.54) but for the above interferometer:

$$\boldsymbol{S}_{out}(x, y) = \int \mathbf{M}_{tot}(x, y, \nu)\boldsymbol{S}_{in}(x, y, \nu)d\nu \tag{2.60}$$

where, $\mathbf{M}_{tot}(x, y, \nu)$ is the product of the Mueller matrices for each of the interferometer components, and $\boldsymbol{S}_{in}(x, y, \nu)$ is the Stokes vector for light entering the interferometer mapped to the sensor coordinates (x, y) for a general spec-

[7]Figure kindly provided by Joseph Allcock [61]

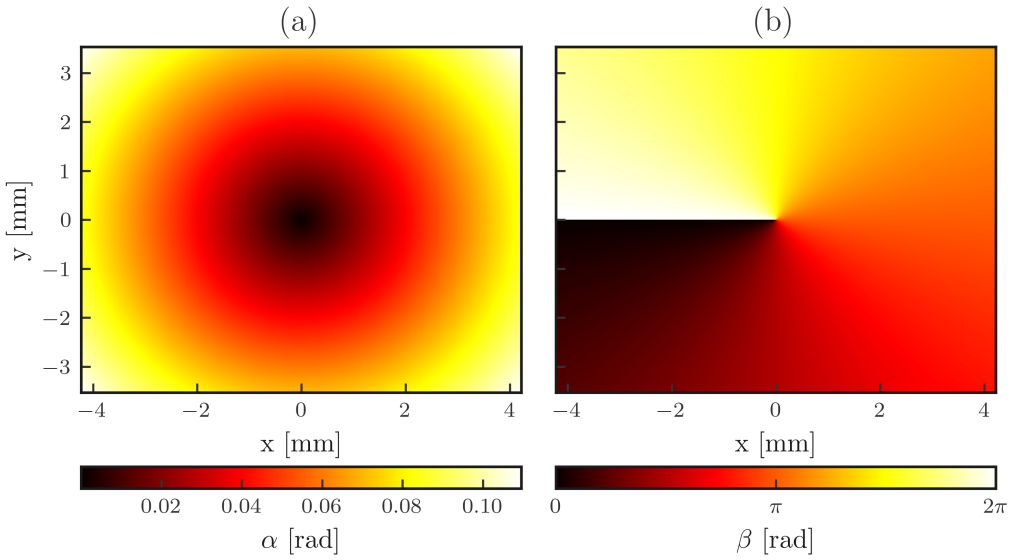

Figure 2.5: In this figure we show how (a) the incidence angle α and (b) the azimuthal angle vary across the sensor. These images were simulated for a imaging lens focal length f_3 of 50 mm which matches that used later in this thesis.

trum with frequencies, ν. The first value S_0 from $\boldsymbol{S}_{out}(x, y)$ will then give us the irradiance measured at each sensor pixel. Examples of the interferograms produced this system for cut-angles of 0°, 3°, 90° are shown in fig. 2.6. The spatial frequency of the fringes reach a maximum at $\theta \approx 45°$. These figures have been modelled using a crystal known as alpha Barium Borate (α-BBO), which all the crystals discussed in this work are made of. The generally accepted refractive indices for α-BBO are $n_E \approx 1.56$, $n_O \approx 1.68$ [63].

2.5 Single-Delay CIS

Until recently all coherence imaging systems in use imparted a single phase delay at each pixel, aptly called *single-delay* systems. The simplicity of these systems is one of their biggest advantages, hence we used one as an example of a general interferometer setup in the last section.

These systems can be categorised by the method they use to encode their

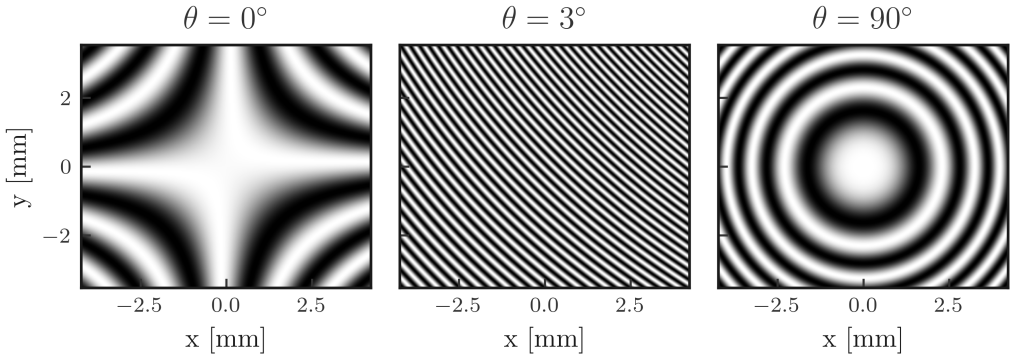

Figure 2.6: Shown are three interferograms simulated using the interferometer shown in fig. 2.4. In each the cut-angle of the crystal has been changed to show the distinctive hyperbolic pattern created by a pure waveplate ($\theta = 0°$), a striping pattern created when $0° < \theta < 90°$ and a circular pattern produced using a crystal with $\theta = 90°$.

interferometer delay: a linear phase mask (LPM) or a pixelated phase mask (PPM). The latter of these is used in this research and therefore is discussed in greater detail.

2.5.1 Linear Phase Mask

A linear phase mask can be obtained using a crystal which creates a physical separation, in a given direction, between the ordinary and extra-ordinary rays. In previous CIS implementations this was achieved with a Savart plate [30]. A Savart plate consists of two identical linear retarders with a cut-angles of 45° bonded together so that their fast-axes are at right-angles to each other. This results in a spatial displacement of the o and e rays with respect to each other but no phase delay for rays normally incident on the crystal as the second crystal cancels out the offset of the first. A phase shear is created for off-axis rays, however it can be shown that the imparted delay due to this shear is reduced by a factor of $\sqrt{2}$ compared to a single crystal with $\theta = 45°$ and an equivalent thickness.

When choosing a Savart plate thickness there are two important consider-

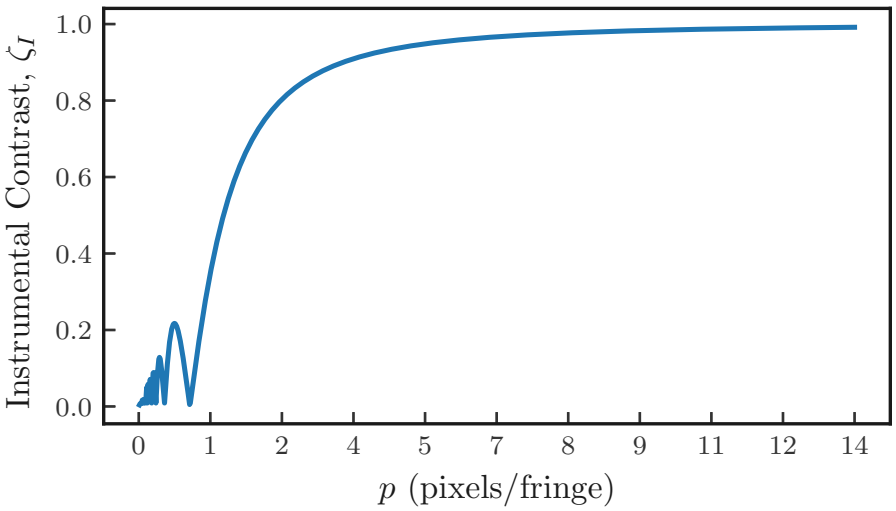

Figure 2.7: Here we plot eq. (2.62) to show how instrumental contrast is affected by fringe width. We draw specific attention to how instrumental contrast decreases quickly for fringe widths < 8 pixels.

ations: spatial resolution and fringe contrast. The resolution of LPM system parallel to its fringes is defined by the sensor and pixel sizes, this is not the case perpendicular to the fringes. In the perpendicular direction, the resolution is defined by the fringe width (in pixels) [30]. It is therefore prudent to decrease the fringe width as much as possible by increasing the strength of the phase shear across the sensor, however this reduces the fringe contrast.

It can be shown that for a system whose fringes are perfectly aligned with the x-axis the phase across the sensor is given by eq. (2.61), where p is the fringe width in pixels and d is the pixel size in the y direction. Additionally, it has been shown that the instrumental contrast of this instrument is given by eq. (2.62) [61].

$$\Phi(\mathbf{r}, \tau) = \frac{2\pi}{pd} y \tag{2.61}$$

$$\zeta_I = |\mathrm{sinc}(\pi/p)| \tag{2.62}$$

Figure 2.7 shows how below 8 pixels/fringe instrumental contrast decreases

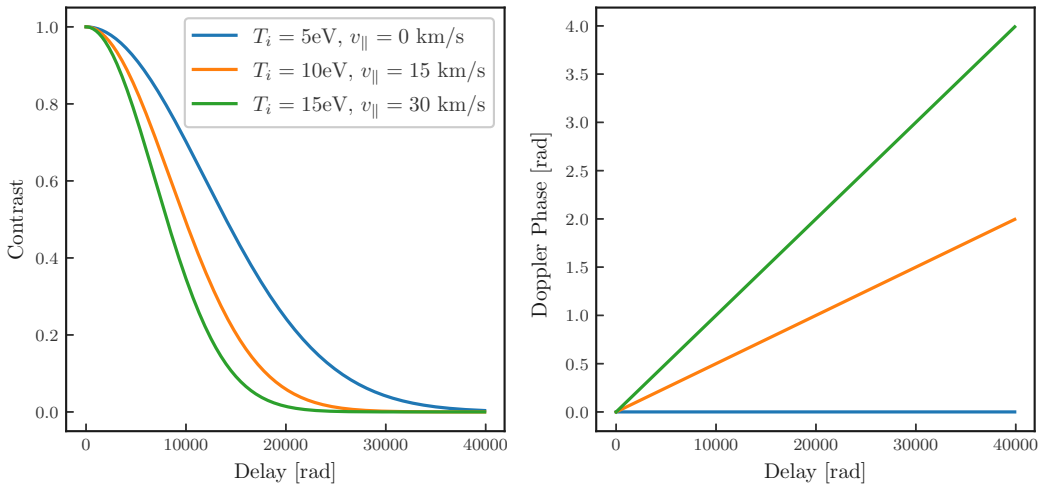

Figure 2.8: Here we show how Doppler contrast (left) and phase (right) vary with interferometer delay. We see that contrast decreases with delay at a rate proportional to the temperature of the emitting species. Conversely the right figure shows how Doppler phase increases linearly with delay. The slope of this line is directly proportional to velocity, therefore the blue line representing a stationary emitter is 0 for all delays.

rapidly. For this reason it has been common for linear phase mask systems to operate with $p = 10$ resulting in $\zeta_I = 0.98$.

Fringe width is not the only consideration in LPM systems though. In order to effectively use an linear phase mask system the phase delay at each pixel must be higher than that typically provided by a Savart plate only. This has been achieved on previous devices by adding a higher order[8] waveplate alongside the Savart plate. In doing this a user increases their accuracy in velocity measurements, however, measured contrast generally decreases as we increase interferometer delay therefore reducing measurement accuracy in ion temperature, as seen for example in fig. 2.8.

More recently, coherence imaging studies have made use of a displacer plate[9] instead of a waveplate-Savart setup. The displacer plate would be pro-

[8]Higher order refers to a waveplate designed so that the phase difference between the fast and slow axes is an integer multiple of 2π, plus the desired phase delay

[9]The term *displacer plate* refers to a uniaxial crystal with a cut-angle between $(0, 90)$ degrees, which creates both a phase delay and phase shear similar to a waveplate-Savart plate combination

duced with a cut-angle and thickness which will give an appropriate phase shear and offset for the specific line and plasma condition of interest. In practice decreasing the number of crystals in the system can have positive effects on instrumental contrast as it reduces the number of surfaces and by extension limits the effects of surface non-uniformities.

2.5.2 Pixelated Phase Mask

To accurately ascertain the unique spectral information from which a interferogram was produced one must sample the interferogram delay multiple times per 2π step. However, the number of discrete samples can be smaller than what is used in linear phase mask systems and can instead be achieved using polarisers.

It has been shown that the measured irradiance following linear polariser incident with light of two orthogonal circular polarisations is given by, eq. (2.63), where I denotes irradiance, r and l refer to right and left circularly polarised light, θ is the angle the polarisers transmission axis makes with the horizontal and $\Delta\phi$ is the phase difference already present between the 2 rays [64].

$$I = \frac{1}{2}\left[I_r + I_l + 2\sqrt{I_r I_l}\cos(\Delta\phi + 2\theta)\right] \tag{2.63}$$

It follows that by rotating a polariser in front of a sensor one can sample the interferogram at any point in its cycle. Traditionally, this technique has been implemented by taking multiple images while a polariser rotates, however a system of this nature is then limited in the time domain. Modern manufacturing has thankfully mitigated this issue with the creation of a camera sensor with pixel-level polarisers [65, 66].

The first instance of a pixelated polarised sensor being used in a coherence imaging system was presented by Allcock et al. [67]. The sensor used consists

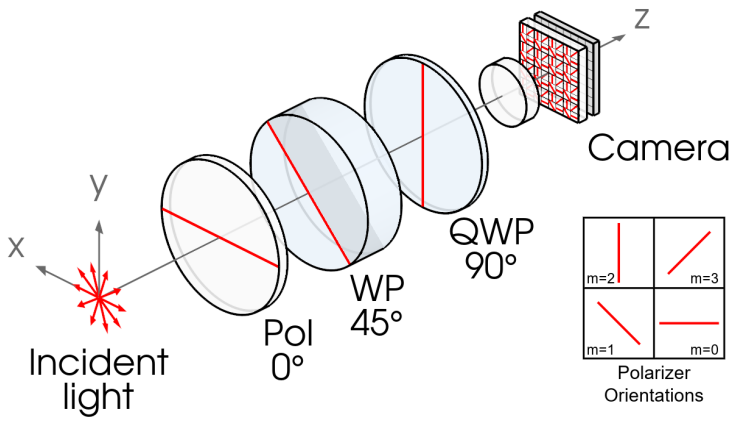

Figure 2.9: Schematic of a single-delay CIS instrument with a pixelated polarised sensor. Also shown is the orientation of each polariser within the 2x2 super-pixel. Here POL indicates the polariser, WP the waveplate and QWP the quarter waveplate. The red lines on each interferometer component indicate the transmission/fast axis of each component and correspond to the orientation values shown below each component.

of four polarisers bonded to individual pixels in a 2x2 array across the sensor, with each pixel in the array given an index m from 0 to 3. The transmission axis of each polariser in the grid is rotated by an additional 45° compared to the previous pixel index as shown in fig. 2.9. This results in the quadrature sampling of an interferogram which provides sufficient information for physical studies.

Figure 2.9 also shows the general setup for a single-delay pixelated CIS system, which includes a zero-order quarter waveplate (QWP) oriented at 45° to the waveplate. This QWP creates two opposite circular polarisations of light which are then sampled by the pixelated polarised sensor. The Mueller matrix for this system is given by eq. (2.64).

$$\mathbf{M}_{tot} = \mathbf{M}_{pm}\left(\rho_{pm}\right)\mathbf{M}_{qwp}\left(\tfrac{\pi}{2}\right)\mathbf{M}_{wp}\left(\tfrac{\pi}{4},\phi(\nu)\right)\mathbf{M}_{pol}\left(0\right) \tag{2.64}$$

where ρ_{pm} is the orientation of the pixel polariser. Using eq. (2.60) the stokes vector at the sensor is then given by

$$\mathbf{S}_{out} = \frac{S_0(\nu)}{4}\Big(1 + \cos(\phi(\nu) + 2\rho_{pm})\Big)\begin{pmatrix}1\\1\\0\\0\end{pmatrix} \tag{2.65}$$

It is assumed that the sensitivity of each pixel is not polarisation dependent, therefore with $g(\nu) \equiv S_0(\nu)/I_0$ and applying the same techniques used in eq. (2.39), the measured irradiance is given by eq. (2.66). In eq. (2.67) we have replaced the additional delay imparted by the polariser, $2\rho_{pm}$, with $m\frac{\pi}{2}$ where m is the pixel index we previously assigned to each polariser within the repeating 2x2 grid as denoted in fig. 2.9.

$$\begin{aligned} I &= \int_{-\infty}^{\infty} \frac{S_0(\nu)}{4}\Big(1 + \cos(\phi(\nu) + 2\rho_{pm})\Big)d\nu \\ &= \frac{I_0}{4}\left(1 + \mathbb{R}\left\{\int_{-\infty}^{\infty} g(\nu)\exp\Big(i\Big[\phi(\nu) + 2\rho_{pm}\Big]\Big)\,d\nu\right\}\right) \\ &= \frac{I_0}{4}\Big(1 + \zeta(\hat{\tau}_0)\cos\left[\Phi(\tau_0)\right]\Big) \end{aligned} \tag{2.66}$$

$$\Phi(\tau_0) = \phi_0(\tau_0) + \phi_D(\hat{\tau}_0) + \phi_A(\hat{\tau}_0) + m\frac{\pi}{2} \tag{2.67}$$

2.6 Multi-Delay CIS

In section 2.5 we explored two common ways to construct a coherence imaging system, both of which centred around a single interferometer delay at each pixel. However, the use of one fixed interferometer delay may not always provide enough spectral resolution to conduct physical studies, therefore systems which sample at multiple fixed delays have been produced. We will discuss this further in chapter 4.

The use of multiple interferometer delays is not a new concept. One early

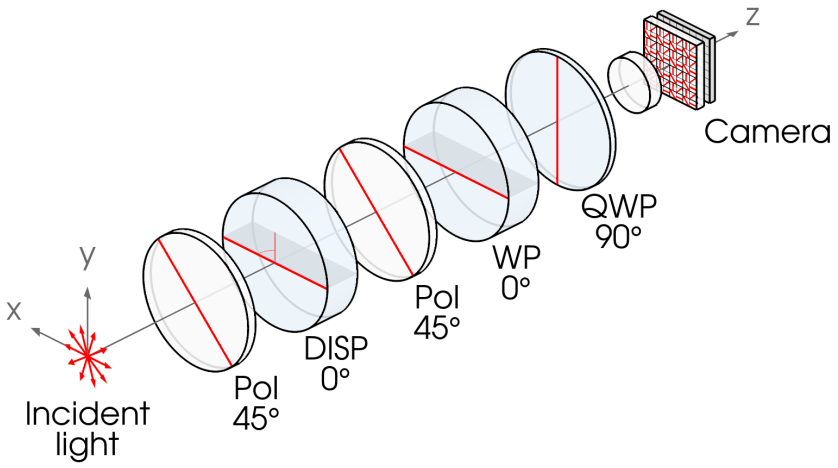

Figure 2.10: Analogously to fig. 2.9, here we show the component layout used by Allcock to produce 4 interferometer delays [67]. Where POL denotes a polariser, DISP a displacer plate, WP a waveplate and QWP a quarter wave-plate. The transmission/fast-axis of each component is indicated by the red line on each component, corresponding to the angles shown below each label.

use of this technique was in 1967 by Michel et al. who measured the plasma temperature of a Cd lamp using a Michelson interferometer with six fixed delays [68]. Previous CIS experiments have also used multiple fixed delays. In this case, discharges were repeated and the interferometer delay changed for each discharge. Both of these methods would have significant draw backs if implemented on a modern fusion device. For this reason, Allcock developed a single CIS instrument capable of of measuring multiple interferometer delays simultaneously [61].

The interferometer designed by Allcock was similar to a single-delay PPM system with an additional polariser and a displacer plate added, fig. 2.10. Using Mueller calculus, eq. (2.68), we can see that the measured interferogram is a sum of 4 distinct interferograms, eq. (2.69), one corresponding to each of the linear retarder's delays and two corresponding to the sum and difference of those crystal delays. The notation used in eq. (2.69) will be used throughout this text so we will clearly define it now: Φ_n and ζ_n are the measured phase and contrast, respectively, of a given interferogram and n denotes the index

label of that interferogram. The index 1 corresponds to the delay imparted by the first crystal in the interferometer, 2 the second, $2+1$ the sum of both crystal delays and $2-1$ the difference between the crystal delays.

$$\mathbf{M}_{tot} = \mathbf{M}_{pm}\left(\rho_{pm}\right)\mathbf{M}_{qwp}\left(\tfrac{\pi}{2}\right)\mathbf{M}_{wp}\left(\tfrac{\pi}{4},\phi_2(\nu)\right)\mathbf{M}_{pol}\left(0\right)\mathbf{M}_{disp}\left(\tfrac{\pi}{4},\phi_1(\nu)\right)\mathbf{M}_{pol}\left(0\right) \tag{2.68}$$

$$I = \frac{I_0}{8}\Big(1+\zeta_1\cos\left[\Phi_1\right]+\zeta_2\cos\left[\Phi_2\right]+\frac{1}{2}\zeta_{2+1}\cos\left[\Phi_{2+1}\right]+\frac{1}{2}\zeta_{2-1}\cos\left[\Phi_{2-1}\right]\Big) \tag{2.69}$$

Allcock used this instrument to measure electron density and ion temperature on Magnum PSI through the H_γ Balmer emission line. Although the study of this line and physical quantities related to it are useful for fusion devices, in the research we extend this system and techniques to continue the work done by Silburn on MAST studying impurity flows in MAST-U [43].

2.7 Previous CIS Investigations

Coherence imaging has been used on various fusion devices since Howard et al. began studying emission from the H1-heliac stellarator using a 16-channel photo-multiplier tube [69, 56]. This system was temporally multiplexed, in contrast to the spatially multiplexed systems discussed so far, where interferometer delay was scanned rapidly using an alternating voltage. Applying such a voltage to a waveplate resulted in a change in the plate's birefringence via the electro-optic effect. Similar studies were done on the WEGA stellerator with a CCD detector [70]. This was later improved by Howard et al. to use a ferroelectric liquid crystal which allowed delay switching using lower voltages [70].

Development in the field of CIS then settled, generally, on spatially multiplexed designs with the installation of systems on DIII-D and MAST [58, 43,

71, 72]. Both systems took the form of what we call a single-delay linear phase mask setup similar to that discussed earlier, consisting of a waveplate-Savart plate combination, and were used to measure C III ion flows to good accuracy. The installation of second CIS system on DIII-D, by Samuell et al, to study ion flow in helium discharges proved to be equally successful, with a focus on the mitigation of systematic errors, as such systems are highly sensitive to environmental factors [73]. On MAST, Silburn assumed that flow across magnetic field lines was small compared to parallel transport, therefore radial camera sightlines could be used to define the rest frame phase [30]. This served the same purpose as an in-situ laser system installed at DIII-D [74, 75], both techniques are discussed further in section 3.4 as this work provides an alternative to both techniques.

In later work, including that after 2015 on DIII-D, the waveplate-Savart plate combination was replaced with a displacer plate with a cut-angle $0° < \theta < 90°$, the exact specification of which depended on the device requirements. Ion flows were measured on both ASDEX-Upgrade and Wendelstein 7-X (W7-X), with counter-streaming C III flows[10] being observed on W7-X and an additional measurement of neutral deuterium flows on ASDEX-Upgrade showed that neutrals do typically follow the bulk ion flow [76, 77]. The addition of a CIS system on ASDEX-Upgrade was also its first use in a metal walled fusion device, leading to a discussion on reflections. This was seen by Gradic et al. who stated that "reflections could significantly disturb the quantitative analysis of the flows" [76]. Plans to study this using two CIS systems with opposite views are in place, to allow for a CIS system to be installed on the similarly metal-walled future device ITER. Ion temperature measurements have also subsequently been made on W7-X taking account of the Zeeman effect due to

[10]Counter-streaming flows refer to plasma flows where ions or electrons move in opposite directions along the magnetic field lines within the plasma.

the strong magnetic fields present in stellarators, compared to those present in the divertor regions of tokamaks [35].

Since these measurements CIS development has focused on designs creating multiple fixed interferometer delays. This was previously achieved on the H-1NF stellarator, where Doppler broadening was measured in argon plasmas [56]. However, in this case identical plasmas were produced in order to capture images at each delay. Initial attempts by Peter Urlings to measure charge-exchange recombination emission on Korea Superconducting Tokamak Advanced Research (KSTAR) with a single instrument encoding multiple spatial carriers, albeit inconclusive, provided the inspiration for later work by Joseph Allcock [53, 61].

Allcock presented designs for a multi-delay CIS system which used two uniaxial crystals to encode four spatial carriers using an imaging sensor with pixel level polarisers. This design and the theory behind it was discussed in detail in section 2.6 as it informs the design used in this research. Using this system, termed a *quad-delay* CIS, Allcock measured electron densities and ion temperatures on Magnum-PSI through the H_γ emission of the plasma. The use of multiple delays here was key to the accurate quantitative analysis Allcock produced as multiple broadening mechanisms, namely Doppler and Stark broadening and Zeeman splitting, complicated the emission spectrum of the plasma.

Finally, Kriete et al. at W7-X have used Allcock's design to produce their own quad-delay CIS for the measurement of C III ion temperatures [78]. As on Magnum-PSI, the use of multiple delays enabled Kriete et al. to produce T_i profiles from measurements of Doppler broadening that agree with spectrometers to within 10%, while accounting for strong Zeeman splitting.

2.8 Summary

In this chapter, we introduced the foundational theories of coherence imaging, encompassing Fourier transform spectroscopy, and polarisation interferometry. Within this, we have shown how by studying the underlying physical phenomena that affect a given spectrum one can quantify parameters such as ion velocities, temperatures or electron densities. Through the principles of polarisation interferometry the scanning of interferometer delays is neatly contained within a single image. Also, discussed is the evolution of this field from the comparatively simple designs of the Michelson interferometer to the complexity of spatially multiplexed CIS instruments encoding multiple spatial carriers. In the next chapter we provide further detail on how modern CIS instruments produce their images, with special attention given to the multi-delay systems currently in use as this underpins the design of the instrument used in the work. We also present the mathematics required to extract phase and contrast images from a CIS interferogram along with the design and novel techniques for calibrating the new MAST-U CIS diagnostic.

Chapter 3

MAST-U Coherence Imaging Diagnostic

In chapter 2, we introduced the theory which underpins coherence imaging spectroscopy as a technique for measuring the lineshape of plasma spectra. We also presented the technical details of how CIS instruments, up to now, have been constructed, with a focus on pixelated phase mask type systems.

In this chapter we present a novel CIS system design which uses a pixelated polarised sensor to produce three fixed interferometer delays which have been optimised for both phase and contrast measurements[11]. This is an evolution of Allcock's quad-delay CIS system, which has been modified to increase signal-to-noise ratio and enable the robust simultaneous measurement of C III velocities and temperatures in MAST-U plasmas (section 4.4). We also describe the MAST-U Multi-Wavelength Imaging diagnostic (MWI), an 11-channel optical cavity polychromator, which houses our CIS instrument. The use of a CIS instrument within a polychromator comes with significant challenges, these will be discussed in detail along with our novel solutions to them.

[11]The contents of this chapter has been recently published in the peer-reviewed journal Review of Scientific Instruments - R.S. Doyle et al. Rev. Sci. Instrum. 1 May 2024; 95 (5): 053505. doi.org/10.1063/5.0205584

Our focus then turns to the demodulation techniques used to extract phase and contrast images from CIS interferograms.

Finally, we discuss how we calibrate our instrument without an in-situ system or a tuneable laser, both of which are typically present on other fusion devices. This is a significant challenge but in this chapter we present two new techniques which account for the temperature and wavelength dependence of alpha-barium borate crystals, enabling accurate calibration of our system. Application of these techniques to experimental MAST-U data is presented in chapter 4.

3.1 Triple-Delay Coherence Imaging

Across all areas of science it is known that to conduct meaningful experiments one must obtain data with an adequate signal-to-noise ratio and sample at an appropriate frequency to isolate the quantities of interest. For imaging systems this is especially important, but challenging as often one can not control the amount of light emitted from a source and cameras are limited by frame rate and/or exposure time. These problems are also in conflict with each other as exposure time is typically inversely proportional to signal-to-noise, except in the case of saturation. Often the goal of an imaging system is to record at the highest frame-rate a sensor allows, while using the entire range of possible sensor values with 0 dB of gain. This is especially true when dealing with highly dynamic plasmas where integrating over transient events may affect physical studies.

As mentioned in section 2.7, it has been shown on the linear plasma experiment Magnum PSI that a quad-delay CIS system can produce adequate results for physical studies [61]. Although the plasma used in this study facilitated a proof of concept, they did not present the same challenges as working with

large fusion device plasmas such as those found in MAST-U. We have seen that detachment in the MAST-U SXD is strong and readily occurs as a consequence of the divertor shape [22]. In these conditions the ionisation region of the divertor leg, where C III emission is strong, moves high in the divertor limiting how much can be imaged. Additionally, the existence of high-frequency edge-localised modes (ELMs) during MAST-U shots provides further difficulties for designing a CIS system for MAST-U. In order to conduct accurate physical studies it was important the camera be able to sample at a higher frequency than the ELM frequency to avoid integration across these unstable conditions.

Due to the unavailability of optical ports on MAST-U this study is confined to a single divertor port, HL-06, shared with the MAST-U MWI. The MWI was designed to accommodate a CIS system on its eleventh channel, however this poses further optical problems, which are discussed in section 3.2. All these difficulties pointed to one solution, we must design a system which is be capable of higher optical throughput than a quad-delay system, while maintaining the spectral information to conduct physical studies. To this end we now present the triple-delay CIS instrument which we have constructed to address the above issues.

3.1.1 CIS Design

In order to increase the signal transmitted through the interferometer cell the central polariser of a quad-delay CIS system has been removed. With this change, we must modify the orientation of each interferometer component to create three distinct delays, shown with respect to the horizontal in fig. 3.1.

The first retarder is an 8 mm α-BBO displacer plate with a cut-angle θ of 45°, which as seen in chapter 2 imposes a delay ϕ_1 between the ordinary and extra-ordinary rays. Similarly, the second crystal is a 9.8 mm α-BBO crystal with a cut-angle of 0° producing a delay ϕ_2. Both crystals were inherited from

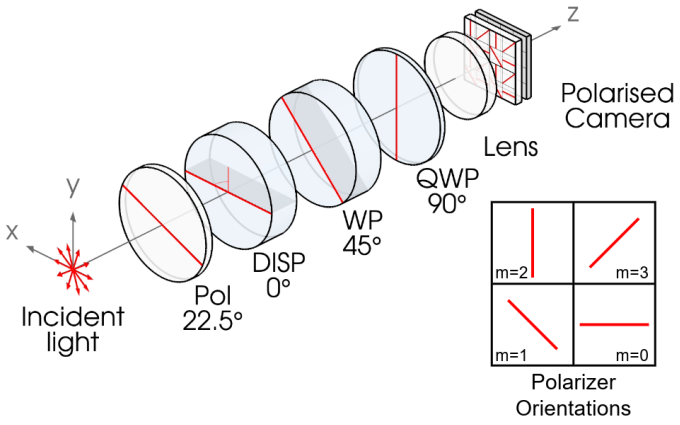

Figure 3.1: Shown here are the orientations of each CIS component within the temperature-controlled cell of our system. Together these components produce a three distinct interferometer delays. Similar to the pixelated phase mask systems discussed in chapter 2, we have also shown the orientation of each sensor polariser within the 2x2 grid.

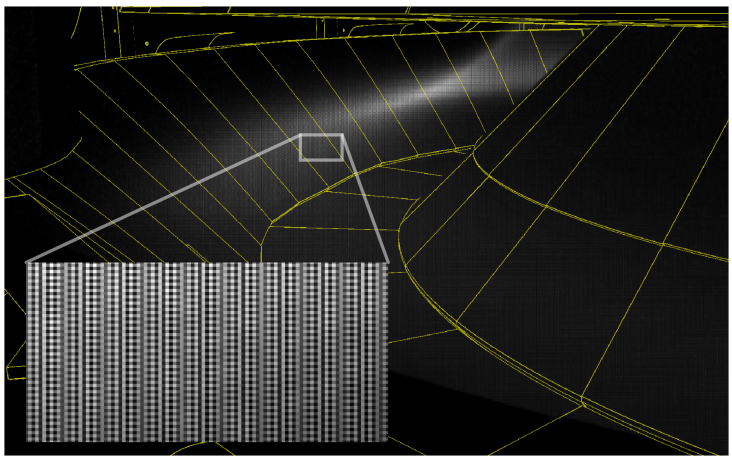

Figure 3.2: Here we show a simulated triple-delay CIS image of a MAST-U plasma in its Super-X divertor configuration. Overlaid on this image is a CAD wireframe of the MAST-U lower divertor and a zoomed in image of the interferogram showing both the pixelated and phase shear patterns.

previous CIS systems, the first from the Magnum-PSI system and the second from the original MAST CIS system [43, 61]. It follows that the image shown in fig. 3.2, which contains a simulated MAST-U SXD plasma, will then be the sum of three interferograms corresponding to the delays ϕ_2, $\phi_{2+1} = \phi_2 + \phi_1$ and $\phi_{2-1} = \phi_2 - \phi_1$. Figure 3.3 shows these delays modelled at 464.9 nm.

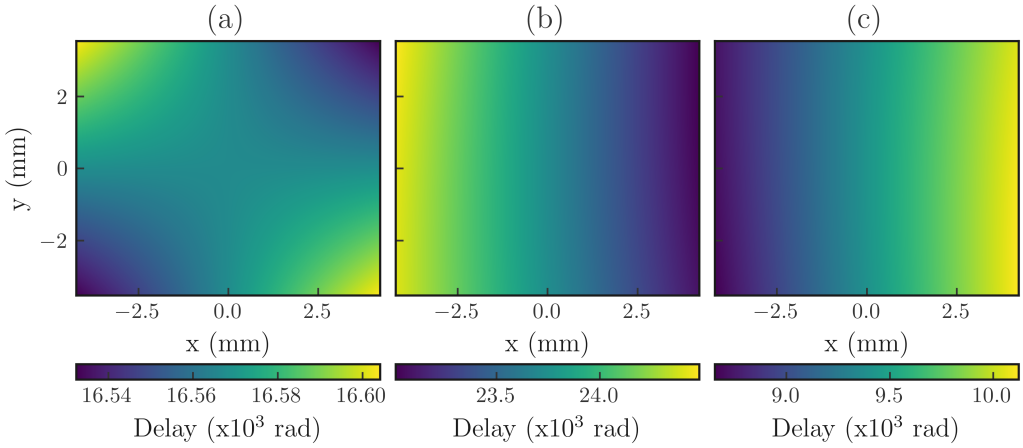

Figure 3.3: Modelled delays imparted by each component of the CIS interferometer at 464.9 nm assuming thin lenses. (a) Waveplate only, ϕ_2 (b) Sum of crystal delays, ϕ_{2+1} (c) Difference between crystal delays, ϕ_{2-1}

The polarised camera used in this work is a FLIR Blackfly S, whose polarisers are arranged in a 2x2 grid, as shown in fig. 3.1. This grid is repeated across the sensor which has dimensions 2448x2048 pixels and a pixel size of 3.45 μm. The orientation of the transmission axis of each pixel's polariser is given by $\rho_{pm} = m\frac{\pi}{4}$, where $m \in \{0, 1, 2, 3\}$ is the pixel index within the 2x2 array. In order to limit the effect of ambient temperature changes on the system, the main interferometer components were installed within an Andover 50mm filter oven which was connected to a temperature controller set at 35 $\pm$ 0.2 °C. The effects of crystal temperature on interferometer delay are significant, our solutions to this are discussed further in section 3.4.2.

The interferometer was then installed on the last channel the MAST-U MWI diagnostic [79, 80]. The MWI, shown in fig. 3.4b, is an 11-channel optical cavity polychromator capable of imaging 11 distinct spectral lines using different spectral bandpass filters. Figure 3.5 then shows full light path of the system from the intermediate image point created by the MWI optics to the FLIR camera sensor. For our study the spectral filter used was custom made by Chroma Technology and is centred at 464.8 nm with a bandwidth of 2.1 nm. The imaging lens, l_2 has a focal length of 50 mm. The collimating

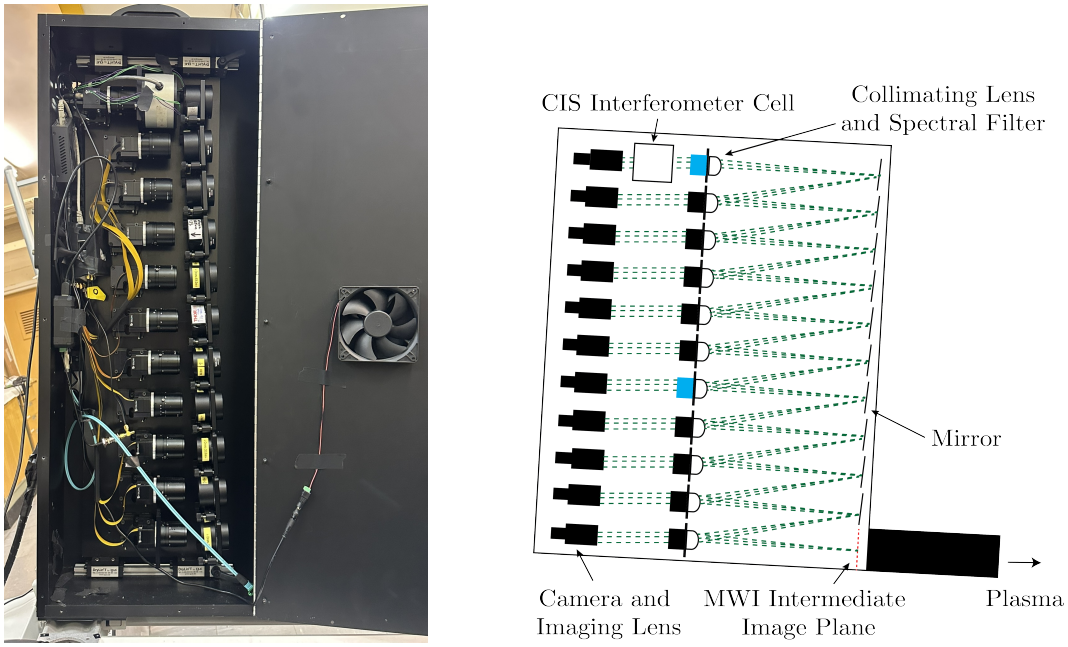

(a) (b)

Figure 3.4: (a) Image of the MAST-U MWI, showing each of the 11 channels with the MAST-U CIS installed at the top of the image. (b) Schematic of the MAST-U MWI, where the spectral filters marked in blue indicate that the CIS measures the same spectral line as that MWI channel.

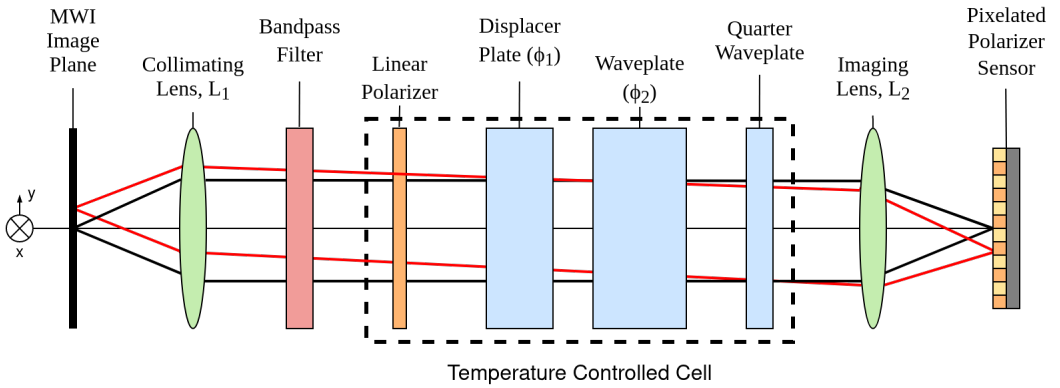

Figure 3.5: Detailed schematic of triple-delay pixelated CIS interferometer set up contained within the MAST-U MWI. Here we see that light from the MWI image plane is collimated before passing through a spectral bandpass filter. Light from the plasma then enters the interferometer temperature-controlled cell before being focused onto the camera sensor by the imaging lens.

lens l_1 initially was a 750 mm Thorlabs achromatic doublet lens identical to the other MWI lenses, however this was later modified to correct for issues relating to focal planes, discussed in section 3.2.1. A table summarising all of the component specifications is given in appendix A.

The equation for the interferogram produced by this instrument can be found using Mueller calculus, where the Mueller matrix of the instrument is given by eq. (3.1). The definition of each matrix can be found in appendix B.

$$\begin{aligned}\mathbf{M}_{tot} \equiv \mathbf{M}_{pol}\left(m\frac{\pi}{4}\right) \times \mathbf{M}_{qwp}\left(\frac{\pi}{2}\right) \times \mathbf{M}_{ret}\left(\frac{\pi}{4}, \phi_2\right) \\ \times \mathbf{M}_{ret}\left(0, \phi_1\right) \times \mathbf{M}_{pol}\left(\frac{\pi}{8}\right)\end{aligned} \tag{3.1}$$

Following the same processes laid out in chapter 2 the irradiance measured at the camera sensor is given by eq. (3.2). Comparing this equation to eq. (2.69) we can see that the signal related to each component has increased by a factor of $\sqrt{2}$, however this comes at a cost of 1 fewer fixed delay, though we will see in chapter 4 that 3 interferometer delays are sufficient for accurate physical studies. The measured interferogram, I_{out}, can then be demodulated, via the process of *synchronous demodulation*, discussed in section 3.3, to extract the measured phase (Φ_n) and contrast (ζ_n) images, given by eqs. (3.3) and (3.4).

$$I_{out} = \frac{I_{in}}{4}\left(1 + \frac{\sqrt{2}}{2}\zeta_2 \cos\left(\Phi_2\right) + \frac{\sqrt{2}}{4}\zeta_{2-1}\cos\left(\Phi_{2-1}\right) - \frac{\sqrt{2}}{4}\zeta_{2+1}\cos\left(\Phi_{2+1}\right)\right) \tag{3.2}$$

$$\Phi_n = \phi_{0,n} + \phi_{D,n} + \phi_{A,n} + m\frac{\pi}{2} \tag{3.3}$$

$$\zeta_n = \zeta_{0,n} + \zeta_{D,n} + \zeta_{A,n} \tag{3.4}$$

3.2 MWI Related Issues

Coherence imaging systems are, by their nature, highly sensitive optical systems that require precise tuning to achieve usable results. Although the MAST-U MWI was designed to accommodate the CIS interferometer cell it is not an ideal location for it. The MWI entrance optic consists of 8 lenses of a fixed focal length, commonly known as prime lenses, followed by 11 bandpass filters and 10 mirrors oriented at 3° to enable the reflection of light up the polychromator with a specific wavelength range being extracted at each channel. For operational reasons and due to the physical design it was not possible to modify the MWI for this research. Upon installation of our CIS system into the MWI problems of image ghosting and separation of focal planes were observed, both of which would be detrimental to experimental operation of our instrument. In the following sections we discuss our solutions these problems.

3.2.1 CIS Focus Planes

The MWI fore-optics consist of 8 off-the-shelf achromatic doublet lenses of varying focal lengths, up to 800 mm, with manufacturer-quoted tolerances of $\sim 1\%$. The order of these components in the MWI snout is designed to result in an intermediate image created at the location shown in fig. 3.4b. However, using a large number of lenses consecutively in this way naturally results in a range of possible locations at which the intermediate image is formed, causing imperfect collimation of incoming light. This is not an issue for the MWI as each channel's imaging lens is focused individually using a target reticule placed at the same location as the theoretical image plane, however as we will discuss now, this is not acceptable for pixelated phase mask coherence imaging systems.

In section 2.4.4 we introduced the notion of collimating light before it passes

through the interferometer cell. In doing this we map each position on the camera's sensor plane to a different angle of incidence with respect to the optical axis, z and the horizontal, x, through the crystals. Therefore all light from a given spatial location in the image experiences an identical delay which differs from all other spatial locations, as seen in fig. 3.3. In practice perfect collimation is never achieved, so in the case where the imaging lens of the system is focused to the plasma, light from the same plasma location will experience different interferometer delays. If not properly accounted for, this would be interpreted as an additional broadening of the spectral shape through a reduction in instrumental contrast. Conversely, the instrumental contrast can be maximised by focusing the imaging lens to the interference fringes. In this instance, the plasma would now be out of focus resulting in a decrease in spatial resolution. Both situations are not ideal for experimental operation.

This scenario can arise if the intermediate image plane of the MWI, fig. 3.4b, is not in the expected location and thus does not produce an image at the mirror of each channel. By placing a target reticule at the designed intermediate image plane of the MWI and checking the focus values for each channel we confirmed that there is a discrepancy between the expected and actual image plane locations. If the reticule and the image plane were in identical locations we would expect the imaging lens of each channel to be focused to infinity, this was not found to be the case. Second confirmation was found by focusing the CIS imaging lens to infinity and replacing the achromatic doublet lens of channel 11, which has a focal length of 750 mm, with an identical 600 mm version. Focus and image contrast in this case were significantly improved.

Further improvements were made by moving the lens closer to the mirror by ~ 50 mm. This change did have the adverse effect of increasing the vignetting of the system, however this should not affect experimental operation as the image circle is much larger the effective plasma area. Together this suggests

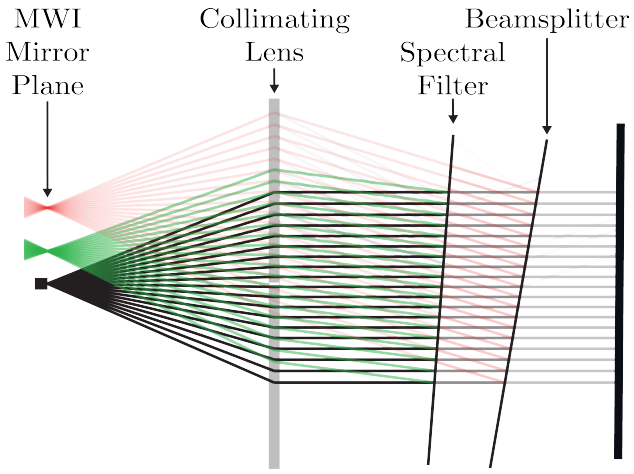

Figure 3.6: Using a point source (black) we show that when the beamsplitter and spectral filter are not aligned the light reflecting off the beamsplitter (red) is focused to a different location to that reflected off the spectral filter (green).

that the optimal focal length lens for the eleventh channel of the MWI would be ~ 650 mm.

In this configuration, average instrumental contrasts of 0.95, 0.7, and 0.6 were measured for ζ_2, ζ_{2+1} and ζ_{2-1}, respectively, while maintaining good image focus. Representing up to a factor of 2 increase in instrumental contrast compared to using the 750 mm imaging lens.

3.2.2 CIS Ghosting

The spectral emission line of interest for this study is C III at 464.9 nm, however this line is also measured by one of the MWI channels. As the MAST-U MWI cameras are capable of operating at 400-800 Hz compared to the $\sim$ 150 Hz of the CIS it is advantageous to run both systems simultaneously. Therefore, a 50/50 beamsplitter was required on the MWI channel measuring the same spectral line. This was placed after the MWI spectral bandpass filter but before the imaging lens, so other spectral channels would not be affected by multiple planes of reflection, as shown in fig. 3.6. However, this led to ghosting on the CIS channel, fig. 3.7a.

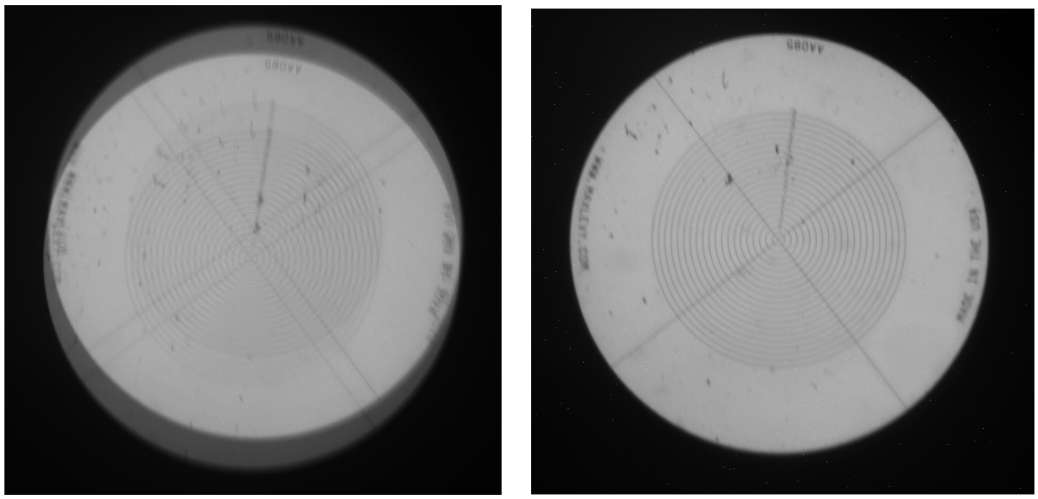

(a) (b)

Figure 3.7: Here image (a) shows the image ghosting effect observed on the CIS channel of the MWI due to the misalignment of the spectral filter and beamsplitter of an earlier MWI channel measuring the same line. Image (b) then shows that the ghosting effect is no longer visible after decreasing the distance between the beamsplitter and spectral filter.

To investigate this we intentionally misaligned the beamsplitter to different degrees, so that the beamsplitter and filter faces were not parallel, as seen in fig. 3.6. In doing this we determined that a small offset between the faces was the cause of this ghosting. As the spectral filter does not have a transmission ratio of 100% or an anti-reflective coating on its rear face, we believe that double reflections were occurring between the 2 components. Because these components are in the *collimated* region, the effect of double reflections should be negligible. However, if the component surfaces are not parallel to one another, the propagation angle of the light with respect to the collimating lens will change thus mapping the light to a different spatial location when it passes back through the lens, fig. 3.6. The effects of non-perfect collimation discussed in the previous section were found to be negligible compared angular misalignment of the beamsplitter and filter faces.

This effect was mitigated by installing the beamsplitter so that it was in contact with the spectral filter, thus reducing the air gap to near zero and

ensuring both components were aligned, fig. 3.7b. This was confirmed by comparing fig. 3.7b to the same image taken when the MWI channel filter-beamsplitter pair was replaced with a mirror, which can be thought of as the *ideal* case. To avoid ghosting in future imaging diagnostics of this type we suggest that the first spectral filter be produced with a transmission ratio of 50%, removing the need for a beamsplitter, while the filter on the CIS channel can have a ratio of ∼100%.

3.3 Interferogram Demodulation

The important quantities for physical studies measured by a CIS system are the contrast ζ_n and phase Φ_n of the interference patterns created. However, with our instrument we only measure a single interferogram within which coherence information at three fixed delays is encoded. We therefore need to untangle these coherence images. The background brightness I_0 can also be thought of as a fourth image.

In chapter 2, we discussed Fourier transform spectroscopy and its role in the operation of a CIS instrument. To extract the above quantities we apply Fourier techniques through a process called *synchronous demodulation*. Here we lay out how we apply this technique to our instrument but more information can be found in the book on this topic by Servin et al. [81].

Figure 3.8 shows a raw calibration image taken at 467.8 nm by our instrument in the MWI using a cadmium spectral lamp. We can see the same distinctive pixelated interferogram pattern as shown in fig. 3.2. Taking the 2D Fourier transform of this image and plotting the power spectral density we can see multiple distinct peaks in frequency space. In the centre we see the underlying intensity image known as the DC component. Surrounding this we see

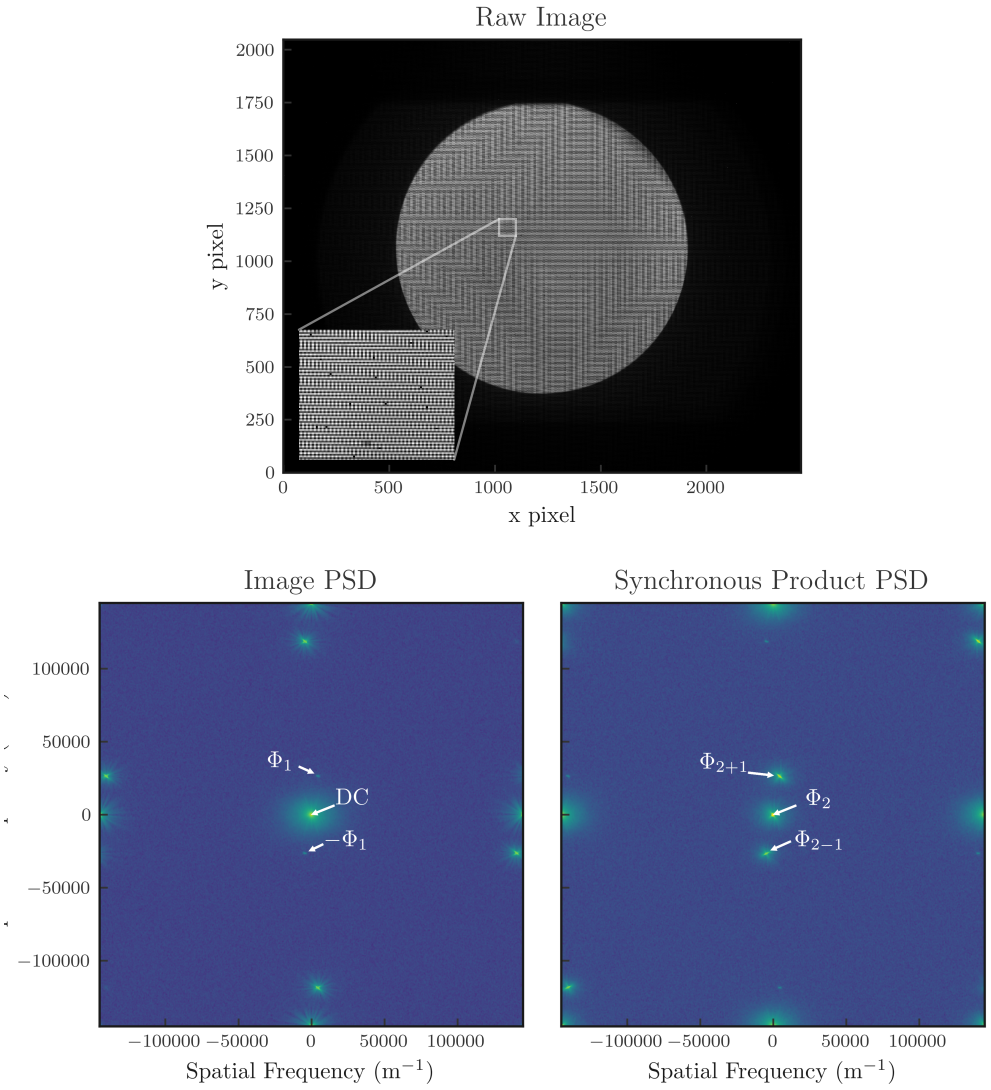

Figure 3.8: Shown at the top of this figure is an example of the raw calibration image taken by our instrument using a cadmium spectral lamp, with an expanded view of the pixelated phase mask shown also. The bottom row shows the power spectral density (PSD) of the raw image (left) and the PSD of synchronous product image (right). On these images we have labelled the relevant carrier frequencies.

the spatial carrier signals[12] for Φ_1, the existence of which is due purely to the misalignment of our instrument's components which will be discussed in section 3.4.1. To extract the DC image we use a standard low-pass filter. At and near the horizontal and vertical Nyquist frequencies we see additional peaks. These peaks are the spatial carrier signals related to each of the delay components of a triple-delay CIS. More specifically the peaks at the Nyquist frequency are Φ_2, the carrier associated with the delay imparted by the waveplate only.

The other carrier peaks are related to the *sum* (Φ_{2+1}) and *difference* (Φ_{2-1}) terms. It is clear from our notation that the spatial frequency of Φ_{2+1} must be higher than the Nyquist frequency and is therefore being aliased back into the valid frequency space. This obscures the underlying information captured within this interferogram. Additionally the location of these carriers in frequency space makes it very difficult to apply standard Fourier windowing techniques.

As discussed in section 2.5.2, the pixelated sensor adds an additional phase term $m\frac{\pi}{2}$ to the phase, eq. (3.3). Synchronous demodulation says that as this is a known frequency component it can be easily removed from the interferogram by dividing the interferogram by the complex exponential of that frequency, eq. (3.5), where $\Phi_n^* = \Phi_n - m\frac{\pi}{2}$. Figure 3.8 also shows the power spectral density of eq. (3.5). We can see that the three pixelated carrier terms are now located around the centre of the frequency space where they can now be extracted by standard Fourier techniques. Windowing around these carriers allows us to rewrite eq. (3.5) in a simpler form neglecting the higher frequency terms (i.e. any term including $m\pi$), eq. (3.6). Equation (3.6) also shows that following the individual carrier windowing, in frequency space, each phase and contrast image can be calculated as the argument and absolute value,

[12]Spatial carrier signal refers to the spatially varying signal which carries spectral information about the incident light. These spatial carriers manifest as a discrete peaks in frequency space.

respectively, of the resulting carrier.

$$
\begin{aligned}
I_{out}\exp\Big(-im\frac{\pi}{2}\Big) = \frac{I_{in}}{4}\Bigg(&\exp\Big(-im\frac{\pi}{2}\Big) \\
&+ \frac{\sqrt{2}}{4}\zeta_2\Big[\exp(i\Phi_2^*) + \exp(-i[\Phi_2^* + m\pi])\Big] \\
&+ \frac{\sqrt{2}}{8}\zeta_{2+1}\Big[\exp\Big(i\Phi_{2+1}^*\Big) + \exp\Big(-i[\Phi_{2+1}^* + m\pi]\Big)\Big] \\
&- \frac{\sqrt{2}}{8}\zeta_{2-1}\Big[\exp\Big(i\Phi_{2-1}^*\Big) + \exp\Big(-i[\Phi_{2-1}^* + m\pi]\Big)\Big]
\end{aligned}
\tag{3.5}
$$

$$
\begin{aligned}
I_{out}\exp\Big(-im\frac{\pi}{2}\Big) = \frac{I_{in}}{4}\Bigg(&\frac{\sqrt{2}}{4}\zeta_2\exp\Big(i\Phi_2^*\Big) + \frac{\sqrt{2}}{8}\zeta_{2+1}\exp\Big(i\Phi_{2+1}^*\Big) \\
&- \frac{\sqrt{2}}{8}\zeta_{2-1}\exp\Big(i\Phi_{2-1}^*\Big)
\end{aligned}
\tag{3.6}
$$

3.4 Diagnostic Calibration

As with all diagnostics, accurate calibrations are imperative for effective physical studies. For CIS systems this means we must regularly measure three quantities, the group delay ($\hat{\phi}_n$), rest frame phase ($\phi_{n,0}$) and instrumental contrast ($\zeta_{n,0}$).

To measure the group delay of a CIS system requires scanning over a wavelength (frequency) range of ± 50 pm, small enough to determine the derivative of delay with respect to wavelength at a given wavelength of interest for the application, shown in terms of frequency in eq. (2.37) [82]. Such measurements can only be taken with a tunable laser. Similarly, $\phi_{,n,0}$ and $\zeta_{,n,0}$ must be determined at the exact wavelength of interest using a coherent source. For C III, this is typically achieved using a tunable laser and is the method used at W7-X [82] and DIII-D [42], however a tunable laser was not available to us for our studies. Nevertheless, we note that both the group delay and rest-frame phase have previously been determined without the use of a tunable laser; both

will be discussed in the following sections [83, 30].

Further to this, as previously mentioned the delay imparted by an α-BBO crystal is temperature dependent. In section 3.4.2 we show that, although important, the temperature controlled cell used in our instrument can not on its own provide a temperature stable enough for accurate studies. This problem has also been mitigated on W7-X with an in-situ calibration system, in which light from a spectral lamp inside the instrument housing is directed to the interferometer via a movable mirror [84]. Using this method, calibrations can be taken before and after each shot. Temperature effects were also mitigated to good accuracy on DIII-D using precision temperature stabilisation [74]. Unfortunately the design of the MWI and the proximity of its entrance optics to the MAST-U vessel and other diagnostics meant it would not be possible to construct similar systems inside or outside the MWI.

Although the inability to construct or use industry standard techniques to calibrate our system was a significant challenge we sought to develop techniques and extend existing ones to overcome them. In section 3.4.1 we present an extension to a pre-existing calibration method, whereby the crystal dispersion is determined by fitting instrument parameters to phase measurements taken at multiple known wavelengths [83]. In section 3.4.2 we present a characterisation of the temperature dependence of our CIS instrument's delay. Together, these techniques maintain the cost-effective nature of CIS systems and reduce the complexity of their implementation and operation by eliminating the need for an in-situ system or expensive tunable laser. We believe these attributes are fundamental benefits of these diagnostics which should be maintained to enable implementation on future smaller plasma systems.

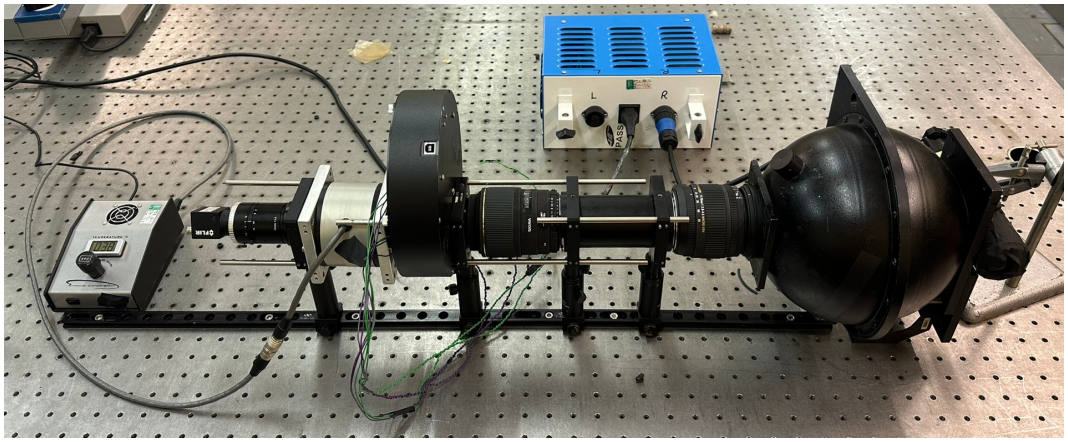

Figure 3.9: Optical bench setup for measuring the phase images used to characterise the dispersion of our instrument. Shown from left to right: Temperature control unit, FLIR Blackfly S camera, 50 mm MWI imaging lens, CIS interferometer cell, rotating filter wheel, collimating lens setup including two Sigma F-mount lenses and an integrating sphere with cadmium lamp behind it and power supply shown in the top of the image.

3.4.1 Wavelength Dependant Behaviour

As carbon arc lamps can not achieve the temperatures required to emit at the C III line of interest to this study, we have employed the method presented by Allcock for determining the interferometer delay at 464.9 nm [61, 83]. This process involves fitting instrument parameters to phase images taken at wavelengths across a large range. This is analogous to the calibration of a grating spectrometer where measurements at known wavelength constrain a model for the instrument function of the spectrometer. By doing this the group delay can then be calculated along with the phase difference $\Delta\phi_n$ between the wavelength of interest to a given study and a close-by ($\pm$5 nm) measured wavelength.

In order to apply this technique to our system, images were taken at 6 wavelengths using 3 spectral lamps and 4 spectral bandpass filters. A cadmium lamp provided lines at 467.82, 479.99 and 508.58 nm and a zinc lamp the lines at 468.01, 472.22 and 481.05 nm. The lamps were shone through an integrating sphere to provide even illumination across the front optics, with

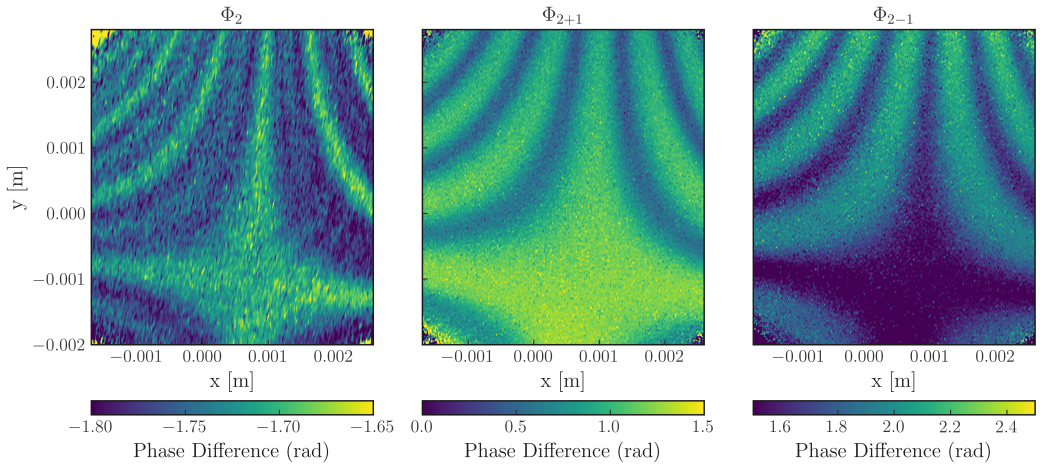

Figure 3.10: These three figures show the phase difference measured between 467.82 and 468.01 nm. From these figures we can see a clear hyperbolic structure with an unexpectedly high frequency. This artefact was later found to be caused by component misalignment.

each filter placed in a motorised filter wheel to ensure they could be changed quickly, minimising the time between images (fig. 3.9). The six interferograms were then demodulated as per the process described in section 3.3 to give three phase images per wavelength, where here $\Phi_n \equiv \phi_{n,0}$ as a spectral lamp produces a thin rest-frame spectral line.

Upon examination of the difference between the phase images at different wavelengths we found an unexpected additional *hyperbolic* structure. This is shown in fig. 3.10 where the phase images taken at Cd 467.82 nm where subtracted from the close-by Zn line at 468.01 nm. Although we would expect phase difference between these wavelengths to be hyperbolic for Φ_2, their proximity to each other means that the variation across the image should be on the order of 0.01 rad with no high frequency structure. For Φ_{2+1} and Φ_{2-1}, we would expect the phase difference to slowly vary across the sensor by $\sim$0.3 rad, similar to that seen in fig. 3.3.

The shape of this pattern is familiar as it is similar to the expected phase shape of our second crystal, the higher-order waveplate. However, the spatial frequency of the pattern does not match that created by the crystal. We pro-

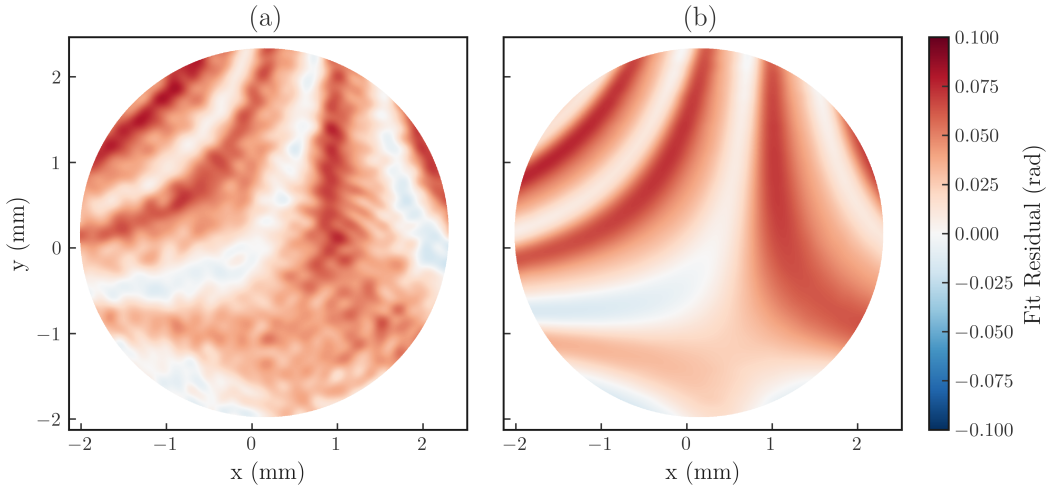

Figure 3.11: (a) Residual produced on ϕ_2 when fitting instrument parameters to data taken at 467.82nm, showing a clear hyperbolic pattern that is not being accounted for. (b) Residual produced when fitting to a synthetic Φ_2 image at 467.82 nm calculated using an instrument whose waveplate has been misaligned by 5.8°.

posed that this may be due to a rotational misalignment of the interferometer components relative to each other. For the remainder of this thesis we will use the term *misalignment* to refer to a deviation away from the angle at which a component's fast/transmission axis makes with the horizontal in an ideal system configuration, fig. 3.1.

We initially tested this theory by fitting the imaging lens focal length, crystal thickness and Sellmeier coefficients to a single Φ_2 image, producing the residual plot shown in Fig. 3.11a. Using these parameters and Mueller calculus we calculated and demodulated a synthetic interferogram to produce a Φ_2 image. By manually changing the orientation of the waveplate in our calculation we found that a deviation of 5.8° away from ideal resulted in a comparable residual to our measured data, fig. 3.11b, confirming that component misalignment can produce such a pattern. Exactly how each component's misalignment contributes to residuals shown in fig. 3.11 was unknown at the time, therefore it was not possible to determine whether the real misalignment value would be smaller or larger than 5.8°. However, what this test showed was the misalign-

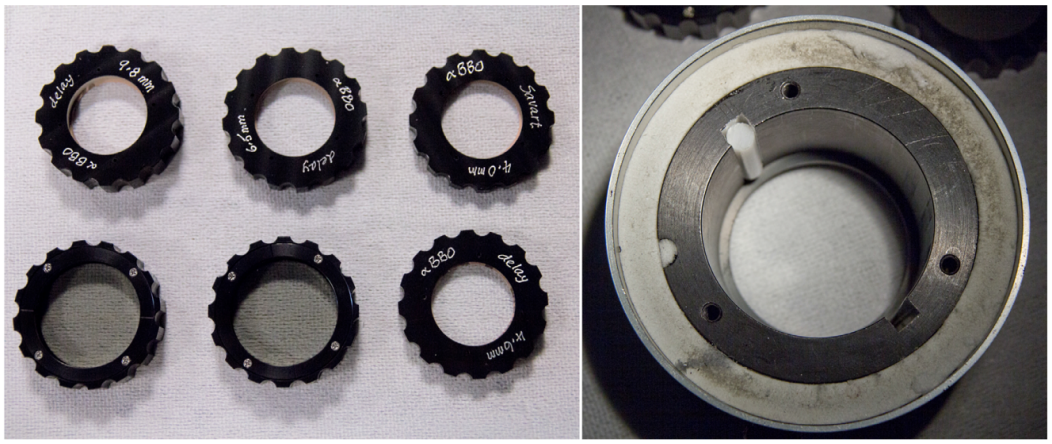

Figure 3.12: Images showing the mounting cogs (left) for CIS components and the temperature controlled cell (right) showing the white dowel used for aligning the components. This dowel also restricts the rotation of any component in the cell to 22.5±1°. Image courtesy of Scott Silburn.

ment of a component does introduce phase artefacts which in principle can be accounted for if we know the orientation of each component. We will see later in this section that the true misalignment was in fact less than 5.8°.

Each crystal is mounted in a metal cog which fits inside the temperature controlled cell fig. 3.12. The fast-axis (retarders) or polarisation axis (polariser) is aligned with the centre of one the cog notches. These axes are marked by the manufacturer, however their tolerances are not known. As the process of rotating the crystal within the mount is manual it is subject to human-error, which we estimate could be up to 5°. Additionally, it is not possible to fix any possible misalignment while the components are in the cell, fig. 3.12, as each component can only be rotated by 22.5±1°. In the case of our system we believe these factors are the source of any misalignment observed. By misaligning any of the components, rays of light which would normally destructively interfere, now only partially interfere thus creating this pattern. This is also the reason for the existence of ϕ_1 peaks in the power spectral density of the raw calibration image shown in fig. 3.8.

To rigorously test this effect we constructed single, triple and quad-delay

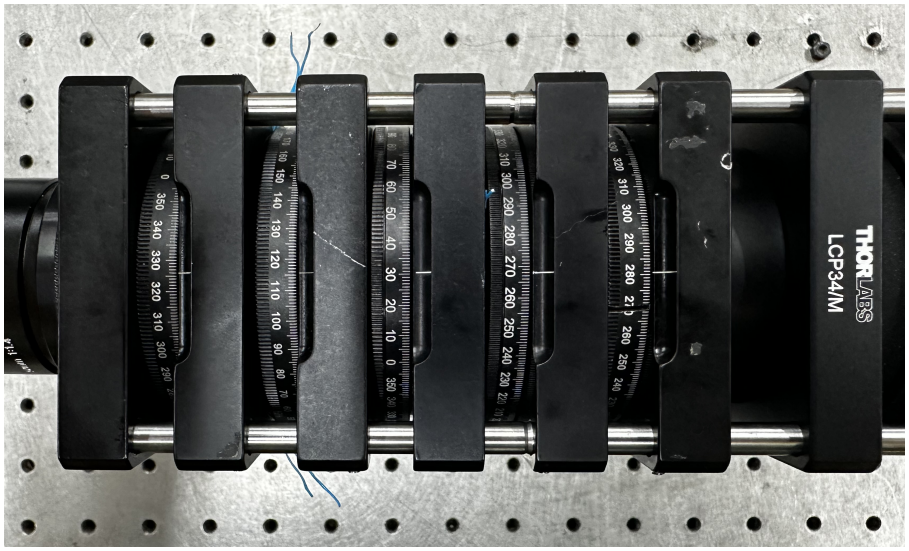

Figure 3.13: Quad-delay CIS system constructed on an optical bench with each interferometer component placed within Thorlabs rotation mounts. The angles shown on these mounts do not correspond to the orientation of the component.

CIS instruments on an optical bench with each component placed within rotatable mounts with a rotation accuracy of 0.5°, fig. 3.13. Before constructing these systems we determined what value on the rotation wheel corresponded to the fast/slow/transmission axis of each component. This was done by minimising the difference between intensity values measured by the crossed polarisers ($m = 1, 3$) within each super-pixel using a simple polariser-component-camera setup.

Using these 'zero-point' values it was possible for us to setup what we will refer to as the *aligned* system state. With this as a start point, components were rotated by 1°, with δ_c denoting the magnitude of this rotation and c the specific component. It was quickly found that only large rotations of the front polariser ($\delta_{pol} > 5°$) caused an appreciable effect on the measured phase. Additionally, in the interest of limiting the number of free test parameters, the waveplate in a given system can be thought of as aligned. As the phase pattern produced by a waveplate has a distinctive hyperbolic shape and is directly measured in Φ_2, it is possible to define the orientation of the waveplate with a

simple fitting procedure. For these reasons, only the QWP and displacer plate were rotated for this test. Summary plots of how these rotations affected the phase measured at each delay can seen in fig. 3.14.

From fig. 3.14 we can see that for Φ_2, rotation of both the displacer plate and QWP will result in an additional hyperbolic component, however the QWP also provides a constant phase shift across the image. This likely due to the the light incident on the sensor being elliptically polarised compared to perfectly circular. Examining Φ_{2+1} and Φ_{2-1}, we can see that without the QWP the additional pattern is purely linear. With QWP rotation that linear pattern still appears even at $\delta_{disp} = 0$ but increases in frequency with δ_{disp} to become dominate at high δ_{disp}.

After confirming these effects experimentally we sought a way to reproduce it in our calculations. From section 2.4.3, we know that the Mueller matrix of each component is a function of its orientation and therefore can be used to mathematically construct an arbitrary CIS configuration. However, we have used this previously to generate interferograms not phase images directly. As we intend to be able fit to any misalignment effects, the generation of an interferogram, which would then need to be demodulated at every iteration, is not computationally efficient. For this reason, we have derived, for the first time, the analytical equations for each phase image produced by a triple-delay CIS instrument, eqs. (3.11) to (3.13). Additionally for the use with other diagnostics around the world, we have derived the same equations for single and quad-delay pixelated CIS instruments which can be found in appendix C. As these equations contain a large number of variables and complex exponentials we have substituted sections of variables common to all three phase equations with $\eta_{1,\pm}$, $\eta_{2,\pm}$ and $\eta_{3,\pm}$, where $\eta_{i,\pm} \in \mathbb{C}$. These equations are functions of the orientation of each component n, ρ_n, and the delay imparted by the quarter waveplate, ϕ_{qwp}, as $\phi_{qwp} \neq \frac{\pi}{2}$ for all λ.

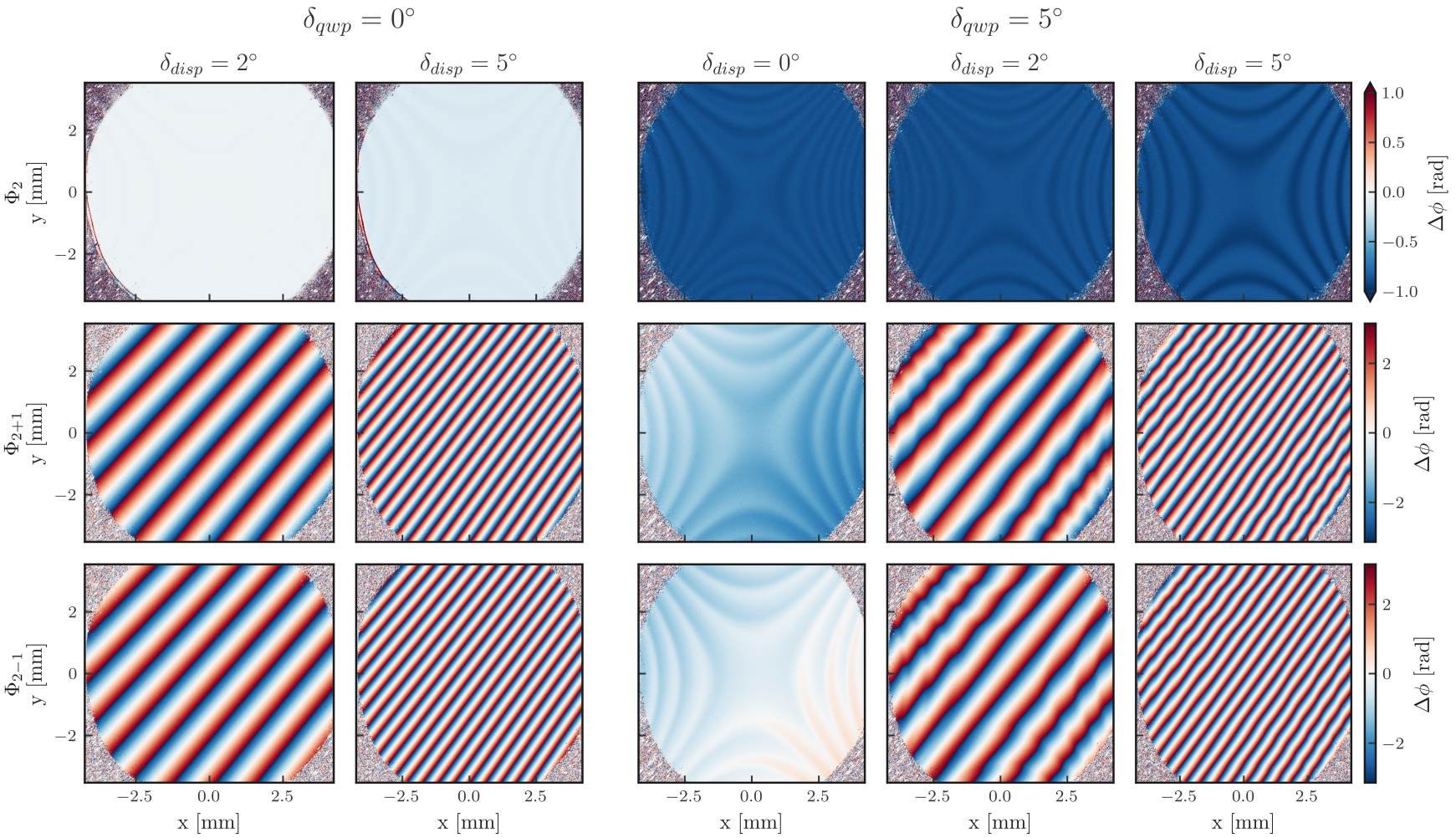

Figure 3.14: Shown is the phase difference between an aligned triple-delay system and various misaligned states. In column 1 and 2 only the displacer plate has been rotated by 2° and 5°. In columns 3-5 the QWP has been rotated by 5° and the displacer plate by 0°, 2° and 5°. In all plots alignment was maintained for the waveplate and polariser.

$$\begin{aligned} \eta_{pol} &= \exp(2i\,\rho_{pol}) \quad \eta_{disp} = \exp(2i\,\rho_{disp}) \\ \eta_{wp} &= \exp(2i\,\rho_{wp}) \quad \eta_{qwp} = \exp(2i\,\rho_{qwp}) \end{aligned} \tag{3.7}$$

$$\eta_{1,\pm} = \frac{\eta_{disp}^2 \pm \eta_{pol}^2}{\eta_{pol}\eta_{disp}^2\eta_{wp}^2\eta_{qwp}^2} e^{-i\phi_{\,qwp}} \tag{3.8}$$

$$\eta_{2,\pm} = \left[\eta_{disp}^2 \pm \eta_{pol}^2\right]\left[\pm\eta_{qwp}^2\left(1 + e^{i\phi_{\,qwp}}\right) \mp \eta_{wp}^2\left(-1 + e^{i\phi_{\,qwp}}\right)\right] \tag{3.9}$$

$$\eta_{3,\pm} = \left[\eta_{qwp} \pm \eta_{wp} + e^{i\phi_{\,qwp}}\left(\eta_{qwp} \mp \eta_{wp}\right)\right] \tag{3.10}$$

$$\Phi_2 = \arg\left(2\,\eta_{1,+}\left[2\,\eta_{2,+} + \left(\eta_{wp}^2 - \eta_{disp}^2\right)\left(\eta_{3,-}\,e^{i\phi_2} + \eta_{3,+}\,e^{-i\phi_2}\right)\right]\right) \tag{3.11}$$

$$\begin{aligned} \Phi_{2+1} = \arg\Big(\eta_{1,-}\Big[2\,\eta_{2,-}\,e^{i\phi_1} &+ \left(\eta_{disp}^2 + \eta_{wp}^2\right)^2\left(\eta_{3,-}\,e^{i\phi_{2+1}}\right) \\ &+ \left(\eta_{disp}^2 - \eta_{wp}^2\right)^2\left(\eta_{3,+}\,e^{-i\phi_{2-1}}\right)\Big]\Big) \end{aligned} \tag{3.12}$$

$$\begin{aligned} \Phi_{2-1} = \arg\Big(\eta_{1,-}\Big[2\,\eta_{2,-}\,e^{-i\phi_1} &+ \left(\eta_{disp}^2 + \eta_{wp}^2\right)^2\left(\eta_{3,+}\,e^{-i\phi_{2+1}}\right) \\ &+ \left(\eta_{disp}^2 - \eta_{wp}^2\right)^2\left(\eta_{3,-}\,e^{i\phi_{2-1}}\right)\Big]\Big) \end{aligned} \tag{3.13}$$

It can be shown that under ideal conditions eqs. (3.11) to (3.13) reduce to ϕ_2, ϕ_{2+1} and ϕ_{2-1} as calculated using eq. (2.50). Examining these equations we can now attribute the hyperbolic artefacts seen in our Φ_2 images to the addition of complex constant and term related to the reciprocal of ϕ_2 itself. For Φ_{2+1} and Φ_{2-1} we see the addition of terms relating to the delay imparted by the displacer plate, ϕ_1, and ϕ_{2+1} for ϕ_{2-1} and vice versa. This explains why we observe a strong linear pattern on Φ_{2+1} and Φ_{2-1} for misaligned system but with an underlying hyperbolic pattern too.

Before applying these equations to our wavelength fitting procedure we confirmed their accuracy by calculating the phase difference expected for the misaligned states we measured experimentally. A summary of these results

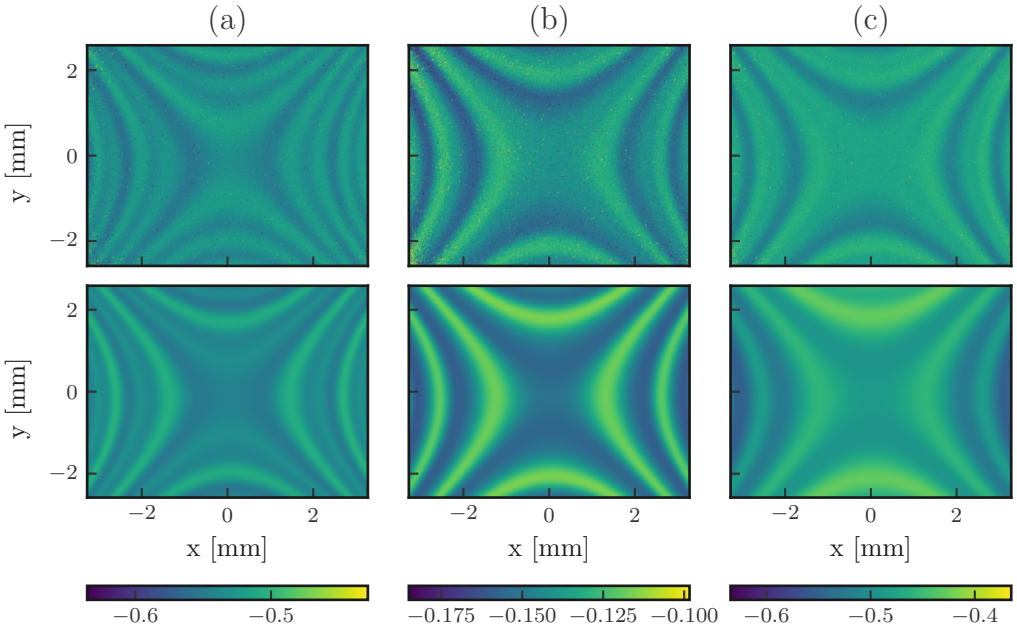

Figure 3.15: Shown are the measured (top row) and calculated (bottom row) phase changes for Φ_2 due to the following misalignments: (a) $\delta_{disp} = 0°$, $\delta_{qwp} = 2°$, (b) $\delta_{disp} = 5°$, $\delta_{qwp} = 0°$, (c) $\delta_{disp} = 5°$, $\delta_{qwp} = 2°$. We estimate the uncertainty in these angles to be $\pm 0.5°$.

is shown in fig. 3.15, where we can see that the calculated phase difference (bottom row) for each case is a close match to what we measure (top row). We can attribute any quantitative difference between these images to the accuracy in the rotation mount markings, which is significant for such small rotations. Notwithstanding this, the maximum discrepancy observed is small at 0.04 rad.

Returning to the calibration of our experimental system, as mentioned, the interferometer was constructed within the temperature controlled cell and installed on an optical bench as shown in fig. 3.9. At which time interferograms were measured at 467.82, 468.01, 472.22, 479.99, 481.05 and 508.58 nm, and their phase images extracted. Using these and the fitting procedure we have described, which now includes eqs. (3.11) to (3.13), a large set of instrument parameters can be fit to.

To ensure a solution could be found accurately and within a reasonable time

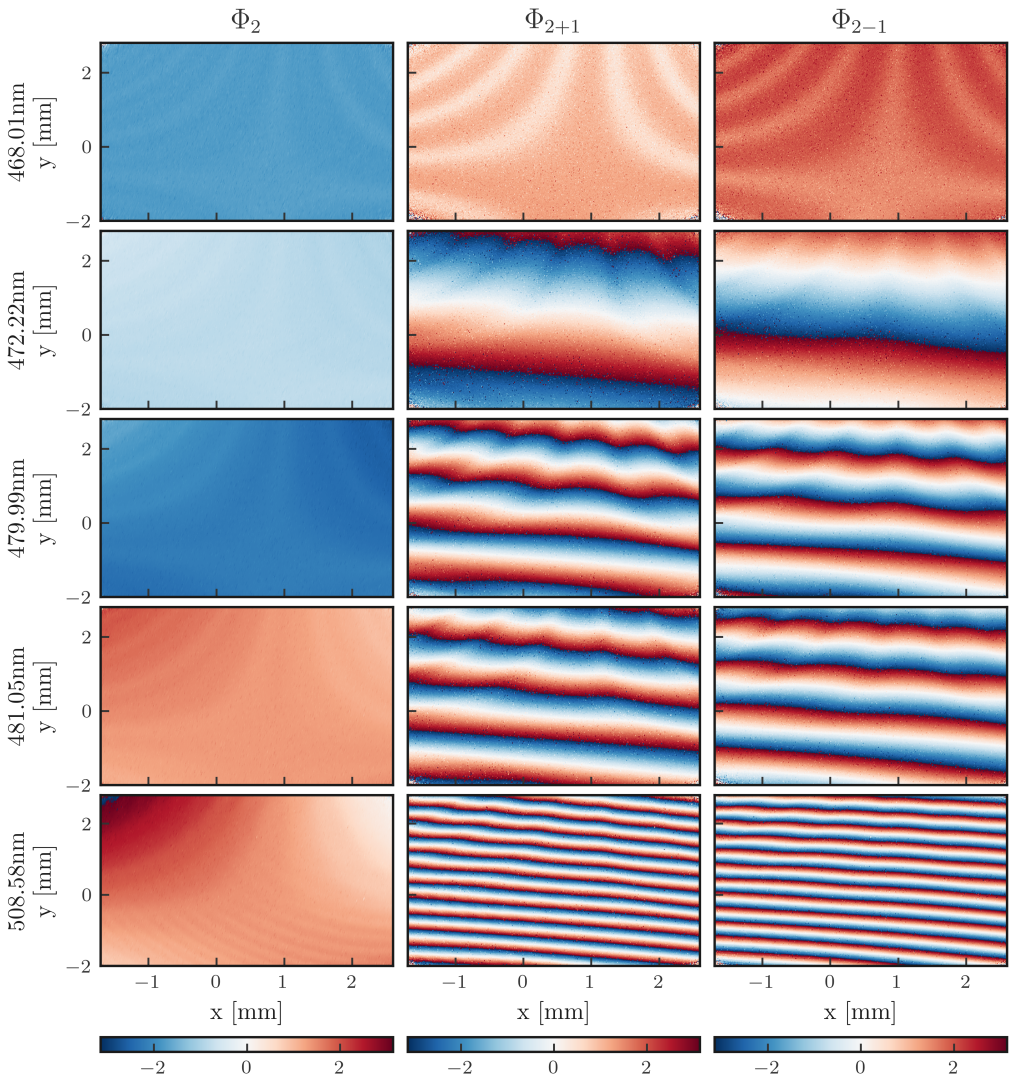

Figure 3.16: Shown are the differences in phase between images measured at the wavelengths shown on the left and the phase images measured at 467.82nm. Each column shows a specific instrument delay: Φ_2, Φ_{2+1} and Φ_{2-1} (left to right). The hyperbolic artefact due to misalignment is also clearly visible in some of the images.

period, the fit was performed against the difference between the phase images at the above wavelengths and that measured at 467.82 nm, shown in fig. 3.16. For example image 1 would be the difference in the phase images taken at 468.01 and 467.82 nm. The performance increase compared to fitting to the absolute phase images directly has been shown to be up to a factor of 2300, and is due to a decrease in the density of local maxima in parameter space

[83]. The data taken at 472.2 nm was reserved for testing as the wavelength difference between it and Cd 467.82 is similar to that of C III, while the other wavelengths were used for fitting. Tables 3.1 and 3.2 show the nominal and optimised instrument parameters.

Parameter	**Nominal**	**Optimised**
f_3 (mm)	50	49.41
Component Orientations		
$\rho_{pol}(^\circ)$	287.18	287.21
$\rho_{disp}(^\circ)$	264.68	260.43
$\rho_{wp}(^\circ)$	309.68	309.68
$\rho_{qwp}(^\circ)$	354.68	350.30

Table 3.1: Nominal and optimised instrument parameters for the MAST-U CIS system, where f_3 is the focal length of system imaging lens and ρ is the orientation of a given component in the interferometer cell.

Parameter	**Disp. Plate**		**Waveplate**	
	Nominal	Optimised	Nominal	Optimised
ψ_x (°)	0	1.39	0	0.3726
ψ_y (°)	0	-1.91	0	-0.6604
θ (°)	45	45	0	-0.223
A_e (μm^2)	2.3753	2.3778	2.3753	2.3734
B_e (μm^2)	0.01224	0.01164	0.01224	0.01287
C_e (μm^2)	-0.01667	-0.02244	-0.01667	-0.01724
D_e (μm^2)	-0.01667	-0.01484	-0.01516	-0.01809

Table 3.2: Nominal and optimised crystal specific parameters for the MAST-U CIS system. ψ_x and ψ_y are the tilts of each crystal about the x and y axis of the instrument, respectively. θ is the cut angle of the crystal and A_e, B_e, C_e, D_e are the Sellmeier coefficients of the crystal.

The accuracy of this fitting was then verified by calculating the phase difference for 472.2 nm and comparing it to the measured difference, fig. 3.17. It can be seen that the residuals between the calculated and measured phase difference when using eqs. (3.11) to (3.13) (bottom row) are reduced by up to a factor of 4 compared to those produced when not accounting for the crystal misalignment (middle row). Additionally, the prominence of the additional hyperbolic component in the fit residuals has been significantly reduced.

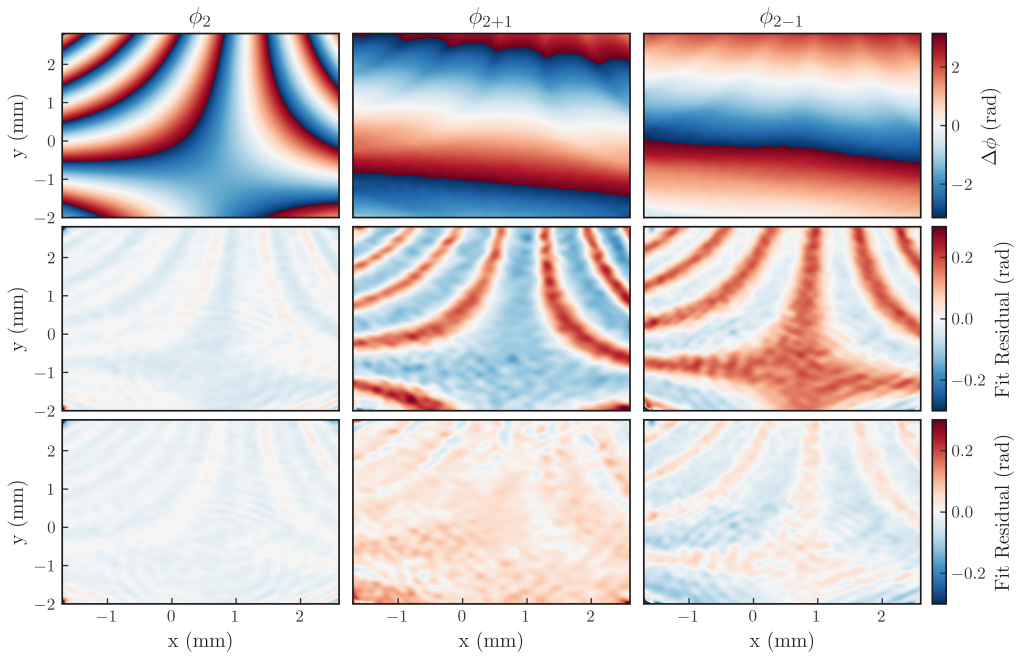

Figure 3.17: The top row shows the difference in the phase images measured at 467.82 nm and 472 nm, where the ϕ_{2+1} and ϕ_{2-1} images clearly show an embedded hyperbolic pattern. The middle row shows the fit residuals when using the ideal equation for delay imparted by a linear retarder [62]. The final row shows a clear decrease in the fit residuals when using eqs. (3.11) to (3.13).

The results shown in fig. 3.17 have also been seen at the other four measured wavelengths, confirming that this method can be used to calibrate across a wide wavelength range. With this and the fact that the wavelength difference between C III and Cd 467.82 nm is smaller than the test 472 nm line we are confident that this method can be used to calibrate our instrument for C III at 464.9 nm. Despite good quantitative match shown, we can not discount the possibility of an alternative underlying reason for this pattern. This would require further testing using optical equipment capable of determining the orientation of each component exactly, as suggested section 5.4. As the modifications presented in this section increase the number of fitting parameters we have seen up to a 20% increase in computational time. However, as this fitting is only required once per instrument installation this increase will not have a significant effect on implementation.

3.4.2 Temperature Dependant Behaviour

Coherence imaging spectroscopy provides users with a powerful tool to measure plasma parameters in 2D, however, we have already seen that calibrating these systems can be challenging. The delay of birefringent crystals is dependent on temperature, an effect that can be attributed to a combination of the changes in the refractive indices, n_e and n_o (thermo-optic effect) and thermal expansion. Additionally, we expect the temperature dependence of Φ_{2+1} and Φ_{2-1} to be equal to the sum and difference, respectively, of $\frac{d\phi}{dT}$ for each crystal. This issue has been mitigated on other devices through radial sightlines or in-situ calibration [43, 35]. However, such solutions in our case are not practical and, more broadly, for future diagnostics may become less reliable on devices capable of long pulse times. As mentioned, in the case of the MAST-U MWI, an in-situ system was not practical due to the proximity of the front optics of the MWI to the vessel and other sensitive diagnostics. Further to this, the method of assuming the plasma is stationary along a given radial sightline can also not be used due to the viewing angles of the MWI front optics [43].

Another solution to this problem is precision temperature control of the interferometer control similar to that used on DIII-D [74]. However, the MWI was constructed to host an Andover 50 mm filter oven only and modification of the internal mountings of this MWI channel were not possible. As mentioned in section 3.1, the filter oven was set to 35°± 0.2 °C. To understand the effect of the oven's temperature stability we can use eq. (3.14), which describes temperature dependence of the phase delay produced by a waveplate for light at normal incidence. This is based on the thermo-optic effect and thermal expansion, where α and $\frac{dB}{dT}$ are thermal constants and $B_0 = n_e - n_o$. Using eq. (3.14) and thermal constants taken from literature [85], it can be estimated that an accuracy of $\pm 0.2°$ in the crystal temperature stability corresponds to

a phase stability on ϕ_2 of ± 0.19 rad. This is equivalent to a measured velocity of 3.1 km/s, which is large compared to the CIS accuracy of 1 km/s and measurements of < 30 km/s seen on MAST [43, 86]. In light of this we sought a new method of calibrating the diagnostic to temperature changes.

$$\frac{\Delta\phi}{\Delta T} \approx \phi_0 \left(\alpha + \frac{1}{B_0} \frac{dB}{dT} \right) \tag{3.14}$$

The simplicity of eq. (3.14) is lost when dealing with off axis rays and crystals with cut-angle, θ greater than 0. This is due to the fact that thermal expansion of an α-BBO crystal occurs at different rates parallel ($\alpha_{\parallel}$) and perpendicular ($\alpha_{\perp}$) to the crystallographic axis. Together these give the general equation for the thickness of a crystal accounting for thermal expansion, eq. (3.15), with the equations for the thermo-optic effect shown in eq. (3.16) for clarity.

$$L(T) = L_0 + L_0(\alpha_{\parallel} \sin\theta + \alpha_{\perp} \cos\theta)\Delta T \tag{3.15}$$

$$n_e(T) = n_{e,0} + \frac{dn_e}{dT}\Delta T,\ n_o(T) = n_{o,0} + \frac{dn_o}{dT}\Delta T \tag{3.16}$$

Using eqs. (3.15) and (3.16), the stability of ϕ_{2+1} and ϕ_{2-1} can then be calculated as ± 0.3 and ± 0.074 rad, respectively, by substituting into eq. (2.50), which are equivalent to 3.5 and 2 km/s. Where $\alpha_{\parallel} = 3.28 \times 10^{-6}$/K, $\alpha_{\perp} = 1 \times 10^{-6}$/K [85], and $\frac{dn_e}{dT} = -9.3 \times 10^{-6}$/K and $\frac{dn_o}{dT} = -16.6 \times 10^{-6}$/K are the thermo-optic coefficients as specified by the manufacturer of our crystals. As the accuracy of these thermal constants is unknown, we chose to verify them by measuring the change in phase images, produced at 467.8 nm using a cadmium spectral lamp, over a period of 40 hours and compare to the expected phase change calculated using eqs. (3.15) and (3.16).

To measure the changes in crystal temperature, two 100 k$\Omega \pm 1\%$ ther-

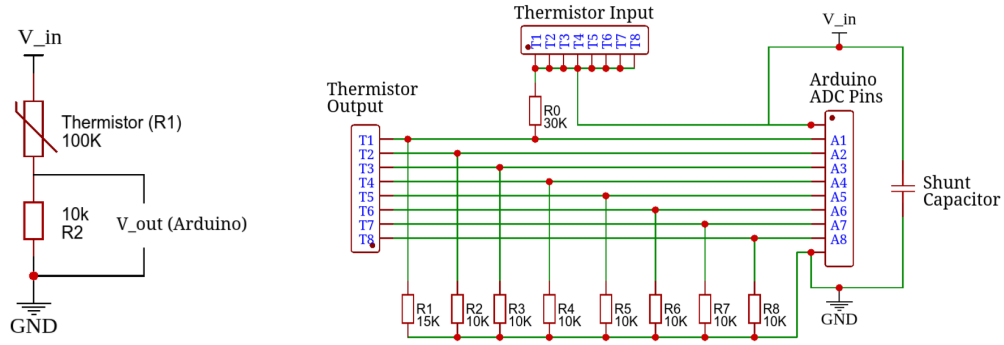

(a) (b)

Figure 3.18: (a) shows the voltage dividing circuit that was used to measure the resistance of the thermistors. (b) shows the general circuit diagram for the temperature measurement system including the Arduino ADC connector

mistors were affixed to each crystal mount using an adhesive with a thermal conductivity of 2 W/mK, chosen to closely match the expected conductivity of α-BBO of 1.7 W/mK [87]. The resistance of each thermistor was determined using a voltage divider circuit, fig. 3.18a. These were connected to a 16-channel 24bit Arduino ADC and an Arduino Uno, the circuit diagram for which is shown in fig. 3.18b and the device in fig. 3.19. The ADC board has an internal voltage reference of 4.096 V, however we found that this was not stable enough for our measurements which require an input voltage which is known precisely. To achieve this, we set the first arduino channel to measure the voltage drop in across a 15 kΩ resistor in series with a 30 kΩ resistor, the accuracy of the resistors used was 0.1%. A shunt capacitor was also added across the power input to add additional stability during measurements.

The main thermistor circuit used a 10 kΩ resistor in series with the thermistor. This was chosen to ensure that at all temperatures the read voltage remained between 0 and $V_{in}/2$, which is the limit of the ADC. The resistance of the thermistor could then be calculated using eq. (3.17) and from this the temperature of the crystal, T_n using eq. (3.18), where $\beta = 4540$ K, $R_{25} = 100$ kΩ and all other variables are as defined in fig. 3.18a.

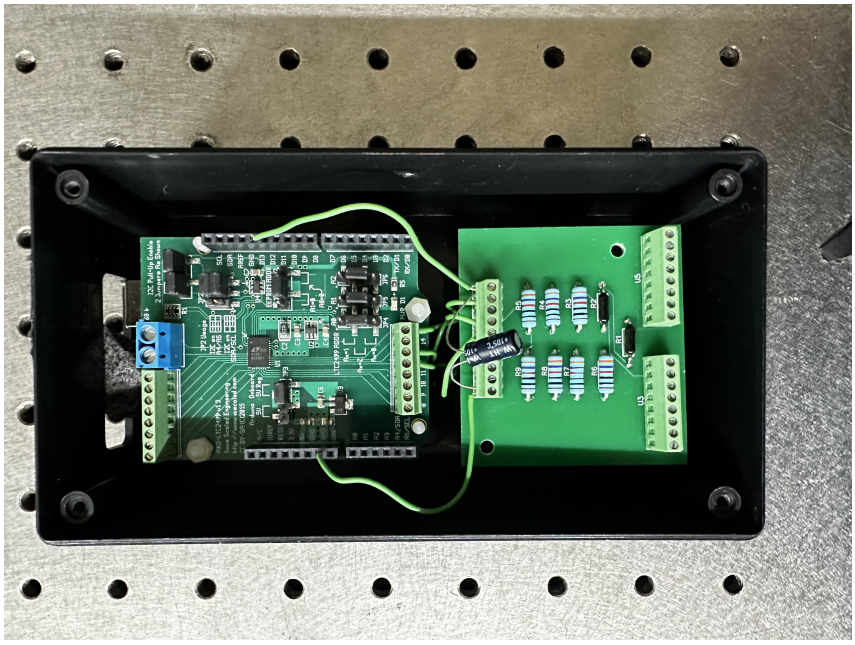

Figure 3.19: Shown is an image of the crystal temperature measurement system. On the left we can see the ADC breakout board which is attached to the Arduino Uno underneath and on the right the voltage divider PCB detailed in fig. 3.18b.

$$R_1 = R_2 \left(\frac{V_{in}}{V_{out}} - 1 \right) \tag{3.17}$$

$$T_n = \left(\frac{1}{298.15} + \left[\frac{1}{\beta} \ln \left(\frac{R_1}{R_{25}} \right) \right] \right)^{-1} - 273.15 \tag{3.18}$$

In fig. 3.20, we show the mean phase change of a region at the centre of each phase image over time. The data representing the displacer plate, ϕ_1, was obtained by removing ϕ_2 from the measured ϕ_{2+1} and ϕ_{2-1} phase images. Also plotted is the change in the measured temperature of each crystal. We can see from the plot of ϕ_2 that using eq. (2.50) and accounting for thermal effects, we can predict the change in the delay imparted by the waveplate to good accuracy. The small discrepancy observed can be attributed to errors in the thermal coefficients and the alignment of the crystal.

The same can not be said for the change in the delay imparted by the displacer plate which shows a strong disagreement between the calculated and measured phase changes. Reasonable modification of the thermal coefficients

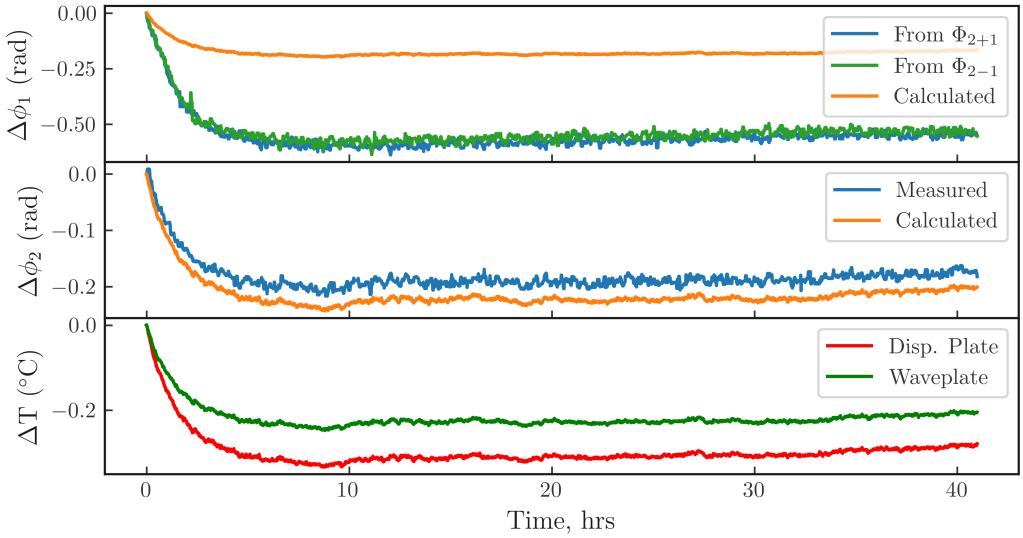

Figure 3.20: Shown in the top two plots is the change in delay imparted by the displacer plate, $\phi_{,1}$, and waveplate, $\phi_{,2}$, due to temperature changes. The green and blue lines show the change measured with a Cadmium lamp, and the orange lines show the calculated change based on the measured temperature variations (shown in the bottom plot) and eq. (2.50), which accounts for thermal expansion and the thermo-optic effect. Prior to taking these measurements, the system temperature was left to stabilise. Ensuring that any temperature changes after t=0 are due to environment changes.

(±50%) did not provide good enough agreement to suggest errors in these as the sole cause. However, a change in the tilt of the displacer plate about the x and y axis on the order of 10^{-3} rad did provide a large enough change in the incidence angles to give quantitative agreement with individual pixel measurements. One possible cause of the discrepancy is crystal misalignment induced by thermal stresses between the crystal and its mount. Confirming this as the cause would require a much more detailed study, which was not needed in this case.

$$\begin{aligned} \Phi_{1,i}(T) &= \phi_{0,1} + \Delta T \left[\frac{d\phi_1}{dT} + C_i \right] \\ \Phi_2(T) &= \phi_{0,2} + \Delta T \left[\frac{d\phi_2}{dT} + C_2 \right] \end{aligned} \tag{3.19}$$

It was found that a linear modification of the delay calculated using eq. (2.50) and eqs. (3.15) and (3.16) through eq. (3.19) would provide agreement with

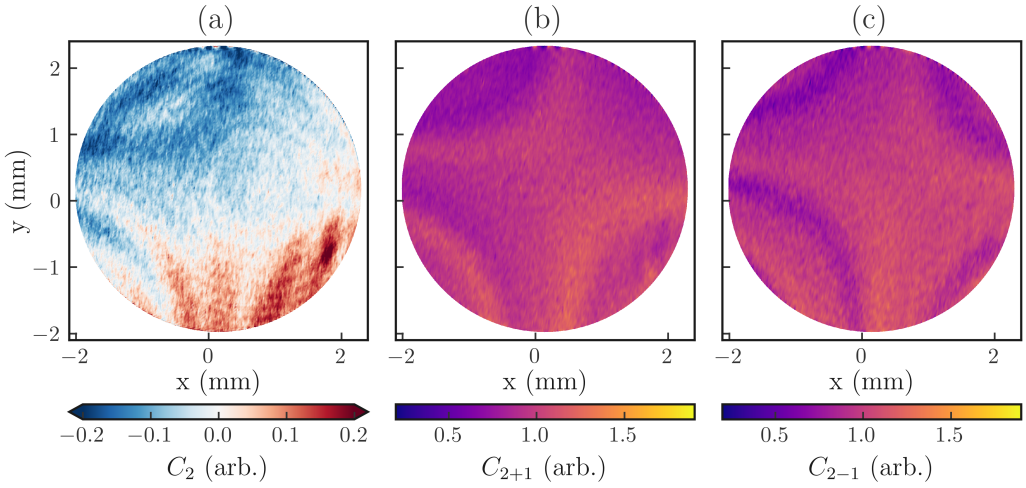

Figure 3.21: Fitting parameter C_n plotted across the image circle, where (a) shows the fitting executed for ϕ_2, (b) for ϕ_{2+1} and (c) for ϕ_{2-1}

measured data. Where Φ_n is the measured phase (i denotes which image ϕ_1 was calculated from), ϕ is the calculated phase at $\Delta T = 0$, C_i is a fitting parameter for each pixel and $\frac{d\phi}{dT}$ is the change in phase due to thermal expansion and the thermo-optic effect.

Although ϕ_2 showed a good agreement with the measured data, we decided to fit to Φ_2 along with Φ_{2+1} and Φ_{2-1}, to correct for the small differences observed in fig. 3.20. We believe the small difference between $\Phi_{1,2+1}$ and $\Phi_{1,2-1}$, seen in fig. 3.20, is due to how the additional hyperbolic pattern seen in section 3.4.1 affects Φ_{2+1} and Φ_{2-1}. The technique described in section 3.4.1 was not required here as by fitting to C_i at every pixel all non-temperature dependent phenomena (such as errors due to misalignment) are captured by the fitting, as seen in fig. 3.21.

$$\Phi_{2\pm1}(T) = \Phi_2(T) \pm \Phi_{1,2\pm1}(T) \tag{3.20}$$

Using eq. (3.20), we can accurately predict the change in the measured ϕ_{2+1} and ϕ_{2-1}. Figure 3.22 shows a comparison of the mean measured variation and that calculated using eq. (3.20) over the same region used in fig. 3.20. It is

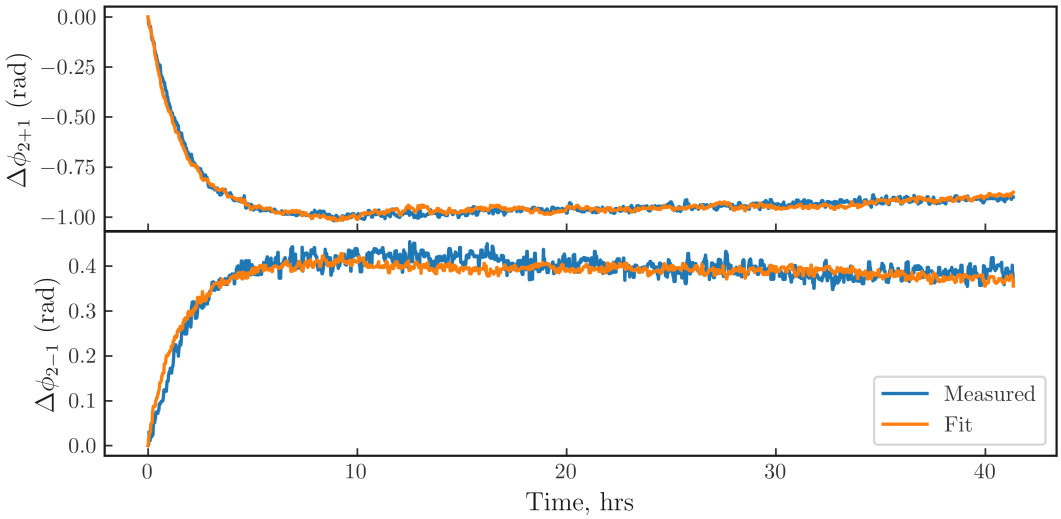

Figure 3.22: In this figure we compare the change in the measured ϕ_{2+1} and ϕ_{2-1} terms with those calculated using eq. (3.20). It is clear from these plots that the temperature fitting discussed in this section can effectively capture any additional temperature effects not accounted for by eqs. (3.15) and (3.16)

clear from this that eq. (3.20) can accurately account for the discrepancy seen in the predicted $\Delta\phi_1$ seen in fig. 3.20.

Although the results in fig. 3.22 are promising, they provide little information about whether eq. (3.19) could be used as a way to generate CIS calibrations long-term using only crystal temperature. To test this, calibration images were taken nine days after the data in fig. 3.22, during which temperature control was maintained and the instrument was left untouched. This data was compared to the phase images calculated using the crystal temperature at that time, shown in fig. 3.23.

It is clear from the residual images in fig. 3.23 that eq. (3.19) can be used to predict CIS calibration images to good accuracy, with absolute residual means of 0.013, 0.021 and 0.019 rad on Φ_2, Φ_{2+1} and Φ_{2-1}, respectively. This corresponds to a reduction in uncertainty for Φ_2, when compared to that related to the temperature control cell's accuracy, of a factor of 15 and acceptable errors on the other two terms. It is important to note that the main source of discrepancy seen in fig. 3.23 is noise, which can be mitigated

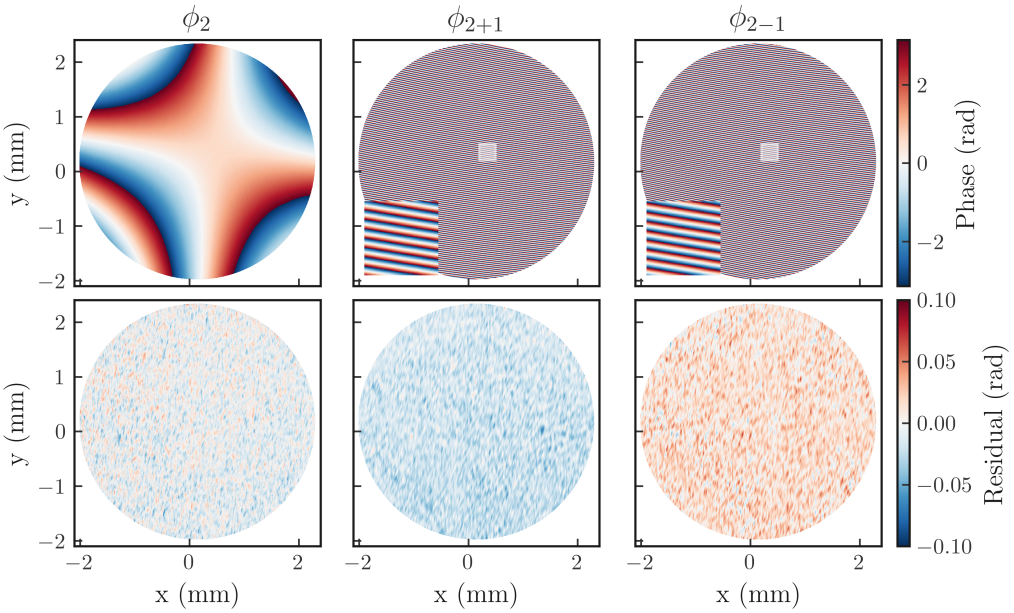

Figure 3.23: Shown on the top row are the Φ_2, Φ_{2+1}, Φ_{2-1} taken from measurements made 9 days after the data that was fit to in fig. 3.22. The bottom row shows the residual between the top row and the corresponding calculated phase images, where we can see that noise is the primary residual source.

in future studies by stacking and averaging over a large set of frames taken at much lower exposure times. We can also see that residuals for Φ_{2+1} and Φ_{2-1} are of similar magnitude but opposite sign. This will be useful when applying calibrations to plasma experiments for physical studies, as these errors will partially cancel out.

Adding this procedure in the installation workflow of a CIS instrument will have an effect on implementation time as measurements must be taken over an extended period. However, this process is not labour intensive and analysis can be done automatically within a few hours, therefore we do not expect this to be an obstacle for future systems.

3.4.3 Determining Calibration Parameters

To operate our instrument effectively we applied the techniques described in the previous sections to determine $\phi_{n,0}$, $\hat{\phi}_n$ and $\zeta_{n,0}$.

Rest Frame Phase and Group Delay

For rest frame phase, $\phi_{n,0}$ we must first determine the rest frame phase for Cd 467.82 nm at the time of the specific MAST-U shot. The acquisition code we have written for the MAST-U CIS also logs the crystal temperatures at the start and end of each shot ($\sim$1 s apart). We can then use the average of these values combined with our temperature characterisation data and eqs. (3.19) and (3.20) to calculate Φ_2, Φ_{2+1}, Φ_{2-1} for Cd 467.82.

These phase images must then be shifted in wavelength space to the centre-of-mass wavelength of C III at 464.9 nm. We can do this by calculating the expected phase difference between 467.82 and 464.9 nm accounting for misalignment using eqs. (2.50) and (3.11) to (3.13) and the instrument parameters shown in tables 3.1 and 3.2. Applying this to our calculated 467.82 nm phase image we obtain $\phi_{n,0}$ at 464.9 nm and the crystal temperature of a given shot.

As discussed in chapter 2, the group delay $\hat{\phi}_n$ of a retarder describes the dispersion of the crystal. For our purposes we rewrite eq. (2.37) as eq. (3.21). As group delay is a property of a crystal itself its value at a given pixel is independent of the instrument configuration. Therefore, we can use the same set of Sellmeier coefficients found in using our wavelength fitting procedure to define $\frac{d\phi_n}{d\lambda}$. This derivative can be determined numerically using eq. (2.50) or analytically by differentiation, the latter of which was used in this study.

$$\hat{\phi}_n = -\lambda_0 \left.\frac{d\phi_n}{d\lambda}\right|_{\lambda=\lambda_0} \tag{3.21}$$

Instrumental Contrast

During the work in section 3.4.2, we confirmed that instrumental contrast is not strongly correlated to changes in crystal temperature, as seen by Silburn et al. [43]. A maximum contrast variation of 0.015 was observed across the

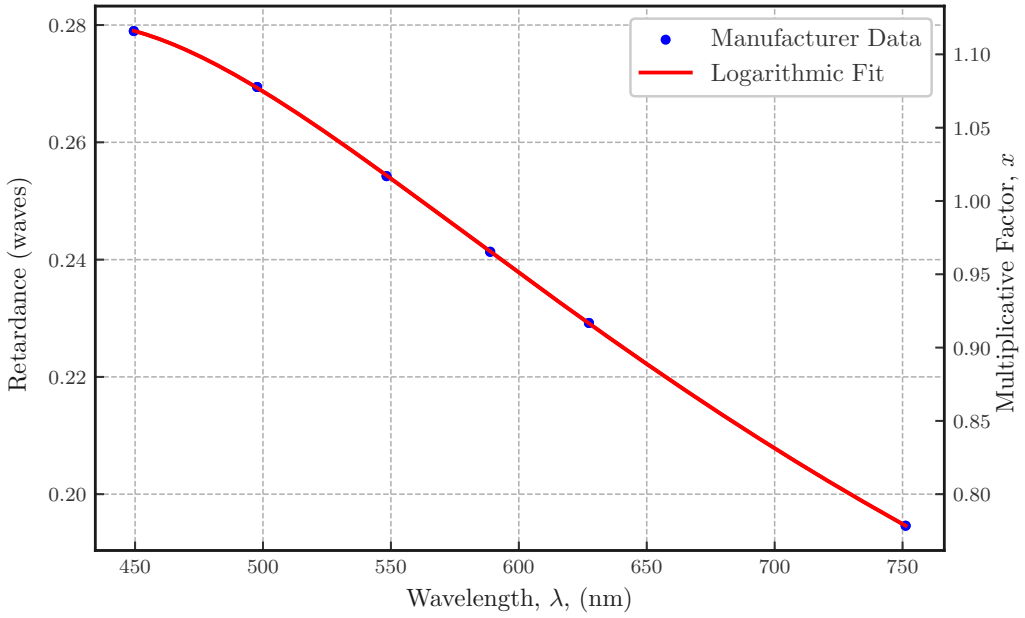

Figure 3.24: Here we show the retardance of the quarter waveplate used in this research as a function of wavelength (blue). This data was supplied by the manufacturer. In red we show the third order logarithmic fit function we have applied to the data in order to obtain the retardance at the wavelengths of interest to this study.

40 hours which is on the order of the contrast fluctuations attributed to noise in the measured interferogram. Therefore, for current studies on MAST-U fitting between crystal temperature and instrumental contrast is not required. However, instrumental contrast will be measured at regular intervals to account for possible degradation of sensor polarisers due to neutron flux.

Although instrumental contrast is not directly dependent on wavelength, the measured contrast during calibration is dependent on the retardance of the QWP, which is dependent on wavelength. The QWP used in this work is non-ideal across a wide wavelength range with a retardance vs wavelength curve shown in fig. 3.24. By fitting a third-order logarithmic function to the manufacturer's data—which provided the most accurate fit—we determined the retardance at the wavelength of interest for this study.

It has been shown that for pixelated phase mask CIS instruments the effect

of QWP retardance on contrast can be accounted for through a pixel dependent factor, $1/\zeta_m$ where ζ_m is given by eq. (3.22) and x is the multiplicative deviation of the delay from a pure quarter wave [61]. This factor is included in the synchronous demodulation process (section 3.3) when multiplying the interferogram by the known pixel phase mask.

$$\zeta_m = \begin{cases} 1 & \text{if } m = 0, 2 \\ \sin\left(\frac{\pi}{2}x\right) & \text{if } m = 1, 3 \end{cases} \tag{3.22}$$

3.4.4 Camera Photon Transfer Curve

Finally, it is useful for us to define our camera's susceptibility to noise by determining the Photon Transfer Curve (PTC) of the FLIR sensor, fig. 3.25. The PTC of a camera is an excellent way to characterise the performance of a sensor, particularly in terms of its noise characteristics and sensitivity to light, as it is a plot of the relationship between the mean signal and the corresponding noise level. We did this by illuminating the sensor with a uniform light source the intensity of which we varied to measure the sensor's output signal variance as a function of the mean signal level.

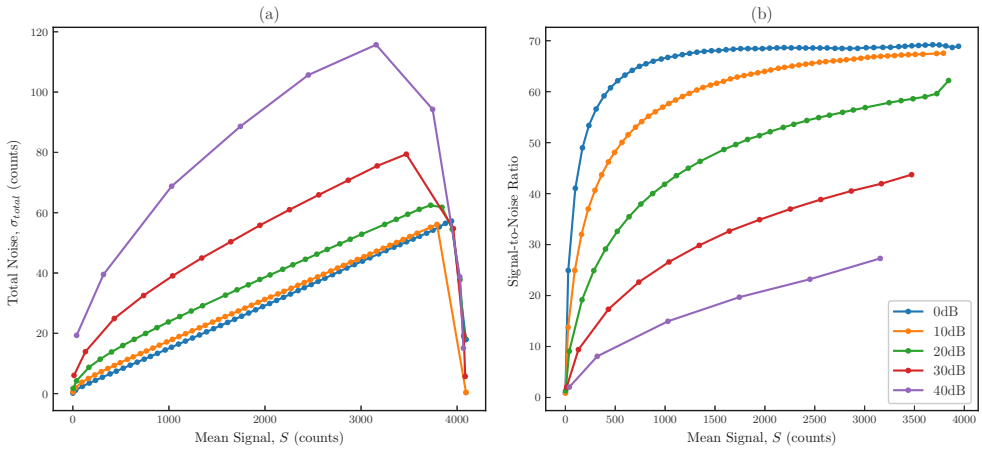

Figure 3.25: In (a) we show the photon transfer curve of our FLIR camera at various gain settings. (b) shows the how the camera's signal-to-noise varies with gain across the measurement range.

From fig. 3.25a, we can see that the FLIR pixelated sensor is quite robust to noise at gain levels up to 20 dB. This is significant when considering the minimal C III light expected in the MAST-U Super-X divertor. Additionally, the shape of the divertor leg means that there will likely be a strong thin peak in intensity near the leg which will decrease sharply as you move across the sensor to a more radial sightline, fig. 3.2. For this reason, it is important the signal-to-noise ratio (SNR) of the sensor remains high at low intensities. Figure 3.25b shows that this is the case up to 20 dB of gain, with SNR values greater than 20 at signal levels above 200 counts.

The information in fig. 3.25a is also important when using CIS data to determine plasma parameters such as ion parallel flow velocities, $v_{\|}$ and temperatures, T_i as these errors can be used to determine an appropriate variance for the probability density functions used in fitting algorithms.

3.5 Summary

In this chapter, we introduced a triple-delay pixelated CIS system which has been installed on MAST-U, along with the changes we have made to the MAST-U MWI to accommodate this installation. Image ghosting due to beamsplitter misalignment has been mitigated by installing the MWI spectral filter and beamsplitter in the same optical holder. Issues with the collimation of light entering the CIS interferometer cell have been improved by changing the focal length of the collimating lens on channel 11 of the MWI from 750 mm to 600 mm, thus improving image focus and measured contrast.

In order to account for additional delay components observed when calibrating the system, we have extended previous work on fitting to the wavelength dependence of crystal delay. Our new equations for the measured phase, eqs. (3.11) to (3.13), use the exact orientation of each interferometer com-

ponent to account for these observed effects, however, other physical processes may also contribute to this. It has been seen that by fitting to these equations the additional hyperbolic component has been significantly reduced.

Additionally, we present calibration procedures to account for the temperature and wavelength dependence of instrument delay. By measuring the temperature of each crystal using thermistors affixed to the crystal holder we have shown that linear modification of eq. (2.50), with thermal expansion and the thermo-optic effect accounted for, can effectively predict the temperature dependence of each crystal's imparted delay. This has resulted in negligible residuals primarily due to noise which can be further improved by extending the measurement period and averaging over multiple images.

The combination of these techniques has allowed for effective calibration of the MAST-U coherence imaging diagnostic without the need for in-situ or laser calibration systems.

Chapter 4

Simultaneous Measurement of C III Temperatures and Velocities

In this chapter we present a novel approach to analysing CIS data, only possible with multi-delay instruments like the one discussed in chapter 3. We show that by using this approach we can simultaneously measure ion parallel velocities and temperatures in the MAST-U divertor, two parameters which are routinely measured by CIS systems. As discussed earlier in this thesis the spectral emission we are studying is the C III triplet centred at 464.9 nm. In chapter 2 we discussed how CIS measurements of spectral emission that is not symmetric about its centre-of-mass frequency suffers from additional phase and contrast components which we speak about using the descriptor *asymmetry*. In the case of C III this occurs due to the statistical distribution of the 3 emission peaks. In this chapter we also discuss how oxygen and continuum spectral contamination affect measured CIS data and show how the additional spectral information obtained by using a triple-delay system reduces inversion errors due to this contamination. Finally, we present experimental data taken by our instrument at MAST-U and compare inverted velocity and temperature profiles to simulations and spectrometer measurements.

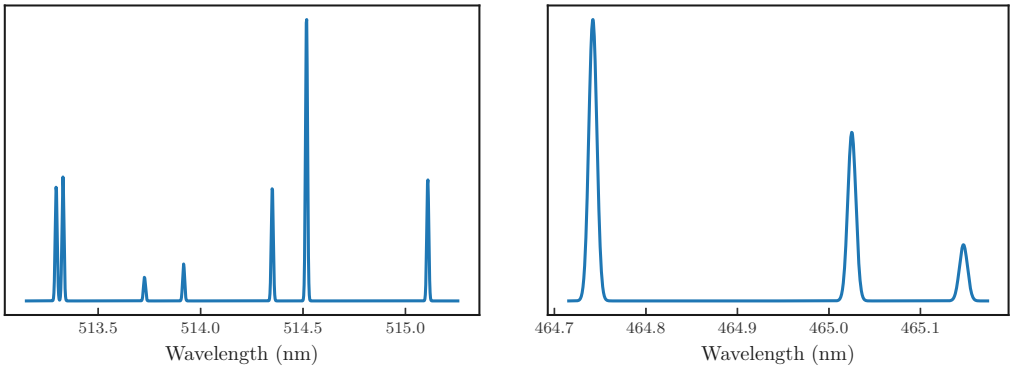

(a) (b)

Figure 4.1: Here we show the emission spectra for (a) C II and (b) C III in their rest frame. For illustration purposes the spectra were simulated with a temperature of 1eV and therefore display some broadening.

4.1 Modelling the Lineshape of Carbon III

The use of graphite (carbon) as a fusion device wall is nothing new, in fact due to its high melting point and abundance, graphite is one of the most common wall types for devices across the world. However, due to chemical and physical sputtering the plasma contained within these devices are routinely contaminated by carbon impurities. This contamination does not necessarily have a negative impact on these machines, as carbon has been shown to be a good power radiator thus improving detachment conditions and confinement [88, 89]. It is therefore not surprising that carbon ions have been the focus of multiple physical studies some which were discussed in chapter 2.

The two most prevalent carbon species in the MAST-U divertor are C^{1+} and C^{2+}. Both ions emit a multiplet spectrum, fig. 4.1, with C II emission containing seven peaks and C III three peaks. As discussed in chapter 2, multiplet emission can be handled by CIS instruments however it poses additional challenges proportional to the number of components. For this reason, we focus on C III in this study.

Next we turn to the processes that affect C III emission in MAST-U, namely

Doppler broadening and shifts which we introduced in detail in chapter 2. In this analysis we have made the valid assumption that the plasma, locally, is in thermal equilibrium, meaning each C III peak will be broadened by the same amount. Given that Doppler broadening is symmetric about a given emission line, we can conclude that it does not contribute to the asymmetry of the spectrum, and therefore the Doppler contrast is determined by eq. (4.1).

$$\zeta_D = \exp\left(-\frac{T_i}{T_C}\right) \tag{4.1}$$

$$T_C = \frac{2m_i\, c^2}{e\hat{\phi}_0^2} \tag{4.2}$$

Analogously, we expect that emitting ion velocities are locally uniform. Therefore, Doppler shifts can be thought of a shift in the centre-of-mass frequency of the spectrum, with the local Doppler phase is given by eq. (4.3). In both cases the group delay, $\hat{\phi}_0$, used is calculated at the centre-of-mass frequency of the rest-frame spectra. As group delay does not vary greatly over the wavelength range of the C III spectrum it is not necessary to speak about the group delay at each individual C III peak.

$$\phi_D = \frac{\hat{\phi}_0}{c} v \tag{4.3}$$

If we assume no spectral contamination is present the asymmetry terms for our instrument can then be reliably calculated using eqs. (4.4) to (4.6) and the accepted intensities of each C III peak given in table 4.1. In this scenario these images can be pre-calculated and used to calibrate out these effects before analysis takes place. However, we will see in section 4.4.2 that spectral contamination is present in MAST-U and therefore removal of the asymmetry terms from demodulated CIS data can not take place. Nevertheless, the relative intensities of each C III line are well understood; therefore, this will serve

Relative Freq. Diff., $\Delta\nu_i$ (x10^{-4})	**Relative Intensity**, I_i
2.9939	0.556
-3.09362	0.333
-5.71563	0.111

Table 4.1: Given are the accepted relative intensities, I_i of each C III emission line along with the relative frequency difference, $\Delta\nu_i = (\nu_i - \nu_c)/\nu_c$ between the line's emission frequency and the centre-of-mass frequency of the spectra. These values can be used to reliably calculate the asymmetry phase and contrast images for a given CIS instrument.

as *a priori* information for our inversions later in this chapter.

$$G_A = \sum_i^N I_i \exp\Big(i\,\Delta\nu_i\,\hat{\phi}_0\Big) \tag{4.4}$$

$$\zeta_A = |G_A| \tag{4.5}$$

$$\phi_A = \arg\left(G_A\right) \tag{4.6}$$

4.2 Simultaneous Fitting Technique

The goal of this research is to show the capabilities of CIS instruments to simultaneously produce 2D poloidal profiles of ion flow velocities and temperatures, however the images measured by any CIS instrument are, by definition, line integrated across 3D space. We therefore must invert this data onto a 2D grid. In this study we use an orthogonal magnetic field aligned grid. This means that our grids follow the same magnetic surfaces as the bulk plasma flow. This is beneficial when speaking about parallel velocity but also allows us to describe how velocities and temperatures change perpendicular to the magnetic field. We also show in section 4.2.1 that gridding in this way allows us to increase the effectiveness of our fitting procedure using regularisation. These grids have been created using reconstructed magnetic geometries calculated by EFIT++ and the tool DivGeo, a software wildly used in conjunction

with SOLPS-ITER, a scrape-off layer modelling code [90]. In section 4.2.2, we will also use SOLPS-ITER simulations of MAST-U plasmas, kindly provided by David Moulton at UKAEA, to test our inversion process. Plots of the two grids used in this section are shown in fig. 4.2 along with a projection of some of the sightlines of our CIS instrument viewing the MAST-U divertor. We can see that some sightlines pass straight through the divertor to the inner target on the left, while others loop around in R-Z space covering more grid cells.

Along with velocity and temperature values, each grid cell j in the poloidal cross-sections shown in fig. 4.2 has its own local emissivity e_j which acts as a weighting on how much of the C III emission in that cell contributes to the line-integrated spectrum. From the underlying intensity image I_p of our measured interferogram, where p is the pixel sightline index, we can determine the local emissivity. Since the line integration along each pixel sightline is linear, as expressed in eq. (4.7) where $L_{p,j}$ represents the length of each sightline in a given grid cell, we can apply a standard simultaneous algebraic reconstruction technique (SART) to solve for x in the matrix inversion problem $y = Ax+b$ [91]. The performance of this approach for each divertor configuration is presented in section 4.2.2.

$$I_p \propto \sum_{j=1}^{n} e_j L_{p,j} \tag{4.7}$$

4.2.1 Flow and Temperature Inversion Method

To achieve our goal of measuring C III velocities and temperatures in the MAST-U divertor, we sought an inversion method which would be self-consistent and leverage the additional spectral information provided by using three fixed interferometer delays. The method should also be applicable to other multi-delay configurations and combine the contribution of both temperature (contrast) and velocity (phase) into a single quantity which could be fit to using a maximum likelihood estimation. With this in mind the only quantity that

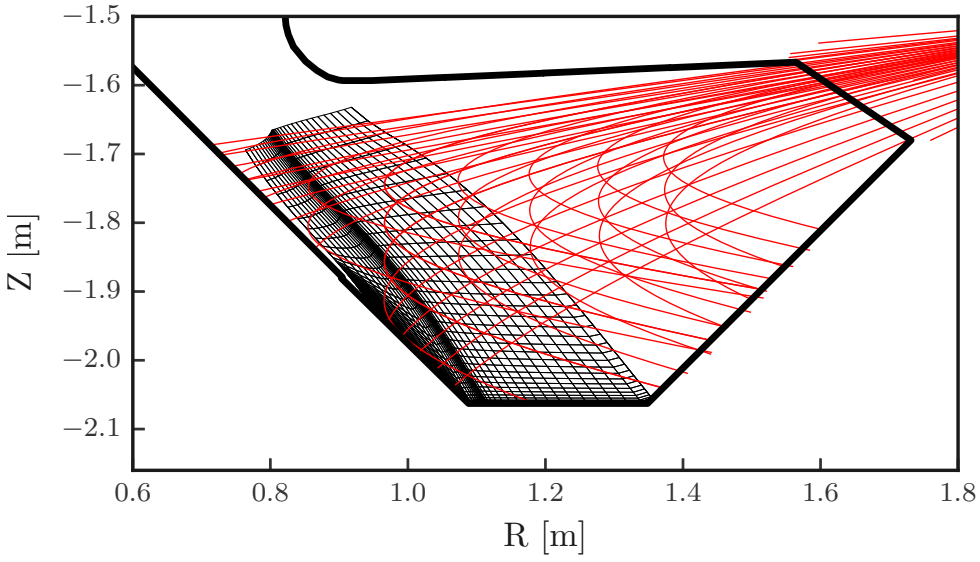

(a)

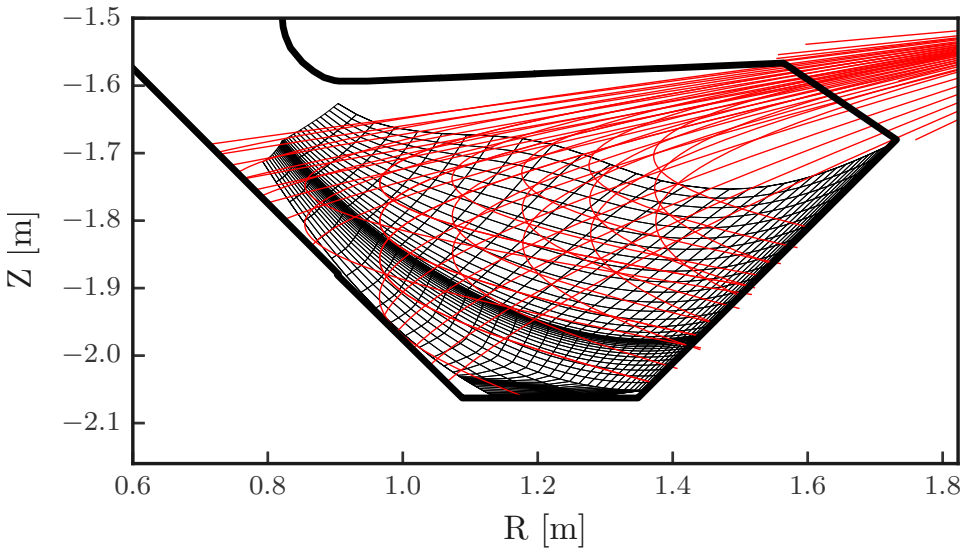

(b)

Figure 4.2: In this figure we show the MAST-U lower divertor region. In this orientation the centre column is located on the left and we move radially outward from there along the x-axis. Within the divertor we show the magnetic geometries of (a) an elongated divertor (ED) configuration and (b) a Super-X divertor (SXD) configuration, along with an orthogonal field aligned grid. In red, we show a span of CIS camera sightlines, displaying how some CIS pixel sightlines loop around in 2D space. These grids were generated using DivGeo and Carre via SOLPS-ITER.

fulfilled these requirements was the degree of coherence of the measured spectrum.

We saw in section 2.3.3 that the line-integrated degree of coherence of a spectrum is given by the product of the measured contrast of the interferogram and the complex exponential of its phase. This product will give us our *observed* degree of coherence, $\mathcal{D}_{p,d}$ for pixel p and interferometer delay d, and is given by eq. (4.8). We also saw it relates to the local contrast and phase terms in eq. (2.43). Using this equality and substituting phase and contrast with our definitions in eqs. (4.1) and (4.3) we arrive at eq. (4.9), which is a function of group delay, $\hat{\phi}_0$ and the set of parameters $\boldsymbol{\theta} = \{e_j, T_i, T_c, v_{||}, \mathbf{B}, \mathbf{l}\}$.

In eq. (4.9), the velocity v of the emitter has been replaced with $v_{||,j}\,\mathbf{B}_j \cdot \mathbf{l}_{p,j}$ as parallel velocity $v_{||,j}$ is the quantity of interest to us, where $\mathbf{B}_j$ is the magnetic field vector at grid cell j and $\mathbf{l}_{p,j}$ is the line of sight vector for each pixel passing through the grid. Implicit in this is the assumption that cross-field flows are negligible in our phase measurements, a common assumption with other CIS velocity studies [43, 71]. In the case of our instrument, lines of sight that are tangential (or near-tangential) to the MAST-U torus will carry more weight in our analysis due to the division of I_p in eq. (4.9).

$$\mathcal{D}_{p,d} = \check{\zeta}_{p,d} \exp\Big(i\check{\phi}_{p,d}\Big) \tag{4.8}$$

$$\begin{aligned} \textstyle\sum_j \gamma_{p,j}(\hat{\phi}_0;\boldsymbol{\theta}) &= \mathcal{D}_{p,d} \\ &= \frac{1}{I_p}\int_L e_j \zeta_{p,j} \exp(i\Phi_{p,j})\, dL \\ &= \frac{1}{I_p}\int_L e_j \exp\left(-\frac{T_{i,j}}{T_{c,d}}\right) \exp\left(-\frac{i\hat{\phi}_{0,d}}{c} v_{||,j}\, \mathbf{B}_j \cdot \mathbf{l}_{p,j}\right) dL \end{aligned} \tag{4.9}$$

Likelihood Equations

To determine the ion temperature and parallel flow velocity profiles from demodulated CIS images, a method which iteratively changes these profiles and

compares the calculated, $\gamma_{p,j}(\hat{\phi}_0;\boldsymbol{\theta})$ and measured, $\mathcal{D}_{p,d}$ degree of coherences is required. The standard maximum likelihood estimation (MLE) approach fulfils this requirement. The likelihood function is defined in eq. (4.10) where the final line of eq. (4.9) has been discretised to give eq. (4.11), and $\odot$ denotes the element-wise product $L_{p,j}$ and e_j. We have assumed that the random error in $\mathcal{D}_{p,d}$ is normally distributed and uncorrelated with the pixel and delay specific standard deviation, $\sigma_{p,d}$. As eq. (4.11) includes the emissivity profile, the inversion process we will continue to discuss could, with modifications, be used to determine e_j along with $v_{\parallel,j}$ and $T_{i,j}$. However, it was decided that as our instrument is contained within the MAST-U MWI the SART algorithm, discussed earlier, used for inverting MWI data should also be used in our study [92].

$$\mathcal{L}(\mathcal{D}_{p,d} \mid \boldsymbol{\theta}) \propto \exp\left(-\frac{1}{2}\left[\frac{|\mathcal{D}_{p,d} - \sum_j \gamma_{p,j}(\hat{\phi}_{0,d};\boldsymbol{\theta})|}{\sigma_{p,d}}\right]^2\right) \tag{4.10}$$

$$\gamma_{p,j}(\hat{\phi}_0;\boldsymbol{\theta}) = \frac{L_{p,j} \odot e_j}{\sum_{j'} L_{p,j'} e_{j'}} \exp\left(-\frac{T_{i,j}}{T_{c,d}}\right) \exp\left(-i\,\frac{\hat{\phi}_0}{c}\, v_{\parallel,j}\, B_{p,j}\right) \tag{4.11}$$

Equation (4.11) is weighted by the relative intensity of the C III emission in a given cell as areas of higher density contribute more to the measured contrast. For notational ease, we have replaced $\mathbf{B}_j \cdot \mathbf{l}_{p,j}$ with the matrix $B_{p,j}$.

We assume now that all our data points are statistically independent, and therefore the total likelihood function is given by the product of the individual likelihoods, eq. (4.12). This assumption does potentially introduce additional uncertainties in our inversions as the noise in neighbouring pixels is correlated, resulting in profiles which appear more defined than they should be. However, this is mitigated later by our use of regularisation. In the case of MAST-U, we generally do not have any prior information about the plasma therefore the posterior probability density function (PDF) is proportional to the total

likelihood function eq. (4.12). If prior information, $P(\boldsymbol{\theta})$ about the model parameters was known, in the case of repeat experiments or when inverting consecutive CIS frames, the posterior PDF can be determined using Bayes' theorem $P(\boldsymbol{\theta} \mid \boldsymbol{\mathcal{D}}) \propto \mathcal{L}(\boldsymbol{\mathcal{D}})P(\boldsymbol{\theta})$.

$$\begin{aligned} P(\boldsymbol{\theta} \mid \boldsymbol{\mathcal{D}}) \propto \mathcal{L}(\boldsymbol{\mathcal{D}} \mid \boldsymbol{\theta}) &\propto \prod_d \prod_p \mathcal{L}(\mathcal{D}_{p,d} \mid \boldsymbol{\theta}) \\ &\propto \prod_d \prod_p \exp\left(-\frac{\chi^2}{2}\right) \end{aligned} \tag{4.12}$$

$$\chi^2 = \left[\frac{|\mathcal{D}_{p,d} - \sum_j \gamma_{p,j}(\hat{\phi}_{0,d}; \boldsymbol{\theta})|}{\sigma_{p,d}}\right]^2 \tag{4.13}$$

Finally eq. (4.12) can then be further simplified for fitting by defining the log-likelihood, L. The optimal solution for both the T_i and $v_\parallel$ profile can therefore be found by maximising L.

$$L = \ln\left(P(\boldsymbol{\theta} \mid \boldsymbol{\mathcal{D}})\right) \propto \sum_d \sum_p -\frac{\chi^2}{2} \tag{4.14}$$

To perform this fitting the L-BFGS-B algorithm type was chosen [93]. This algorithm is an optimisation technique used to efficiently solve non-linear maximisation problems, particularly in high-dimensional parameter spaces. It is similar to the BFGS method, which approximates the Hessian matrix to guide optimisation, but is more memory efficient as it only stores a limited number of past solutions. Generally speaking, memory usage is not an issue for our use case but the added ability of the L-BFGS-B method to impose bounds on T_i and $v_\parallel$ is useful. This method balances computational efficiency and precision, enabling effective maximisation of L while respecting constraints imposed by the user.

Gradient Functions

To improve the performance of our fitting we derived the analytical gradient functions of eq. (4.14) for each parameter, ∇_{v_k} and $\nabla_{T_{i,k}}$. Here we use the index k to denote the grid cell that the gradient was computed at, not to be confused with j and j' which will be used, as before, to sum over all grid cells. Expanding χ^2 and letting $\Gamma_{p,d} = \sum_j \gamma_{p,j}(\hat{\phi}_{0,d}; \boldsymbol{\theta})$ we find that

$$\begin{aligned} |\mathcal{D}_{p,d} - \Gamma_{p,d}|^2 &= (\mathcal{D}_{p,d} - \Gamma_{p,d}) \left(\mathcal{D}^*_{p,d} - \Gamma^*_{p,d}\right) \\ &= \mathcal{D}_{p,d}\mathcal{D}^*_{p,d} - \mathcal{D}_{p,d}\Gamma^*_{p,d} - \mathcal{D}^*_{p,d}\Gamma_{p,d} + \Gamma_{p,d}\Gamma^*_{p,d} \end{aligned} \tag{4.15}$$

where $*$ denotes the complex conjugate. Differentiating eq. (4.15) with respect to each profile's values and simplifying then gives the following analytical equations.

$$\nabla_{\mathbf{v}_k} L_{p,d} = \frac{1}{2\sigma^2_{p,d}} \frac{i\hat{\phi}_{0,d}}{c} B_{p,k} \left[\mathcal{D}^*_{p,d}\gamma_k - \mathcal{D}_{p,d}\gamma^*_k + \gamma^*_k\Gamma_{p,d} - \gamma_k\Gamma^*_{p,d}\right] \tag{4.16}$$

$$\nabla_{\mathbf{v}_k} L = \sum_d \sum_p \nabla_{\mathbf{v}_k} L_{p,d} \tag{4.17}$$

$$\nabla_{\mathbf{T}_{i,k}} L_{p,d} = \frac{1}{2\sigma^2_{p,d}} \frac{1}{T_{c,d}} \left[\mathcal{D}^*_{p,d}\gamma_k + \mathcal{D}_{p,d}\gamma^*_k - \gamma^*_k\Gamma_{p,d} - \gamma_k\Gamma^*_{p,d}\right] \tag{4.18}$$

$$\nabla_{\mathbf{T}_{i,k}} L = \sum_d \sum_p \nabla_{\mathbf{T}_{i,k}} L_{p,d} \tag{4.19}$$

Regularisation

In maximum likelihood fitting, regularisation is a technique used to improve the performance and robustness of a model by adding a term which penalises the likelihood calculation. Including regularisation helps prevent over-fitting by discouraging the algorithm away from overly complicated values that fit the input data well but do not match the expected or realistic conditions. This

approach can lead to more stable fit profiles, particularly when available data is limited or when dealing with high-dimensional parameter spaces.

The two most commonly used techniques are L1 and L2 regularisation, where L1 tends to produce sparse solutions by forcing some profile estimates to zero and L2 spreads profile values more evenly across the features in the input data [94, 95]. L1 regularisation is calculated by adding the absolute values of the profiles to the χ^2, while L2 regularisation incorporates the squared values of the profile into the χ^2, effectively penalising large solution values. In deciding what type of regularisation fits our problem we identified that the C III emission in MAST-U is generally very localised leading to a degree of sparsity in the profiles. However, the velocity and temperature profiles are not expected to be fast varying along or across field lines.

Taking this into account and leveraging the benefits of using field-aligned grids in our inversions, we determined that a gradient-based regularisation scheme, which used the rate of change of each profile in given direction to penalise the solution, would provide the most stable results. For this we chose a central finite difference calculation. Each regularisation term $\beta_{\{\parallel,\perp\}}$ is therefore given by eq. (4.20), where $\parallel$ and $\perp$ indicate the direction on the field aligned grid over which the finite difference is calculated. The profile used in the calculation is denoted by $\mathcal{X}$, n denotes the cell *row* or *column* used, c denotes the cell index within that row or column and $\omega_{\{-,+\}}$ the distance between data points before and after the central point. It is important to be able to control the strength of each regularisation scheme, therefore we also add a weighting parameter $\lambda^{\mathcal{X}}_{\{\parallel,\perp\}}$ to eq. (4.20). The total regularisation term β_R is then given by the sum of all regularisation terms, eq. (4.21), with eq. (4.14) now given by eq. (4.22).

$$\beta_{\{\parallel,\perp\}}(\mathcal{X}) = \lambda^{\mathcal{X}}_{\{\parallel,\perp\}} \sum_{n} \sum_{c=1}^{c-1} \frac{\omega_+^2 \mathcal{X}_{n,c+1} + \mathcal{X}_{n,c}(\omega_+^2 - \omega_-^2) - \omega_-^2 \mathcal{X}_{n,c-1}}{\omega_+ \omega_- (\omega_+ + \omega_-)} \tag{4.20}$$

$$\beta_R = \beta_\parallel(\mathcal{X}_v) + \beta_\perp(\mathcal{X}_v) + \beta_\parallel(\mathcal{X}_T) + \beta_\perp(\mathcal{X}_T) \tag{4.21}$$

$$L = \sum_d \sum_p -\frac{\chi^2}{2} + \beta_R \tag{4.22}$$

4.2.2 Synthetic Testing

To rigorously evaluate the performance and reliability of the MLE fitting procedure developed in this study, we conducted a series of synthetic tests designed to simulate the conditions present in MAST-U. Synthetic testing allows for a thorough examination of the estimator's ability to accurately recover velocity and temperature profiles. In this section we will show how our procedure is robust to noise in contrast and phase images.

The synthetic data used in this testing was supplied by David Moulton at UKAEA, consisting of two SOLPS-ITER simulations of MAST-U shots #46860 (SXD) and #47079 (ED). Both simulations are of L-mode density ramp plasmas with 1.5 MW of neutral beam injection (NBI) heating delivered by the south-west NBI on MAST-U. These shots and their simulations were chosen as they closely match the conditions found in the experimental shots we will use later in this chapter, and thus provide an ideal test-bed for our procedure.

Emissivity Fitting

Before testing our simultaneous fitting algorithm we first inverted the emissivities of both simulations. In order to properly replicate experimental data, Gaussian noise was added to the synthetic camera images according to the photon transfer curve of our camera (fig. 3.25). Both fits were run until the

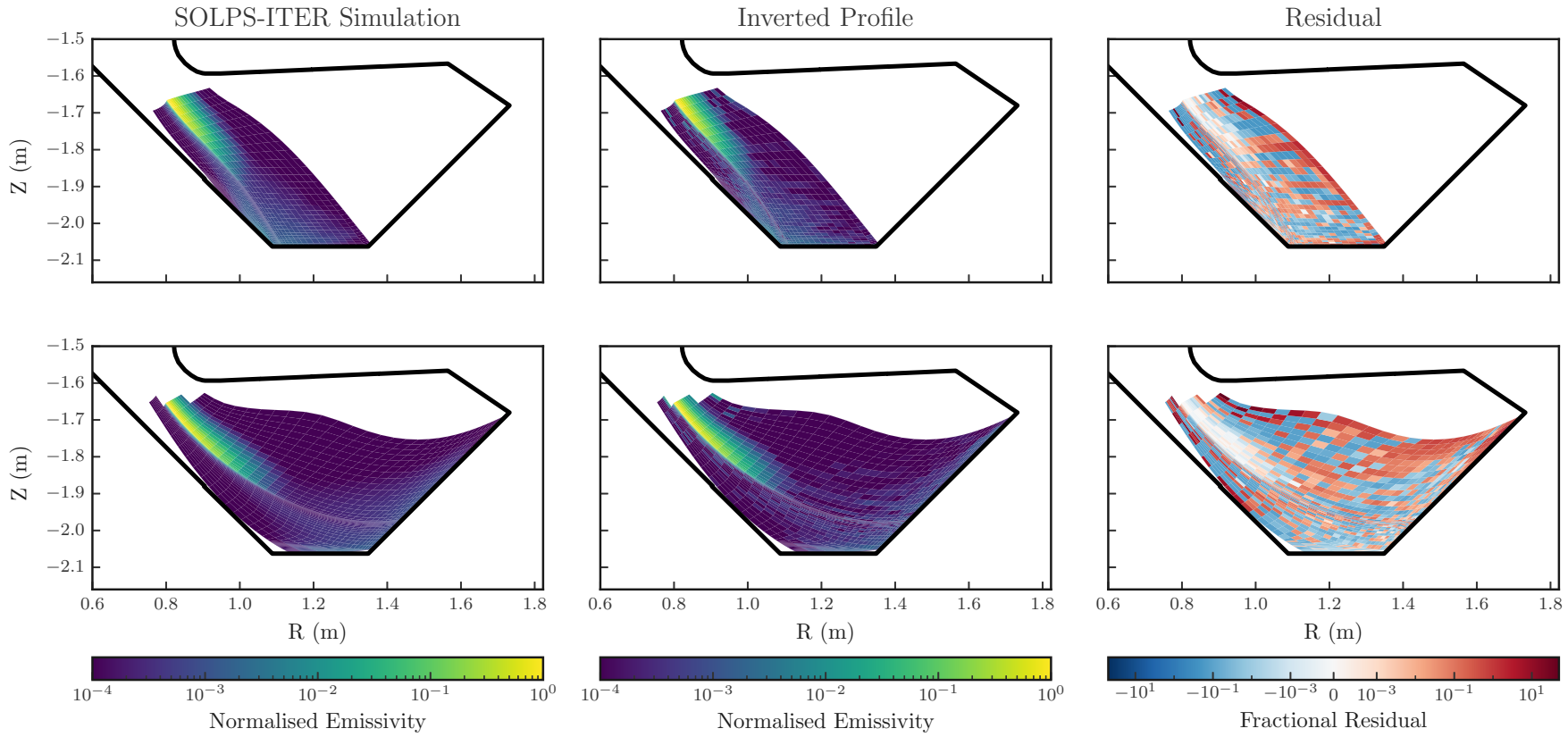

Figure 4.3: In this figure we compare known emissivity profile (left) from SOLPS-ITER simulations of SXD shot #46860 and ED shot #47079 to the inverted emissivity profile (middle) each using a SART algorithm. This fitting was executed on C III emission data which included noise inline with photon transfer curve of the camera used in this research. From the fractional residuals (right) between our inverted profiles and the SOLPS-ITER profiles, we see good performance areas of emission as low as 1% of the maximum.

relative change in the likelihood value was less than 10^{-9}. This value was chosen as it provided good profiles within a reasonable time period of < 6 hrs running on a standard home PC. Figure 4.3 show a comparison between the emissivity profile obtain directly from SOLPS-ITER (left) and the fitted profiles using the SART algorithm (middle). We can see from the fractional residual profiles (right) that this fitting method is robust to the noise expected from our system on MAST-U in areas of emission $> 1\%$, which is equivalent to camera sensor values > 40 counts. Consequently, in regions where emission is less than 1%, noise becomes the primary limiting factor for the accuracy of our inversion. In section 4.4, we will see that this level of precision significantly exceeds the requirements of our study, reinforcing our confidence in determining accurate experimental emissivity profiles. This is crucial, as any discrepancies in these profiles would propagate errors to our velocity and temperature fitting algorithm.

Velocity and Temperature Fitting

Similar to our emissivity fitting, here we seek to replicate the experimental phase and contrast images expected from our diagnostic. To do this we, again, consider noise, which will be a propagation of sensor noise through the demodulation process to the contrast and phase images produced. To accurately predict this noise we mapped the underlying intensity (DC) and contrast values to the noise in demodulated contrast and phase images. As the measured phase will always be wrapped between $[-\pi, \pi)$ it is not necessary to include it in the noise mapping. That being said we will see that the noise in the recovered phase images is a function of the input contrast and intensity.

To determine the standard deviation (std. dev.) of the demodulation noise we used the mapping parameters to produce a large number of triple-delay interferograms and applied noise according to our camera's photon transfer

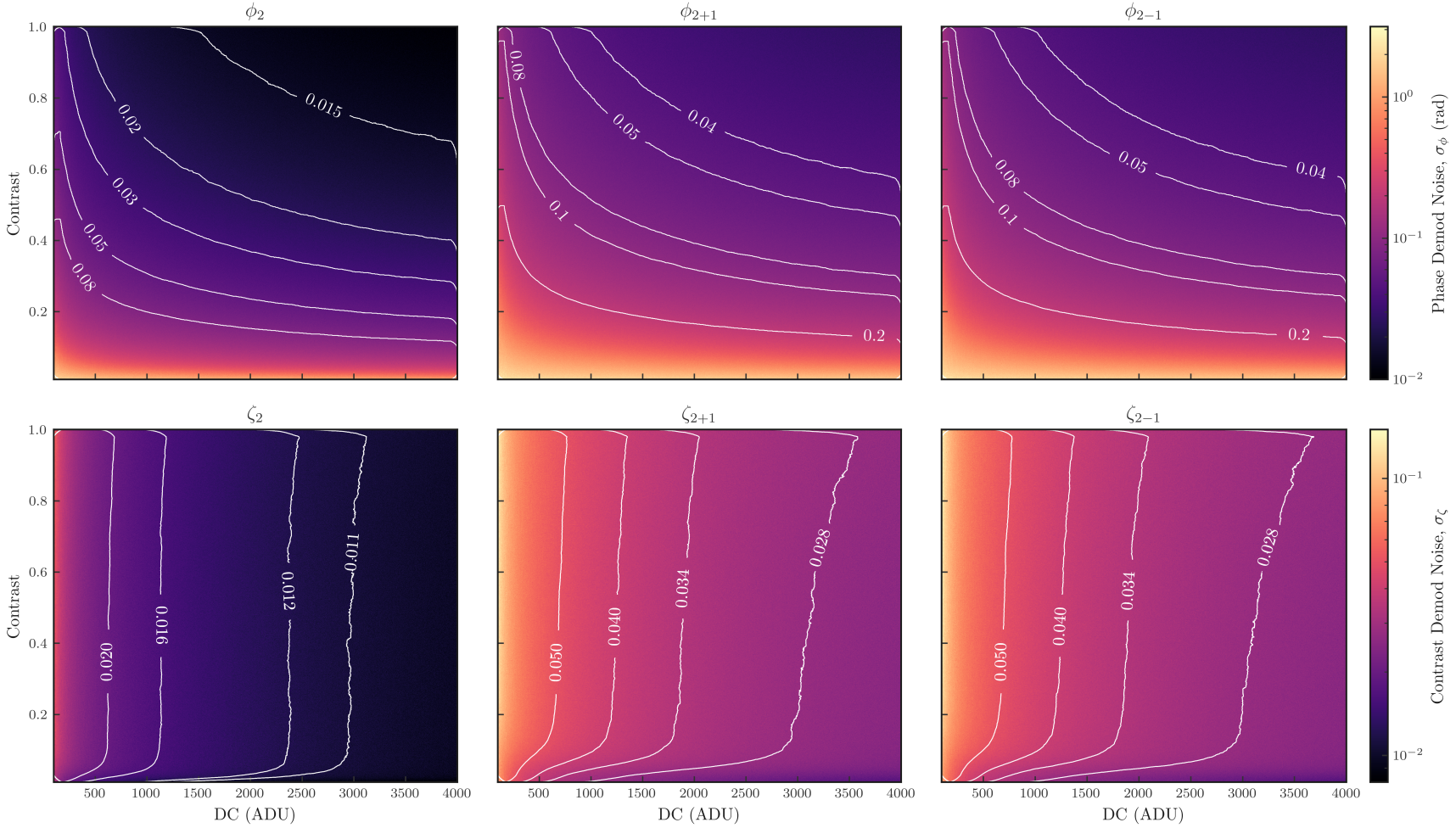

Figure 4.4: The top row here shows the standard deviation in the each phase image produced by our system for given contrast and DC values. The bottom row shows the same for each contrast term. These values were calculated by determining the standard deviation in the phase and contrast images recovered from demodulating noisy interferograms simulated using the input values on the x and y axes of these plots.

curve. These images were then demodulated and compared to the interferogram input values. As the interferogram is a flat field, similar to that used when calibrating the MAST-U CIS with spectral lamps (chapter 3), we were able to determine the noise std. dev. by looking at the std. dev. of a large central portion of the image. As expected fig. 4.4 shows that the demodulation noise for both phase and contrast is determined by the underlying intensity and contrast of the interferogram. It also shows that phase noise has a stronger dependence on the underlying contrast, whereas the contrast noise depends strongly on the interferogram DC. Using these plots as look-up tables we were then able to apply appropriate noise to our synthetic phase and contrast images, which were calculated from the aforementioned SOLPS-ITER simulations.

Figures 4.5 to 4.8 show a comparison between the resulting velocity and temperature fits performed using our synthetic noisy phase and contrast images and the process described earlier for each divertor configuration.

We can see from figs. 4.5 to 4.8 that noise does affect our ability to recover the velocity and temperature profiles. However, our fit residuals of, in general, ≤ 0.5 km/s and ≤ 0.5 eV show an accuracy comparable to or greater than that seen in other CIS and spectrometer studies [96, 43, 73]. The larger discrepancies observed in the private flux region (PFR), the area close to the inner tiles on the left side of each figure, and the outer scrape-off layer high in the divertor are likely due to several factors that will also apply to MAST-U experimental plasmas. Unlike regions lower in the divertor, these areas have very low emissivity yet are located close to regions of very high emissivity. Consequently, sightlines pass through both regions making it more difficult to resolve details where the emissivity (and thus SNR) is low. This interpretation is supported by the fact that detail is successfully recovered in areas of low emissivity deep in the divertor, as here the emissivity does not vary rapidly.

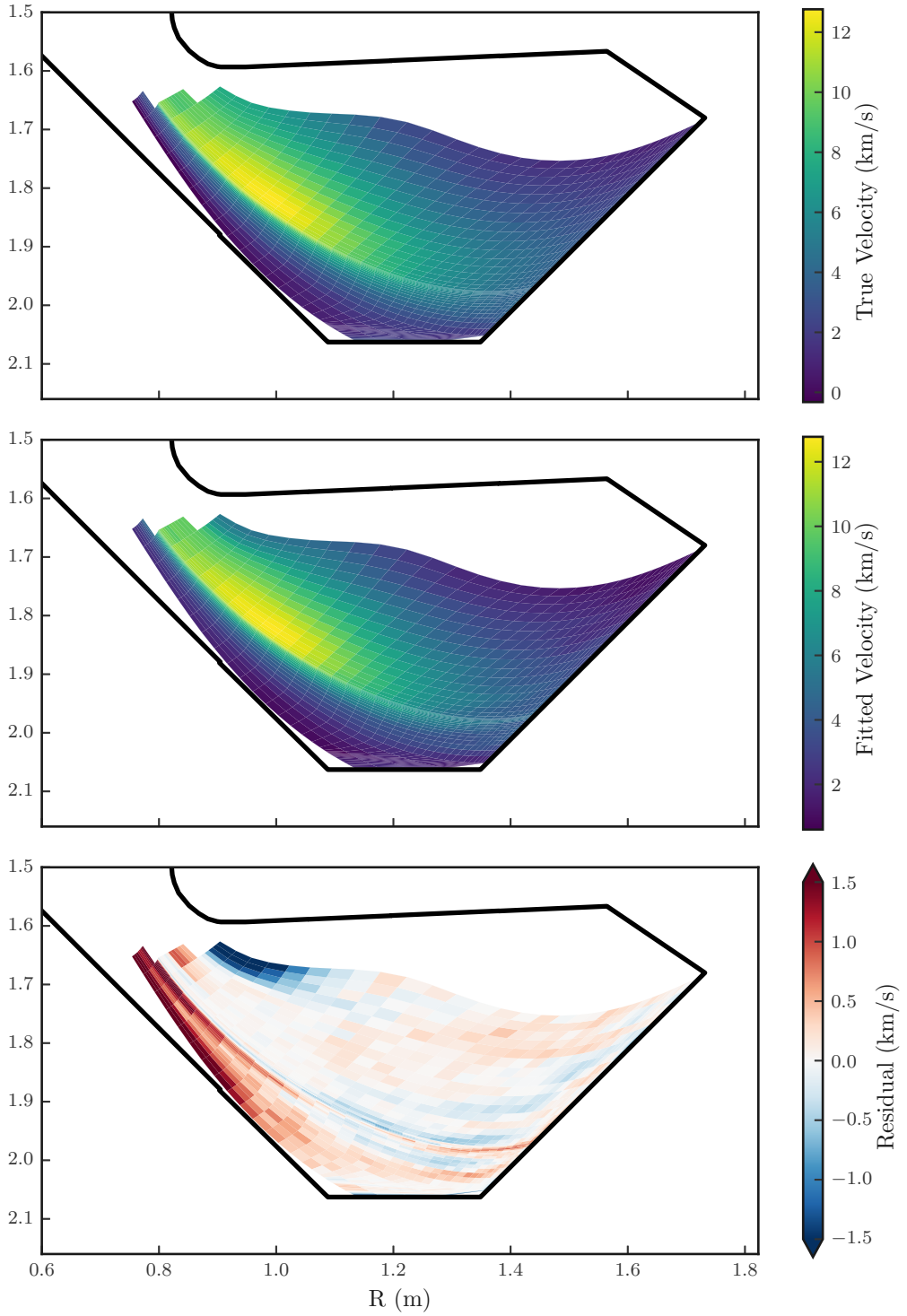

Figure 4.5: In this figure we compare the known velocity profile (top) from a SOLPS-ITER simulation of SXD shot #46860 to the inverted profile (middle row) produced using phase and contrast images with noise added according to fig. 4.4. The accuracy of this fitting, indicated by average residuals ≤ 0.5 km/s, is shown to be comparable or greater than that found in other velocity studies.

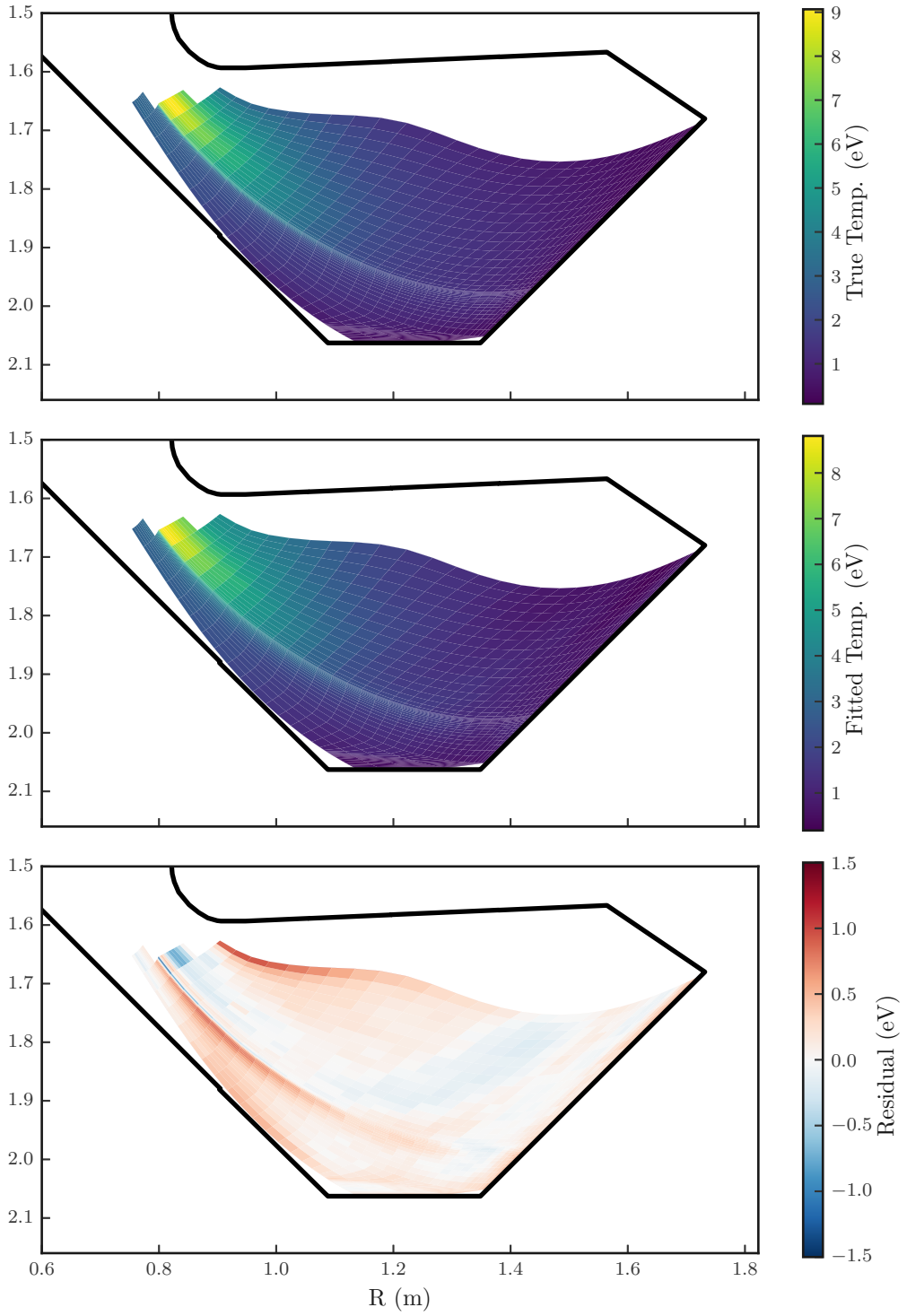

Figure 4.6: This figure is a continuation of fig. 4.5, where here we show the performance recovering the temperature profile for SXD shot #46860. Similar to the residuals in fig. 4.5, here we again see performance acceptable for physical studies and in line with or better than previous temperature studies.

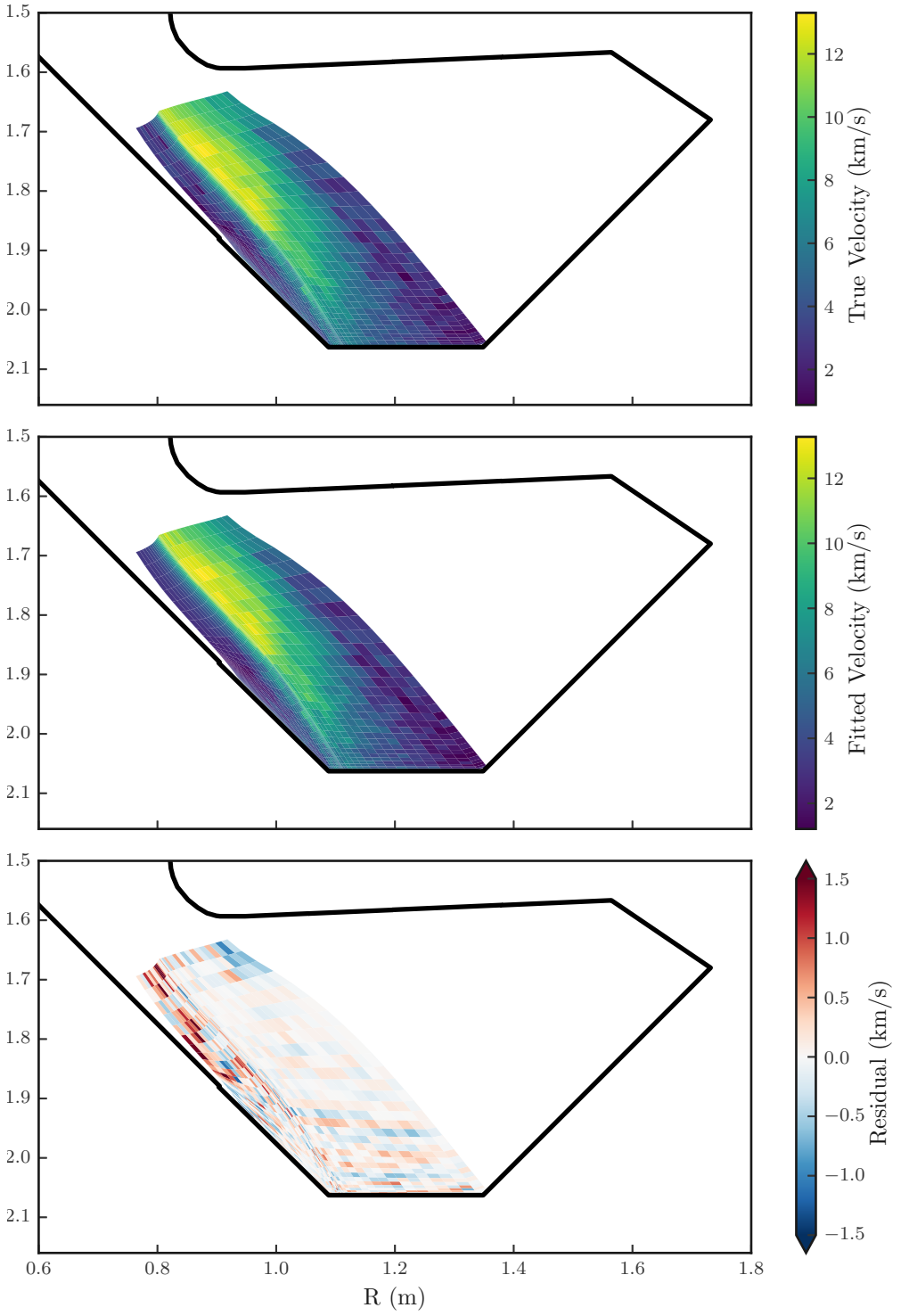

Figure 4.7: Here we compare the known velocity profile (top) for ED shot #47079 to the inverted profile (middle row) produced using phase and contrast images with noise added according to fig. 4.4. The residuals in this plot are comparable to those shown in fig. 4.5, and therefore acceptable for this study.

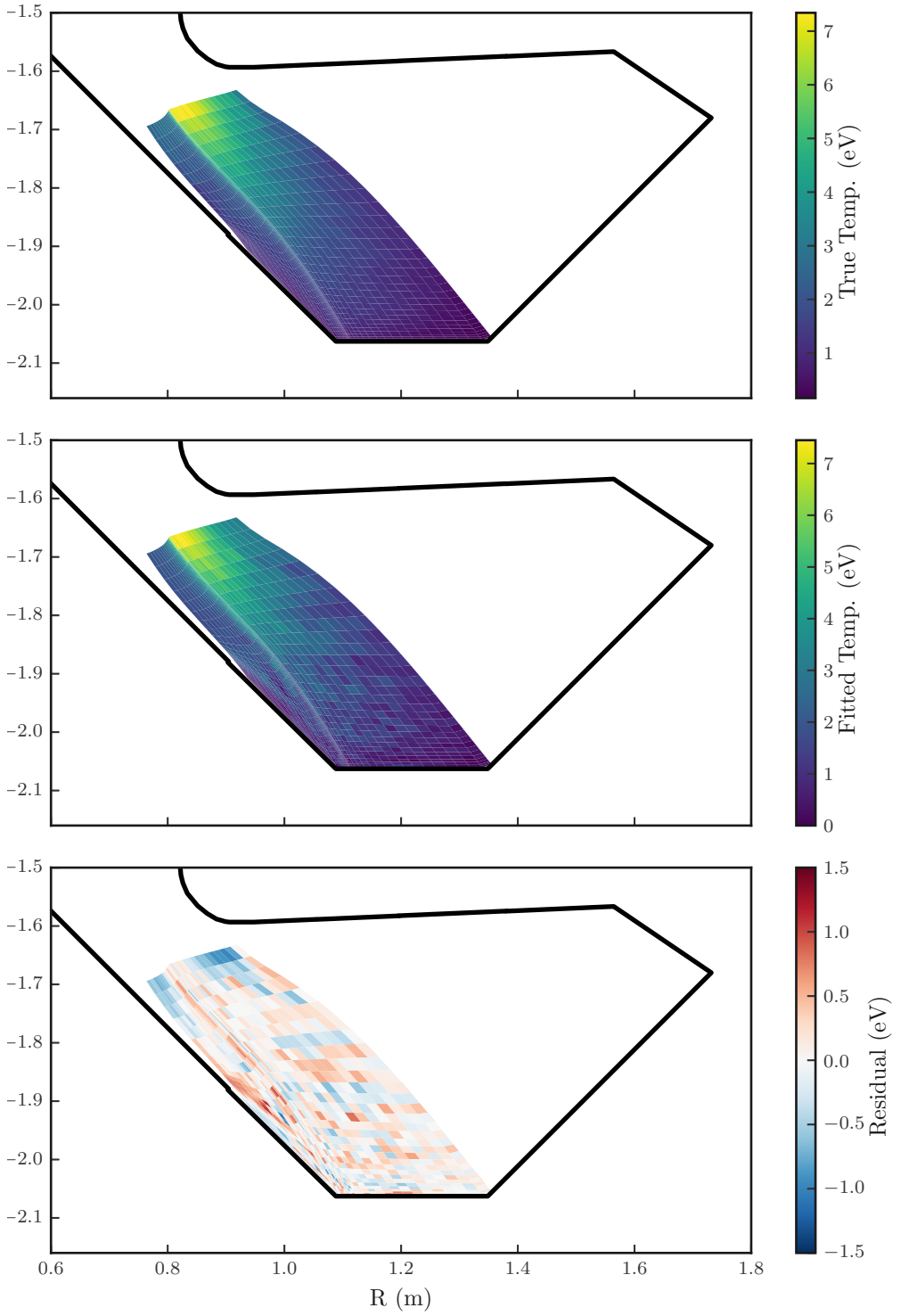

Figure 4.8: Continuing on from fig. 4.7, we see that the performance recovering the temperature profile is also acceptable for the studies discussed later in this chapter.

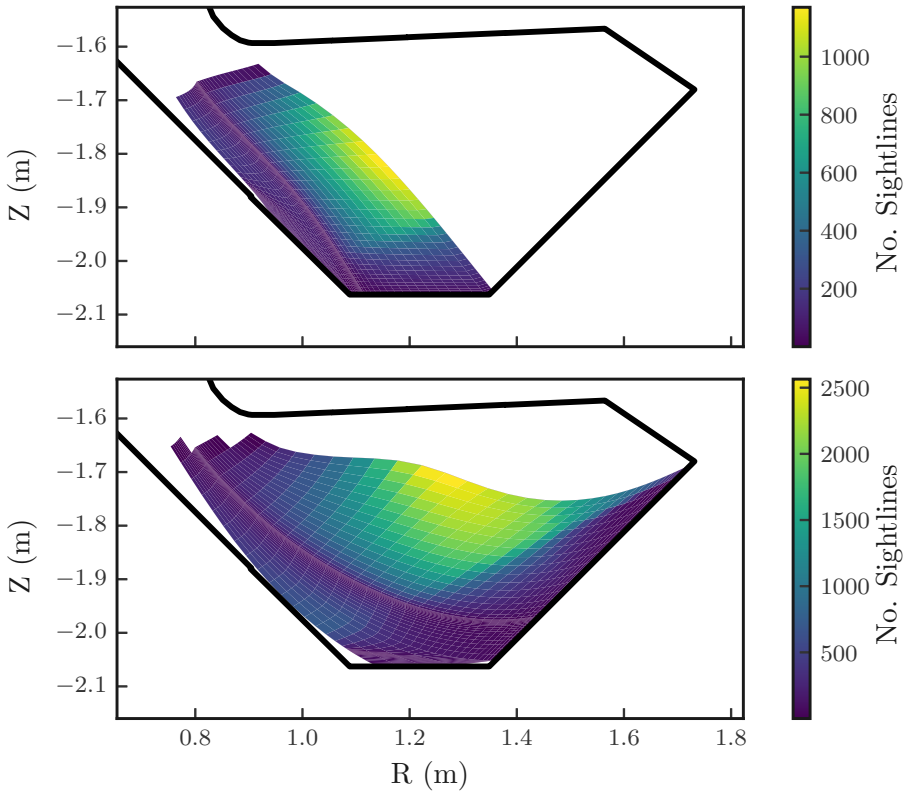

Figure 4.9: In this figure we show the sightline coverage for the ED (top) and SXD (bottom) magnetic geometries used during inversion testing. We can see how to view vector of the MAST-U MWI, and thus the CIS, which points diagonally downward from right to left, yields much greater sightline coverage the outer SOL.

These plots also indicate that the algorithm finds it more difficult to determine the profile in the first few grid cells along each field line. We can attribute this difficulty to the relative lack of sightline coverage in these upper regions compared to areas lower in the divertor, as shown in fig. 4.9. We will see later this chapter that this lack of sightline coverage where C III emits strongest has a knock-on effect to experimental measurements suggesting that future CIS instruments would benefit from a more optimised viewing vector.

It is important to note that the effects discussed above arise due to the presence of noise. We know this because the same fits were performed on noise-free phase and contrast images, which produced absolute residuals $<<$ 0.5 eV

and 0.5 km/s. It is clear from this result and figs. 4.5 to 4.8 that our procedures can reliably recover the expected profiles with acceptable accuracy, particularly in regions of significant physical interest.

4.3 Spectral Contamination

In the previous section we showed that our fitting procedure was capable of dealing with noise representative of that expected from experimental plasmas. However, the spectrum used in section 4.2 was purely C III where the asymmetry component of the degree of coherence was known exactly. Although we expect table 4.1 to hold, in practice it is likely that the measured spectrum from any fusion device would fall foul to spectral contamination. In this section, we discuss the most common forms of spectral contamination: continuum emission, oxygen contamination, and Zeeman splitting. We also modify the equations presented earlier to account for their presence on MAST-U. Furthermore, we demonstrate that, in the absence of relevant independent measurements, a multi-delay system is required to recover accurate profiles while accounting for these effects.

4.3.1 Continuum Emission

Continuum emission in tokamaks arises from the interactions between charged particles. This emission is attributed to Bremsstrahlung radiation which also includes synchrotron radiation [97, 98, 99]. Arising from the deflection of high-energy electrons by the electric fields of ions, Bremsstrahlung emits photons across a broad spectrum.

The effect this emission will have on the degree of coherence of the measured light is dependent on the bandpass of the filter used in the interferometer. It has been shown that the degree of coherence of a spectrum in the presence of

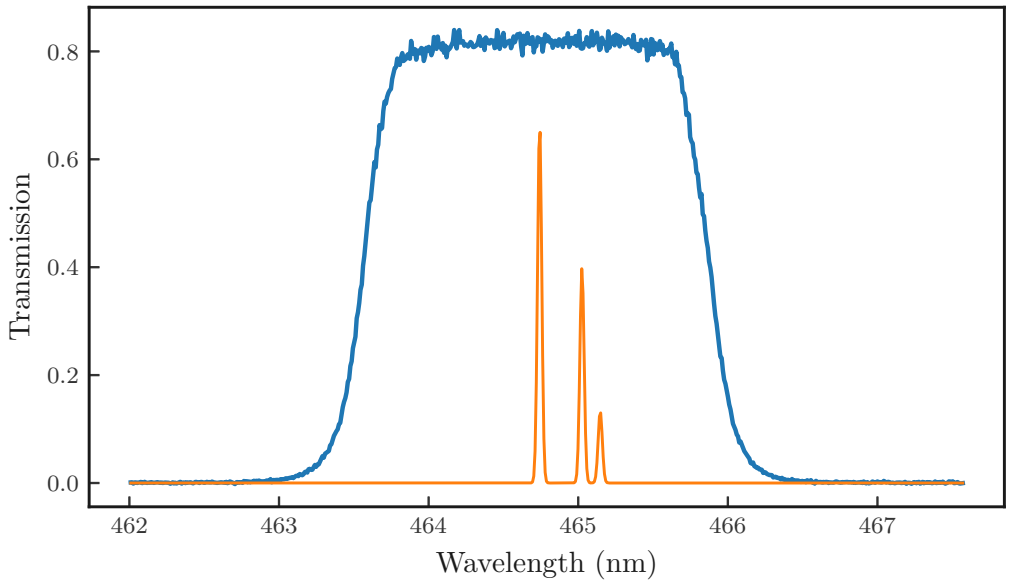

Figure 4.10: Shown is the filter bandpass (blue) for the C III spectral filter used in this study, with a bandwidth of 2.1 nm and centred at 464.8 nm. For reference a simulated example C III spectrum (orange) is also shown.

continuum emission is given by eq. (4.23), where I_L and I_c are the intensities of the C III and continuum spectrum, respectively, with $I_L + I_c = 1$ [67]. The degree of coherences for each are given by γ_L and γ_c.

$$\gamma = \gamma_L \left(I_L + I_c \frac{\gamma_c}{\gamma_L} \right) \tag{4.23}$$

However, if the contrast response of the filter bandpass at the delays of the interferometer is near zero, $|\gamma_c| \approx 0$, then $\gamma = I_L \gamma_L$. A study of this for the filter bandpass used in this work, fig. 4.10, shows that this is in fact the case, fig. 4.11. Therefore, eq. (4.13) becomes eq. (4.24), where $I_\Delta = (I_p - I_c)/I_p$ is the fraction of the measured DC at each pixel p, I_p, which can be attributed to the C III emission. This reduces the measured contrast according to the relative intensities of the spectral line and continuum emission. In general, I_c can be obtained from divertor spectroscopy however we intend for our instrument to operate independent of other diagnostics therefore we can add this term as a fitting parameter. With this the gradients for our fitting are now given by

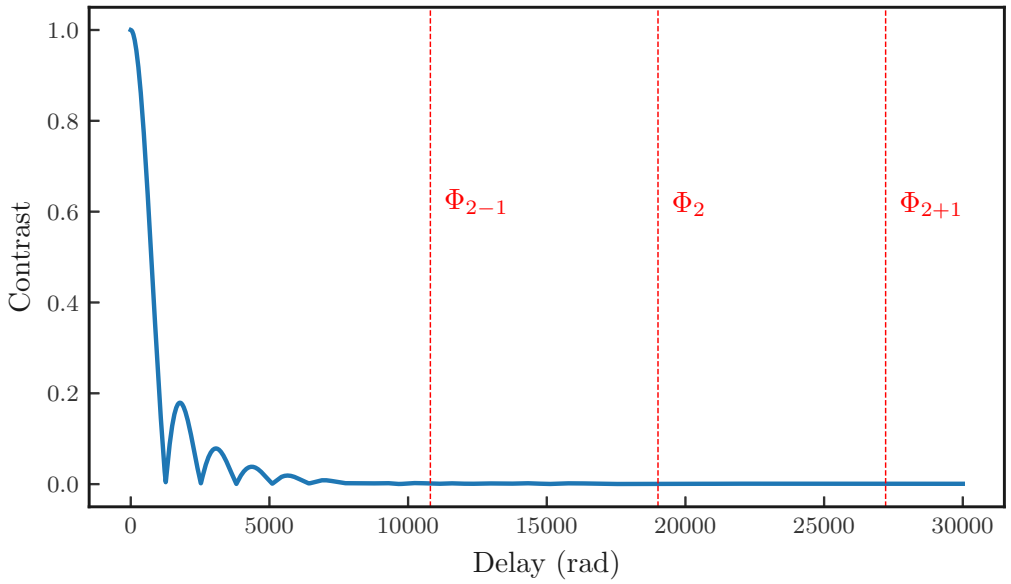

Figure 4.11: In this figure we show how the magnitude of the Fourier transform of filter bandpass in fig. 4.10, $|\gamma_c|$ varies over a range of interferometer delays. These values can be thought of as a 'contrast' contribution. Marked in red are the interferometer delays relevant to our study, where we can see that $|\gamma_c| \approx 0$.

eqs. (4.25) and (4.26) and the gradient with respect to I_c is given by eq. (4.27).

$$\chi^2 = \left[\frac{|\mathcal{D}_{p,d} - I_\Delta \sum_j \gamma_{p,j}(\hat{\phi}_{0,d}; \boldsymbol{\theta})|}{\sigma_{p,d}}\right]^2 \tag{4.24}$$

$$\nabla_{\mathbf{v}_k} L = \sum_d \sum_p \frac{I_p - I_c}{I_p} \nabla_{\mathbf{v}_k} L_{p,d} \tag{4.25}$$

$$\nabla_{\mathbf{T}_{i,k}} L = \sum_d \sum_p \frac{I_p - I_c}{I_p} \nabla_{\mathbf{T}_{i,k}} L_{p,d} \tag{4.26}$$

$$\nabla_{\mathbf{I}_c} L = \sum_p \sum_d \frac{1}{2\sigma_{p,d}^2} \frac{1}{I_p} \left[\mathcal{D}^*_{p,d}\Gamma_{p,d} + \mathcal{D}_{p,d}\Gamma^*_{p,d} - 2I_\Delta \Gamma^*_{p,d}\Gamma_{p,d}\right] \tag{4.27}$$

4.3.2 Oxygen Contamination

Spectral contamination from other lines is also possible. Here we will consider the oxygen II (O II) line at 464.9135 nm, as it falls in the middle of the C

III triplet and has been observed on MAST before [100, 43]. When dealing with the presence of another spectral line we cannot disregard the degree of coherence in the same way as with continuum emission as this line will have a contrast response across a wide delay range. Instead, we can think of this line a creating a C III *quadruplet* spectrum and apply the same methods as we have earlier when dealing with multiplet spectra.

The existence of an O II line will modify the asymmetry degree of coherence according to its relative intensity to the other C III lines. The degree of coherence is now given by the product of the Doppler and asymmetry terms, $\gamma = \gamma_D \cdot \gamma_A$, where γ_A is given by eq. (4.28). In this case eq. (4.13) is now given by eq. (4.30), where the asymmetry phase and contrasts have now not been removed from $\mathcal{D}_{p,d}$ as these are no longer reliably known. However, similar to the background if the relative intensity of the oxygen peak is known the asymmetry can be calculated and removed as was assumed in section 4.2.2.

$$\gamma_A = \sum_i^N I_i \exp\left(i \frac{\nu_i - \nu_c}{\nu_c} \hat{\phi}_0 \right) \tag{4.28}$$

$$\nu_c = \sum_i^N \nu_i I_i \tag{4.29}$$

$$\chi^2 = \left[\frac{|\mathcal{D}_{p,d} - \gamma_A \sum_j \gamma_{p,j}(\hat{\phi}_{0,d}; \boldsymbol{\theta})|}{\sigma_{p,d}} \right]^2 \tag{4.30}$$

The gradients of the likelihood function in the case of line contamination are made more complicated by the fact that the intensity of the contaminating line modifies the centre-of-mass frequency of the spectrum. This is not a factor, however, in the case of the velocity and temperature gradients which are now given by eqs. (4.31) and (4.32).

$$\nabla_{\mathbf{v}_k} L = \frac{1}{2\sigma_{p,d}^2} \frac{i\hat{\phi}_{0,d}}{c} B_{p,k} \left[\gamma_A \gamma_k (\mathcal{D}^*_{p,d} - \gamma^*_A \Gamma^*_{p,d}) - \gamma^*_A \gamma^*_k (\mathcal{D}_{p,d} - \gamma_A \Gamma_{p,d}) \right] \tag{4.31}$$

$$\nabla_{\mathbf{T}_{i,k}} L = \frac{1}{2\sigma_{p,d}^2} \frac{1}{T_{c,d}} \left[\gamma_A \gamma_k (\mathcal{D}^*_{p,d} - \gamma^*_A \Gamma^*_{p,d}) + \gamma^*_A \gamma^*_k (\mathcal{D}_{p,d} - \gamma_A \Gamma_{p,d}) \right] \tag{4.32}$$

However, when differentiating with respect to the relative oxygen intensity, I_O we have to consider two scenarios: $I_i = I_O$ and $I_i \neq I_O$. The general equation for the differential of each line is given by eq. (4.33), where $\gamma_a(I_i, \nu_i)$ is given by eq. (4.34) and ν_O is the frequency of the O II line. The full differential is then given by eq. (4.35).

$$\frac{\partial}{\partial I_O} \gamma_a(I_i, \nu_i) = -i\, \hat{\phi}_0\, \nu_i\, \frac{\nu_O}{\nu_c^2}\, I_i\, \exp\left(2i\hat{\phi}_0 \frac{\nu_i}{\nu_c} \right) \exp\left(-i\hat{\phi}_0 \right) \tag{4.33}$$

$$\gamma_a(I_i, \nu_i) = I_i \exp\left(i \frac{\nu_i - \nu_c}{\nu_c}\, \hat{\phi}_0 \right) \tag{4.34}$$

$$\nabla_{\mathbf{I}_O} L = -\frac{1}{2\sigma_{p,d}^2} \left[\frac{\partial \gamma_A}{\partial I_O}\, \Gamma_{pd}\, (\mathcal{D}^*_{p,d} - \gamma^*_A \Gamma^*_{p,d}) + \frac{\partial \gamma^*_A}{\partial I_O}\, \Gamma^*_{p,d}\, (\mathcal{D}_{p,d} - \gamma_A \Gamma_{p,d}) \right] \tag{4.35}$$

$$\frac{\partial \gamma_A}{\partial I_O} = \sum_i^N \frac{\partial}{\partial I_O} \gamma_a(I_i, \nu_i) \tag{4.36}$$

Implicit in this derivation is the assumption that the oxygen ion temperature and velocity are equal to that of the carbon ions. In practice we would expect the velocities to differ if the plasma was in thermal equilibrium, however as we are considering the O II line to be a minor impurity line (i.e. its intensity small compared to the total C III emission) the errors in phase created by a difference in oxygen velocity will be much less than our demodulation errors, therefore our assumption holds. If this was not the case, or a multi-species plasma was used, a more complex likelihood equation would need to be used. This may also require more than three interferometer delays as this would now be a multi-species problem and therefore is outside the scope of this study.

4.3.3 Zeeman Splitting

In section 2.1.1, we introduced Zeeman splitting, which is the separation of the fine structure of atomic energy levels in the presence of magnetic fields. In spec-

troscopic terms, this can manifest as a broadening of the emission spectrum if other broadening mechanisms are present or due to limited spectral resolution. The degree of Zeeman splitting is directly proportional to the strength of the applied magnetic field. Consequently, it has played a significant role in previous CIS studies, particularly on the stellarator W7-X, which operates with significantly higher magnetic fields compared to those found in the MAST-U divertor [35, 96]. In contrast, on MAST, where the magnetic field is less than < 0.5 T, the effects of Zeeman splitting were determined to be negligible at the selected delays [30].

In a study of the typical magnetic fields on MAST-U, we found that the field was of a similar magnitude to that on MAST, with the exception of regions high in the divertor near the centre column ($R \approx 0.8$ m). To determine whether Zeeman splitting would have an appreciable effect on our study, we analysed the magnetic field from the Super-X divertor shot #47079 used in section 4.2.2. This magnetic geometry represents the worst-case scenario for this effect, as, for spectroscopic studies, Zeeman splitting is also a function of θ_M, the angle between the line-of-sight vector of the sensor and the magnetic field vector. Figure 4.2b shows that a number of camera sightlines are sometimes nearly parallel to the field, where the effect is strongest.

$$\begin{aligned}\zeta_Z \approx |\, &\sin^2\theta_M \cos^2\rho_\Delta \\ &+ \tfrac{1}{2}\left(1 + \cos^2\theta_M - \sin^2\chi\cos[2\rho_\Delta]\right)\cos\left(\frac{e\,|\mathbf{B}|\,\hat{\phi}_0}{4\,\pi\,m_e\,\nu_0}\right)|\end{aligned} \tag{4.37}$$

It has also been shown that at $\theta_M > 0$, the measured contribution of Zeeman splitting depends on ρ_Δ, the angle between the front polariser of a CIS interferometer and the 2D magnetic field projection [61]. Using eq. (4.37), and calculating θ_M and ρ_Δ for our SXD grid and the interferometer discussed in chapter 3, the expected line-integrated Zeeman contrast for each delay is shown in fig. 4.12. From these figures, we can see that the effect is negligible

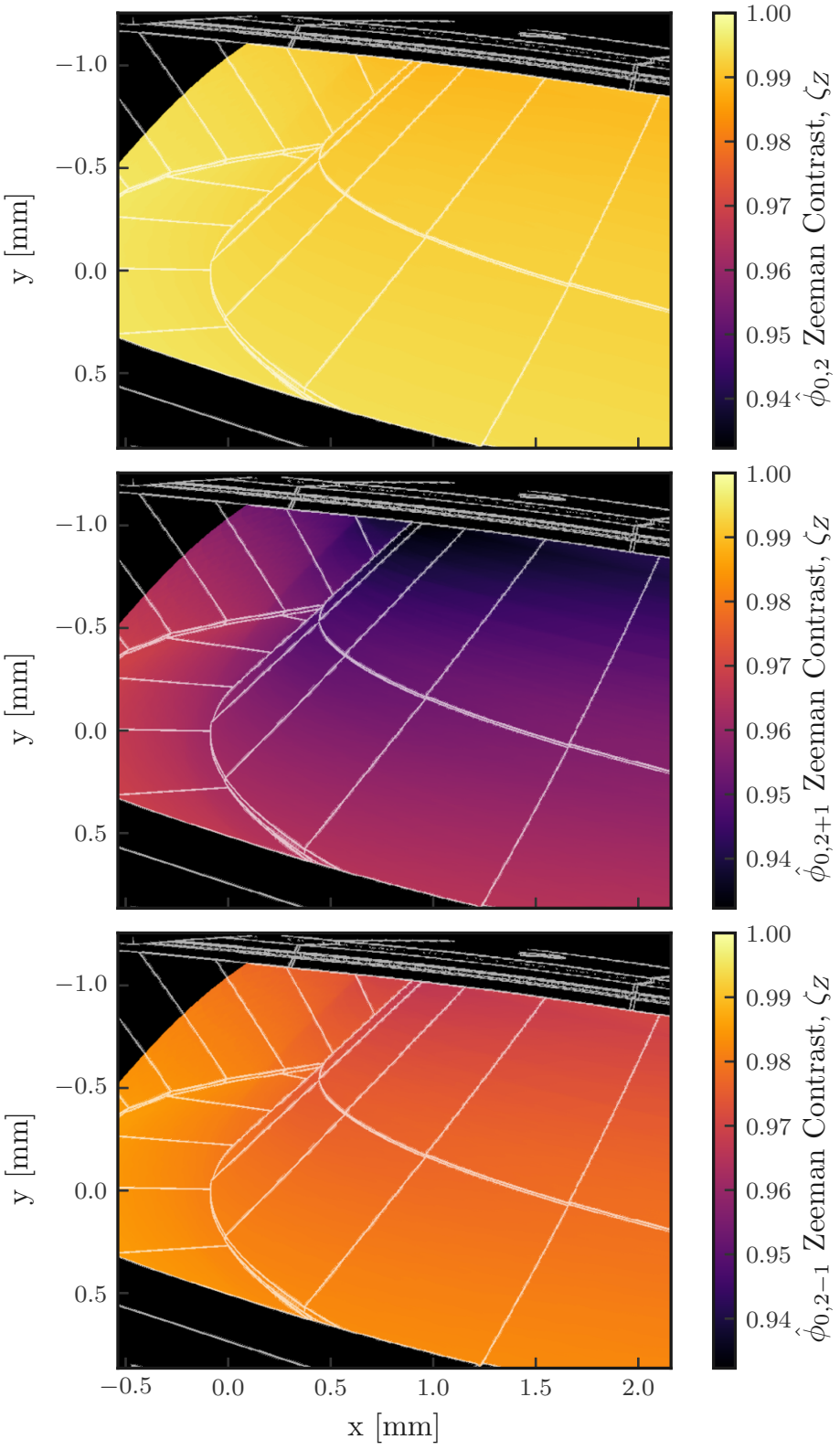

Figure 4.12: Calculated Zeeman contrast component for a typical MAST-U plasma. These images represent a worst case scenario where the magnetic geometry is Super-X and the interferometer front polariser aligns with the 2D projection of the magnetic field.

for group delays $\hat{\phi}_{0,2}$ and $\hat{\phi}_{0,2-1}$. For $\hat{\phi}_{0,2+1}$, the Zeeman contrast is negligible except for in the region close to the baffle. However, we will see in section 4.4 that the underlying intensity (DC) in this area is very low. Consulting fig. 4.4, we can see that for low DC values, the expected noise in the contrast images will be equal to or greater than the effects of Zeeman splitting. Therefore, we do not consider Zeeman splitting in the MAST-U divertor to have a significant effect on our data.

4.3.4 Performance Comparison - Single-Delay

The additional spectral information available to us by using three interferometer delays has the potential to reduce the errors in inverted profiles for contaminated spectra. To verify this we modified the synthetic Super-X divertor images used in section 4.2.2 to now represent a spectrum contaminated with O II emission of a normalised intensity of 5%, the worst case scenario assumed in during studies on MAST [30]. Line-integrated background emission of 200 counts, equivalent to $\sim 5\%$ of the total emission, was also added. This value was chosen to be higher than the expected noise in DC and thus have a significant effect on the fitting procedure. The choice of a single value also means the effect of the background emission will be more prevalent in areas of low C III emission, as expected in experiment. These images were then inverted for a triple-delay and single-delay CIS system using the maximum likelihood method presented earlier. A comparison of performance of these fits can be seen in fig. 4.13.

Comparing the triple-delay residuals shown in fig. 4.13 to those in figs. 4.5 and 4.6 we see a small increase in residuals in areas of low SNR. However, in areas close to the separatrix where velocities and temperature are higher, as seen in the top plots of fig. 4.13, we see comparable fit performance to that seen without contamination. Conversely, the use of a single interferometer delay

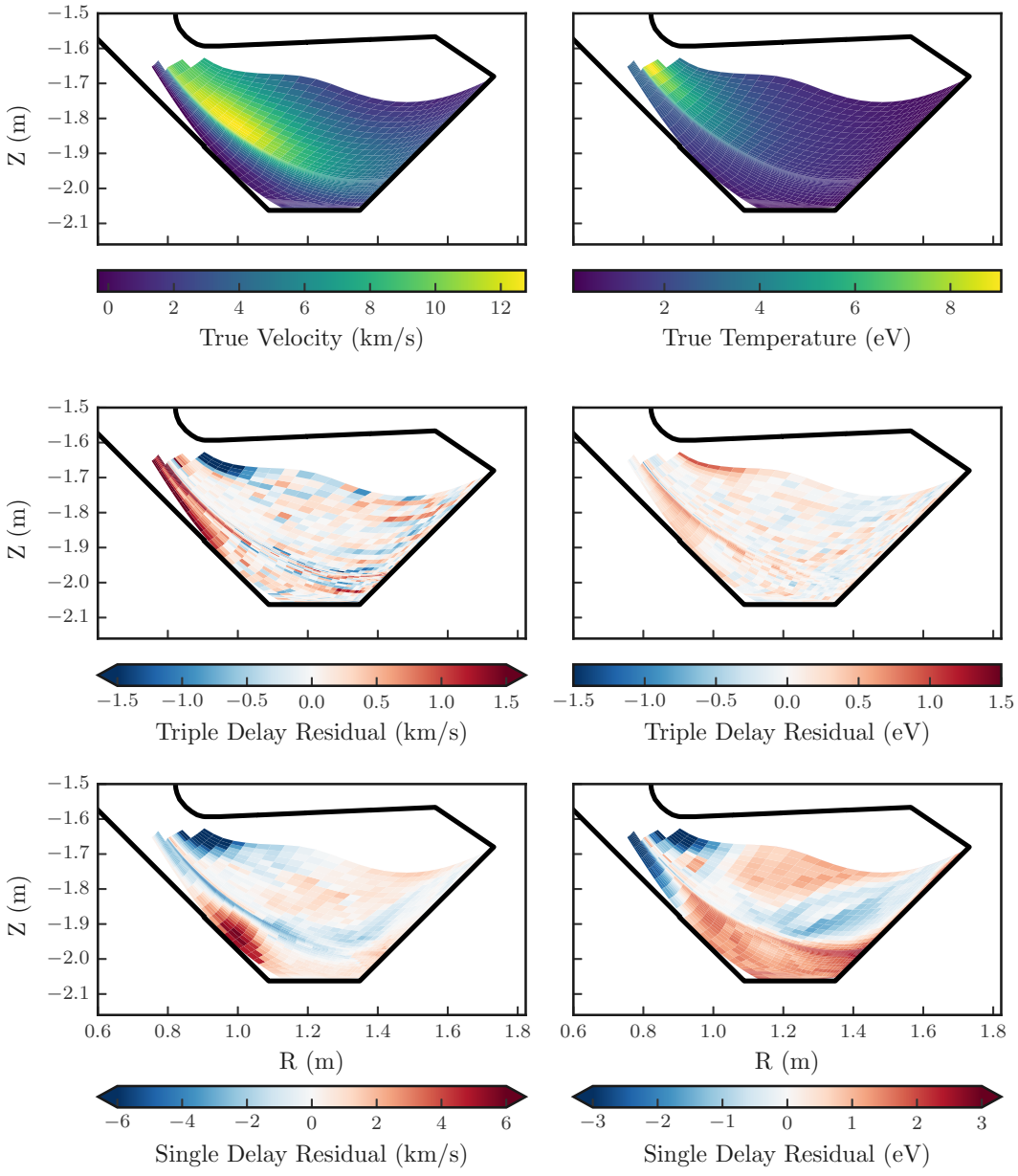

Figure 4.13: Comparison of the residuals in the inverted velocity (left) and temperature (right) profiles resulting from phase images contaminated with oxygen (O II) emission, using a triple (middle) and single (bottom) delay CIS systems. Where we see maximum residuals up to a factor of 4 higher using a single-delay interferometer.

cannot provide enough spectral information when dealing with contaminated or complex spectra to infer accurate data for physical studies. We do however note that when fitting to uncontaminated data using single-delay system we saw comparable performance to that seen using three delays. This suggests that a single-delay CIS system is sufficient to determine both $v_{\parallel}$ and T_i profiles simultaneously when observing clean spectra often present in small laboratory plasma devices.

4.4 MAST-U Experiments

After confirming the capabilities of our inversion process to produce accurate C^{2+} profiles it was time to collect data from the MAST-U divertor. As discussed in chapter 3, we installed a triple-delay coherence imaging system within the MAST-U MWI for the 3^{rd} MAST-U campaign (MU03). The view of the MWI coupled with our expectation that most plasmas during MU03 would be strongly detached, which would provide little useful data for this study, narrowed our experimental window considerably.

We identified experiment stream EXH-08 (Eurofusion WPTE RT-07) as an ideal candidate for obtaining good quality C III data. This experimental stream also included shots #46860 and #47079, the simulations of which we used for our synthetic testing, which occurred during MU02. The primary goal of EXH-08 was to study detachment with the view to creating a lower detachment front or possibly attached plasmas using higher input powers. As the ionisation region is higher up the divertor leg than the area which the MWI was positioned to study (i.e. $Z < -1.75$m), significant C III emission would only be visible to the MWI/CIS in low detachment conditions. Such conditions were present in shot #48333 (SXD) and #48334 (ED), therefore these shots will be the focus of the following work. A summary of the conditions present

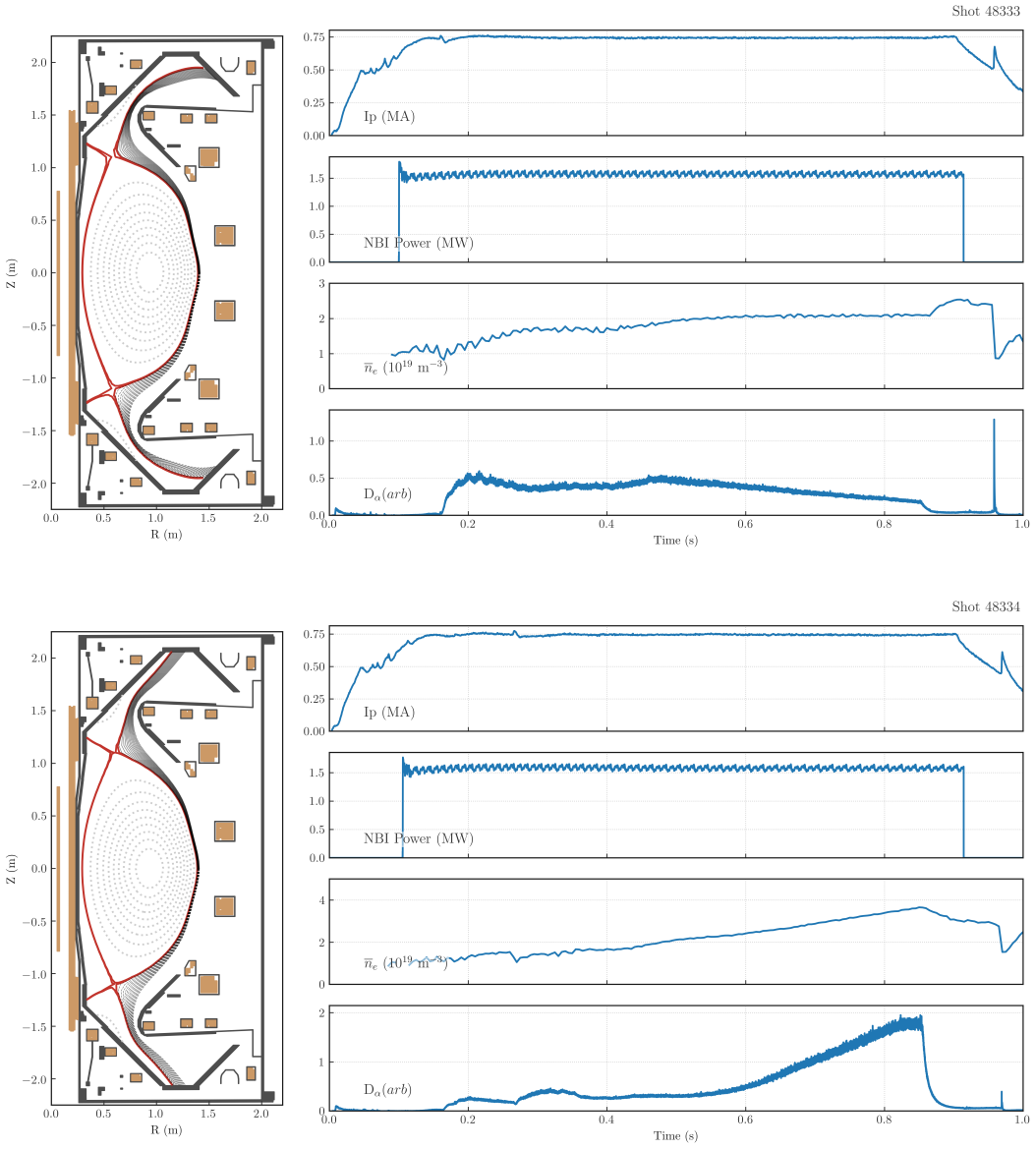

Figure 4.14: Here we plot a summary of the conditions present across MAST-U shots #48333 (top) and #48334 (bottom). On the left we show the magnetic geometries at 605 ms and 598 ms. On the right from top to bottom we show plasma current, I_p, input NBI power, line-averaged core electron density $\bar{n}_e$ and D_α emission. Examination of $\bar{n}_e$ shows that shot #48333 was a flat-top experiment and #48334 was a density ramp experiment.

during these shots is shown in fig. 4.14.

During these shots the CIS camera operated at 150 Hz with 16 dB of gain, yielding a large number of frames. These settings were determined to yield a higher exposure value during the main plasma time period ($0.5 - 0.8$ s)

but below the camera's saturation point in order to maximise signal to noise. However, as we saw in fig. 4.3, we expect the emission to decrease quickly as the camera sightlines move away from the upper baffle. Therefore, frames were ranked in order of peak measured intensity. With these conditions in mind, we found that multiple frames fulfilled our requirements and therefore an additional selection criteria would be required.

The prospect of a later qualitative comparison between the inverted profiles produced by this research and simulations, we believed, would be a powerful one. However, in the absence of direct simulations of these shots we turned to the simulations used in the previous sections. As mentioned, these simulations were conducted under the same campaign scenarios as our experimental data and therefore should produce similar plasma conditions. A common method for time slice selection when comparing simulations to diagnostic data is to choose times when the upstream conditions, namely n_e and T_e, match those used in the simulations. Figure 4.15 shows a comparison between the upstream conditions in the simulations and those measured by the midplane Thompson scattering system for shots #48333 and #48334 at our selected times of 605 ms and 598 ms, respectively, and the experimental measurements of the conditions present during the simulated shots.

We can see from fig. 4.15 that the upstream conditions in the MU03 shots compared to the MU02 ones are very similar. This is also true for simulated temperatures outside the separatrix in the SOL for both magnetic geometries. Comparing the upstream electron densities we see good agreement across the profile for the ED case but up to a factor of 2 overestimation in the SXD case. This is not a concern, but something we will return to later in section 4.4.3, as this will likely result in a greater level of detachment in the simulation of #48680 compared to our measurements of #48333.

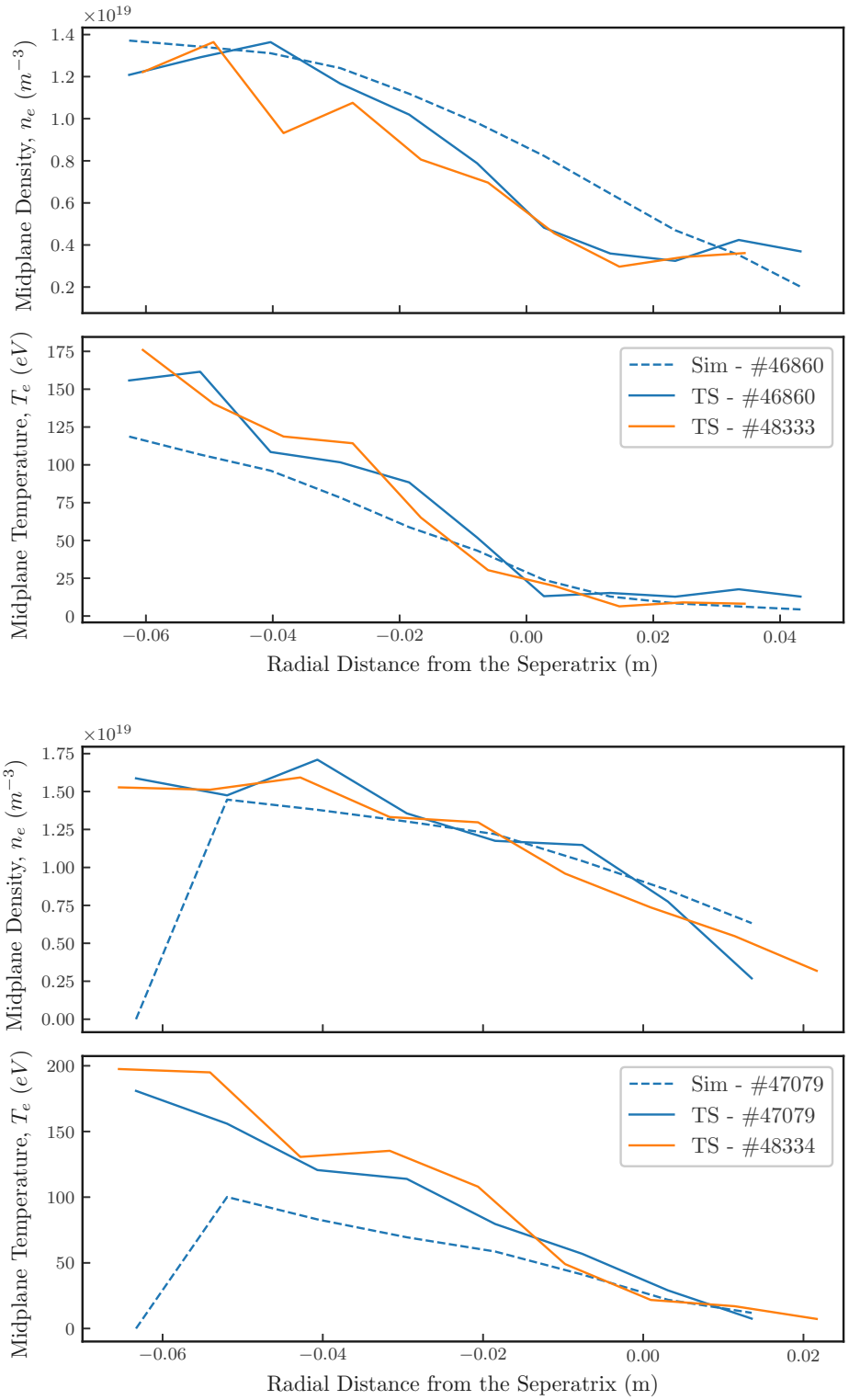

Figure 4.15: Here we compare the upstream plasma profiles for the SXD and ED shots used in this study. The first 2 graphs relate to the Super-X divertor shots (#48680 and 48333) and the bottom 2 the elongated divertor shots (#47079 and 48334). In all cases we see a good match between upstream TS profile, with the only discrepancy coming between the simulated and measured density profiles of the SXD shots.

4.4.1 Line-of-sight Integrated Data

With our frames of interest selected we turned to extracting the phase and contrast images for both shots from the raw interferograms fig. 4.16. Before demodulating, a mean dark frame, obtained from pre-shot frames, was subtracted from each image. Additionally, median filters were applied along the interference fringes for each of the pixelated-phase mask sub-images to minimise noise while maintaining spectral resolution. The interferograms were subsequently demodulated using the process described in section 3.3, resulting first in the DC images for each shot, also shown in fig. 4.16. This figure allows us to see the differences in the line-of-sight emission for a SXD and ED shot. Although these images are broadly similar, the divertor leg in the SXD case is more horizontal and thus higher in the divertor resulting in marginally less measured emission. In section 4.4.2, these images will be inverted to determine the exact position of the C III front, a powerful metric in divertor impurity studies.

As discussed in chapters 2 and 3, the resulting demodulated phase and contrast images contain both the spectral information of interest and instrumental parameters which must be calibrated out. To determine the instrumental contrast and rest frame phase, calibration images were taken inside the MAST-U hall using a cadmium lamp and a filter centred on the Cd I line at 467.8nm. Light from the Cd lamp was passed through an integrating sphere affixed to the calibration arm of the MWI in order to fully illuminate the sensor area. The sphere also created a large spread of incidence angles, replicating experimental conditions.

In order to use these calibration images, the discrepancy in temperature and wavelength must be accounted for as per section 3.4. During each MAST-U shot and the calibration process the temperature of both crystals

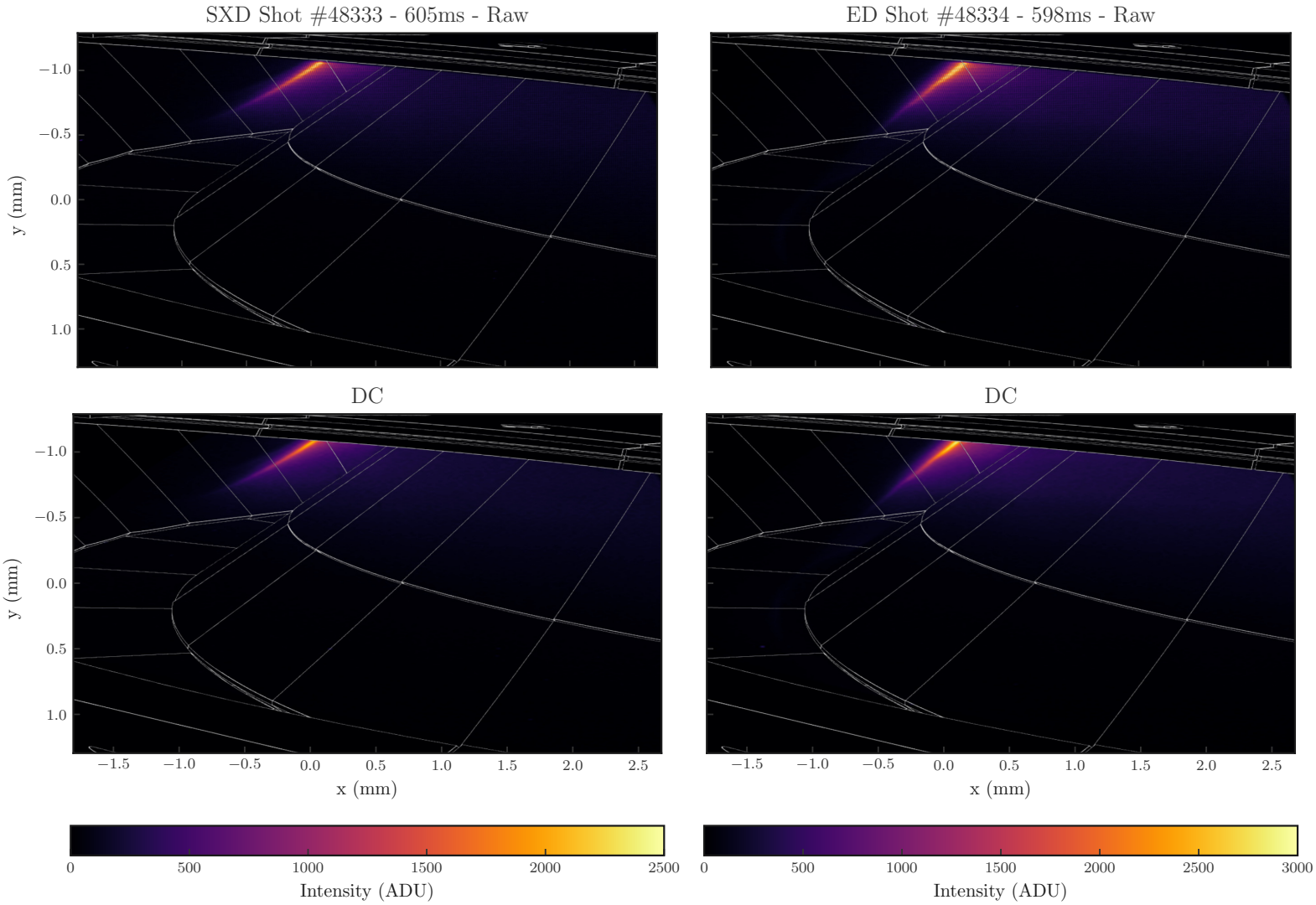

Figure 4.16: Caption on the next page.

Figure 4.16: In the top row of this figure we show the raw interferograms measured by the MAST-U CIS #48333 (left) at 605 ms and #48334 (right) at 598 ms. Below them are the recovered DC images for both frames. These, as expected, show strongly localised emission in the areas where the camera's sightlines are tangent to the magnetic field. Overlaid on these plots is a CAD mesh of the MAST-U divertor region with the inner divertor tile (T3) on the right, T4 at the bottom and in the top left of each plot in the distance we can see the outer divertor tile T5.

was measured, providing us with ΔT for each experiment. Using the calibration parameters determined in section 3.4.2 and eqs. (3.19) and (3.20), the Cd calibration images were shifted in temperature space. As our experiments are conducted using C III additional shifting in wavelength space was also required. Using the instrument parameters determined via the fitting process described in section 3.4.1, we calculated the expected phase shift between 467.8 nm and 464.9 nm (C III) and applied this shift to the temperature-shifted phase images.

As the instrumental contrast of the system is not expected to be strongly related to crystal temperature or wavelength changes, this was taken directly from the demodulated Cd images. However, in the case of our system a small correction was applied during the demodulation process, as described in section 3.4.3, to account for the wavelength dependence of the QWP. The demodulated phase and contrast images for both shots following the removal of the rest frame phase and instrumental contrast are shown in figs. 4.17 and 4.18.

Striping Artefact

On examination of the calibrated phase images for both shots we can see an unexpected diagonal low frequency striping pattern. During the course of this study attempts were made to understand the origins of this artefact which we will detail now. This pattern is also visible, but to a lesser extent, in the contrast images.

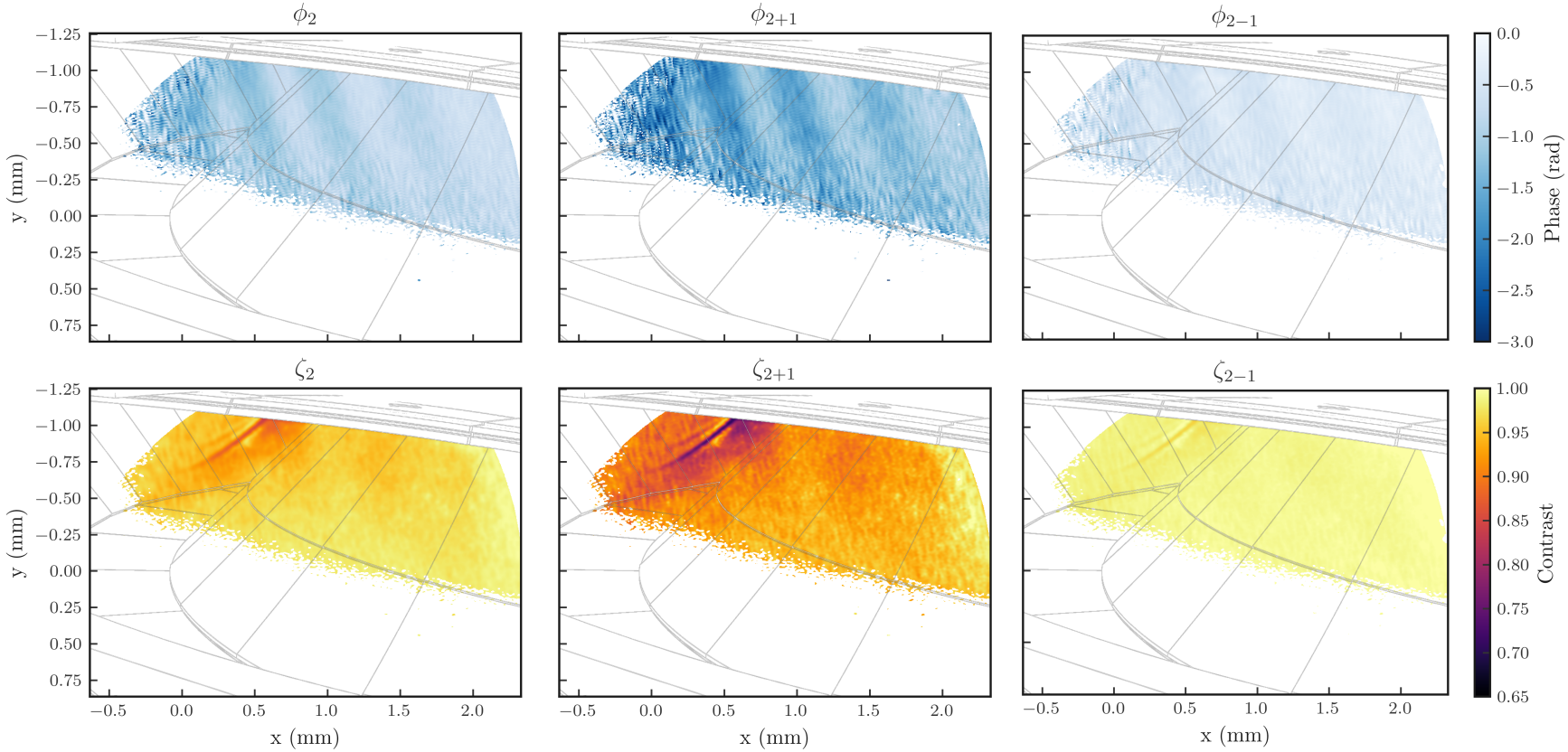

Figure 4.17: In this figure we show the demodulated phase (top row) and contrast (bottom row), for each interferometer delay, measured by our instrument at 605 ms of shot #48333. In these plots, especially the phase image for ϕ_{2+1} (tope middle), we can see a diagonal striping pattern of unknown origin which we discuss in section 4.4.1.

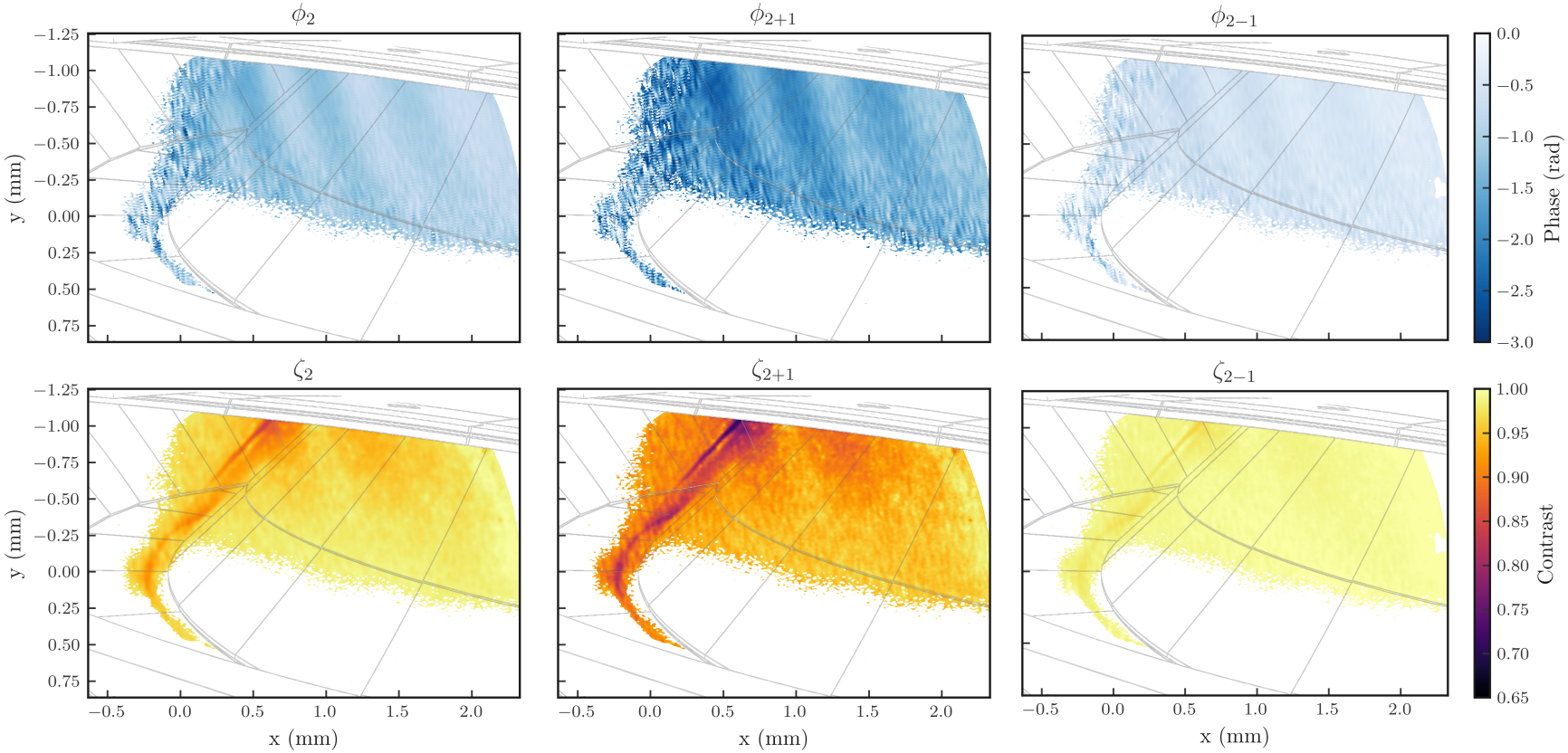

Figure 4.18: As in fig. 4.17, here we show the demodulated phase and contrast measured by our instrument at 598 ms of shot #48334. These phase images also display striping artefacts.

Initial suggestions for the pattern centred on the MAST-U MWI, and optical polychromators generally. It is feasible that stray light within the MWI may be reaching the CIS camera through or around the interferometer cell. However, this suggestion was later discounted as we would expect similar artefacts to be visible when calibrating the CIS. Suggestions that additional reflections and 2nd order effects due to the MWI mirrors and filters were also discounted on the same grounds. Additionally, testing with and without the MWI C III beamsplitter proved that it was not the cause of these artefacts either. At the time of writing this thesis initial results from MU04 show this pattern remains even though the MAST-U CIS has been moved to the first channel of the MWI and therefore is shielded from effects due to the polychromator.

Our attention then turned to the interferometer itself, with the suggestion that double reflections between the interferometer components may produce this effect. This suggestion was soon also rejected on the same grounds as before, that we would expect it in our calibration images too. Additionally, a similar pattern was not observed during extensive testing of our CIS system on an optical bench, where multiple different CIS configurations were created over the course of this study. Further evidence that the specific interferometer design and components in this work are not the source has emerged from initial MU04 results, where a single-delay CIS system has been installed within the MWI and has observed the same striping pattern.

With this we are satisfied that this artefact is at least not solely due to interactions between our CIS system and the MWI, and turned to spectral contamination as a possible cause. We do not believe this pattern is due to oxygen or continuum contamination as we did not observe it in during the course of the work in section 4.3. However to confirm this, we created synthetic interferograms with significantly larger oxygen and background intensities than

those expected on MAST-U. As expected the resulting phase images did not bear any artefact similar to figs. 4.17 and 4.18. Out of band emission was also suggested as a possible contamination source, namely IR which was not being blocked by the filter. Infrared emission of varying intensities and wavelengths above 1000 nm were tested but did not reproduce this pattern.

Lastly, our attention turned to the MAST-U divertor itself. Using Cherab, we simulated plasmas with reflections from the divertor tiles included [101]. As graphite is not highly reflective this had a minimal effect on the demodulated images and also did not produce a striping pattern.

Artefact Removal

As we were unable to determine the cause of the low-frequency pattern visible in the demodulated images of our experimental data, our focus turned to computational techniques to remove the artefact. During analysis of the pattern in time across a given shot we noticed that it appeared to be fixed in position. As expected the absolute values of the phase and contrast varied during the shot but the relative change between the maximum and minimum values in the artefact showed little variation. This suggested to us that the variation observed was due to the expected change in the Doppler phase and contrast across the shot and in fact the striping pattern remained effectively constant.

With this we identified the technique *Principle Component Analysis* as a possible way to identify the time-independent component within our phase images [102, 103]. Principal Component Analysis (PCA) is a statistical technique that transforms complex data into a set of uncorrelated variables called principal components, each representing a direction of maximum variance in the data. This technique, unfortunately, proved incapable of removing the artefacts while maintaining the underlying spectral information. We believe this is because the variation in Doppler phase and contrast in time across the shot

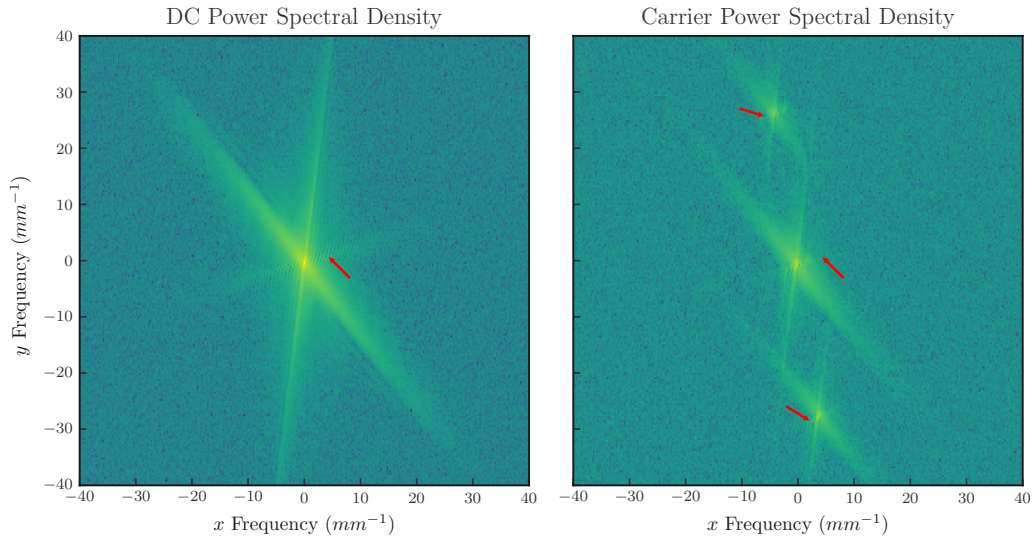

Figure 4.19: Shown in this figure is the DC (left) and carrier (right) power spectral densities for shot #48333 at 605 ms. Indicated by the red arrows are the diagonal lines, in frequency space, which correspond to the striping pattern observed in our demodulated data.

compared to noise is not large enough for the technique to separate it from the artefact. This is not surprising as one goal of the experimental scenarios used in this study was to keep the plasma as constant as possible.

We then attempted to remove the pattern directly in the spatial frequency domain. On examination of the power spectral density of each frame we were able to identify the spatial frequency components that cause the pattern, fig. 4.19. Although, in frequency space, this artefact can be seen near the DC we have found its effect to be negligible due to its relative magnitude to the central DC carrier.

With the pattern located in frequency space it was possible to mask this area during demodulation in order to remove the striping pattern. Such masking is common in Fourier domain work, however the close proximity of this to the base carrier necessitated great care be taken during the process. This combined with the fact that the artefact's oscillation direction is close to the direction of the divertor leg, means that inevitably some spatial resolution will likely be lost. Although this is an unfortunate consequence, it is necessary to

obtain meaningful spectral information from our diagnostic at this time. The resulting filtered phase images are shown in the figs. 4.20 and 4.21, where we have converted the phase to line-integrated velocity and areas of low SNR have been masked. The line-integrated temperatures shown in these figures are a conversion of the images in figs. 4.17 and 4.18, as we found that the Fourier filtering which produced the velocity images actually introduced worse artefacts in the temperature (contrast) images than the original striping pattern, which is barely visible in figs. 4.17 and 4.18.

In the next section, we invert these line-integrated images to determine the experimental $v_{\parallel}$ and T_i profiles for the MAST-U shots in question.

4.4.2 2D Poloidal Profiles

Using the inversion process we presented earlier in this chapter and the line-integrated data for shots #48333 and #48334 shown in section 4.4.1, we now present the first measurements of 2D C III temperature and parallel velocity profiles from the MAST-U divertor, figs. 4.22 and 4.23, along with the emissivity profiles for these shots as measured by our instrument. Overlaid on these plots is the magnetic geometry, calculated by EFIT++, at the relevant shot times. In red, we show the separatrix and as expected we can see the C III emission is peaked close to the separatrix and decreases as we move radially out into the SOL.

Comparing the SXD geometry shot (48333; fig. 4.22) to the ED shot (48334; fig. 4.23), we observe that the C III emission begins at a similar location in the divertor and decays along the leg as expected. However, the actual onset of C III emission likely occurs higher up the divertor leg. Due to limited sightline coverage in this region, as discussed in section 4.2.2, we were unable to meaningfully resolve the emissivity there—an issue also seen in other studies using the MAST-U MWI [92].

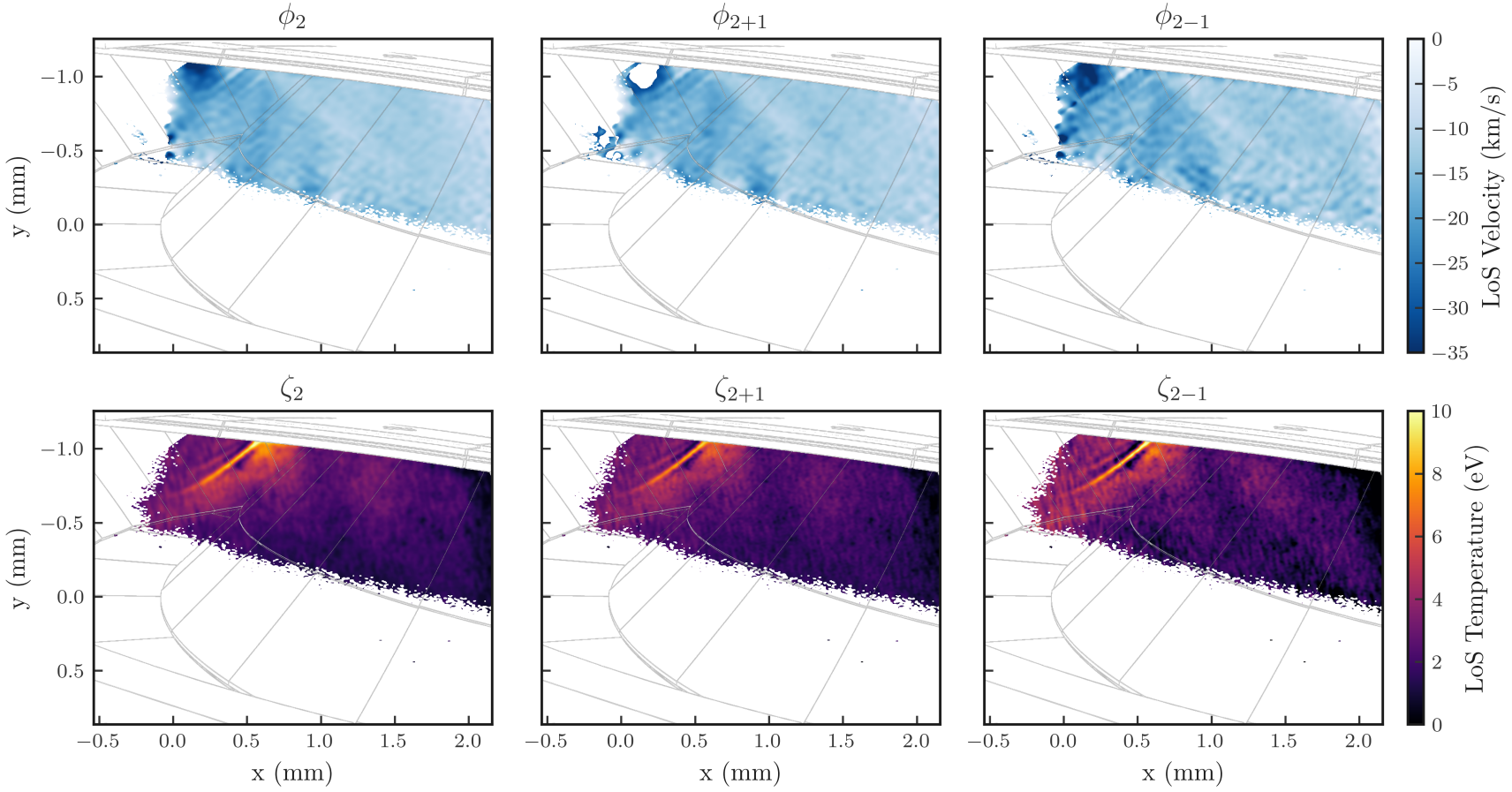

Figure 4.20: Shown are the line-integrated velocity (top) measurements following additional Fourier domain filtering of shot #48333 and a conversion from phase to velocity. The temperature (bottom) images shown are a conversion of the contrast images shown in fig. 4.17 as the striping artefacts are less prevalent. Areas of low SNR have also been masked off here.

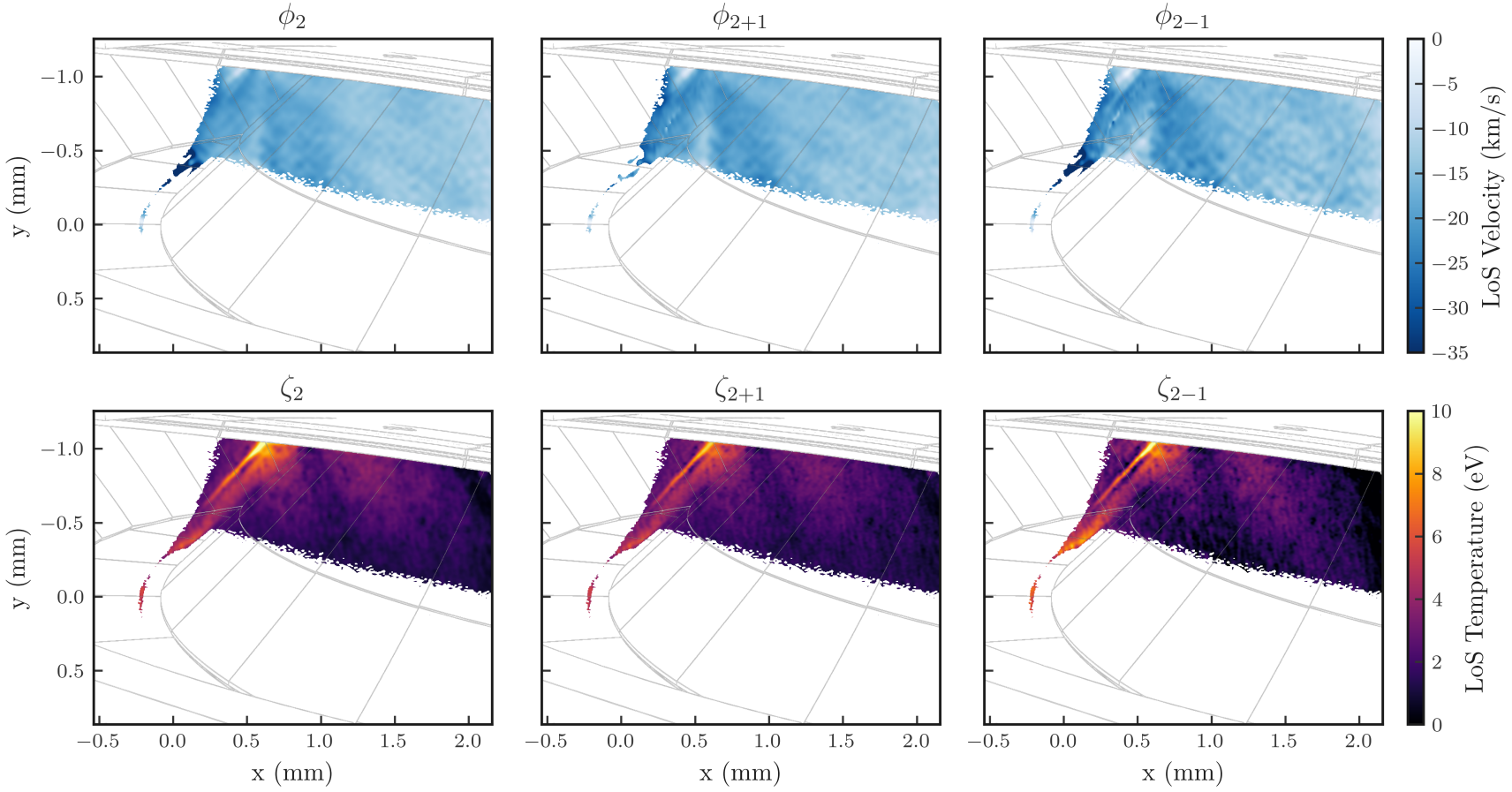

Figure 4.21: As in fig. 4.21, this plot shows the line-integrated velocity (top) measurements following additional Fourier domain filtering of shot #48334, however the temperature (bottom) images are a direct conversion of the contrast images shown in fig. 4.18. Areas of low SNR have also been masked off here.

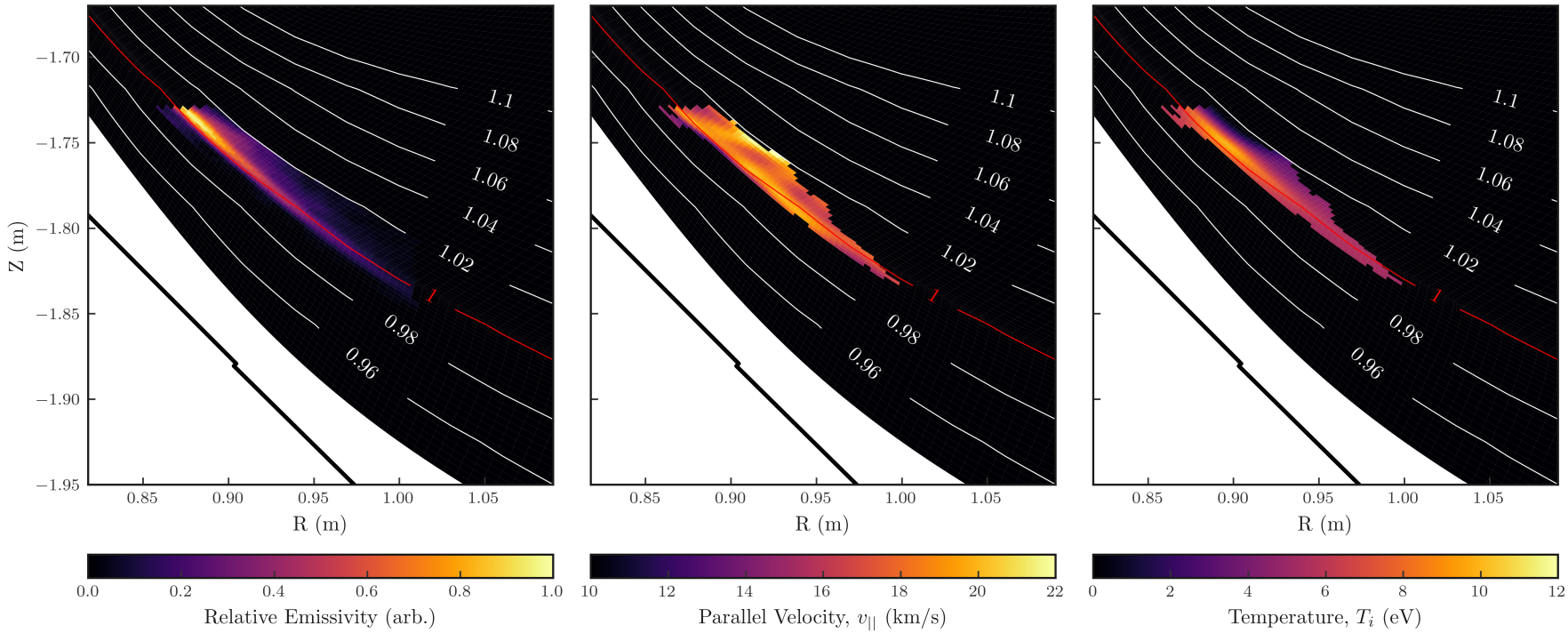

Figure 4.22: Going from left to right here we show the 2D inverted profiles of C III emissivity, parallel velocity and ion temperature measured by the MAST-U CIS at 605 ms of Super-X shot #48333. As before left most boundary is the inner MAST-U divertor tiles with the distance from the centre column increasing along the x-axis. Overlaid on these plots are magnetic flux surfaces at various values of normalised poloidal flux (ψ_N) calculated by EFIT++, with the separatrix shown in red.

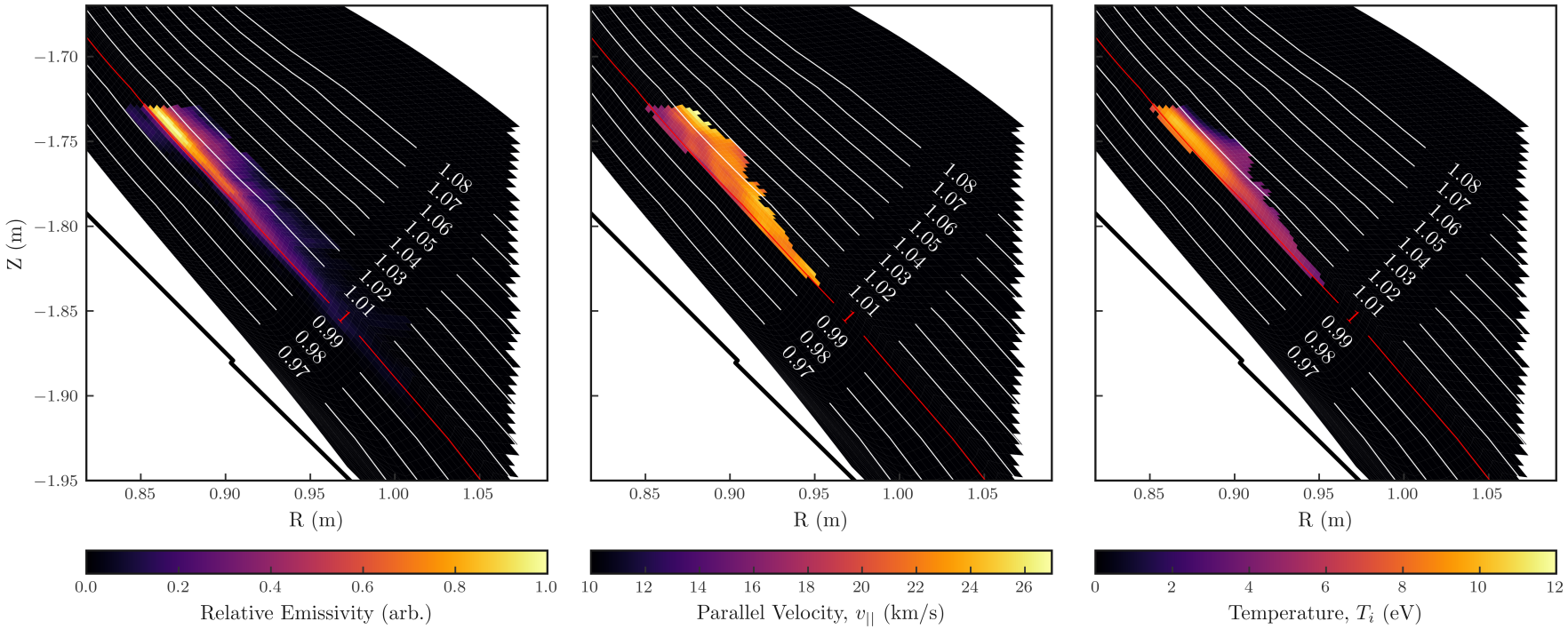

Figure 4.23: Similarly to fig. 4.22, here we show the 2D profiles of emissivity, parallel velocity and ion temperature obtained from CIS data taken at 598 ms of elongated divertor shot #48334. The magnetic geometry and separatrix are also shown.

To verify the accuracy of these inversions we consulted the MAST-U Divertor Monitoring Spectrometer (DMS) which during some of MU03 collected data at the C III wavelength range for comparison with this research [36]. The DMS measures data along 30 sightlines in the lower divertor and 10 at the outboard midplane. From these we identified 4 sightlines that would pass through the C III emission region shown in figs. 4.22 and 4.23. Using the line-of-sight vectors for these and our inverted profiles we calculated the spectrum that each DMS sightline would measure if it viewed the plasma from the MWI port (HL-06). These are shown along with the actual spectra measured by the DMS from HL-02 in figs. 4.24 and 4.25.

We note that no C III data was obtained by the DMS during shot #48333 so the spectra used in fig. 4.24 was obtained from shot #48330. We do not expect any significant difference between these shots as #48333 was a direct repeat of #48330. The CIS data was taken from #48333 as it possessed a higher SNR than obtained during #48330.

Examining figs. 4.24 and 4.25, we observe that the calculated spectra are significantly shifted from the rest frame, consistent with the Doppler shifts expected from light emitted by a moving source. Comparing this to the spectral shifts measured by the DMS, we find excellent agreement for sightlines 26 and 25 in both shots, as well as for sightlines 24 and 23 in fig. 4.25. Minor discrepancies can likely be attributed to a combination of the DMS's resolution and the accuracy of its wavelength calibration. A more noticeable discrepancy is observed for sightlines 23 and 24 in fig. 4.24, where low signal-to-noise is likely the primary source of error in the CIS measurement, while the resolution of the DMS also contributes to the discrepancy. Additionally, the DMS spectrum for sightline 23 clearly shows significantly lower C III emission compared to the background, as confirmed by the emissivity profiles in figs. 4.22 and 4.23.

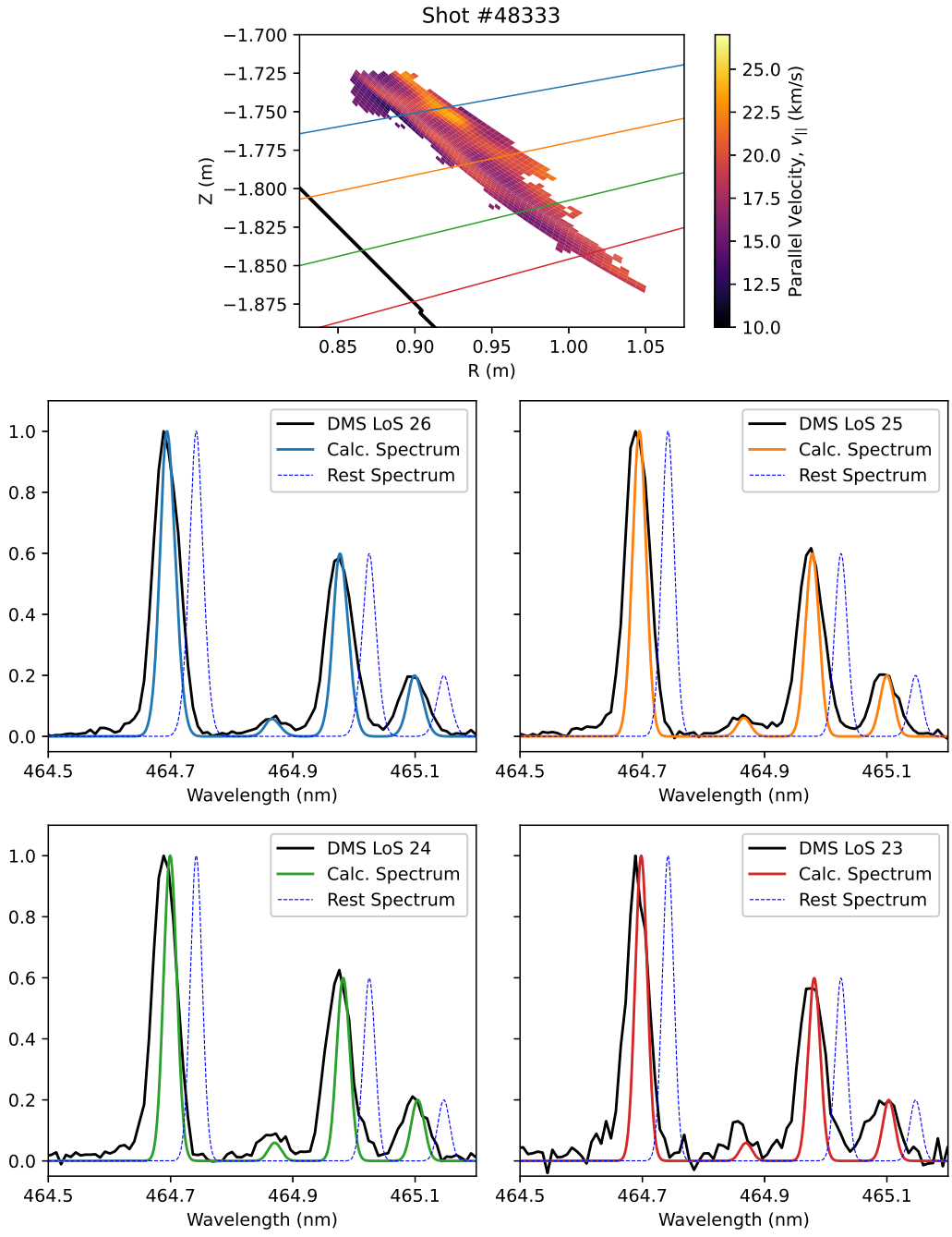

Figure 4.24: At the top of this figure we show the inverted parallel velocity profile from our study along with a 2D projection of the four DMS sightlines that pass through this area of the divertor. The subsequent 4 plots show a comparison of the measured DMS spectrum (black) from each of these sightlines and the calculated spectra using the 2D profiles shown in fig. 4.22 and the coloured sightline in the top plot. For reference the rest frame C III spectrum is also shown in each plot.

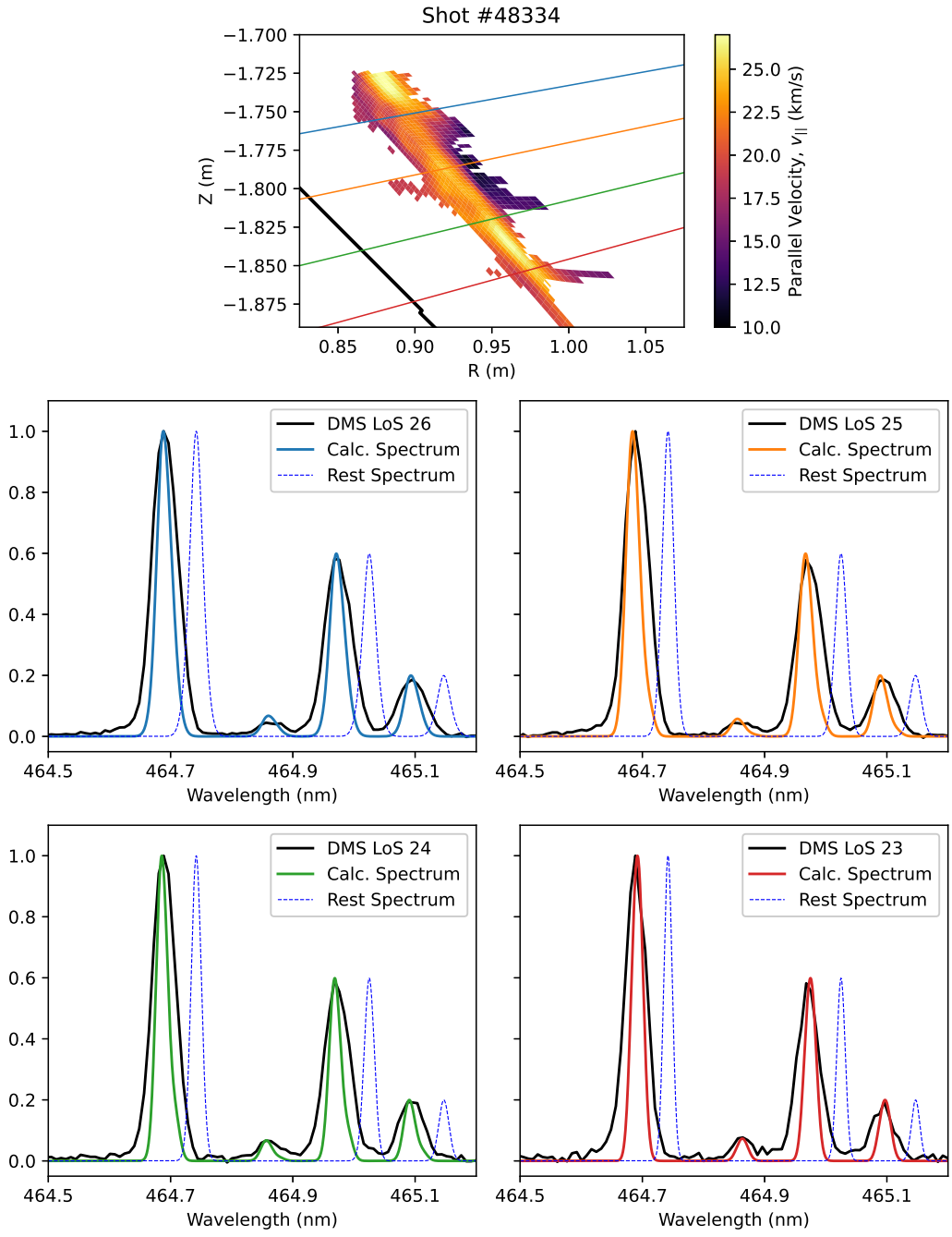

Figure 4.25: As in fig. 4.24, here we show the measured DMS C III spectra (black), corresponding to each DMS sightline (coloured lines) shown in the top plot of the inverted parallel velocity profile of shot #48334, to the calculated spectra using these sightlines and the 2D profiles found in fig. 4.23.

In addition to confirming the ability of our instrument to measure flow velocities, figs. 4.24 and 4.25 also show that our inversion process, combined with the additional spectral information from our triple-delay CIS system, can account for oxygen contamination intensity to very good accuracy. A key factor in producing accurate profiles.

Although the temperature data presented in figs. 4.22 and 4.23 is encoded within the spectra shown, a comparison of the Doppler broadening was not possible due to the unavailability of the spectrometer's instrument function for this research. We believe that the instrumental broadening of the DMS is significant, as temperatures in the range of 20–30 eV would be required to produce the spectra shown in figs. 4.24 and 4.25. These temperatures are comparable to those observed at the outboard midplane (fig. 4.15) and are therefore much higher than expected in the divertor. At such temperatures, we would also expect $C^{,4+}$ to be the dominant ion species rather than $C^{,2+}$. This comparison should be a focus of future MAST-U CIS studies and will be discussed in greater detail in section 5.4.

4.4.3 Comparison with Simulations

Returning to the simulations used for testing our inversion process in section 4.2.2, we now compare the conditions found in those simulations to those during shots #48333 and #48334 with a view to informing future impurity transport studies. In order to do this we must first compare the C III emission structure in each scenario and define a spatial location about which to conduct our velocity and temperature comparisons.

Comparison of C III Front Location

In detachment studies it is common to define different *fronts*. These fronts refer to a plane, typically perpendicular to the magnetic geometry, beyond which the

plasma conditions are dominated by a different species or physical phenomena to before the front [36]. For example, the detachment front typically defines the poloidal location along the divertor leg where neutral gas density begins to increase quickly. Previous work on the TCV tokamak in Lausanne has used the C III emission front to track detachment conditions, as this front will move further away from the target as the degree of detachment increases [104]. In this study, and other work, the location of the C III emission front is defined as the location where the emission is 50% of the peak C III emission.

The C III front position for the simulations can be easily obtained from SOLPS-ITER as the entire scrape-off layer emissivity profile is available. In the case of both the ED and SXD simulations, peak C III emission is located near the upper divertor baffle with the front high in the divertor, therefore the simulation represents a highly detached plasma.

To determine the front position in experiment we must also find the peak emission location however this is likely located above $Z = -1.73$ m and therefore outside the effective viewing range of our instrument, as seen in figs. 4.22 and 4.23. We instead have approximated the C III front position from using an earlier frame in each shot. In general, MAST-U shots typically reach stability following ramp-up and initial fuelling between 400-600 ms, fig. 4.14, after which time the experiment goals, such as a density ramp, would be executed. We have seen from our data that at this point the plasma is in its least detached state, and therefore more of the C III profile is visible allowing for a better estimate of the front location. After this time the C III front will move up the divertor leg if the plasma becomes more detached.

By determining the emissivity value at the C III front we can locate this point on subsequent frames. This is only possible because our camera settings do not change frame to frame during a shot. Locating the front in this way is important for *density ramp* shots (#48334) where the midplane density

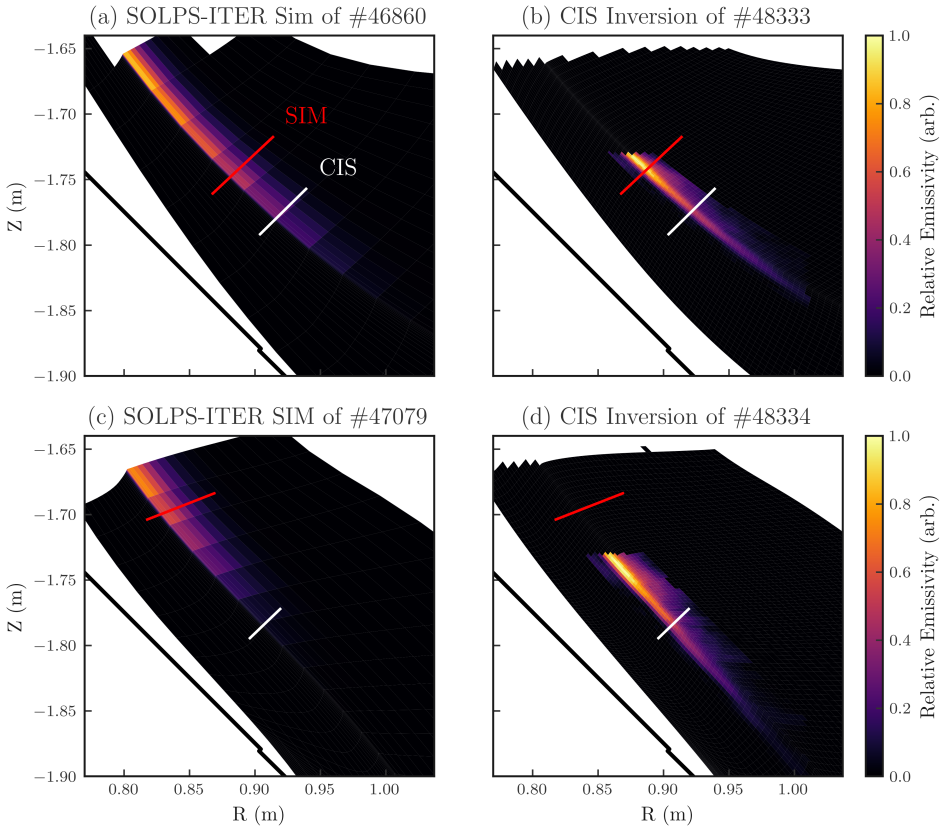

Figure 4.26: Here we compare the C III emission profiles calculated by SOLPS-ITER for (a) shot #46860 at 450 ms and (c) shot #47079 at 540 ms, to the measured emission profiles from our instrument viewing the divertor plasma of shot (b) #48333 and (d) #48334 at 605 and 598 ms, respectively. We also show the C III fronts for the simulations (red) and CIS measurements (white) as calculated by the 50% emission method described in this section.

increases over time thus inducing greater detachment. Whereas in the case of *flat-top* experiments (#48333), the density is kept approximately constant (fig. 4.14) thus we observe very little movement of the C III profile. A comparison of the emissivity profiles of each shot and simulation are shown again in fig. 4.26 along with the positions of the C III front in each case. The experimental front positions were determined using CIS data taken at 406 ms for shot #48333 and 557 ms for #48334.

We can see from fig. 4.26 that, in both divertor configurations, significantly less detached conditions were present during our experimental shots compared to those predicted by SOLPS-ITER. For the SXD case, figs. 4.28a and 4.28b,

the difference in the front position can be explained by the discrepancy in the upstream density seen in fig. 4.15. The higher electron densities shown here in the simulation will result in higher upstream pressures and therefore likely a greater degree of detachment. However, this can not be said for the ED case where the difference in upstream density is minimal but we see a much larger difference in front location, figs. 4.28c and 4.28d. We do not believe that the method used for determining the experimental front position would lead to such a large discrepancy, however confirming this would require C III emission data higher in the divertor not available to us. We therefore leave this to a future detachment study, section 5.4.

Comparison of Velocity and Temperature Profiles

Using the fronts shown in fig. 4.26 as a reference, it is useful to compare the behaviour of C III velocities and temperatures around these points to those predicted by SOLPS-ITER.

From fig. 4.27, we observe that velocities in the simulations (10-13 km/s) are up to 50% lower than those measured by the CIS (15-26 km/s). Based on the comparison of our measurements to spectrometry earlier in this section, we are confident in the accuracy of our measured velocity profiles. This suggests that the simulations significantly underestimate the C III velocity. However, it is possible that the increased level of detachment in the simulations affects the overall magnitude of the predicted velocities. This explanation is consistent with the larger discrepancies observed in the Super-X divertor profiles (4.27a and c), where we also observe a greater difference between the C III front positions of these plasmas (fig. 4.26).

A closer examination of the velocities around the C III front (figs. 4.28 and 4.29), just outside the separatrix, reveals qualitative agreement in velocity behaviour before and after the front position in most cases. All profiles—except

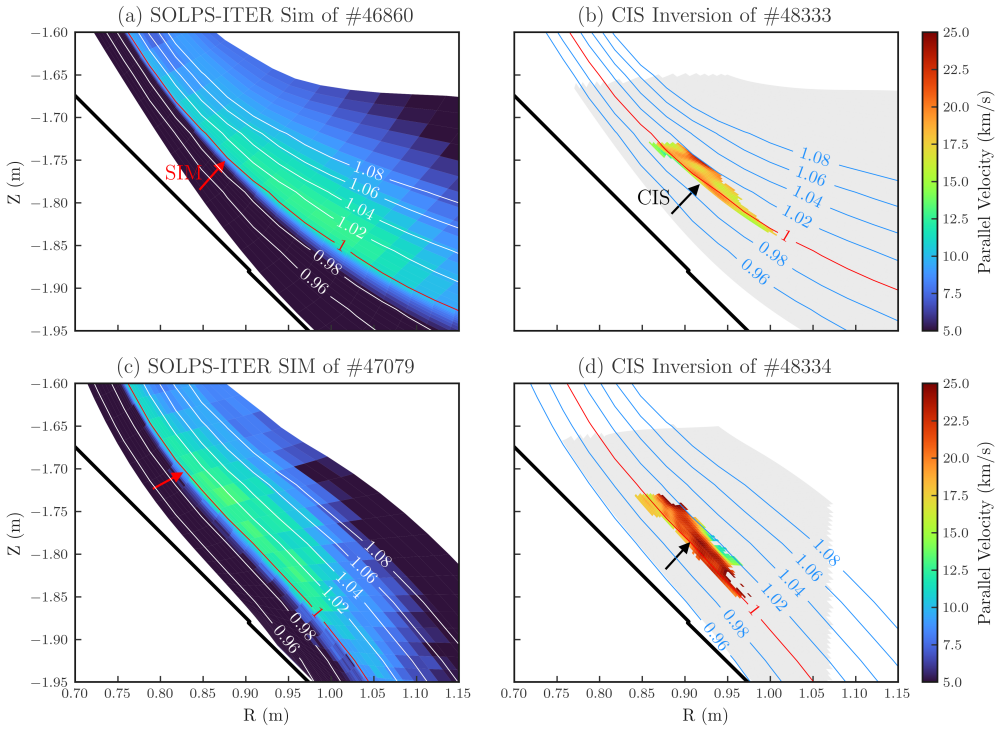

Figure 4.27: In this figure we compare the velocity profiles produced by the SOLPS-ITER simulations of shots (a) #46860 and (c) #47079 to the inverted CIS profiles measured at (b) 598 ms of shot #48333 and (d) 605 ms of shot #48334. The arrows here indicate the C III fronts for each plasma and overlaid is the magnetic geometry with the separatrix indicated in red.

for the SXD simulation—show an increase in velocity up to the region near the front, followed by a decrease thereafter. In fig. 4.28, the simulation of the SXD shot 48680 shows a peak velocity of 11.6 km/s at 0.13 m from the front position. To compare this to the 1D profile derived from our inversion, we fit a quadratic function to the data. This approach highlights the trend of the profile in 1D, analysis of which may otherwise be skewed by localised regions, such as the sudden drop in velocity before the front in fig. 4.28 and after the front in fig. 4.29, likely caused by residual striping artefacts discussed earlier. From this fit, we find a peak velocity of approximately 19.1 km/s at the front, which is significantly different from the value predicted by SOLPS-ITER.

Conversely, an examination of the elongated divertor shots shows much closer agreement in ion behaviour, fig. 4.29. While there remains a signific-

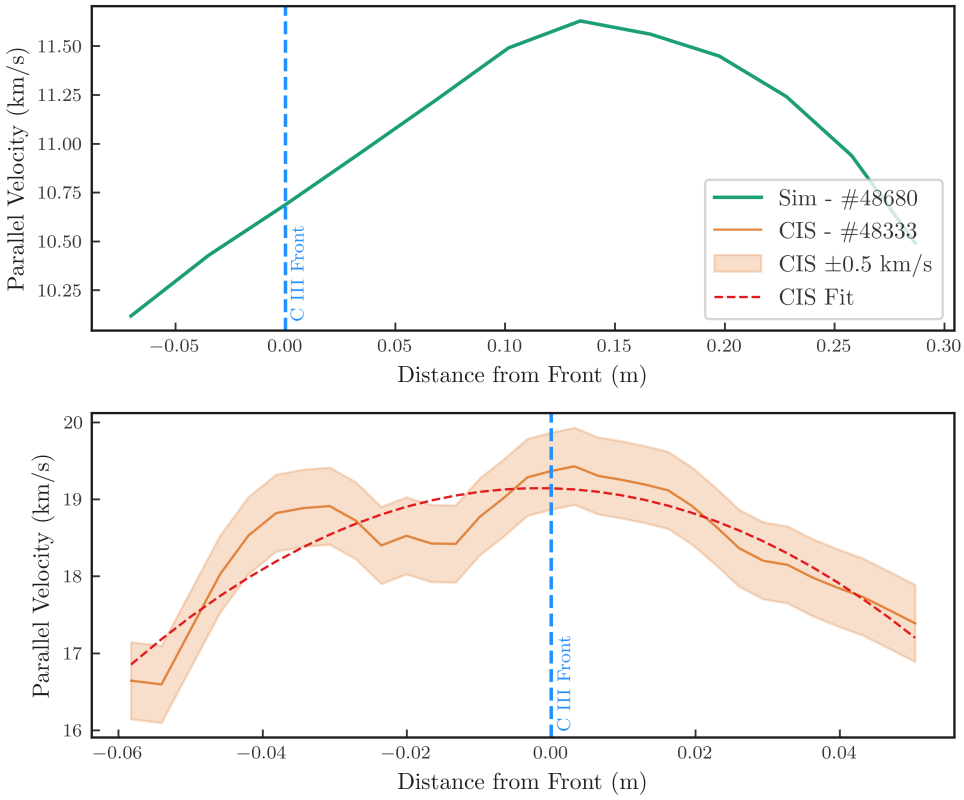

Figure 4.28: Here we compare 1D slices of the velocity profiles produced by the SOLPS-ITER simulation of #48680 (top) to the inverted velocities measured by our instrument at 605 ms of shot #48333 (middle). These plots are given as functions of distance from the C III front for the purposes of comparison, with the x-axis on the top plot extended to show the peak velocity location in the simulations. For reference an error of 0.5 km/s has been added to the CIS data in line with residuals seen earlier in this chapter. A quadratic fit of the CIS data is also shown (red) to indicate the peak velocity location.

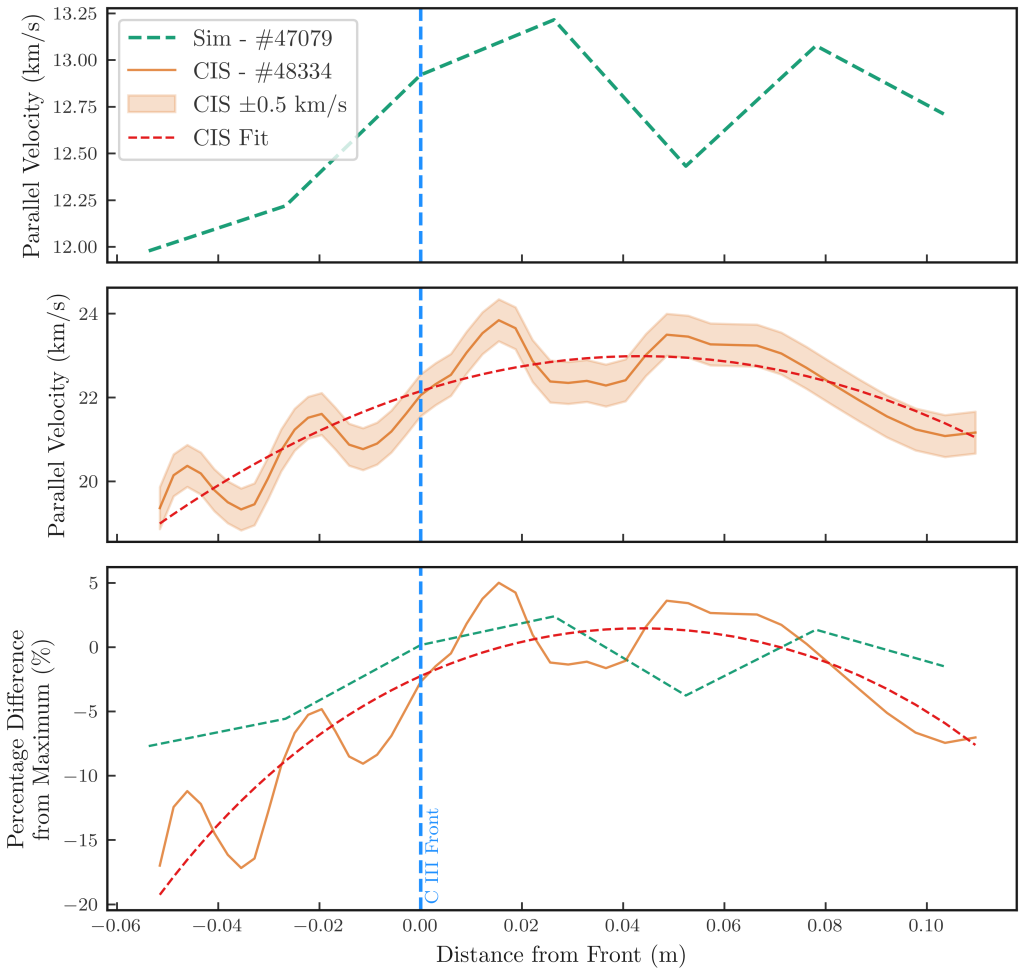

Figure 4.29: Similarly to fig. 4.28, in this figure we compare a 1D slice of the velocity profiles produced by the SOLPS-ITER simulation of #47079 (top) to the inverted velocities measured by our instrument at 598 ms of shot #48334 (middle). All plots in this case share the same x-axis. Error of 0.5 km/s has also been added to the CIS data and a quadratic fit of the CIS data shown in red. The bottom plot shows the percentage difference in velocity relative to the maximum of each profile.

ant difference in the magnitude of the peak velocities—with SOLPS-ITER predicting 13.2 km/s and a fit to our measurements showing 23.2 km/s—the difference in their locations is relatively small: 0.03 m from the front for the simulation compared to 0.04 m for our measurements. Comparing how each profile changes as a percentage of its maximum, we see that our measurements indicate up to a factor of 2 stronger acceleration towards the front. Beyond the front the behaviour is broadly similar in both profiles with the experimental data indicating that the velocity drops off sooner than the simulation would suggest.

We observe similar behaviour in the measured velocity relative to the C III front in fig. 4.28. However, a comparison to simulations in this case is less meaningful due to the large discrepancy in the peak velocity location. Together, these results suggest that SOLPS-ITER is capable of predicting the behaviour of C^{2+} ions around the C III front. However, for these predictions to be trusted, SOLPS-ITER must first accurately predict the emission front location, as this appears to significantly influence the predicted velocity profiles.

Further study of this region and the dynamics at play would benefit from an increase in the spatial resolution in the parallel direction on both the simulations to bring it in line with our CIS measurements.

Turning to a comparison of the temperature profiles measured and predicted, shown in fig. 4.30, the results are clearer. The temperatures decrease steadily from approximately of 9 eV to as low as 4.5 eV, as expected due to the cooling effect of the divertor. This range aligns well with the temperatures at which C III is the most abundant carbon species, as calculated from atomic data [30].

A closer examination of the profiles along the leg at the separatrix (fig. 4.31) reveals that in both cases, our measurements match the simulations well in

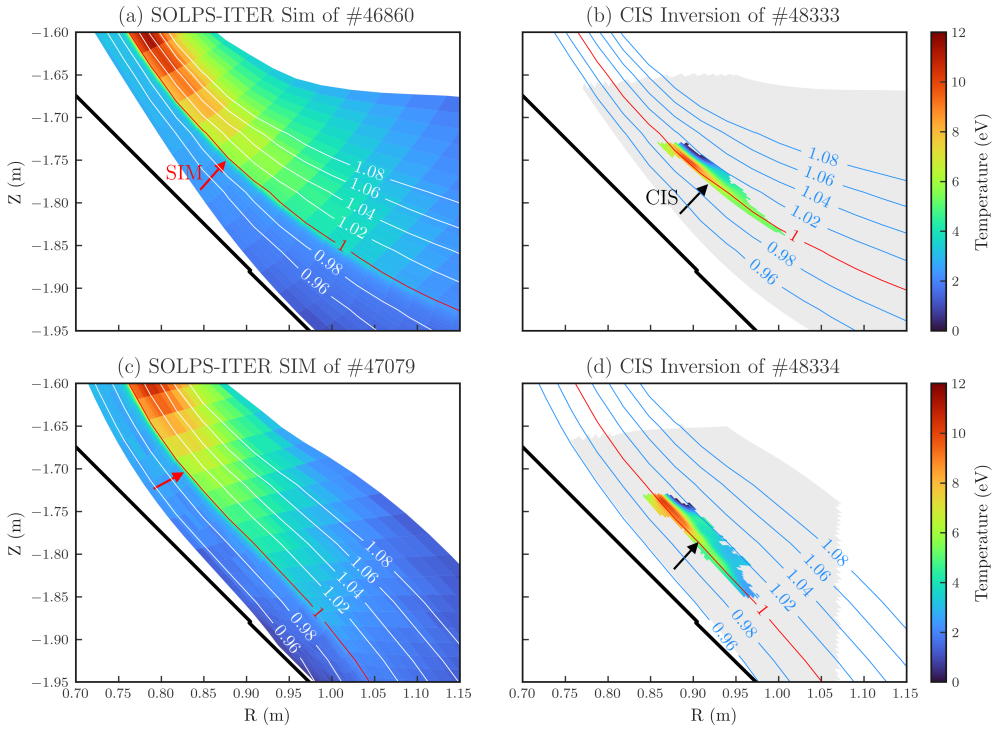

Figure 4.30: Similar to fig. 4.27, here we show a comparison between the temperature profiles produced by the SOLPS-ITER simulations of shots (a) #46860 and (c) #47079 to the inverted CIS profiles measured at (b) 605 ms of shot #48333 and (d) 598 ms of shot #48334. The magnetic geometries including separatrix in red and C III fronts are also indicated.

the region following the C III front. However, before the front, we measure temperatures up to 2 eV higher than those predicted by the simulations. We note that the temperature increase before the front in the SXD measured profile and after it in the ED case aligns with the decreases in velocity observed in figs. 4.28 and 4.29. Therefore, we believe these increases are also due to the striping artefacts. That being said, we have confidence in the overall trend of the measurements across the profile and attribute the small discrepancies with the simulations to the accuracy of the experimental magnetic reconstructions performed by EFIT++.

Despite this, the profiles indicate that SOLPS-ITER is capable of predicting the temperature of C^{2+} ions around the C III front with good accuracy. This result is unsurprising, as density and temperature are often used as input

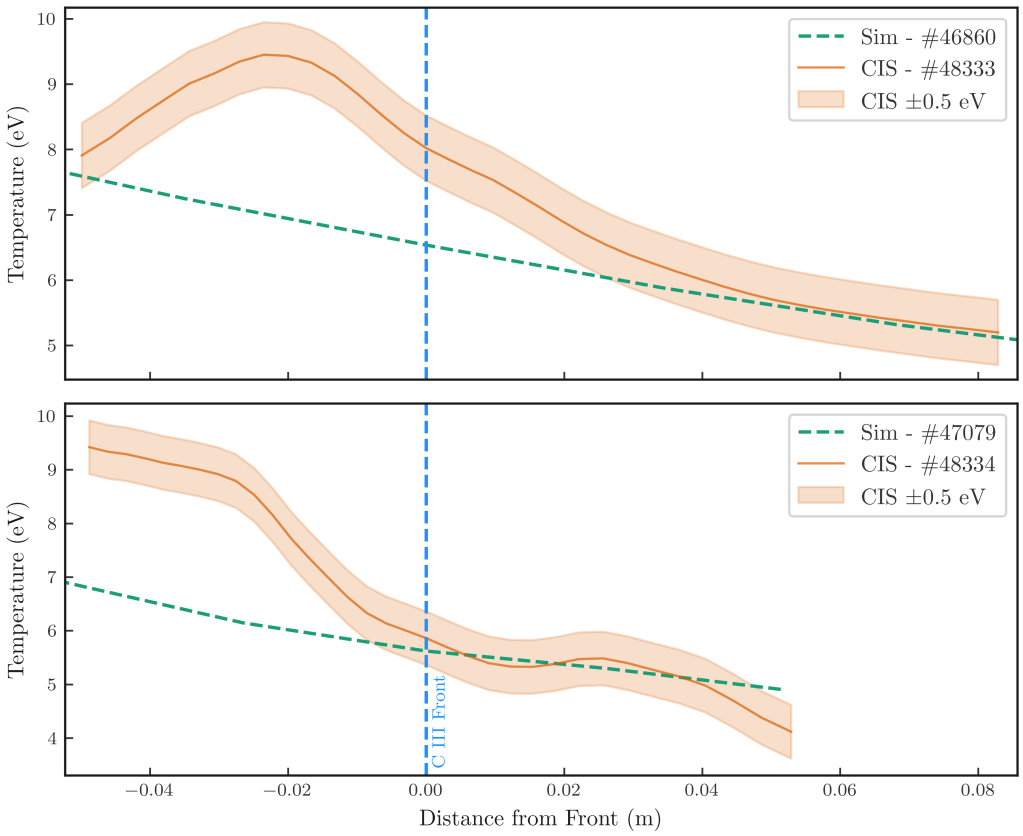

Figure 4.31: Here we compare a 1D slice of the temperature profiles produced by the SOLPS-ITER simulations of #46860 (top) and #47079 (bottom) to the inverted temperatures measured by our instrument at 598 ms of shot #48333 (top) and 605 ms of shot #48334 (bottom), as functions of distance from the C III front. Errors of ±0.5 eV have been added to our data in line with the fit residuals from our testing earlier in this chapter.

conditions in SOLPS-ITER simulations, and one would therefore expect good agreement in these parameters. With this in mind, it appears that the models SOLPS-ITER uses for ion transport require further examination. Based on our results, SOLPS-ITER cannot accurately predict the magnitude of ion velocities.

Finally, upon further examination of the experimental emissivity profiles in fig. 4.26, we observe that the perpendicular emissivity profile is significantly more peaked near the separatrix compared to the simulations. This behaviour is also reflected in the temperature profiles (fig. 4.30), suggesting that cross-field transport plays a much larger role in the simulations than in experiment.

We propose this as a potential cause for the substantial difference in parallel velocity. A combination of particle balance and energy conservation across the field could result in lower velocities in the simulations if the temperatures are higher.

4.5 Summary

In this chapter, we presented a novel analysis technique for coherence imaging spectroscopy (CIS) data, enabled by the use of the triple-delay instrument described in chapter 3. Unlike traditional single-delay approaches, this method facilitated the first simultaneous measurement of two critical plasma parameters on MAST-U: ion parallel velocities and temperatures. This dual capability represents a significant enhancement in diagnostic data availability, as no other instrument on MAST-U is currently capable of producing these profiles.

This analysis employed a maximum likelihood estimation fitting method, relating the degree of coherence of the measured CIS spectra—calculated using the demodulated phase and contrast images—to 2D poloidal projections of C III emissivity, velocity, and temperature. The fitting algorithm, L-BFGS-B, was selected for its capability to handle non-linear problems and accept bounds on the resultant data. We provided the equations for this method along with analytical expressions for the gradient in velocity and temperature.

Focusing on the C III triplet centred at a wavelength of 464.9 nm, we addressed the inherent challenges posed by spectral asymmetries resulting from the statistical distribution of the triplet's emission peak intensities. Additionally, we investigated the impact of spectral contamination on CIS measurements, particularly from oxygen and continuum emission, and introduced modified fitting equations to account for these effects. We also demonstrated that accounting for contamination would not have been possible without the

additional spectral information provided by the multiple interferometer delays produced by our instrument.

Striping artefacts observed in the measured CIS data were identified and removed using additional frequency-domain filtering. While the source of these artefacts remains unknown, we presented the results of our investigation to inform future studies.

The accuracy of our 2D profiles was evaluated by comparing the velocities to the C III spectra measured by the MAST-U divertor monitoring spectrometer (DMS), with which we found excellent agreement in regions of high signal-to-noise. Comparisons of temperature profiles to the DMS data were not possible, as we were unable to estimate the instrumental broadening of the system. Additionally, we compared our results with simulations, demonstrating good agreement between SOLPS-ITER and our data in the behaviour of C III around the emission front. However, we observed discrepancies in the magnitude of the velocity profiles, with simulations predicting lower velocities.

The profiles presented in this chapter represent the first experimental demonstration of the capability of a single CIS instrument to determine the velocity and temperature of an ion from a contaminated multiplet spectrum.

Chapter 5

Summary and Future Work

The research presented in this thesis represents significant advancements in the development and application of coherence imaging spectroscopy (CIS) as a plasma diagnostic. Through modifications to the MAST-U Multi-Wavelength Imaging (MWI) system and the development of robust calibration methods, we have enabled the deployment of a triple-delay pixelated CIS system on MAST-U. Furthermore, the novel analysis methodology facilitated by this triple-delay system has allowed for the simultaneous measurement of 2D C^{2+} parallel velocity and temperature profiles under conditions of spectral contamination, for the first time on MAST-U. These achievements not only enhance the diagnostic capabilities of CIS systems but also lay the groundwork for future innovations in tokamak plasma studies.

5.1 Triple-Delay Coherence Imaging

In chapter 3, we presented a coherence imaging spectroscopy (CIS) system comprising four key components: a linear polariser, displacer plate, waveplate, and quarter-waveplate, along with a FLIR Blackfly S camera equipped with a pixelated polariser array bonded to its sensor. This system represents an evolution of earlier CIS designs that measured multiple fixed delays, but is the first

of its kind to measure three fixed interferometer delays in this manner. This advancement enhanced the system's optical throughput compared to a quad-delay configuration, thereby enabling its use under low-light conditions while maintaining the high spectral resolution needed for imaging reactor plasmas and inferring physics parameters.

The integration of this system within the MAST-U MWI diagnostic—an optical polychromator—posed significant challenges related to image ghosting and focal plane position. In this thesis, we outlined solutions to these issues: image ghosting was eliminated by placing a beamsplitter in direct contact with the spectral bandpass filter, and the focal plane issue was resolved by adjusting the focal length of the system's collimating lens. These solutions facilitated the installation of this CIS system within an optical polychromator and provides a reference for future diagnostic designs, such as optical polychromators exclusively incorporating CIS systems.

5.2 Calibration Procedures

The calibration procedures developed for our triple-delay CIS system are a cornerstone of its success, addressing the challenges posed by equipment unavailability and diagnostic size restrictions commonly encountered on large fusion devices. Unlike previous CIS diagnostics, the absence of a tunable laser or the capacity to install an in-situ calibration mechanism on MAST-U necessitated the development of alternative strategies to ensure measurement accuracy and reproducibility. This thesis presents a comprehensive calibration framework designed to overcome these constraints.

To calibrate our system at 464.9 nm—the centre-of-mass wavelength of C III—we employed a previously established method that fits phase images measured at known wavelengths to instrument parameters such as crystal thickness,

lens focal length and crystal Sellmeier coefficients [83]. Through this process, we discovered that small rotational misalignments of components within the interferometer could significantly affect the measured phase, leading to incorrect inferences of instrument parameters. Using Mueller calculus, we derived and presented analytical equations for directly calculating the phase produced by a triple-delay pixelated CIS system. Analogous equations for a single and quad-delay pixelated CIS system have also been presented in appendix C of this thesis. By incorporating the orientation of each component into the fitting process, this method achieved up to a factor of 4 reduction in magnitude of misalignment artefacts, enabling effective system calibration.

In addition to generating phase calibration images for our system at the C III wavelength, we addressed the variation in these images due to temperature changes. This issue, typically resolved in CIS systems through in-situ calibration or precise temperature control—neither of which were available to us—was tackled by characterising the temperature dependence of each interferometer delay. This involved measuring the temperature of each crystal over an extended period and linearly fitting the observed variations in phase images to the crystal temperatures. This approach enabled accurate prediction of phase measurements based solely on measured crystal temperatures and calibration images previously acquired at known temperatures.

These advancements not only enhance the reliability of CIS systems but also provide a blueprint for adapting coherence imaging diagnostics in resource-constrained environments. The success of these calibration procedures underscores their broader applicability and their potential for integration into future diagnostic systems across a wide range of fusion devices.

5.3 MAST-U CIS Measurements of Temperature and Velocity

The goal of this thesis was to develop a coherence imaging spectroscopy system capable of measuring 2D C^{2+} parallel velocities and temperatures profiles in the MAST-U divertor for the first time. Achieving this objective represents a significant advancement in fusion diagnostic capabilities, providing data that could validate simulations and inform studies on detachment, a critical area of interest for future reactor design. The ability to measure ion temperature profiles also contributes to studies on the thermodynamic interplay between ions and electrons that leads to non-thermal equilibrium in the divertor ($T_i/T_e \neq 1$) [40].

In chapter 4, we presented an inversion procedure employing the L-BFGS-B algorithm to determine C^{2+} $v_{\parallel}$ and T_i profiles through logarithmic maximum likelihood estimation. The variable used to compute this log-likelihood function was the degree of coherence for each interferometer delay, enabling us to relate velocity to measured phase images and temperature to measured contrast. Using phase and contrast images calculated from SOLPS-ITER simulations of MAST-U elongated and Super-X divertor plasmas, with noise representative of experimental conditions applied, we demonstrated that this process could recover simulated $v_{\parallel}$ and T_i profiles with accuracies comparable to or better than those reported in previous CIS studies.

One of the key challenges in spectroscopic diagnostics is managing spectral contamination. When measuring C III in MAST-U, we observed significant contamination, primarily from background continuum emission and an O II emission line within the C III triplet. By inverting contaminated phase and contrast images, we showed that accurate profile determination under these

conditions requires the additional spectral information provided by a triple-delay or equivalent multi-delay diagnostic. However, for uncontaminated spectra, such as those typically encountered in laboratory plasma settings, a multi-delay CIS system would not be required to achieve the same level of accuracy.

Experimental deployment of our triple-delay system on MAST-U yielded 2D velocity and temperature profiles for Super-X divertor shot #48333 and elongated divertor shot #48334. For shot #48333, velocities ranged from 16.5–19.1 km/s, and temperatures ranged from 5–9.5 eV. For shot #48334, velocities were slightly higher, ranging from 19–24 km/s, while temperatures remained similar at 4–9.5 eV. The differences in velocity profiles reflect both the distinct magnetic geometries—lower detachment and flux expansion in the elongated case likely contributing to higher velocities—and the differing shot conditions, with the elongated shot exhibiting steadily increasing density compared to the constant core density observed in the Super-X configuration.

A notable success of this study was the direct comparison of our experimental profiles with Doppler shift measurements from the MAST-U Divertor Monitoring Spectrometer (DMS). This comparison showed a high level of agreement, validating the accuracy and reliability of our triple-delay system. However, a comparison of Doppler broadening (temperatures) was not possible due to the unavailability of the spectrometer's instrument function.

Further comparisons with the SOLPS-ITER simulations used to test our inversion process showed good quantitative agreement between the predicted and measured temperatures beyond the C III front in both divertor configurations. However, the same quantitative agreement was not observed before the C III front or in the velocity profiles, with differences of up to 9 km/s observed near the front. Despite this, when comparing how the velocities behaved relative to their maxima good agreement was found in the elongated case after the C III front and agreement within a factor of 2 before the C III

front. In the Super-X divertor case, the simulation's predicted peak velocity location was significantly farther from the front than observed experimentally, making a similar comparison impossible. These findings indicate that while SOLPS-ITER can, in general, effectively predict C^{2+} temperatures in the MAST-U divertor, further refinements are necessary to improve its ability to quantitatively model parallel velocities.

5.4 Future Work

The insights gained from the MAST-U experiments highlight the transformative potential of our triple-delay instrument in the study of fusion plasmas. By expanding diagnostic capabilities, this work not only establishes a foundation for deploying similar systems on next-generation fusion devices but also provides critical insights into the behaviour of impurity ions in the MAST-U divertor. In the following sections, we outline the diagnostic developments and studies that should be undertaken to further enhance CIS systems and deepen our understanding of their underlying principles. Additionally, we propose further physics studies aimed at improving simulation accuracy and advancing our understanding of divertor conditions.

5.4.1 Diagnostic Knowledge and Upgrades

Misalignment Study

In chapter 3, we demonstrated how the misalignment of components within a CIS interferometer can create artefacts in the measured phase images. Using the equations derived in this thesis—eqs. (3.11) to (3.13)—along with similar equations for single and quad-delay CIS systems derived in appendix C, a sensitivity study should be undertaken. The aim of this study would be to determine whether specific CIS configurations are more sensitive to misalign-

ments than others and to identify whether particular configurations are more affected by the misalignment of specific components within the interferometer.

To conduct this study, a high-precision optical setup should be constructed to minimise sources of error arising from the alignment of the crystal faces. Instrument parameters such as the focal length of the imaging lens, crystal thickness, crystal cut angle, and fast-axis orientation should be determined to high accuracy. Each component should be mounted within rotatable mounts that allow precise and quantifiable rotation, such as those provided by Thorlabs. With this setup different CIS configurations can be constructed and each component iteratively rotated, similar to the procedure undertaken by us in section 3.4.1. By measuring the phase at each iteration and precisely knowing the orientation of each component one could further refine our understanding of how misalignment affects measured phase.

Multi View CIS

A significant drawback of installing our instrument within the MAST-U MWI relates to the limited viewing angle of the MWI. This, combined with the high degree of detachment typically present in the MAST-U divertor, results in an inability to measure the entire C III emission region. For this reason, we suggest that future MAST-U CIS studies adopt a similar approach to that used in the installation of an X-point Imaging (XPI) system on MAST-U [22]. The XPI system was specifically designed to address gaps in the MWI's coverage, particularly high in the divertor and around the divertor entrance and baffle. Since, under detached conditions, the C III front is expected to fall within this region, the installation of two CIS systems—one with a view similar to the MWI and another with a view equivalent to the XPI—would enable a more comprehensive study of C^{2+} ion behaviour before and after the C III front.

5.4.2 Physics Studies

Simulation Validation

Further to the comparisons presented in section 4.4.3, a detailed study into SOLPS-ITER's ability to predict the behaviour of C^{2+} ions should be conducted. Initial simulations should focus on accurately predicting the location of the C III front to facilitate further investigations. Care should be taken when determining profiles across magnetic field lines, as the simulations used in this study demonstrated that SOLPS-ITER tends to underestimate the rate at which temperatures and velocities decrease perpendicular to the magnetic field.

Once confidence in SOLPS-ITER's ability to predict C^{2+} behaviour is established, it would be possible to conduct predictive studies under various conditions, such as those detailed below. However if ion behaviour can not be effectively simulated, such studies would inform the future development of SOLPS-ITER models and, consequently, future reactor design.

If effective simulation is achieved, studies should focus on predicting how fuelling rates and locations, as well as flux expansion, affect C^{2+} and other ion species in the divertor. This work would complement current detachment studies, which primarily focus on the region following the ionisation front where D_2 Fulcher emission is high [22, 105].

Investigation of T_i/T_e profiles

Measuring ion temperature (T_i) and electron temperature (T_e) in the divertor region of a tokamak is pivotal for advancing our understanding of plasma behaviour and improving fusion reactor performance. The ratio T_i/T_e plays a crucial role in influencing plasma dynamics, including energy transport, stability, and interactions with material surfaces. Combining our instrument's

capability to measure T_i profiles with another CIS system configured for T_e measurements would enable a detailed study of this ratio under the unique conditions present in MAST-U.

Recent studies have highlighted the importance of such measurements, with high-resolution spectroscopy on TCV providing insights into plasma detachment and energy dissipation mechanisms, showing that $T_i/T_e \simeq 1$ [106]. However, on MAST-U, retarding field energy analysers have observed this ratio to be closer to 0.5 [40]. This discrepancy suggests that a more detailed spatial study, facilitated by an imaging system such as ours, would be invaluable for understanding the conditions under which each ratio holds. Such investigations would provide critical data for optimising plasma performance and material interactions in tokamak reactors.

Appendix A

Component Specifications

Table A.1 summarises the specifications of each component used in the triple-delay pixelated CIS diagnostic developed in this work for MAST-U. All details in table A.1 were obtained from the manufacturer of each component.

Component	Manufacturer	Description
Camera[1]	Teledyne	**FLIR Blackfly S BFS-U3-51S5P-C** Sony IMX250MZR Polarised Sensor 2448x2048 px - CMOS Pixel Size: 3.45μm Quantum Efficiency: 17% at 435nm Polariser extinction ratio: 400 (at 435 nm)
C III Filter	Chroma Technology	CWL: 464.8±0.25 nm, Δ_{FWHM}: 2.1±0.1 nm
Collimating Lens, l_1	Eksma Optics	**110-0527E** $\varnothing$= 50.8 mm, f=600 mm
Imaging Lens, l_2	VS Technology	**SV-5014H** 50 mm f/1.4-16, C-Mount
α-BBO Waveplate[2]	CLaser Photonics	$\varnothing$= 30 mm, AR coated 400 - 700nm, L = 9.8 mm
α-BBO Displacer Plate[1]	Union Optics	Cut angle, $\theta = 45°$, $\varnothing$= 30 mm, L = 8 mm
Polariser[2]	Newport	Newport model **20LP-VIS** $\varnothing$= 30.5 mm, Extinction ratio = 25000 : 1
Temperature Controller[2]	Andover Corp	Andover Model **101FRDC00-CTRL** Regulation range 30°C - 60°C Regularion accuracy ±0.2°C
Temperature Cell[2]	Andover Corp	Andover Model **101FRDC00-50** $\varnothing_{inside}$ = 50 mm, $\varnothing_{outside}$ = 90 mm

Table A.1: Summary of component specifications for the MAST-U triple-delay CIS diagnostic. [1]Component previously used on Magnum-PSI in a quad-delay CIS system [61]. [2]Component previously used on MAST in a single-delay CIS system [30]. Each crystal and polariser was placed in custom mount designed at Australian National University. All quoted tolerances are those reported by the manufacturer of the component.

Appendix B

Triple-Delay CIS Mueller Matrices

In this thesis we presented the construction and use of a triple-delay pixelated CIS system. In chapters 2 and 3, we showed how Mueller matrices and Stokes vectors could be used to derive an equation for the interferogram produced by our system. The total Mueller matrix of a triple-delay system is given by eq. (B.1).

$$\begin{aligned}\mathbf{M}_{tot} \equiv \mathbf{M}_{pol}\left(m\frac{\pi}{4}\right) \times \mathbf{M}_{qwp}\left(\frac{\pi}{2}\right) \times \mathbf{M}_{ret}\left(\frac{\pi}{4}, \phi_2\right) \\ \times \mathbf{M}_{ret}\left(0, \phi_1\right) \times \mathbf{M}_{pol}\left(\frac{\pi}{8}\right)\end{aligned} \tag{B.1}$$

Below are the explicit Mueller matrices for each triple-delay CIS component, as defined by eq. (B.1).

$$\mathbf{M}_{pol}\left(\frac{\pi}{8}\right) = \frac{1}{4}\begin{pmatrix} 1 & \sqrt{2} & \sqrt{2} & 0 \\ \sqrt{2} & 1 & 1 & 0 \\ 0 & 1 & 1 & 0 \\ 0 & 0 & 0 & 0 \end{pmatrix} \tag{B.2}$$

$$\mathbf{M}_{ret}\left(0,\phi_1\right)=\begin{pmatrix}1&0&0&0\\0&1&0&0\\0&0&\cos(\phi_1)&-\sin(\phi_1)\\0&0&\sin(\phi_1)&\cos(\phi_1)\end{pmatrix} \tag{B.3}$$

$$\mathbf{M}_{ret}\left(\frac{\pi}{4},\phi_2\right)=\begin{pmatrix}1&0&0&0\\0&\cos(\phi_2)&0&\sin(\phi_2)\\0&0&1&0\\0&-\sin(\phi_2)&0&\cos(\phi_2)\end{pmatrix} \tag{B.4}$$

$$\mathbf{M}_{qwp}\left(\frac{\pi}{2}\right)=\begin{pmatrix}1&0&0&0\\0&1&0&0\\0&0&0&1\\0&0&-1&0\end{pmatrix} \tag{B.5}$$

$$\mathbf{M}_{pol}\left(m\frac{\pi}{4}\right)=\frac{1}{2}\begin{pmatrix}1&\cos\left(m\frac{\pi}{2}\right)&\sin\left(m\frac{\pi}{2}\right)&0\\\cos\left(m\frac{\pi}{2}\right)&\cos^2(m\frac{\pi}{2})&\cos\left(m\frac{\pi}{2}\right)\sin\left(m\frac{\pi}{2}\right)&0\\0&\cos\left(m\frac{\pi}{2}\right)\sin\left(m\frac{\pi}{2}\right)&\sin^2(m\frac{\pi}{2})&0\\0&0&0&0\end{pmatrix} \tag{B.6}$$

Appendix C

General CIS Phase Equations

In section 3.4.1, we presented the first analytical equations to calculate the phase images, Φ_2, Φ_{2+1} and Φ_{2-1}, produced by an arbitrary triple-delay CIS instrument based on the orientations of its components. In this appendix we complete this work by presenting analogous equations for the two other CIS configurations which consist of 3 and 5 interferometer components. The following equations were derived using Mueller calculus through the same process as in section 3.4.1, and will use equivalent notation repeated here for clarity.

$$\begin{aligned} \eta_{pol} &= \exp(2i\,\rho_{pol}) \quad \eta_{disp} = \exp(2i\,\rho_{disp}) \\ \eta_{wp} &= \exp(2i\,\rho_{wp}) \quad \eta_{qwp} = \exp(2i\,\rho_{qwp}) \end{aligned} \tag{C.1}$$

Similar to a triple-delay system, a double-delay system is a special case of a 4 component CIS interferometer, which contains a linear polariser, displacer plate, waveplate and quarter waveplate in that order. It only differs from a triple-delay system by the orientation of its front polariser, which is oriented parallel to the waveplate, eq. (C.2), resulting in only Φ_{2+1} and Φ_{2-1} being measured. As eqs. (3.12) and (3.13) use the exact orientation of each component ρ_n, these equations are also valid for a double-delay system.

$$\mathbf{M}_{tot} \equiv \mathbf{M}_{pol}\left(m\frac{\pi}{4}\right) \times \mathbf{M}_{qwp}\left(\frac{\pi}{2}\right) \times \mathbf{M}_{ret}\left(\frac{\pi}{4}, \phi_2\right) \times \mathbf{M}_{ret}\left(0, \phi_1\right) \times \mathbf{M}_{pol}\left(\frac{\pi}{4}\right) \tag{C.2}$$

C.1 Single-Delay

As discussed in section 2.5.2, a single-delay PPM CIS system contains three components: a linear polariser, waveplate and quarter waveplate. When oriented according to eq. (C.3) it will produce a single interferometer delay equal to that calculated via eq. (2.50). The general equation phase image produced by this system is given by eq. (C.6).

$$\mathbf{M}_{tot} = \mathbf{M}_{pm}\left(m\frac{\pi}{4}\right)\mathbf{M}_{qwp}\left(\frac{\pi}{2}\right)\mathbf{M}_{wp}\left(\frac{\pi}{4}, \phi(\nu)\right)\mathbf{M}_{pol}\left(0\right) \tag{C.3}$$

$$\eta_{1,\pm} = 4\frac{\eta_{wp}^2 \pm \eta_{pol}^2}{\eta_{pol}\eta_{wp}^2\eta_{qwp}^2}e^{-i\phi_{\,qwp}} \tag{C.4}$$

$$\eta_{2,\pm} = \eta_{qwp} \pm \eta_{wp}\left[\eta_{qwp} \mp \eta_{wp}\right]e^{i\phi_{\,qwp}} \tag{C.5}$$

$$\Phi = \arg\left(2\,\eta_{1,+}\,\eta_{2,+}\,\eta_{2,-} + \eta_{1,+}\left[\eta_{2,+}^2 + \eta_{2,-}^2\right]\right) \tag{C.6}$$

C.2 Quad-Delay

The final configuration, of which the quad-delay system used on Magnum PSI is a special case, is a 5 component CIS system [67]. The component order is: linear polariser, displacer plate, linear polariser, waveplate and quarter waveplate. Using these components 4 distinct interferometer delays can be created when components are oriented as indicated in eq. (C.7), where the

linear polarisers are distinguished by p_1 and p_2. This configuration is discussed in greater detail in section 2.6.

$$\mathbf{M}_{tot} = \mathbf{M}_{pm}\left(\rho_{pm}\right)\mathbf{M}_{qwp}\left(\tfrac{\pi}{2}\right)\mathbf{M}_{wp}\left(\tfrac{\pi}{4},\phi_2(\nu)\right)\mathbf{M}_{p_2}\left(0\right)\mathbf{M}_{disp}\left(\tfrac{\pi}{4},\phi_1(\nu)\right)\mathbf{M}_{p_1}\left(0\right) \tag{C.7}$$

Similar to appendix C.1, below we redefined η_1, η_2 and η_3 for simplicity. The general equation of the phase image, Φ_1, associated with the displacer plate is then given by eq. (C.11) and Φ_2, Φ_{2+1} and Φ_{2-1} are given by eqs. (C.12) to (C.14), respectively.

$$\eta_{1,\pm} = \frac{\eta_{p1}^2 \pm \eta_{p2}^2}{\eta_{disp}^2\,\eta_{p1}\,\eta_{p2}^2\,\eta_{wp}^2\,\eta_{qwp}^2} e^{-i\phi_{\,qwp}} \tag{C.8}$$

$$\eta_{2,\pm} = \left(\eta_{disp}^2 \pm \eta_{p1}^2\right)\left(\eta_{disp}^2 \pm \eta_{p2}^2\right) \tag{C.9}$$

$$\eta_{3,\pm} = \eta_{qwp} \pm \eta_{wp} + e^{i\phi_{\,qwp}}\left(\eta_{qwp} \mp \eta_{wp}\right) \tag{C.10}$$

$$\Phi_1 = \arg\left(-\frac{\eta_{2,-}}{\eta_{disp}^2\eta_{p1}\eta_{p2}}\left[e^{i\phi_1} + e^{-i\phi_1}\right]\right) \tag{C.11}$$

$$\begin{aligned}\Phi_2 = \arg\Big(&\left[2\,\eta_{1,+}\eta_{3,-}\eta_{3,+}^2 - \eta_{1,-}\left(\eta_{3,-}^2 e^{i\phi_2} + \eta_{3,+} e^{-i\phi_1}\right)\right] \\ &\cdot\left[\eta_{2,+} + 4\,\eta_{disp}\,\eta_{p1}\,\eta_{p2}\right]\Big)\end{aligned} \tag{C.12}$$

$$\begin{aligned}\Phi_{2+1} = \arg\Big(&\eta_{1,-}\,\eta_{2,-}\left(\eta_{3,-}^2 e^{i\phi_{2+1}} + \eta_{3,+}^2 e^{-i\phi_{2-1}}\right) \\ &- 2\,\eta_{1,+}\,\eta_{2,-}\,\eta_{3,-}\,\eta_{3,+}^2\,e^{i\phi_1}\Big)\end{aligned} \tag{C.13}$$

$$\begin{aligned}\Phi_{2-1} = \arg\Big(&\eta_{1,-}\,\eta_{2,-}\left(\eta_{3,-}^2 e^{i\phi_{2-1}} + \eta_{3,+}^2 e^{-i\phi_{2+1}}\right) \\ &- 2\,\eta_{1,+}\,\eta_{2,-}\,\eta_{3,-}\,\eta_{3,+}^2\,e^{-i\phi_1}\Big)\end{aligned} \tag{C.14}$$

Bibliography

[1] H. Ritchie and P. Rosado, "Energy mix," *Our World in Data*, 2024. https://ourworldindata.org/energy-mix.

[2] D. J. Ward, I. Cook, Y. Lechon, and R. Saez, "The economic viability of fusion power," *Fusion Engineering and Design*, vol. 75-79, pp. 1221–1227, 11 2005.

[3] R. Toschi, "Nuclear fusion, an energy source," *Fusion Engineering and Design*, vol. 36, pp. 1–8, 4 1997.

[4] J. Ongena and G. V. Oost, "Energy for future centuries will fusion be an inexhaustible, safe and clean energy source?," *Fusion Science and Technology*, vol. 41, pp. 3–14, 2002.

[5] J. D. Lawson, "Some criteria for a power producing thermonuclear reactor," *Proceedings of the Physical Society. Section B*, vol. 70, p. 6, 1 1957.

[6] K. S. Krane and W. G. Lynch, "Introductory nuclear physics," *Physics Today*, vol. 42, pp. 78–78, 1 1989.

[7] K. D. Meaney, Y. Kim, H. Geppert-Kleinrath, H. W. Herrmann, A. S. Moore, E. P. Hartouni, D. J. Schlossberg, E. Mariscal, J. Carrera, and J. A. Church, "Total fusion yield measurements using deuterium-tritium gamma rays," *Physics of Plasmas*, vol. 28, 10 2021.

[8] J. Wesson and D. J. Campbell, *Tokamaks*. Oxford University Press, 2011.

[9] R. Betti and O. A. Hurricane, "Inertial-confinement fusion with lasers," *Nature Physics 2016 12:5*, vol. 12, pp. 435–448, 5 2016.

[10] R. Aymar, P. Barabaschi, and Y. Shimomura, "The iter design," *Plasma Physics and Controlled Fusion*, vol. 44, p. 519, 4 2002.

[11] R. Kemp, R. Wenninger, G. Federici, H. Reimerdes, R. Ambrosino, R. Brown, and M. Coleman, "Exploring a broad spectrum of design options for demo," *Fusion Engineering and Design*, vol. 136, pp. 970–974, 11 2018.

[12] R. J. Goldston, "Heuristic drift-based model of the power scrape-off width in low-gas-puff h-mode tokamaks," *Nuclear Fusion*, vol. 52, p. 013009, 12 2011.

[13] J. Milnes, N. B. Ayed, F. Dhalla, G. Fishpool, J. Hill, I. Katramados, R. Martin, G. Naylor, T. O'Gorman, and R. Scannell, "Mast upgrade – construction status," *Fusion Engineering and Design*, vol. 96-97, pp. 42–47, 10 2015.

[14] P. M. Valanju, M. Kotschenreuther, S. M. Mahajan, and J. Canik, "Super-x divertors and high power density fusion devices," *Physics of Plasmas*, vol. 16, 5 2009.

[15] W. Morris, J. R. Harrison, A. Kirk, B. Lipschultz, F. Militello, D. Moulton, and N. R. Walkden, "Mast upgrade divertor facility: A test bed for novel divertor solutions," *IEEE Transactions on Plasma Science*, vol. 46, pp. 1217–1226, 5 2018.

[16] A. Loarte, B. Lipschultz, A. S. Kukushkin, G. F. Matthews, P. C. Stangeby, N. Asakura, G. F. Counsell, G. Federici, A. Kallenbach, K. Krieger, A. Mahdavi, V. Philipps, D. Reiter, J. Roth, J. Strachan, D. Whyte, R. Doerner, T. Eich, W. Fundamenski, A. Herrmann, M. Fenstermacher, P. Ghendrih, M. Groth, A. Kirschner, S. Konoshima, B. Labombard, P. Lang, A. W. Leonard, P. Monier-Garbet, R. Neu, H. Pacher, B. Pegourie, R. A. Pitts, S. Takamura, J. Terry, and E. Tsitrone, "Chapter 4: Power and particle control," *Nuclear Fusion*, vol. 47, p. S203, 6 2007.

[17] R. A. Pitts, S. Carpentier, F. Escourbiac, T. Hirai, V. Komarov, A. S. Kukushkin, S. Lisgo, A. Loarte, M. Merola, R. Mitteau, A. R. Raffray, M. Shimada, and P. C. Stangeby, "Physics basis and design of the iter plasma-facing components," *Journal of Nuclear Materials*, vol. 415, pp. S957–S964, 8 2011.

[18] J. H. You, H. Greuner, B. Böswirth, K. Hunger, S. Roccella, and H. Roche, "High-heat-flux performance limit of tungsten monoblock targets: Impact on the armor materials and implications for power exhaust capacity," *Nuclear Materials and Energy*, vol. 33, p. 101307, 10 2022.

[19] E. Havlíčková, J. Harrison, B. Lipschultz, G. Fishpool, A. Kirk, A. Thornton, M. Wischmeier, S. Elmore, and S. Allan, "Solps analysis of the mast-u divertor with the effect of heating power and pumping on the access to detachment in the super-x configuration," *Plasma Physics and Controlled Fusion*, vol. 57, 8 2015.

[20] A. Fil, B. Lipschultz, D. Moulton, A. Thornton, B. Dudson, O. Myatra, and K. Verhaegh, "Comparison between mast-u conventional and super-x configurations through solps-iter modelling," *Nuclear Fusion*, vol. 62, p. 096026, 8 2022.

[21] D. Moulton, J. R. Harrison, L. Xiang, P. J. Ryan, A. Kirk, K. Verhaegh, T. A. Wijkamp, F. Federici, J. G. Clark, and B. Lipschultz, "Super-x and conventional divertor configurations in mast-u ohmic l-mode; a comparison facilitated by interpretative modelling," *Nuclear Fusion*, vol. 64, p. 076049, 6 2024.

[22] K. Verhaegh, J. Harrison, B. Lipschultz, N. Lonigro, S. Kobussen, D. Moulton, N. Osborne, P. Ryan, C. Theiler, T. Wijkamp, D. Brida, G. Derks, R. Doyle, F. Federici, A. Hakola, S. Henderson, B. Kool, S. Newton, R. Osawa, X. Pope, H. Reimerdes, N. Vianello, and M. Wischmeier, "Investigations of atomic and molecular processes of nbi-heated discharges in the mast upgrade super-x divertor with implications for reactors," *Nuclear Fusion*, vol. 64, p. 086050, 7 2024.

[23] R. Maurizio, A. W. Leonard, J. H. Yu, J. Harrison, K. Verhaegh, N. Lonigro, and A. G. McLean, "Solps-iter modeling of divertor detachment in mast-u's super-x double null configuration and comparison to experiment," *Nuclear Materials and Energy*, vol. 41, p. 101736, 12 2024.

[24] I. H. Hutchinson, "Principles of plasma diagnostics," *Principles of Plasma Diagnostics*, 7 2002.

[25] H. J. Leggate, "Impurity transport modelling in the scrape off layer of the mast tokamak using divimp-osm-eirene and carbon injection," 2015.

[26] R. A. Pitts, "Ion velocity distributions at the tokamak edge," *Physics of Fluids B: Plasma Physics*, vol. 3, pp. 2871–2876, 10 1991.

[27] N. Yoneda, T. Shikama, K. Hanada, S. Mori, T. Onchi, K. Kuroda, M. Hasuo, A. Ejiri, K. Matsuzaki, Y. Osawa, Y. Peng, Y. Kawamata, S. Sakamoto, H. Idei, T. Ido, K. Nakamura, Y. Nagashima, R. Ikezoe,

M. Hasegawa, A. Higashijima, T. Nagata, and S. Shimabukuro, "Toroidal flow measurements of impurity ions in quest ech plasmas using multiple viewing chords emission spectroscopy," *Nuclear Materials and Energy*, vol. 26, p. 100905, 3 2021.

[28] K. Uehara, T. Kawakami, H. Amemiya, K. Höthker, A. Cosler, and W. Bieger, "Measurements of ion temperature and flow velocity using symmetric and asymmetric double probes in the boundary plasma of the jft-2m tokamak," *Nuclear Fusion*, vol. 38, p. 1665, 11 1998.

[29] B. LaBombard, J. Goetz, C. Kurz, D. Jablonski, B. Lipschultz, G. McCracken, A. Niemczewski, R. L. Boivin, F. Bombarda, C. Christensen, S. Fairfax, C. Fiore, D. Garnier, M. Graf, S. Golovato, R. Granetz, M. Greenwald, S. Horne, A. Hubbard, I. Hutchinson, J. Irby, J. Kesner, T. Luke, E. Marmar, M. May, P. O'Shea, M. Porkolab, J. Reardon, J. Rice, J. Schachter, J. Snipes, P. Stek, Y. Takase, J. Terry, G. Tinios, R. Watterson, B. Welch, and S. Wolfe, "Scaling and transport analysis of divertor conditions on the alcator c-mod tokamak," *Physics of Plasmas*, vol. 2, pp. 2242–2248, 6 1995.

[30] S. A. Silburn, "A doppler coherence imaging diagnostic for the mega-amp spherical tokamak," 2014.

[31] M. Kočan, J. P. Gunn, S. Carpentier-Chouchana, A. Herrmann, A. Kirk, M. Komm, H. W. Müller, J. Y. Pascal, R. A. Pitts, V. Rohde, and P. Tamain, "Measurements of ion energies in the tokamak plasma boundary," *Journal of Nuclear Materials*, vol. 415, pp. S1133–S1138, 8 2011.

[32] K.-S. Chung, "Mach probes," *Plasma Sources Science and Technology*, vol. 21, 12 2012.

[33] N. Asakura, "Understanding the sol flow in l-mode plasma on divertor tokamaks, and its influence on the plasma transport," *Journal of Nuclear Materials*, vol. 363-365, pp. 41–51, 6 2007.

[34] S. K. Erents, R. A. Pitts, W. Fundamenski, J. P. Gunn, and G. F. Matthews, "A comparison of experimental measurements and code results to determine flows in the jet sol," *Plasma Physics and Controlled Fusion*, vol. 46, p. 1757, 9 2004.

[35] D. Gradic, V. Perseo, D. M. Kriete, M. Krychowiak, R. König, Y. Feng, M. Otte, T. S. Pedersen, Y. Gao, M. Jakubowski, G. Schlisio, and F. Warmer, "2d coherence imaging measurements of c2+ion temperatures in the divertor of wendelstein 7-x," *Nuclear Fusion*, vol. 61, 10 2021.

[36] K. Verhaegh, B. Lipschultz, J. R. Harrison, N. Osborne, A. C. Williams, P. Ryan, J. Allcock, J. G. Clark, F. Federici, B. Kool, T. Wijkamp, A. Fil, D. Moulton, O. Myatra, A. Thornton, T. O. Bosman, C. Bowman, G. Cunningham, B. P. Duval, S. Henderson, and R. Scannell, "Spectroscopic investigations of detachment on the mast upgrade super-x divertor," *Nuclear Fusion*, vol. 63, p. 016014, 12 2022.

[37] J. Gafert, K. Behringer, D. Coster, C. Dorn, K. Hirsch, M. Niethammer, and U. Schumacher, "First experimental determination of ion flow velocities and temperatures in the asdex upgrade divertor," *Plasma Physics and Controlled Fusion*, vol. 39, p. 1981, 12 1997.

[38] Fredriksen, W. J. Miloch, N. Gulbrandsen, and L. N. Mishra, "On the use of a retarding field energy analyzer for plasma flow analysis," *Contributions to Plasma Physics*, vol. 53, pp. 86–91, 1 2013.

[39] K. Kreuger, Z. Huang, M. Jiang, G. Xu, W. Zhang, H. Wang, J. Cheng, W. Hong, L. Yan, and C. Xiao, "Simultaneous ion temperature and flow measurements using a retarding field analyzer in the hl-2a tokamak," *https://doi.org/10.1080/10420150.2013.831855*, vol. 168, pp. 776–788, 10 2013.

[40] Y. Damizia, S. Elmore, K. Verhaegh, P. Ryan, S. Allan, F. Federici, N. Osborne, J. W. Bradley, the MAST-U Team, and the EUROfusion Tokamak Exploitation Team, "Ion temperature measurements in the mast-u divertor during steady state plasmas and elm burn through phenomena," 11 2024.

[41] K. Verhaegh, B. Lipschultz, J. Harrison, F. Federici, D. Moulton, N. Lonigro, S. Kobussen, M. O'Mullane, N. Osborne, P. Ryan, T. Wijkamp, B. Kool, E. Rose, C. Theiler, and A. Thornton, "The role of plasma–atom and molecule interactions on power particle balance during detachment on the mast upgrade super-x divertor," *Nuclear Fusion*, vol. 63, p. 126023, 10 2023.

[42] S. L. Allen, C. M. Samuell, W. H. Meyer, A. E. Jaervinen, G. D. Porter, and T. Rognlien, "Calibrated helium and carbon ion flow measurements in the diii-d divertor plasma," *Nuclear Materials and Energy*, vol. 19, pp. 137–142, 5 2019.

[43] A. S. SCOTT, "A doppler coherence imaging diagnostic for the mega-amp spherical tokamak," 2014.

[44] T. Morgan, "Measurement of mast edge ion temperatures and velocities," 2011.

[45] J. R. Harrison and et al., "Overview of physics results from mast upgrade towards core-pedestal-exhaust integration," *Nuclear Fusion*, vol. 64, p. 112017, 8 2024.

[46] H. P. Summers, "The adas user manual," 2004.

[47] T. Fujimoto, *Plasma Spectroscopy*. Springer, 2008.

[48] N. Konjević, A. Lesage, J. R. Fuhr, and W. L. Wiese, "Experimental stark widths and shifts for spectral lines of neutral and ionized atoms (a critical review of selected data for the period 1989 through 2000)," *Journal of Physical and Chemical Reference Data*, vol. 31, pp. 819–927, 9 2002.

[49] M. Born, E. Wolf, A. B. Bhatia, P. C. Clemmow, D. Gabor, A. R. Stokes, A. M. Taylor, P. A. Wayman, and W. L. Wilcock, *Principles of Optics: Electromagnetic Theory of Propagation, Interference and Diffraction of Light*. Cambridge University Press, 7 ed., 1999.

[50] N. Wiener, *Time Series*. M.I.T. Press, 1964.

[51] S. P. Davis, M. C. Abrams, and J. W. Brault, "5 - Nonideal (real-world) interferograms," in *Fourier Transform Spectrometry* (S. P. Davis, M. C. Abrams, and J. W. Brault, eds.), pp. 67–80, San Diego: Academic Press, 2001.

[52] C. Shannon, "Communication in the presence of noise," *Proceedings of the IRE*, vol. 37, pp. 10–21, jan 1949.

[53] P. Urlings, "Multiple delay coherence imaging charge exchange recombination spectroscopy — eindhoven university of technology research portal," 2015.

[54] C. Fabry and A. Pérot, "héorie et applications d'une nouvelle méthode de spectroscopie interférentiell," *Ann. de Chim. et de Phys*, vol. 16, pp. 115–144, 1899.

[55] J. M. Vaughan, "The fabry-perot interferometer: History, theory, practice and applications," *The Fabry-Perot Interferometer: History, Theory, Practice and Applications*, pp. 1–583, 1 2017.

[56] C. A. Michael, "Doppler spectroscopy of argon plasmas in h-1nf using a coherence imaging camera," 2003.

[57] E. Hecht, *Hecht's Response*, vol. 48. AIP Publishing, 1 2010.

[58] J. Howard, R. Jaspers, O. Lischtschenko, E. Delabie, and J. Chung, "Imaging charge exchange recombination spectroscopy on the textor tokamak," *Plasma Physics and Controlled Fusion*, vol. 52, p. 125002, 11 2010.

[59] W. H. Steel, *Interferometry*. Cambridge University Press, 1983.

[60] M. C. Simon and K. V. Gottschalk, "Waves and rays in uniaxial birefringent crystals," *Optik*, vol. 118, pp. 457–470, 10 2007.

[61] J. S. Allcock, "New techniques for coherence imaging fusion plasmas," 2021.

[62] F. E. Veiras, L. I. Perez, and M. T. Garea, "Phase shift formulas in uniaxial media: an application to waveplates," *Applied Optics, Vol. 49, Issue 15, pp. 2769-2777*, vol. 49, pp. 2769–2777, 5 2010.

[63] G. Tamošauskas, G. Beresnevičius, D. Gadonas, and A. Dubietis, "Transmittance and phase matching of bbo crystal in the 3x02212;5 x003bc;m range and its application for the characterization of mid-infrared laser

pulses," *Optical Materials Express, Vol. 8, Issue 6, pp. 1410-1418*, vol. 8, pp. 1410–1418, 6 2018.

[64] M. P. Kothiyal and C. Delisle, "Shearing interferometer for phase shifting interferometry with polarization phase shifter," *Applied Optics, Vol. 24, Issue 24, pp. 4439-4442*, vol. 24, pp. 4439–4442, 12 1985.

[65] J. E. Millerd, N. J. Brock, J. B. Hayes, M. B. North-Morris, M. Novak, and J. C. Wyant, "Pixelated phase-mask dynamic interferometer," *https://doi.org/10.1117/12.560807*, vol. 5531, pp. 304–314, 8 2004.

[66] M. Novak, J. Millerd, N. Brock, M. North-Morris, J. Hayes, and J. Wyant, "Analysis of a micropolarizer array-based simultaneous phase-shifting interferometer," *Applied Optics, Vol. 44, Issue 32, pp. 6861-6868*, vol. 44, pp. 6861–6868, 11 2005.

[67] J. S. Allcock, S. A. Silburn, R. M. Sharples, J. R. Harrison, N. J. Conway, and J. W. Vernimmen, "2d measurements of plasma electron density using coherence imaging with a pixelated phase mask," *Review of Scientific Instruments*, vol. 92, p. 073506, 7 2021.

[68] J. J. MICHEL, "Mesure de la visibilitÉ d'une raie de plasma," *Le Journal de Physique Colloques*, vol. 28, pp. C2–109, 3 1967.

[69] J. Howard, "Electro-optically modulated polarizing fourier-transform spectrometer for plasma spectroscopy applications," *Applied Optics, Vol. 41, Issue 1, pp. 197-208*, vol. 41, pp. 197–208, 1 2002.

[70] J. Chung, R. König, J. Howard, M. Otte, and T. Klinger, "Time resolved coherence-imaging spectrometer on wega stellarator," *Plasma Physics and Controlled Fusion*, vol. 47, p. 919, 5 2005.

[71] T. R. Weber, S. L. Allen, and J. Howard, "C-iii flow measurements with a coherence imaging spectrometer," *Review of Scientific Instruments*, vol. 83, pp. 10–102, 10 2012.

[72] T. R. Weber, G. D. Porter, E. T. Meier, S. L. Allen, and J. Howard, "Impurity flow measurements at diii-d using a coherence imaging spectrometer," *Journal of Nuclear Materials*, vol. 438, pp. S1257–S1260, 7 2013.

[73] C. M. Samuell, S. L. Allen, W. H. Meyer, R. C. Isler, A. Briesemeister, R. S. Wilcox, C. J. Lasnier, A. G. McLean, and J. Howard, "Verification of doppler coherence imaging for 2d ion velocity measurements on diii-d," *Review of Scientific Instruments*, vol. 89, p. 93502, 9 2018.

[74] S. L. Allen, C. M. Samuell, W. H. Meyer, and J. Howard, "Laser calibration of the diii-d coherence imaging system," *Review of Scientific Instruments*, vol. 89, 10 2018.

[75] C. M. Samuell, S. L. Allen, W. H. Meyer, and J. Howard, "Absolute calibration of doppler coherence imaging velocity images," *Journal of Instrumentation*, vol. 12, p. C08016, 8 2017.

[76] D. Gradic, O. P. Ford, A. Burckhart, F. Effenberg, H. Frerichs, R. König, T. Lunt, V. Perseo, and R. C. Wolf, "Doppler coherence imaging of divertor and sol flows in asdex upgrade and wendelstein 7-x," *Plasma Physics and Controlled Fusion*, vol. 60, p. 084007, 8 2018.

[77] V. Perseo, F. Effenberg, D. Gradic, R. König, O. P. Ford, F. Reimold, D. A. Ennis, O. Schmitz, and T. S. Pedersen, "Direct measurements of counter-streaming flows in a low-shear stellarator magnetic island topology," *Nuclear Fusion*, vol. 59, p. 124003, 9 2019.

[78] D. M. Kriete, V. Perseo, D. Gradic, D. A. Ennis, R. König, D. A. Maurer, and W.-X. Team, "Multi-delay coherence imaging spectroscopy optimized for ion temperature measurements in the divertor plasma of the wendelstein 7-x stellarator," *Review of Scientific Instruments*, vol. 95, p. 073503, 07 2024.

[79] X. Feng, A. Calcines, R. M. Sharples, B. Lipschultz, A. Perek, W. A. Vijvers, J. R. Harrison, J. S. Allcock, Y. Andrebe, B. P. Duval, and R. T. Mumgaard, "Development of an 11-channel multi wavelength imaging diagnostic for divertor plasmas in mast upgrade," *Review of Scientific Instruments*, vol. 92, p. 63510, 6 2021.

[80] A. Perek, W. A. Vijvers, Y. Andrebe, I. G. Classen, B. P. Duval, C. Galperti, J. R. Harrison, B. L. Linehan, T. Ravensbergen, K. Verhaegh, and M. R. D. Baar, "Mantis: A real-time quantitative multispectral imaging system for fusion plasmas," *Review of Scientific Instruments*, vol. 90, p. 102014, 12 2019.

[81] M. Servin, J. A. Quiroga, and J. M. Padilla, *Fringe pattern analysis for optical metrology: Theory, algorithms, and applications.* Wiley-VCH, 2014.

[82] D. Gradic, V. Perseo, R. König, and D. Ennis, "A new calibration implementation for doppler coherence imaging spectroscopy," *Fusion Engineering and Design*, vol. 146, pp. 995–998, 9 2019.

[83] J. S. Allcock, S. A. Silburn, R. M. Sharples, J. R. Harrison, N. J. Conway, T. Long, and N. Lin, "Wavelength calibration of birefringent interferometers for 2-d measurement of plasma flow," *Optics Express, Vol. 31, Issue 2, pp. 1901-1915*, vol. 31, pp. 1901–1915, 1 2023.

[84] V. Perseo, D. Gradic, R. König, O. P. Ford, C. Killer, O. Grulke, and D. A. Ennis, "Coherence imaging spectroscopy at wendelstein 7-x for impurity flow measurements," *Review of Scientific Instruments*, vol. 91, p. 013501, 1 2020.

[85] M. Duda, M. Dŭsek, O. Novák, and M. Smrž, "New measurement of the thermal expansion coefficient of -bab2o4," *Laser Congress 2021 (ASSL,LAC) (2021), paper JM3A.34*, p. JM3A.34, 10 2021.

[86] I. Waters, H. Frerichs, S. Silburn, Y. Feng, J. Harrison, A. Kirk, and O. Schmitz, "Field aligned flows driven by neutral puffing at mast," *Nuclear Fusion*, vol. 58, p. 066002, 6 2018.

[87] P. A. Popov, N. V. Moiseev, A. E. Kokh, and K. A. Kokh, "Thermal conductivity and heat capacity of - and -bab 2o 4 single crystals," *Inorganic Materials*, vol. 47, pp. 163–166, 2 2011.

[88] C. Sang, R. Ding, X. Bonnin, L. Wang, and D. Wang, "Effects of carbon impurities on the power radiation and tungsten target erosion in east," *Physics of Plasmas*, vol. 25, p. 72511, 7 2018.

[89] M. Osakabe, H. Takahashi, K. Nagaoka, S. Murakami, I. Yamada, M. Yoshinuma, K. Ida, M. Yokoyama, R. Seki, H. Lee, Y. Nakamura, N. Tamura, S. Sudo, K. Tanaka, T. Seki, Y. Takeiri, O. Kaneko, and H. Yamada, "Impact of carbon impurities on the confinement of high-ion-temperature discharges in the large helical device," *Plasma Physics and Controlled Fusion*, vol. 56, p. 095011, 7 2014.

[90] T. P. E. Modelling, X. Bonnin, W. Dekeyser, R. Pitts, D. Coster, S. Voskoboynikov, and S. Wiesen, "Presentation of the new solps-iter code package for," *Plasma and Fusion Research*, vol. 11, pp. 1–6, 2016.

[91] A. Andersen, "Simultaneous algebraic reconstruction technique (sart): A superior implementation of the art algorithm," *Ultrasonic Imaging*, vol. 6, pp. 81–94, 1 1984.

[92] T. Wijkamp, J. Allcock, X. Feng, B. Kool, B. Lipschultz, K. Verhaegh, B. Duval, J. Harrison, L. Kogan, N. Lonigro, A. Perek, P. Ryan, R. Sharples, I. Classen, and R. Jaspers, "Characterisation of detachment in the mast-u super-x divertor using multi-wavelength imaging of 2d atomic and molecular emission processes," *Nuclear Fusion*, vol. 63, p. 056003, 3 2023.

[93] R. H. Byrd, P. Lu, J. Nocedal, and C. Zhu, "A limited memory algorithm for bound constrained optimization," *https://doi.org/10.1137/0916069*, vol. 16, pp. 1190–1208, 7 2006.

[94] R. Tibshirani, "Regression shrinkage and selection via the lasso," *Journal of the Royal Statistical Society. Series B (Methodological)*, vol. 58, no. 1, pp. 267–288, 1996.

[95] A. E. Hoerl and R. W. Kennard, "Ridge regression: Biased estimation for nonorthogonal problems," *Technometrics*, vol. 12, no. 1, pp. 55–67, 1970.

[96] D. Gradic, M. Krychowiak, R. König, F. Henke, M. Otte, V. Perseo, and T. S. Pedersen, "Impurity temperatures measured via line shape analysis in the island scrape-off-layer of wendelstein 7-x," *Plasma Physics and Controlled Fusion*, vol. 64, 7 2022.

[97] M. Bakhtiari, G. J. Kramer, M. Takechi, H. Tamai, Y. Miura, Y. Kusama, and Y. Kamada, "Role of bremsstrahlung radiation in limiting the energy of runaway electrons in tokamaks," *Physical Review Letters*, vol. 94, p. 215003, 6 2005.

[98] I. Fidone, R. L. Meyer, G. Giruzzi, and G. Granata, "Temperature dependence of synchrotron radiation loss in inhomogeneous tokamak plasmas," *Physics of Fluids B: Plasma Physics*, vol. 4, pp. 4051–4056, 12 1992.

[99] M. N. Rosenbluth, "Synchrotron radiation in tokamaks," *Nuclear Fusion*, vol. 10, p. 340, 9 1970.

[100] A. Tabasso, G. F. Counsell, D. Hole, and J. P. Coad, "Observations of hydrocarbon film deposition in the mast tokamak," *Journal of Nuclear Materials*, vol. 306, pp. 73–77, 11 2002.

[101] C. Giroud, A. Meakins, M. Carr, A. Baciero, and C. Bertrand, "Cherab spectroscopy modelling framework (version v0.1.0)," 2018.

[102] I. Jolliffe, *Principal Component Analysis*. Springer-Verlag, 2 ed., 2002.

[103] A. A. Green, M. Berman, P. Switzer, and M. D. Craig, "A transformation for ordering multispectral data in terms of image quality with implications for noise removal," *IEEE Transactions on Geoscience and Remote Sensing*, vol. 26, pp. 65–74, 1988.

[104] T. Ravensbergen, M. van Berkel, A. Perek, C. Galperti, B. P. Duval, O. Février, R. J. van Kampen, F. Felici, J. T. Lammers, C. Theiler, J. Schoukens, B. Linehan, M. Komm, S. Henderson, D. Brida, and M. R. de Baar, "Real-time feedback control of the impurity emission front in tokamak divertor plasmas," *Nature Communications 2021 12:1*, vol. 12, pp. 1–9, 2 2021.

[105] N. Osborne, K. Verhaegh, M. D. Bowden, T. Wijkamp, N. Lonigro, P. Ryan, E. Pawelec, B. Lipschultz, V. Soukhanovskii, and T. van den Biggelaar, "Initial fulcher band observations from high resolution spec-

troscopy in the mast-u divertor," *Plasma Physics and Controlled Fusion*, vol. 66, p. 025008, 12 2023.

[106] L. Martinelli, D. Mikitchuck, B. P. Duval, Y. Andrebe, P. Blanchard, O. Février, S. Gorno, H. Elaian, B. L. Linehan, A. Perek, C. Stollberg, and B. Vincent, "Implementation of high-resolution spectroscopy for ion (and electron) temperature measurements of the divertor plasma in the tokamak à configuration variable," *Review of Scientific Instruments*, vol. 93, p. 123505, 12 2022.